In recent years, the ability to fabricate and investigate graphene-based nanostructures has been increasing constantly. In addition, great progress has been made towards reaching the coherent ballistic transport regime in graphene systems. These developments call for a generic theoretical description and analysis of the electronic properties of ballistic graphene nanostructures, in particular in view of effects related to the system boundaries. In this thesis we provide an analytical theory of edge effects on the spectral density of states and the quantum transport properties of these systems, extending semiclassical approaches to the case of graphene. It is shown that the characteristics of the system edges have strong impact on spectrum and conductance. Numerical tight-binding simulations support these analytical predictions. Finally, numerical studies of graphene nanoribbons are presented, which show that edge scattering can have important consequences on quantum interference effects also in weakly disordered systems.

Universitätsverlag Regensburg

ISBN 978-3-86845-084-2

gefördert von:

Alumni der physikalischen Fakultät der Universität Regensburg e.V.

Universität Regensburg

Jürgen Wurm

Dissertationsreihe Physik - Band 25

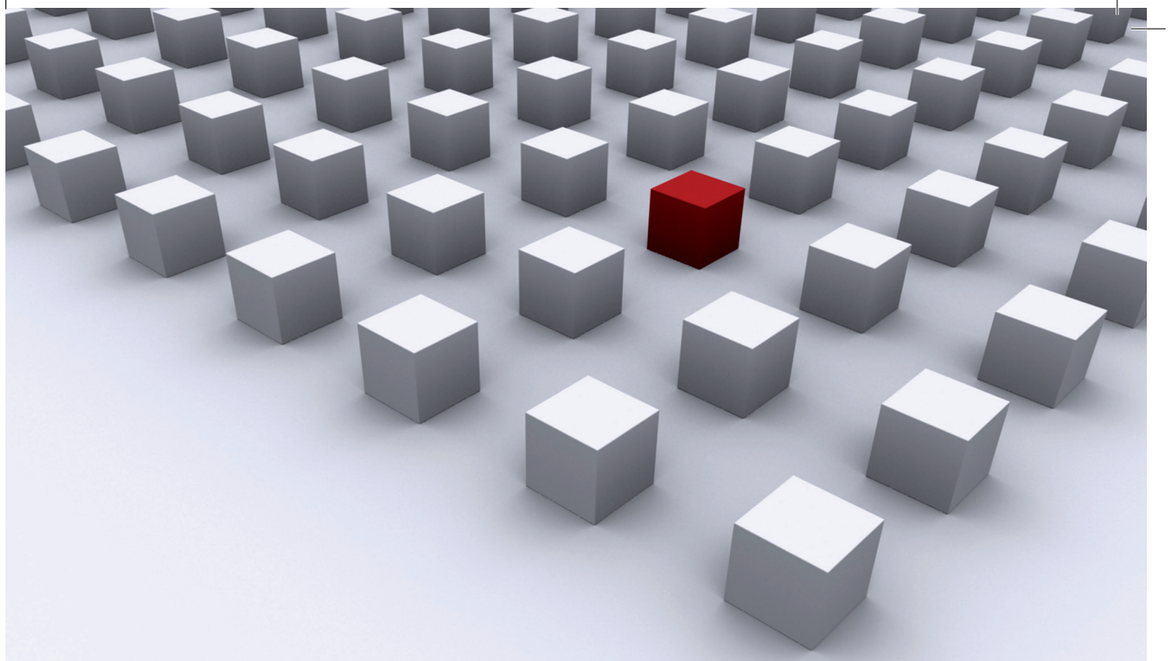

Jürgen Wurm

Dirac fermions in graphene nanostructures:

Edge effects on spectral density and quantum transport

Universitätsverlag Regensburg

25

Dissertationsreihe Physik

Jürgen Wurm

Dirac fermions in graphene nanostructures: Edge effects on spectral density and quantum transport

Dirac fermions in graphene nanostructures:
Edge effects on spectral density and quantum transport

Dissertation zur Erlangung des Doktorgrades der Naturwissenschaften (Dr. rer. nat.)
der Fakultät für Physik der Universität Regensburg
vorgelegt von

Jürgen Wurm

aus Regensburg

Oktober 2011

Die Arbeit wurde von Prof. Dr. Klaus Richter angeleitet.
Das Promotionsgesuch wurde am 05.10.2011 eingereicht.

Prüfungsausschuss:	Vorsitzender:	Prof. Dr. John Lupton
	1. Gutachter:	Prof. Dr. Klaus Richter
	2. Gutachter:	Prof. Dr. Thomas Niehaus
	weiterer Prüfer:	Prof. Dr. Tilo Wettig

Dissertationsreihe der Fakultät für Physik der Universität Regensburg, Band 25

Herausgegeben vom Präsidium des Alumnivereins der Physikalischen Fakultät:
Klaus Richter, Andreas Schäfer, Werner Wegscheider, Dieter Weiss

Jürgen Wurm

Dirac fermions in graphene nanostructures: Edge effects on spectral density and quantum transport

Universitätsverlag Regensburg

Bibliografische Informationen der Deutschen Bibliothek.
Die Deutsche Bibliothek verzeichnet diese Publikation
in der Deutschen Nationalbibliografie. Detailierte bibliografische Daten
sind im Internet über http://dnb.ddb.de abrufbar.

1. Auflage 2012

Leibnizstraße 13, 93055 Regensburg

Konzeption: Thomas Geiger
Umschlagentwurf: Franz Stadler, Designcooperative Nittenau eG
Layout: Jürgen Wurm
Druck: Docupoint, Magdeburg
ISBN: 978-3-86845-084-2

Weitere Informationen zum Verlagsprogramm erhalten Sie unter:
www.univerlag-regensburg.de

Dirac fermions in graphene nanostructures: Edge effects on spectral density and quantum transport

Dissertation zur Erlangung des Doktorgrades
der Naturwissenschaften (Dr. rer. nat.)
der Fakultät für Physik
der Universität Regensburg

vorgelegt von

Jürgen Wurm

aus Regensburg

Oktober 2011

Promotionsgesuch eingereicht am: 05.10.2011

Die Arbeit wurde angeleitet von: Prof. Dr. Klaus Richter

Prüfungsausschuss:

Vorsitzender:	Prof. Dr. John Lupton
1. Gutachter:	Prof. Dr. Klaus Richter
2. Gutachter:	Prof. Dr. Thomas Niehaus
Weiterer Prüfer:	Prof. Dr. Tilo Wettig

Contents

CHAPTER 1

Introduction

During the last decade graphene, a sheet of carbon with a thickness of only one atom, has been one of the most intensively studied material systems in many fields of basic and applied research. Graphene has been studied theoretically already in the late 1940s, when Wallace first considered a two-dimensional sheet of sp^2-bonded carbon atoms and derived its π-band structure in order to understand the electronic band structure of graphite [1]. Graphite consists basically of many graphene layers that are stacked onto each other, and are held together due to van der Waals interaction. Later, McClure discussed graphene in view of the magnetic properties of graphite [2], and also Slonczewski and Weiss calculated the band structure of graphene [3]. Moreover, DiVincenzo and Mele [4] as well as Semenoff [5] recognized in 1984 that for low energies, where the electronic dispersion in graphene is approximately linear, the carrier dynamics can be mapped onto a two-dimensional massless Dirac equation. The velocity of the corresponding particles is about a hundred times smaller than the speed of light, and the spin that occurs in the original Dirac equation is replaced by a *sublattice pseudospin* in the resulting effective equation.

Chemist Hanns-Peter Boehm and coworkers succeeded already in the early 1960s to produce single layers of carbon by reduction of graphite oxide [6], and later actually introduced the term 'graphene' [7]. In the abstract of Ref. [6], the authors write: "Die Bestimmung der Dicke der dünnsten Lamellen aus dem Kontrast im Elektronenmikroskop ergab, daß sie nur aus einigen wenigen, z. T. wahrscheinlich nur aus einer einzigen Kohlenstoff-Sechseckschicht des Graphitgitters bestehen." In fact they found that several of their flakes had thicknesses between 3 and 5 Å. In view of this, it seems rather surprising that graphene has not experienced very much attention until not even ten years ago. Only after Novoselov and coworkers have published a series of papers in 2004 and 2005, the interest in the two-dimensional material increased tremendously. In their 2004 publication, the authors report the isolation of few layer carbon crystals by micromechanical cleavage, a method which has become famous as the 'sticky-tape' or 'Scotch-tape' method [8]. In these samples they also demonstrated the tunability of the carrier density and thus the crossover from electron to hole conduction for the first time. One year later this so-called electrical field effect was also reported in monolayer samples, i. e. graphene [9]. Finally, quantum Hall effect measurements on graphene revealed the predicted unconventional sequence of quantum Hall plateaus, and thus proofed that, at low excitation energies, the charge carriers in graphene indeed behave like massless Dirac fermions [10, 11]. Subsequently the remarkable development of graphene research be-

gan: Within the time period from 2005 to 2009, more than 5000 articles on graphene have been published [12]. One of the aspects that fascinates many researchers is the strict two-dimensional confinement of the charge carriers within the "ultimate flatland" graphene [13]. In 2010, Konstantin Novoselov and Andre Geim were awarded the Nobel Prize in Physics "for groundbreaking experiments regarding the two-dimensional material graphene" [14].

Among the various remarkable physical properties of graphene, we discuss its electronic properties in this work. To be more precise, we focus on energy spectrum and quantum transport properties in the low energy regime, where the Dirac equation is a valid description. Many interesting features arise from the corresponding linear energy dispersion and the spinor character of the charge carriers. The already mentioned unconventional quantum Hall effect, which is in fact observable even at room temperature [15], is only one example. However, one facet has attracted particular interest, namely the extraordinarily high electronic mobility in graphene. In suspended samples values above $\mu = 200\,000\,\mathrm{cm}^2/\mathrm{Vs}$ have been reported [16, 17], and in graphene-boron-nitride heterostructures even $\mu \approx 500\,000\,\mathrm{cm}^2/\mathrm{Vs}$ can be reached [18]. As a consequence, ballistic transport is possible in graphene over length scales of several micrometers [18, 19], which allows to study the interesting properties of massless Dirac fermions in a very clean environment. One reason for the high mobility is the suppressed backscattering [20] of charge carriers from smooth disorder potentials due to the pseudospin character, more precisely the so-called chirality, of massless Dirac fermions. The exceptional transport properties have triggered also applied research on electronic devices. In fact, high-frequency graphene transistors [21, 22] and even integrated circuits consisting exclusively of graphene components [23] have been demonstrated recently.

Another touching point of applied and basic research on high quality graphene is the common interest in nanostructures. For device fabrication and dense packing of electronic components, nanostructuring is obviously important. However, also apart from the direct goal of applications, graphene nanostructures have become a field of great experimental and theoretical activity. Geometrically, the simplest graphene nanostructures are graphene nanoribbons, extended stripes of constant width. Already these simple systems show very interesting properties, many of them tracing back to the edge structure. Even more than 20 years after the first theoretical studies [24, 25], and several years after the first experiments [26, 27], the physics of these quasi one-dimensional carbon wires is still not fully understood. One example is the experimentally observed (probably disorder-induced) 'transport gap' [27, 28, 29, 30]. Graphene quantum dots or cavities form a second group of widely studied nanostructures. Various phenomena have been observed experimentally in these systems: Coulomb blockade and single electron transistor action [31, 32, 33, 34], indirect charge detection in adjacent quantum wires [35], as well as magnetic field dependent [36] and spin-resolved [37] level spectroscopy. Also on the theoretical side many studies exist in the literature. It has been suggested to create quantum dots by a combination of nanoribbons and electrostatic gates [38], e. g. in view of forming spin-qubits [39]. Furthermore, investigations have focused on the magnetic field dependence of the dot energy levels [40, 41]. Finally we like to mention numerical simulations of electrostatically defined dots [42], the energy level statistics of closed

[43, 44] and the quantum conductance of open [43, 45] graphene cavities.

In this thesis we aim for a theoretical description of edge effects on the spectral and transport properties of graphene nanostructures. Due to the lack of a gap in the Dirac spectrum, electrostatic potentials cannot effectively confine charge carriers in graphene. In fact, massless Dirac fermions can be transmitted through electrostatic barriers even with unit probability. This phenomenon is known as *Klein tunneling* [46], in analogy to an effect in relativistic quantum mechanics [47]. Consequently, electrons and holes scatter eventually from the edge terminations of the graphene lattice. In ballistic structures, which we study during the main part of this work, the edges are indeed the only relevant source of scattering. However, the coherent dynamics of the charge carriers is strongly affected by the reflection upon the edges. Thus a full theoretical understanding of edge-related effects in graphene nanostructures is highly desirable. It is certainly "a central question in the field of graphene-related research how graphene behaves when it is patterned at the nanometer scale with different edge geometries", as pointed out recently by Tao and coworkers [48]. How do the different edge types and geometries influence physical quantities, like the electronic density of states, and quantum mechanical interference effects, like the weak localization correction to the conductance? It is the main intention of the present thesis to partly answer these questions. To this end we follow mostly an analytical approach, developing a formalism that is based on the Green function of a graphene nanostructure. The different types of edges are incorporated by imposing appropriate boundary conditions. The virtue of this approach is that edge effects are basically separated from the charge dynamics, and thus particularly comprehensible. For the most part of this work we consider graphene structures with typical size scales much larger than the Fermi wavelength. For systems in this regime, the semiclassical theory of quantum systems has been a very successful approach to the describe both spectral and transport properties [49, 50, 51, 52]. Also for investigating graphene in large magnetic fields, semiclassical techniques have been used [53, 54, 55]. In this thesis we generalize several semiclassical methods to the case of graphene nanostructures. In addition to the analytical calculations we also perform numerical tight-binding simulations, using a very flexible and efficient program code developed by Michael Wimmer [56]. We use the numerical calculations to support and complement our analytical findings, but also perform a mainly numerical study of graphene nanoribbons.

This thesis is organized in the following way. We provide a short introduction or motivation at the beginning and a summary of our results at the end of each chapter.

In **chapter 2** we give a brief introduction into the direct and the reciprocal lattice structure of graphene and the effective Dirac theory. We outline the derivation of the energy band structure of bulk graphene within a single-orbital tight-binding model and show how one obtains the well-known Dirac Hamiltonian for low excitation energies. Then we introduce the most common graphene boundary conditions for the effective Dirac equation, namely those corresponding to zigzag, armchair, and infinite mass edges. In particular we discuss how the different edge types affect the effective time reversal symmetries of the Dirac theory.

In **chapter 3** we derive the Green function of ballistic graphene structures. In a first

step we adapt the multiple reflection expansion of Balian and Bloch and generalize it to the graphene case, taking into account the dynamics of sublattice and valley pseudospins. Second, we approximate the resulting exact expansion to leading order in $(k_E L)^{-1}$, where k_E is the Fermi momentum and L is the typical system size. In this semiclassical approximation the Green function is given by a sum over all classical trajectories. The contribution of each trajectory consists of two parts: A scalar term that is identical to the corresponding contribution to the semiclassical Green function for the Schrödinger equation, and a matrix term that describes the graphene specific evolution of the pseudospins along the classical trajectory. However, a second class of leading order contributions has to be taken into account, namely singularities due to multiple reflections close to the same zigzag boundary point. Resumming these contributions, the form of the semiclassical Green function remains unchanged, but the reflections at zigzag edges are renormalized.

Based on these results we study the spectral density of states (DOS) of graphene billiards in **chapter 4**. First we separate the DOS into a smooth and an oscillating part and treat both parts separately. We approximate the smooth part in the semiclassical limit by the first two terms of the so-called Weyl expansion, for which we derive analytical expressions. Further we compare our theory with numerical tight-binding calculations. As for the Schrödinger equation, the leading term scales with the total area of the billiard. The second term, which usually scales with the total length of the system boundary, is distinctly different from that of Schrödinger billiards. We find that only zigzag edges give rise to such a contribution. Therefore our findings suggest that the smooth DOS can be used to characterize the edge structure of graphene billiards. Then we focus on the oscillating part of the DOS. We derive semiclassical (Gutzwiller and Berry-Tabor) trace formulae for chaotic and specific regular graphene billiards, which express the DOS oscillations in terms of the periodic classical orbits of the system. Each orbit contribution is modulated by a graphene specific and edge-dependent pseudospin interference term. For the regular systems we study how the pseudospin interference in combination with the geometric properties affects the oscillatory DOS, and thus the energy eigenvalues. The extended Gutzwiller formula serves as a starting point for the subsequent investigation into the correlations in the spectrum of chaotic graphene billiards. We study the form factor, i. e. the Fourier transform of the spectral two-point correlator, generalizing the corresponding semiclassical theory to the case of graphene. Also here, the edge-dependent interference of pseudospins is the most important feature, to which we pay particular attention. We derive semiclassical expressions for the two leading order contributions to the form factor and show that the total length of intervalley scattering armchair boundary segments sets the relevant time scale for a transition between unitary and orthogonal universality class. The techniques developed here are, with modifications, also used in the following chapters to study the electronic transport.

This brings us to **chapter 5**, where we investigate the electronic transport properties of ballistic graphene cavities. We start from the Kubo formula together with the semiclassical graphene Green function to derive analytical formulae for the average two-terminal conductance (classical conductance and weak localization correction), the universal conductance

fluctuations, and the Fano factor of ballistic chaotic graphene cavities. While the sizes of the weak localization correction and the conductance fluctuations depend sensitively on the edge structure via armchair edges that mediate intervalley scattering, the classical conductance and the dominating contributions to the Fano factor are edge independent. We test our predictions concerning the conductance using tight-binding simulations.

We extend our theory of quantum transport to study the effects of magnetized zigzag edges on the conductance of chaotic graphene cavities in **chapter 6**. Using a simple model to account for the magnetic edge moments, we calculate the weak localization and the size of the universal conductance fluctuations. In this context we investigate mixing of the real spin and time reversal symmetry breaking that result from spin rotations at the magnetic edges. We complete our discussion with numerical calculations of the weak localization correction.

In **chapter 7** we carry out a numerical study of the conductance of disordered graphene nanoribbons. We show that the phenomenon of a so-called perfectly conducting channel, which is known for zigzag ribbons, occurs also in the multichannel regime of metallic armchair ribbons, and explain our findings within the effective Dirac theory. Then we calculate numerically the magnetoconductance of weakly disordered ribbons to support our argumentation and assign the correct universality class to metallic armchair ribbons. Lastly, we perform a numerical simulation of an experiment carried out on graphene nanoribbons in very high magnetic fields. We devise a possible disorder scenario that explains the main experimental results.

Finally, we conclude in **chapter 8**, summarizing the most important findings of this thesis and discussing possible future directions.

In the **appendix** we provide additional and technical material that completes the main text. In App. A.1, we present an expression for the short-distance discontinuity of the free Green function. Edge potentials at zigzag edges are examined in App. A.2. We derive the energy eigenvalues of a rectangle with zigzag and armchair edges in App. A.3, and a semiclassical trace formula for a rectangle with infinite mass boundaries in App. A.4. In App. A.5 we calculate the Kubo conductivity for graphene and discuss the relation between the linear response expression and the Landauer formula for the conductance. The influence of weak bulk disorder on the semiclassical Green function is investigated in App. A.6, and in App. A.7 we generalize two results from Chap. 6 concerning the weak localization.

CHAPTER 2

Graphene and effective Dirac theory

In this chapter we give a short introduction to some basic properties of graphene and introduce various notations that are used throughout this thesis. For a broader overview we refer to the recent review articles Refs. [12, 57, 58]. First we discuss the crystal structure of graphene, a honeycomb lattice with two carbon atoms per unit cell, and the corresponding reciprocal lattice. We sketch the derivation of the electronic energy band structure within a simple tight-binding model and show that, at low excitation energies, the corresponding quasiparticles are located at the corners of the first Brillouin zone (K-points or *valleys*) rather than in its center (Γ-point) as it is the case for example in gallium arsenide. For crystal momenta close to the K-points, i. e. for low excitation energies, we derive the well-known effective wave equation for the envelope wavefunctions, namely the two-dimensional Dirac equation for massless fermions. There are effectively two different K-points that one has to consider as an additional degree of freedom in the effective theory. Unlike other materials with more than one valley, like silicon, the K-points in graphene can be coupled upon confining the quasiparticles. This coupling in turn has important consequences on the observable properties of graphene structures, since the (effective) time reversal symmetries of the system are strongly affected by the valley coupling. Hence, the second part of this chapter is devoted to the antiunitary symmetries of the effective Dirac Hamiltonian, the boundary conditions for Dirac fermions in graphene, and their connection to each other. We discuss the three antiunitary symmetries that are relevant for our work. Two of them can be considered as (effective) time reversal symmetries that reverse the momentum of a state measured from the Γ-point and the K-points, respectively. The third maps states from the two K-points onto each other and leads to their degeneracy. Then we introduce the three most common boundary conditions for graphene structures in the effective theory, namely zigzag, armchair, and infinite mass edges. We present projection operators that can be used to formulate the boundary conditions in a very convenient way. Furthermore, we discuss the effect of the different edge types on the antiunitary symmetries.

2.1 Lattice structure and effective Hamiltonian

2.1.1 Graphene lattice and band structure

The real-space graphene lattice is a honeycomb lattice, i. e. a two-dimensional hexagonal arrangement of carbon atoms as depicted in Fig. 2.1 a). The underlying Bravais lattice is

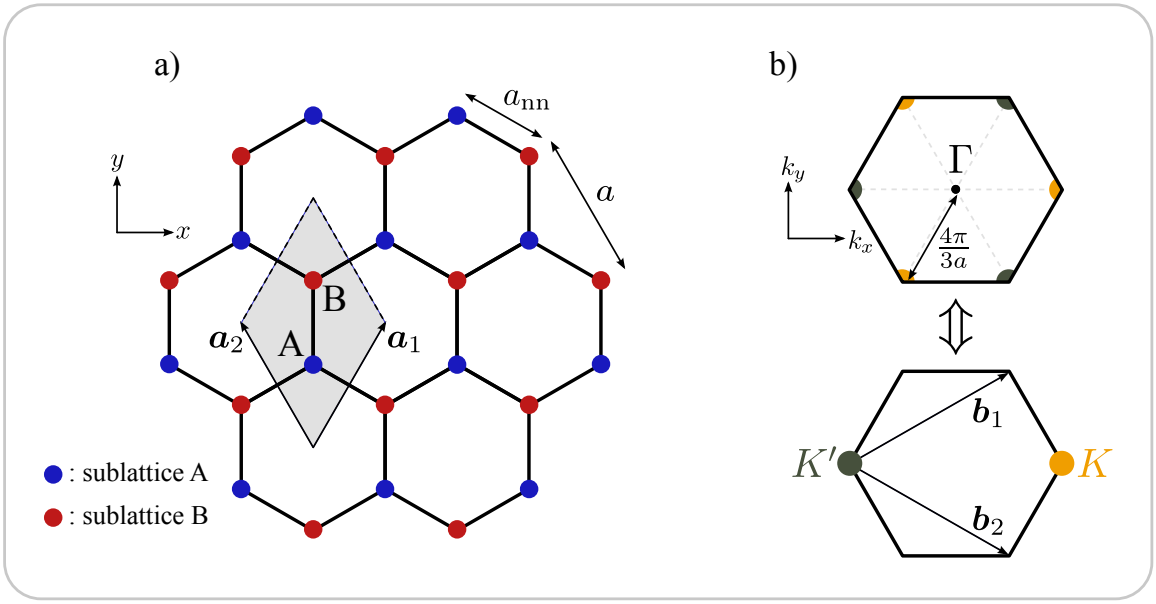

Figure 2.1: a) Lattice structure and unit cell of bulk graphene. The lattice constant is $a \approx 0.246\,\mathrm{nm}$, while $a_{\mathrm{nn}} = a/\sqrt{3}$ is the distance between two nearest-neighbor atoms. The basis vectors $\boldsymbol{a}_1$ and $\boldsymbol{a}_2$ span the primitive unit cell that contains one A-atom (blue) and one B-atom (red). b) First Brillouin zone of the reciprocal graphene lattice. Roughly speaking, only one third of each of the six corner points lies within the Brillouin zone (upper picture). Since three corners with the same color are connected by the primitive reciprocal lattice vectors $\boldsymbol{b}_1$ and $\boldsymbol{b}_2$, we can combine them to give effectively two points $\boldsymbol{K}$ (orange) and $\boldsymbol{K}'$ (green).

triangular with two basis atoms referred to as A and B. The primitive unit cell is spanned by the basis vectors

$$\boldsymbol{a}_1 = \frac{a}{2}\begin{pmatrix} 1 \\ \sqrt{3} \end{pmatrix} \quad \text{and} \quad \boldsymbol{a}_2 = \frac{a}{2}\begin{pmatrix} -1 \\ \sqrt{3} \end{pmatrix}, \tag{2.1}$$

where $a = |\boldsymbol{a}_1| = |\boldsymbol{a}_2| \approx 0.246\,\mathrm{nm}$ is the lattice constant of graphene. With this convention, the carbon atoms are localized at positions

$$\boldsymbol{R}_A = \boldsymbol{R} + \frac{1}{3}(\boldsymbol{a}_1 + \boldsymbol{a}_2) \quad \text{and} \quad \boldsymbol{R}_B = \boldsymbol{R} + \frac{2}{3}(\boldsymbol{a}_1 + \boldsymbol{a}_2), \tag{2.2}$$

with lattice vectors $\boldsymbol{R} = n\boldsymbol{a}_1 + m\boldsymbol{a}_2$ $(n, m \in \mathbb{N})$. Alternatively one can consider the honeycomb lattice as two triangular sublattices A and B, that are shifted against each other, e. g. by the vector $\boldsymbol{R}_B - \boldsymbol{R}_A = a/\sqrt{3}\,\hat{\boldsymbol{y}}$.

We denote the basis vectors of the corresponding reciprocal lattice by $\boldsymbol{b}_1$ and $\boldsymbol{b}_2$. They fulfill the relations

$$\boldsymbol{a}_i \cdot \boldsymbol{b}_j = 2\pi\delta_{ij}\,, \tag{2.3}$$

and hence we can choose

$$\boldsymbol{b}_1 = \frac{2\pi}{a}\begin{pmatrix} 1 \\ 1/\sqrt{3} \end{pmatrix}, \quad \boldsymbol{b}_2 = \frac{2\pi}{a}\begin{pmatrix} 1 \\ -1/\sqrt{3} \end{pmatrix}. \tag{2.4}$$

It follows that the first Brillouin zone is again a regular hexagon with a side length of $K = 4\pi/3a$, which is also the distance of the corners of the Brillouin zone from the Γ-point, as shown in Fig. 2.1 b). The corners of the first Brillouin zone are referred to as K-points of the reciprocal lattice. Since the primitive reciprocal lattice vectors $\boldsymbol{b}_1$ and $\boldsymbol{b}_2$ connect each corner with two others, only two of them are non-equivalent. Therefore it is sufficient to define two K-points [cf. Fig. 2.1 b)], for example

$$\boldsymbol{K} = \begin{pmatrix} K \\ 0 \end{pmatrix}, \quad \boldsymbol{K}' = \begin{pmatrix} -K \\ 0 \end{pmatrix}. \tag{2.5}$$

Within a single-orbital tight-binding model that takes into account one electron in a p_z orbital per carbon atom and up to next-nearest-neighbor hopping, the electronic band structure of graphene has been derived already more than sixty years ago [1]. Here we sketch briefly the derivation for the nearest-neighbor model and refer the reader to Refs. [1, 2, 3, 59, 60] for details. Due to the translational invariance of the extended graphene lattice, a crystal momentum $\boldsymbol{k}$ can be assigned to each energy eigenfunction. Then the Schrödinger equation reads

$$\left(\frac{\hat{\boldsymbol{p}}^2}{2m_\mathrm{e}} + V(\hat{\boldsymbol{x}}) \right) \Psi(\boldsymbol{k}, \boldsymbol{x}) = E(\boldsymbol{k}) \Psi(\boldsymbol{k}, \boldsymbol{x}) \,, \tag{2.6}$$

where V is the lattice-periodic potential originating from the positively charged carbon ions, and m_e is the free electron mass. In tight-binding approximation, Ψ is expanded in terms of the Bloch functions

$$\Phi_{A/B}(\boldsymbol{k}, \boldsymbol{x}) = \frac{1}{\sqrt{N}} \sum_{\boldsymbol{R}_{A/B}} \mathrm{e}^{\mathrm{i}\boldsymbol{k}\cdot\boldsymbol{R}_{A/B}} \, p_z(\boldsymbol{x} - \boldsymbol{R}_{A/B}) \,, \tag{2.7}$$

where $p_z(\boldsymbol{x})$ is the orbital wavefunction of the carbon $2p_z$ orbital and N is the number of lattice sites. Then we have

$$\Psi(\boldsymbol{k}, \boldsymbol{x}) = C_A(\boldsymbol{k}) \Phi_A(\boldsymbol{k}, \boldsymbol{x}) + C_B(\boldsymbol{k}) \Phi_B(\boldsymbol{k}, \boldsymbol{x}) \,, \tag{2.8}$$

which, by construction of the Bloch functions, fulfills $\Psi(\boldsymbol{k}, \boldsymbol{x} + \boldsymbol{R}) = \exp(\mathrm{i}\,\boldsymbol{k}\boldsymbol{R}) \Psi(\boldsymbol{k}, \boldsymbol{x})$ for any lattice vector $\boldsymbol{R}$. With this one can then show that in nearest-neighbor approximation [59, 60]

$$\left[\begin{pmatrix} \varepsilon_0 & -t f(\boldsymbol{k}) \\ -t f^*(\boldsymbol{k}) & \varepsilon_0 \end{pmatrix} - E(\boldsymbol{k}) \begin{pmatrix} 1 & s f(\boldsymbol{k}) \\ s f^*(\boldsymbol{k}) & 1 \end{pmatrix} \right] \begin{pmatrix} C_A \\ C_B \end{pmatrix} (\boldsymbol{k}) = 0 \,, \tag{2.9}$$

with the on-site energy ε_0, the dimensionless overlap parameter s, the nearest-neighbor hopping matrix element $t \approx 2.5 - 3.0\,\mathrm{eV}$ and

$$f(\boldsymbol{k}) = 1 + \mathrm{e}^{-\mathrm{i}\boldsymbol{k}\cdot\boldsymbol{a}_1} + \mathrm{e}^{-\mathrm{i}\boldsymbol{k}\cdot\boldsymbol{a}_2} \,. \tag{2.10}$$

In order to obtain a nontrivial solution to Eq. (2.9), we demand that the matrix of coefficients has a vanishing determinant. With that we get for the dispersion relation in nearest-neighbor tight-binding approximation

$$E_\pm(\boldsymbol{k}) = \frac{\epsilon_0 \pm t|f(\boldsymbol{k})|}{1 \mp s|f(\boldsymbol{k})|} \,. \tag{2.11}$$

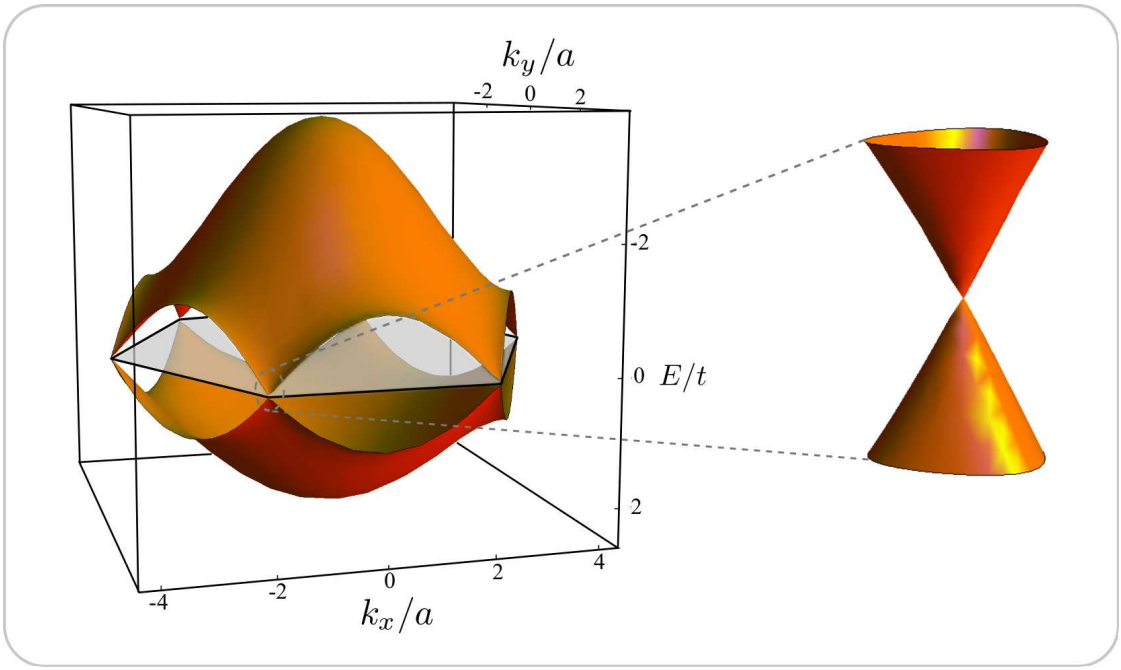

Figure 2.2: Band structure of extended graphene in the first Brillouin zone obtained from the dispersion relation in nearest-neighbor tight-binding approximation (2.11) for $\varepsilon_0 = 0$ and $s = 0.08$. The touching points of the two p_z bands, i. e. the six corners of the Brillouin zone, coincide with the Fermi points when no external potentials are present. Close to the touching points, the dispersion is approximately linear. In this regime the quasiparticle dynamics is described by the effective Dirac Hamiltonian (2.17).

We plot the corresponding band structure in Fig. 2.2. Neglecting the electron spin, there are two bands due to the two orbitals per unit cell. The bands are touching each other at the corners of the first Brillouin zone, since $f(\boldsymbol{K}) = f(\boldsymbol{K}') = 0$. As there are two conduction electrons per unit cell, the lower band is completely filled, while the upper band is completely empty. This means that, without any external potentials, the Fermi energy E_F lies exactly at the touching points. Therefore $\boldsymbol{K}$ and $\boldsymbol{K}'$ are the Fermi points in this case, and thus graphene is sometimes denoted as *semi-metal with zero band overlap* or *zero-gap semiconductor*. Often, graphene flakes are fabricated on top of a highly doped silicon substrate, with an insulating oxide layer in between. In this case the silicon can be used as a back gate and the Fermi energy in the graphene flake can be tuned by changing the back-gate voltage. In this way one can easily move the Fermi energy from the conduction band into the valence band, i. e. switch from the electron to the hole regime, and vice versa. This is not possible in ordinary semiconductor systems, since in these materials conduction and valence band are usually separated by a gap in the order of electron volts.

2.1.2 Effective Dirac Hamiltonian

We derive now an effective Hamiltonian to describe the quasiparticle dynamics in graphene at low energies, i. e. close to the K-points, that are also denoted as *valleys* because they mark the positions of the minima (maxima) of the conduction (valence) band. We introduce the valley index $\tau = \pm 1$ and write

$$\boldsymbol{K}_\tau = K \begin{pmatrix} \tau \\ 0 \end{pmatrix}, \tag{2.12}$$

with $\boldsymbol{K} = \boldsymbol{K}_{+1}$ and $\boldsymbol{K}' = \boldsymbol{K}_{-1}$. Further, we consider a momentum $\boldsymbol{p}$ and a corresponding crystal momentum $\boldsymbol{k}$ next to one of the K-points

$$\boldsymbol{k} = \boldsymbol{K}_\tau + \boldsymbol{p}/\hbar\,. \tag{2.13}$$

For small $\boldsymbol{p}$, we expand Eq. (2.9) for each valley to leading order in $(pa/\hbar)$ and get immediately an effective equation that couples the A- and B-parts of the wavefunctions, namely

$$v_F \begin{pmatrix} 0 & p_x - \mathrm{i}p_y \\ p_x + \mathrm{i}p_y & 0 \end{pmatrix} \Psi_\tau = E\,\Psi_\tau\,, \tag{2.14}$$

where $v_F = \sqrt{3}at/2\hbar \approx 10^6\,\mathrm{m/s}$ is the constant Fermi velocity, and we have replaced the Bloch coefficients according to

$$\begin{pmatrix} C_A \\ C_B \end{pmatrix} \quad \rightarrow \quad \Psi_\tau\,, \quad \Psi_{+1} = \begin{pmatrix} \psi_A \\ \psi_B \end{pmatrix}, \psi_{-1} = \begin{pmatrix} -\psi'_B \\ \psi'_A \end{pmatrix}. \tag{2.15}$$

In position space, the momenta in Eq. (2.14) are replaced by the corresponding differential operators and the ψ_τ are related to the $\boldsymbol{k}$-dependent $C_{A/B}$ via Fourier transform [61]. The effective wave equation (2.14) represents a Dirac equation for massless fermions with (pseudo-) spin 1/2 in two dimensions. This correspondence has been recognized first by DiVincenzo and Mele [4] and Semenoff [5]. Note that the spinors Ψ_τ are not the full wavefunctions, since they are obviously not solutions of the original Schrödinger equation (2.6). Rather they are slowly oscillating envelope wavefunctions, that have to be multiplied with the Bloch functions [cf. Eq. (2.8)], which oscillate on the lattice scale $1/K \sim a$, in order to solve Eq. (2.6). The effective Dirac Hamiltonian in Eq. (2.14) has the same form in both valleys, which is a consequence of the specific choice of the spinors in Eq. (2.15). It will prove useful later to work in a four-dimensional basis, taking into account contributions from both valleys at the same time. Therefore we define the spinor Ψ as

$$\Psi = \left(\psi_A, \psi_B, -\psi'_B, \psi'_A\right)^t \tag{2.16}$$

and finally end up with the 4×4 equation $\mathcal{H}\,\Psi = E\,\Psi$, where the effective Dirac Hamiltonian that describes low-energy quasiparticles in graphene, is given by

$$\mathcal{H} = v_F \tau_0 \otimes \boldsymbol{\sigma} \cdot \boldsymbol{p}\,. \tag{2.17}$$

The Pauli matrices $\boldsymbol{\sigma}$ represent the sublattice degree of freedom, while the Pauli matrices $\boldsymbol{\tau}$ correspond to the valley degree of freedom. The corresponding unit matrices are denoted by σ_0 and τ_0, respectively. To be more specific, eigenstates of σ_z are located exclusively on one sublattice, while eigenstates of σ_x or σ_y have equal density on both sublattices. In the same manner, eigenstates of τ_z consist of contributions from one valley only, while eigenstates of τ_x or τ_y are mixtures of contributions from both valleys. We will use the *valley isotropic* [62] form of the Dirac Hamiltonian (2.17) throughout the remainder of this thesis. Furthermore, we will mostly omit the unit matrices τ_0 and σ_0. Considering an infinitely extended graphene sheet without any further potentials, i. e. in terms of the continuum model free massless Dirac particles, it is easily verified that

$$\Psi_0^{\pm}(\boldsymbol{x}) = \left(\alpha, \pm\alpha\, \mathrm{e}^{\mathrm{i}\varphi_{\boldsymbol{k}}}, \beta, \pm\beta\, \mathrm{e}^{\mathrm{i}\varphi_{\boldsymbol{k}}}\right)^t \mathrm{e}^{\mathrm{i}\boldsymbol{k}\cdot\boldsymbol{x}} \tag{2.18}$$

are eigenstates of the Hamiltonian (2.17) with energies $E_{\pm} = \pm\hbar v_F|\boldsymbol{k}| = \pm\hbar v_F k$, and normalization constants α and β. Here $\boldsymbol{k}$ is an arbitrary momentum vector measured relative to the K-points and $\varphi_{\boldsymbol{k}}$ is its orientation in reciprocal space

$$\cos\varphi_{\boldsymbol{k}} = k_x/k\,, \quad \sin\varphi_{\boldsymbol{k}} = k_y/k\,. \tag{2.19}$$

The spinors in Eq. (2.18) are eigenstates of the sublattice pseudospin in the direction of $\boldsymbol{k}$, i. e. of the so-called *chirality* operator:

$$\frac{\boldsymbol{\sigma}\cdot\boldsymbol{k}}{k}\Psi_0^{\pm}(\boldsymbol{x}) = \pm\Psi_0^{\pm}(\boldsymbol{x})\,. \tag{2.20}$$

In other words, the corresponding quasiparticles are *chiral fermions*. Note that here the chirality does not depend on the valley, but only on the sign of the energy, i. e. the chirality is positive for particles and negative for holes. This is due to our convention (2.16). Another commonly used convention is

$$\tilde{\Psi} = \left(\psi_A, \psi_B, \psi'_A, \psi'_B\right)^t = \mathcal{U}\Psi\,, \tag{2.21}$$

with the unitary transformation

$$\mathcal{U} = \frac{1}{2}(\tau_0 + \tau_z)\otimes\sigma_0 + \frac{\mathrm{i}}{2}(\tau_0 - \tau_z)\otimes\sigma_y\,. \tag{2.22}$$

The corresponding transformed Hamiltonian

$$\tilde{\mathcal{H}} = \mathcal{U}\mathcal{H}\mathcal{U}^{\dagger} = v_F\tau_z\otimes\sigma_x p_x + v_F\tau_0\otimes\sigma_y p_y \tag{2.23}$$

is not valley isotropic, and the free solutions are given by

$$\tilde{\Psi}_0^{\pm}(\boldsymbol{x}) = \left(\alpha, \pm\alpha\, \mathrm{e}^{\mathrm{i}\varphi_{\boldsymbol{k}}}, \mp\beta\, \mathrm{e}^{-\mathrm{i}\varphi_{\boldsymbol{k}}}, \beta\right)^t \mathrm{e}^{\mathrm{i}\boldsymbol{k}\cdot\boldsymbol{x}}\,. \tag{2.24}$$

These are now eigenvalues of the operator $\tau_z\otimes\boldsymbol{\sigma}\cdot\boldsymbol{k}/k$, i. e. the chirality depends on the valley in the transformed basis.

Furthermore the states $\Psi_0^\pm$ undergo a sign change upon rotation of the momentum direction by 2π. To see this, we consider the operator

$$\mathcal{R}(\delta\varphi) = \tau_0 \otimes \mathrm{e}^{\mathrm{i}\delta\varphi/2\sigma_z}\,, \tag{2.25}$$

which rotates the momentum direction by $\delta\varphi$ and also leads to an overall phase of $-\delta\varphi/2$:

$$\mathcal{R}(\delta\varphi)\Psi_0^\pm(\boldsymbol{x}) = \mathrm{e}^{-\mathrm{i}\delta\varphi/2}\left(\alpha, \pm\alpha\,\mathrm{e}^{\mathrm{i}\varphi_{\boldsymbol{k}}+\delta\varphi}, \beta, \pm\beta\,\mathrm{e}^{\mathrm{i}\varphi_{\boldsymbol{k}}+\delta\varphi}\right)^t \mathrm{e}^{\mathrm{i}\boldsymbol{k}\cdot\boldsymbol{x}}\,. \tag{2.26}$$

This geometrical (Berry) phase has indeed important measurable effects, e. g. it is responsible for the so-called *half-integer* step sequence in the quantum Hall effect [10, 11] and the weak antilocalization correction to the quantum conductance of weakly disordered bulk graphene [63, 64].

Before we discuss the boundary conditions on the effective Dirac equation that are necessary to study confined systems, we briefly address the connection of the spinor Ψ with the wavefunctions in the discrete tight-binding model. Since the Bloch theorem is valid only for periodic systems, the wavefunctions $\Psi(\boldsymbol{k}, \boldsymbol{x})$ from Eq.(2.8) are not solutions for confined systems or in the presence of additional potentials. However, the eigenfunctions can always be expressed as superposition of the $\Psi(\boldsymbol{k}, \boldsymbol{x})$

$$\Psi(\boldsymbol{x}) = \int d\boldsymbol{k}\, F(\boldsymbol{k})\Psi(\boldsymbol{k}, \boldsymbol{x})\,, \tag{2.27}$$

with some momentum distribution $F(\boldsymbol{k})$. In tight-binding approximation it is mostly assumed that the p_z orbitals at different lattice sites form an orthonormal set [61], i. e.

$$\Psi(\boldsymbol{x}) = \sum_{\alpha=A,B}\sum_{\boldsymbol{R}_\alpha} \psi_{\mathrm{tb}}(\boldsymbol{R}_\alpha)\, p_z(\boldsymbol{x} - \boldsymbol{R}_\alpha)\,, \tag{2.28}$$

with the tight-binding wavefunctions $\psi_{\mathrm{tb}}(\boldsymbol{R}_\alpha)$, which can be interpreted as the probability amplitudes for the electrons to be close to the atomic site at $\boldsymbol{R}_\alpha$. These in turn are for low energies related to the spinor entries from the effective theory via [61]

$$\psi_{\mathrm{tb}}(\boldsymbol{R}_\alpha) = \mathrm{e}^{\mathrm{i}\boldsymbol{K}\cdot\boldsymbol{R}_\alpha}\psi_\alpha(\boldsymbol{R}_\alpha) + \mathrm{e}^{\mathrm{i}\boldsymbol{K'}\cdot\boldsymbol{R}_\alpha}\psi'_\alpha(\boldsymbol{R}_\alpha)\,. \tag{2.29}$$

We stress that, in general, contributions from both valleys are important, depending on the particular problem.

2.2 Boundary conditions and antiunitary symmetries

2.2.1 Antiunitary symmetries of the effective theory

Universality classes

Apart from the *unitary symmetries*, as there are in graphene e. g. the spatial symmetries of the underlying hexagonal lattice, i. e. the sixfold rotational symmetry, the inversion symmetry, and the mirror symmetries, physical properties of a system can also be affected by the

existence of *antiunitary symmetries*. An operator $\mathcal{T}$ is denoted antiunitary if

$$\langle\alpha|\mathcal{T}^\dagger\mathcal{T}|\beta\rangle = \langle\alpha|\beta\rangle^* = \langle\beta|\alpha\rangle \tag{2.30}$$

for arbitrary states $|\alpha\rangle, |\beta\rangle$. The complex conjugation $\mathcal{C}$ is one example. It is clear that the product of two antiunitary operators, in particular $\mathcal{U} = \mathcal{T}\mathcal{C}$, is unitary, because

$$\langle\alpha|(\mathcal{T}\mathcal{C})^\dagger\mathcal{T}\mathcal{C}|\beta\rangle = \langle\mathcal{C}\alpha|\mathcal{T}^\dagger\mathcal{T}|\mathcal{C}\beta\rangle = \langle\mathcal{C}\alpha|\mathcal{C}\beta\rangle^* = \langle\alpha|\beta\rangle\,. \tag{2.31}$$

But since the complex conjugation is an involution, i. e. $\mathcal{C}^2 = 1$, we have

$$\mathcal{T} = \mathcal{T}\mathcal{C}\mathcal{C} = \mathcal{U}\mathcal{C}\,. \tag{2.32}$$

This means that *any* antiunitary operator can be constructed from a unitary operator and the complex conjugation. Depending on its antiunitary symmetries, a system can be assigned to certain universality or symmetry classes.

A system described by a Hamiltonian H and having an antiunitary symmetry corresponding to an operator $\mathcal{T}$, i. e. $[\mathcal{T}, H] = 0$, belongs to the *orthogonal* universality class if $\mathcal{T}^2 = 1$. By constructing a $\mathcal{T}$-invariant basis set, the Hamiltonian becomes real in this case without being diagonalized (see e. g. p. 20 in Ref. [65]). This means that the system is invariant under orthogonal transformations, in that they leave the Hamiltonian real and conserve its eigenvalues.

On the other hand, if $[\mathcal{T}, H] = 0$ and $\mathcal{T}^2 = -1$, *Kramers' theorem* ensures that the energy spectrum is degenerate. This can be seen immediately, as we have for an arbitrary state $|\alpha\rangle$ in this case

$$\langle\alpha|\mathcal{T}\alpha\rangle = \langle\alpha|\mathcal{T}^\dagger\mathcal{T}\mathcal{T}|\alpha\rangle^* = -\langle\mathcal{T}\alpha|\alpha\rangle^* = -\langle\alpha|\mathcal{T}\alpha\rangle\,. \tag{2.33}$$

Therefore $\langle\alpha|\mathcal{T}\alpha\rangle = 0$, i. e. $|\alpha\rangle$ and its partner state $|\mathcal{T}\alpha\rangle$ are orthogonal. Since $\mathcal{T}$ and H commute, this means that, if $|\alpha\rangle$ is an eigenstate of H with eigenvalue E, then $|\mathcal{T}\alpha\rangle$ is another eigenstate with the same eigenvalue. In other words, the spectrum of H is degenerate. In this case the Hamiltonian has a structure that is denoted quaternionic real [65]. Symplectic transformations conserve both, the eigenvalues and the quaternionic real structure of H [65], and therefore the corresponding universality class is called the *symplectic class*.

Systems that do not have any antiunitary symmetry belong to the *unitary class*, since unitary transformations conserve the hermiticity and the eigenvalues of H. In fact, seven more symmetry classes exist (three 'chiral' and four 'superconducting' classes), however they are not relevant for this work.[1] The three classes introduced above will be important for our further discussion. *Random Matrix Theory* (RMT) delivers predictions about statistical properties of physical systems, which depend in principle only on the specific universality class, and not on the details of the system. In RMT, e. g. Hamiltonians or scattering matrices are replaced by random matrices, with the constraint that they have to be members of

[1] In fact the Dirac Hamiltonian (2.17) is chiral, cf. Eq. (2.20), and thus at zero energy the chiral classes are in principle relevant. However, for finite energies that we consider in this thesis, the chiral and the normal classes lead to the same results [66, 67].

the universal ensemble associated with the symmetry class of the system, i. e. in our case the corresponding orthogonal, symplectic, or unitary ensemble. For an introduction to the topic consider Refs. [65, 68, 69]. The BGS (Bohigas, Gianoni, Schmit) conjecture states that classically chaotic systems, which we study in Chaps. 4-6, are universally described by RMT [70]. We want to mention however, that the assignment of a system to one of the classes above is not always straightforward, as we will see several times during this thesis, when we investigate the spectrum and the conductance of graphene structures. One simple example is treated now, namely bulk graphene without short-range scattering potentials.

Bulk graphene

We consider the idealized case of an infinitely extended sheet of graphene. For now, we focus on unitary operations in the sublattice and valley pseudospin spaces. From these we can construct four antiunitary operators that commute with the Hamiltonian (2.17), namely

$$\mathcal{T}_i = \tau_i \otimes \sigma_y \mathcal{C} \quad \text{with } i \in \{0, x, y, z\}\,. \tag{2.34}$$

It is straightforward to check that

$$\mathcal{T}_i^2 = \begin{cases} +1 & \text{if } i = y\,, \\ -1 & \text{else}\,. \end{cases} \tag{2.35}$$

Usually the $\mathcal{T}_i$ are denoted as (effective) time reversal symmetries (TRS). However, the real physical TRS corresponding to the operation $t \to -t$ is given by $\mathcal{T}_y$. One can see this by considering the tight-binding wavefunctions, which contain the fast oscillations from the K-points explicitly, and performing the time reversion by hand. Since for the full time-dependent Schrödinger equation, time reversion corresponds to complex conjugation, we act with $\mathcal{C}$ on the wavefunction (2.29)

$$\mathcal{C}\psi_{\mathrm{tb}}(\boldsymbol{R}_\alpha) = \mathrm{e}^{\mathrm{i}\boldsymbol{K'}\cdot\boldsymbol{R}_\alpha}\psi_\alpha^*(\boldsymbol{R}_\alpha) + \mathrm{e}^{\mathrm{i}\boldsymbol{K}\cdot\boldsymbol{R}_\alpha}\psi_\alpha'^*(\boldsymbol{R}_\alpha)\,. \tag{2.36}$$

Here we have used that $\boldsymbol{K'} = -\boldsymbol{K}$. Comparing the prefactors of the exponentials, we find that for the four-spinor of the effective theory this is equivalent to the transformation

$$\left(\psi_A, \psi_B, -\psi_B', \psi_A'\right)^T \to \left(\psi_A'^*, \psi_B'^*, -\psi_B^*, \psi_A^*\right)^T\,, \tag{2.37}$$

which is accomplished (up to an irrelevant sign) by $\mathcal{T}_y$. Therefore the real TRS is an orthogonal symmetry, as for spinless free electrons. The operator $\mathcal{T}_y$ inverts the direction of the momentum and at the same time switches the valleys.

Also $\mathcal{T}_x$ plays an important role, namely it ensures the degeneracy of the two valleys. Assume Ψ is a state in valley K, then $\mathcal{T}_x\Psi$ is in valley K$'$ and they are orthogonal due to Kramers' theorem. This means that, if eigenstates exist that 'live' only in one valley, the valleys are independent subsystems with the same energy spectrum. In this case, even though the symmetry $\mathcal{T}_y$ is not broken, it is effectively irrelevant because it connects states

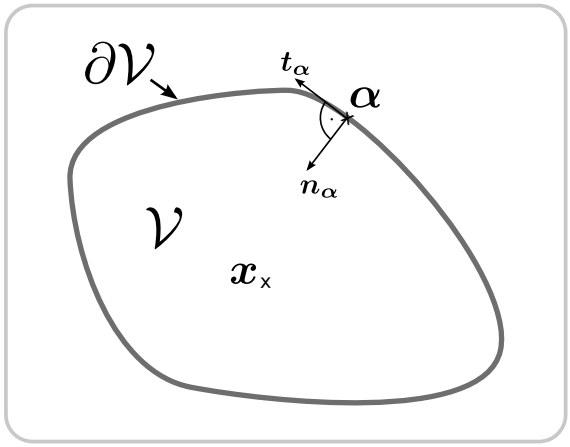

Figure 2.3: Geometrical conventions and notations used throughout this thesis. A ballistic graphene flake is mathematically described by the effective Hamiltonian (2.17) on a two-dimensional domain $\mathcal{V}$ and appropriate boundary conditions on the surface of this domain $\partial\mathcal{V}$. Points within $\mathcal{V}$ are labeled with Latin characters, while Greek characters stand for points on the boundary $\partial\mathcal{V}$. The orientation of the normal and tangential vectors at a boundary point $\boldsymbol{\alpha}$, $\boldsymbol{n_\alpha}$ and $\boldsymbol{t_\alpha} = \boldsymbol{n_\alpha} \times \hat{\boldsymbol{z}}$, respectively, are defined as shown.

from different valleys. If a magnetic field $\boldsymbol{B}$ is applied to the system, the valley index is still a good quantum number, but $[\mathcal{T}_x, \mathcal{H}(\boldsymbol{B})] \neq 0$ and thus the valley degeneracy is lifted [40, 71]. In bulk graphene the valleys are usually decoupled if short-range scattering potentials like vacancies are absent [72].

The operator $\mathcal{T}_0$ has exactly the same form as the TRS operator for electrons with spin 1/2 and broken spin inversion symmetry (e. g. by spin-orbit coupling terms in the Hamiltonian), where the spin operators take the place of the sublattice pseudospin operators in graphene. In systems without intervalley scattering, $\mathcal{T}_0$ can serve as an effective TRS: It inverts the direction of the momentum without switching the valleys and therefore results in an inversion of the sublattice pseudospin, too. This leads for example to the phenomenon of *weak antilocalization* in the average conductance of large, disordered graphene flakes. We will see later that for most systems in which edges play a role, $\mathcal{T}_0$ not conserved. There is, however, an interesting exception, which we discuss in the following subsection and in Chap. 7.

The remaining symmetry $\mathcal{T}_z$ is not of interest for us. For decoupled valleys it is identical to $\mathcal{T}_0$, and for coupled valleys it is not conserved, so that we do not consider $\mathcal{T}_z$ further.

2.2.2 Boundary conditions for Dirac fermions in graphene

In this dissertation we concern ourselves with graphene nanostructures with a phase coherence length that is larger than the size of the system. In conventional two-dimensional electron gases (2DEGs), as realized in semiconductor heterostructures, the charge carriers can be confined by the application of side or top gate voltages. Such voltages shift the Fermi energy locally from the conduction or valence band into the gap of the spectrum. In this way

they define an effective system boundary where electrons are reflected from, and hence are confined. Such electrostatic potentials do, however, not necessarily confine massless Dirac electrons in graphene, as the corresponding energy spectrum does not have a gap. Instead, the Fermi energy can only be shifted from the conduction band into the valence band or vice versa, and electrons can be transmitted into the gated region. Under normal incidence even perfect transmission is possible. In the literature this phenomenon is known as *Klein tunneling* [46] and has been investigated theoretically [73, 74, 75] and experimentally by studying the conductance of graphene p-n junctions [76, 77]. Especially for graphene billiards with classically chaotic counterpart, that are the focus of Chaps. 4 - 6, electrostatic potentials cannot act as confinement [42]. Because of the (partial) transparency of electrostatic barriers for charge carriers in graphene, electrons or holes in graphene nanostructures or flakes are expected to scatter from the edges that eventually terminate the graphene lattice. Therefore, we focus now on the relevant boundary conditions for the effective Dirac Hamiltonian. First we introduce several definitions and notations. We define a graphene structure in general as a two-dimensional domain $\mathcal{V}$ with a boundary $\partial\mathcal{V}$. Throughout this thesis, we use Latin letters for points that lie within the system and Greek letters for points on the boundary. The vectors $\boldsymbol{n}_{\boldsymbol{\alpha}}$ and $\boldsymbol{t}_{\boldsymbol{\alpha}} = \boldsymbol{n}_{\boldsymbol{\alpha}} \times \hat{\boldsymbol{z}}$ represent the normal vector at the boundary point $\boldsymbol{\alpha}$ pointing towards the interior of the system and the tangential vector, together forming a right-handed coordinate system, as shown in Fig. 2.3.

At a given boundary point $\boldsymbol{\alpha}$, every energy independent boundary condition on the four-spinor Ψ can be written as a projection of the sublattice and valley pseudospin into an $\boldsymbol{\alpha}$-dependent direction [78]

$$\mathcal{P}_{\boldsymbol{\alpha}}\Psi|_{\boldsymbol{\alpha}} = 0 \quad \Leftrightarrow \quad \mathcal{M}_{\boldsymbol{\alpha}}\Psi|_{\boldsymbol{\alpha}} = \Psi|_{\boldsymbol{\alpha}} \quad \text{with } \mathcal{P}_{\boldsymbol{\alpha}} = \frac{1}{2}(1 - \mathcal{M}_{\boldsymbol{\alpha}})\,, \tag{2.38}$$

where $\mathcal{P}_{\boldsymbol{\alpha}}$ is a hermitian projection matrix

$$\mathcal{P}_{\boldsymbol{\alpha}}^{\dagger} = \mathcal{P}_{\boldsymbol{\alpha}}\,, \quad \mathcal{P}_{\boldsymbol{\alpha}}^{2} = \mathcal{P}_{\boldsymbol{\alpha}}\,. \tag{2.39}$$

This means that $\mathcal{M}_{\boldsymbol{\alpha}}$ is a hermitian involution:

$$\mathcal{M}_{\boldsymbol{\alpha}}^{\dagger} = \mathcal{M}_{\boldsymbol{\alpha}}\,, \quad \mathcal{M}_{\boldsymbol{\alpha}}^{2} = 1\,. \tag{2.40}$$

During the course of this thesis we are going to deal with several boundary conditions, expressed through different matrices $\mathcal{M}_{\boldsymbol{\alpha}}$. The most commonly considered boundaries are the zigzag, the armchair, and the infinite mass edge. More special boundary conditions result from zigzag edges in the presence of edge potentials. Here we discuss a scalar edge potential that allows for an approximate inclusion of next-nearest-neighbor effects on the zigzag edge state. In Chap. 6 we consider a spin-dependent mass potential at the edges, which models the magnetization of the zigzag edge state. In the following we give an overview of the different types of edges, present the specific forms of $\mathcal{P}_{\boldsymbol{\alpha}}$, and discuss the interplay of the boundary conditions with the antiunitary symmetries of $\mathcal{H}$.

Zigzag edges

When the graphene lattice is terminated along a line including an angle of 0°, 60°, or 120° with the x-axis, the resulting edge is of zigzag type, as depicted in Fig. 2.4 a). The outermost row of atoms contains solely atoms of either A- or B-type, and the orientation of the edge determines the sublattice. We consider a piece of graphene that has a zigzag edge along the line $y = y_0$ and is extended for $y \geq y_0$, i. e. the last row of atoms at the edge contains only B-type atoms. In this case, the microscopic boundary condition is that the tight-binding wavefunction (2.29) vanishes on the (missing) A-type sites of the outermost unit cells [25, 79, 80]. For convenience we define $y = y_0$ to be the position of these fictional A-sites, i. e. the actual graphene lattice begins at $y = y_0 + a/\sqrt{3}$. Then the boundary condition reads

$$\mathrm{e}^{\mathrm{i}Kx}\,\psi_A(x, y_0) + \mathrm{e}^{-\mathrm{i}Kx}\,\psi'_A(x, y_0) = 0 \quad \forall x\,. \tag{2.41}$$

Since this has to hold for all x, ψ_A and ψ'_A have to vanish individually

$$\psi_A(x, y_0) = \psi'_A(x, y_0) = 0 \quad \forall x\,, \tag{2.42}$$

while ψ_B and ψ'_B are not directly affected by the boundary condition.[2] In terms of the four-spinors we can reformulate Eq. (2.42) as

$$\left.\begin{pmatrix} \psi_A \\ \psi_B \\ -\psi'_B \\ \psi'_A \end{pmatrix}\right|_{y=y_0} = \left.\begin{pmatrix} -\psi_A \\ \psi_B \\ -\psi'_B \\ -\psi'_A \end{pmatrix}\right|_{y=y_0} = \underbrace{\begin{pmatrix} -1 & 0 & 0 & 0 \\ 0 & 1 & 0 & 0 \\ 0 & 0 & 1 & 0 \\ 0 & 0 & 0 & -1 \end{pmatrix}}_{\mathcal{M}=-\tau_z\otimes\sigma_z} \left.\begin{pmatrix} \psi_A \\ \psi_B \\ -\psi'_B \\ \psi'_A \end{pmatrix}\right|_{y=y_0}, \tag{2.43}$$

where we can directly read off the matrix $\mathcal{M}$ that occurs in Eq. (2.38). In the same way one can derive the boundary conditions also for other orientations of the zigzag edge. Eventually, the only difference in the boundary conditions results from the sublattice that is present at the edge, namely we find:

$$\mathcal{P}_{\mathrm{zz}} = \frac{1}{2}(1 \pm \tau_z \otimes \sigma_z)\,, \tag{2.44}$$

where the lower sign corresponds to an A-terminated edge and the upper sign to a B-edge. The boundary matrix (2.44) projects the sublattice pseudospin at the zigzag edge into positive or negative $\hat{z}$-direction. This corresponds to the original demand that the wavefunction has to vanish on one sublattice. Furthermore, also the valley pseudospin is projected into $\pm\hat{z}$-direction, i. e. zigzag edges allow for valley-polarized states. In other words, $\mathcal{P}_{\mathrm{zz}}$ is diagonal in the valleyspin space, and thus the valleys are *not* mixed upon scattering from a zigzag edge.

In view of the the (effective) TRS, we consider the symmetry operations and find

$$0 = [\mathcal{T}_y, \mathcal{P}_{\mathrm{zz}}] = [\mathcal{T}_x, \mathcal{P}_{\mathrm{zz}}] \neq [\mathcal{T}_0, \mathcal{P}_{\mathrm{zz}}]\,. \tag{2.45}$$

[2] The effective Dirac equation couples the sublattices, and therefore ψ_B and ψ'_B are affected indirectly.

This means that the intervalley TRS $\mathcal{T}_y$ and the valley degeneracy $\mathcal{T}_x$ are preserved. On the other hand the intravalley TRS $\mathcal{T}_0$ is broken. We discuss some of the consequences of the latter symmetry breaking in Chaps. 4, 5 and 7.

Zigzag edges and next-nearest-neighbor hopping

For the derivation of the effective Hamiltonian in Eq. (2.17) we have considered only nearest-neighbor (nn) hopping in the tight-binding model. In principle, this is a very good approximation for low energies, because next-nearest-neighbor (nnn) hopping gives rise to contributions of second and higher order in ka and thus the nn hopping dominates as $ka \ll 1$. Nevertheless, it has been shown in Ref. [61] that the inclusion of nnn hopping in the graphene tight-binding Hamiltonian has important consequences on the properties of the so-called *zigzag edge states*. These states exist for very low energies and are localized at zigzag edges with an exponential decay of the wavefunction away from the edge [25, 79, 81, 82, 83]. In reference [84] the authors show that, to leading order in ka, the only effect of nnn hopping on the effective Hamiltonian is an additional potential that is present solely on edge atoms.[3] For states in the bulk of a graphene flake the influence of nnn hopping is thus minor, while the zigzag edge states are strongly affected by the edge potential. Not only do they gain a finite velocity, as opposed to the case without nnn hopping, but also the current profile in a graphene ribbon with zigzag edges is qualitatively altered [61] (see also App. A.2).

As an example, we consider again a single B-type zigzag edge with $y_0 = 0$, so that the first row of (B-type) atoms is located at $y_1 = a/\sqrt{3}$. The corresponding additional term in the effective Hamiltonian due to nnn hopping is then [84]

$$\mathcal{H}_{\mathrm{nnn}} = -t' \frac{\hbar v_{_F}}{2} \delta(y - y_1)(1 - \tau_z \otimes \sigma_z)\,, \tag{2.46}$$

where $t' \ll 1$ is the ratio of the nnn and nn hopping constants in the tight-binding model. The projection term $(1 - \tau_z \otimes \sigma_z)$ ensures that the potential is located on the sublattice B only.

We derive now an effective boundary condition for this situation by wavefunction matching at $y = y_1$. Due to the translational invariance along the x-direction, the Bloch theorem implies that eigenstates can be written as

$$\Psi(x, y) = \psi(y) \mathrm{e}^{\mathrm{i}kx}\,, \tag{2.47}$$

and with the definition $k_{_E} = E/\hbar v_{_F}$, the Dirac equation (2.14) gives for the y-dependent part

$$k_{_E} \psi_A(y) = k\psi_B(y) - \frac{\partial \psi_B}{\partial y}(y)\,, \tag{2.48}$$

$$k_{_E} \psi_B(y) = k\psi_B(y) + \frac{\partial \psi_A}{\partial y}(y) - t'\delta(y - y_1)\psi_B(y)\,, \tag{2.49}$$

[3] There is also an irrelevant constant overall shift in the energy, which we omit.

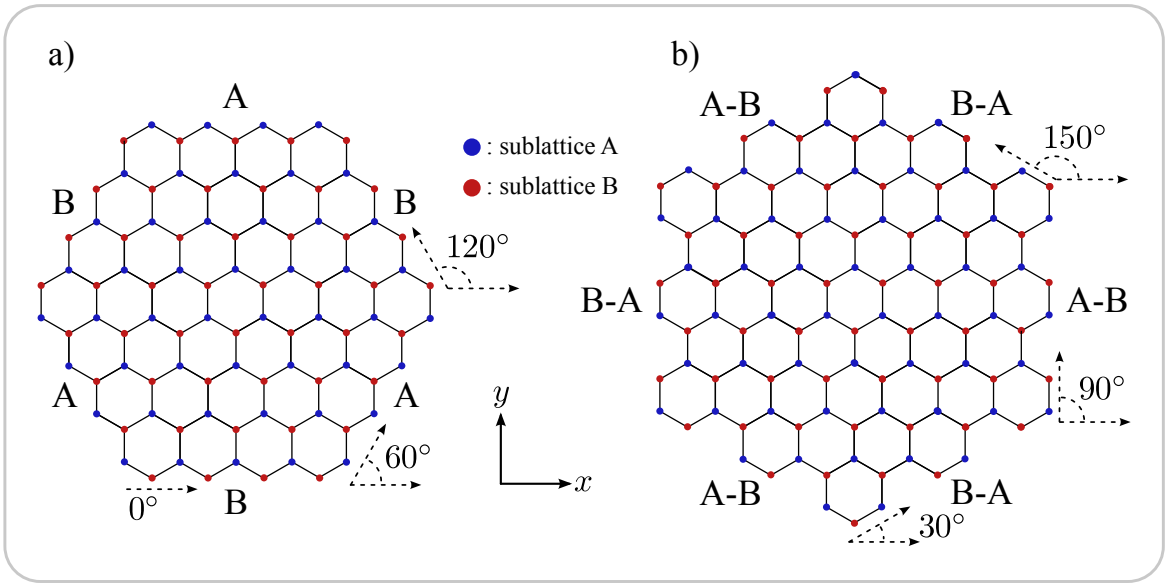

Figure 2.4: Zigzag and armchair type edge terminations of the honeycomb lattice. a) In the zigzag case, each edge is built from atoms of one sublattice only. Following the circumference of a regular zigzag hexagon, the sublattice switches at every side. b) In the armchair case, both sublattices are present at each edge. However, the ordering of the atoms within each edge dimer can be A-B or B-A with respect to the tangential direction.

where we consider the valley $\tau = +1$. We integrate these equations over a small window $[y_1 - \varepsilon, y_1 + \varepsilon]$ around the potential and take the limit $\varepsilon \to 0$ afterwards. Assuming that ψ has at most a finite discontinuity at y_1, we obtain from Eq. (2.48)

$$\lim_{\varepsilon_0 \to 0^+} \left[\psi_B(y_1 + \varepsilon) - \psi_B(y_1 - \varepsilon)\right] = 0\,. \tag{2.50}$$

This means that the B-part of the spinor is continuous. Thus, we divide Eq. (2.49) by $\psi_B(y)$ before we integrate over y and get

$$t' = \lim_{\varepsilon \to 0^+} \int_{y_1-\varepsilon}^{y_1+\varepsilon} dy\, \frac{1}{\psi_B(y)} \frac{\partial \psi_A}{\partial y}(y) = \lim_{\varepsilon \to 0^+} \left[\frac{\psi_A(y_1+\varepsilon)}{\psi_B(y_1+\varepsilon)} - \frac{\psi_A(y_1-\varepsilon)}{\psi_B(y_1-\varepsilon)}\right], \tag{2.51}$$

using integration by parts. This means that, in contrast to ψ_B, the A-part of the spinor has a finite discontinuity at $y = y_1$. For $y < y_1$ we use the actual zigzag boundary condition, $\psi_A(0) = 0$, which leads to the known expressions for the wavefunctions for $y < y_0$ [80, 85]

$$\begin{aligned} \psi_A(y) &= \alpha \sin(qy)\,, \\ \psi_B(y) &= \frac{\alpha}{k_E}\left[\mathrm{i}k \sin(qy) + q\cos(qy)\right]\,. \end{aligned} \tag{2.52}$$

Here k and q are the longitudinal and transverse momenta, respectively, and α is a normalization constant. Since the effective Dirac equation is valid for momenta that are much smaller

than $1/a$, we approximate $k_E a, qa, ka \approx 0$ to get

$$\lim_{\varepsilon\to 0^+} \frac{\psi_A(y_0-\varepsilon)}{\psi_B(y_0-\varepsilon)} = \frac{k_E \sin(qa/\sqrt{3})}{\mathrm{i}k\sin(qa/\sqrt{3}) + q\cos(qa/\sqrt{3})} \approx 0\,. \tag{2.53}$$

Inserting this into Eq. (2.51) finally leads to the effective boundary condition

$$\left.\frac{\psi_A}{\psi_B}\right|_{y=y_0} = t'\,, \tag{2.54}$$

in agreement with a result for similar edge potentials in Ref. [86]. While for edge states this relation has been derived earlier in first order perturbation theory in t' [61], the result (2.54) holds in general, i. e. also for bulk states. In the very same way one derives the effective boundary condition in the valley $\tau = -1$ and also for A-terminated zigzag edges, finally yielding the effective boundary condition matrix

$$\mathcal{P}_{\mathrm{zz}}(t') = \frac{1}{2}\left(1 \pm \tau_z \otimes \sigma_z - \mathrm{i}t'\sigma_y \mp t'\tau_z \otimes \sigma_x\right)\,. \tag{2.55}$$

As before, the lower signs stand for A-terminated edges and the upper for B-termination. We point out that the specific form of the boundary matrix is not unique, however as written in Eq. (2.55), the limit $t' \to 0$ reproduces the case without nnn hopping, Eq. (2.44). In App. A.2, we study the effect of finite t' on the wavefunctions at a zigzag edge.

Considering the antiunitary symmetries, the behavior of $\mathcal{P}_{\mathrm{zz}}(t')$ is the same for zero and finite t'. However, the Hamiltonian in Eq. (2.17) also possesses a unitary electron-hole symmetry, namely σ_z anticommutes with $\mathcal{H}$:

$$\sigma_z \mathcal{H} \sigma_z = -\mathcal{H}\,. \tag{2.56}$$

Thus, for every particle eigenstate Ψ_{p} with a given positive energy k_E, it exists a hole eigenstate $\Psi_{\mathrm{h}} = \sigma_z \Psi_{\mathrm{p}}$ with negative energy $-k_E$. This symmetry is conserved only if nnn hopping is neglected, otherwise it is broken, as we can see e. g. from Eq. (2.55), since the terms with t' do not commute with σ_z. We discuss the effect of this symmetry breaking on the density of states in Sec. 4.1.

Armchair edges

The armchair edge is the second prominent type of boundary that results from termination of the lattice along a line, namely when this line includes an angle of 30°, 90°, or 150° with the x-axis, as depicted in Fig. 2.4 b). This means that every armchair orientation lies exactly between two successive zigzag orientations and vice versa. In Ref. [87] the authors show that for all other orientations, the edge can be approximately treated as a zigzag edge with boundary matrices (2.44). We consider a flake with an edge such that the first row of atoms is along the vertical line $x = x_0 + a/2$ and the flake is extended for $x \geq x_0$. In contrast to the zigzag case, both sublattices are present at an armchair edge, more precisely it consists

of dimers with one A- and one B-atom each, as can be seen in Fig. 2.4 b). Consequently, the boundary condition is that both A- and B-components of the tight-binding wavefunction (2.29) have to vanish along the line $x = x_0$ [79, 80]

$$\mathrm{e}^{\mathrm{i}Kx_0}\,\psi_A(x_0,y) + \mathrm{e}^{-\mathrm{i}Kx_0}\,\psi'_A(x_0,y) = 0 \quad \forall y \tag{2.57}$$

$$\wedge \quad \mathrm{e}^{\mathrm{i}Kx_0}\,\psi_B(x_0,y) + \mathrm{e}^{-\mathrm{i}Kx_0}\,\psi'_B(x_0,y) = 0 \quad \forall y\,. \tag{2.58}$$

Note that this relates the contributions from both K-points to each other, in other words, the armchair edge does couple the valleys. We can cast Eqs. (2.57) and (2.58) into the following matrix equation for the four-spinors

$$\begin{pmatrix} \psi_A \\ \psi_B \\ -\psi'_B \\ \psi'_A \end{pmatrix} = \begin{pmatrix} -\exp(-2\mathrm{i}Kx_0)\psi'_A \\ -\exp(-2\mathrm{i}Kx_0)\psi'_B \\ \exp(2\mathrm{i}Kx_0)\psi_B \\ -\exp(2\mathrm{i}Kx_0)\psi_A \end{pmatrix} \tag{2.59}$$

$$= \begin{pmatrix} 0 & 0 & 0 & -\exp(-2\mathrm{i}Kx_0) \\ 0 & 0 & \exp(-2\mathrm{i}Kx_0) & 0 \\ 0 & \exp(2\mathrm{i}Kx_0) & 0 & 0 \\ -\exp(2\mathrm{i}Kx_0) & 0 & 0 & 0 \end{pmatrix} \begin{pmatrix} \psi_A \\ \psi_B \\ -\psi'_B \\ \psi'_A \end{pmatrix},$$

and after some modifications we identify the boundary matrix for an armchair edge at x_0 as

$$\mathcal{P}_{\mathrm{ac}} = \frac{1}{2}\left(1 \pm \tau_y \mathrm{e}^{2\mathrm{i}Kx_0\tau_z} \otimes \sigma_{\boldsymbol{t}}\right). \tag{2.60}$$

The sign depends on the orientation of the dimers at the edge with respect to the tangential direction $\boldsymbol{t}$ [cf. Fig. 2.4 b)]. For orientations such that the order along $\boldsymbol{t}$ is B-A, as in the case we have considered above, the upper sign is valid. In the other cases, when the order is A-B, the lower sign has to be considered. The boundary matrix (2.60) projects the sublattice pseudospin into a direction parallel or antiparallel to the tangent $\boldsymbol{t}$. The valley pseudospin is projected into a position-dependent direction that, however, always lies in-plane, i. e. there is no preferred valley.

We now study the armchair edges in view of the antiunitary symmetries of $\mathcal{H}$. It it straightforward to show that, irrespective of x_0,

$$0 = [\mathcal{T}_y, \mathcal{P}_{\mathrm{ac}}] \neq [\mathcal{T}_x, \mathcal{P}_{\mathrm{ac}}]\,. \tag{2.61}$$

As expected, the intervalley TRS is preserved and the valley degeneracy is broken because of the valley coupling. For $\mathcal{T}_0$, a more careful consideration is necessary, though. Namely, we find that

$$[\mathcal{T}_0, \mathcal{P}_{\mathrm{ac}}] = 0 \Leftrightarrow \frac{x_0}{a} \mod \frac{3}{8} = 0\,. \tag{2.62}$$

This is due to the fact that if x_0 fulfills the condition in Eq. (2.62), the matrix $\mathcal{P}_{\mathrm{ac}}$ contains no valleyspin matrices other than τ_y. There are two situations in which (2.62) arises naturally. The first is obviously if only a single armchair edge exists, because then one can shift the

coordinate system arbitrarily, e. g. such that $x_0 = 0$. The second is certain armchair graphene nanoribbons, i. e. strips of constant width that are infinitely extended in one direction and confined by two armchair edges in the perpendicular direction. Without loss of generality we can assume $x_0 = 0$ for one edge and $x_0 = W$ for the second edge. Then $\mathcal{T}_0$ is preserved if and only if W is a multiple of $3\,a/8$. However, due to the microscopic structure of the graphene lattice, W is always a multiple of $a/2$ [see for example Fig. 2.1 a)], so that the condition for conserved $\mathcal{T}_0$ relaxes to

$$\frac{2W}{3a} \in \mathbb{N}\,. \tag{2.63}$$

It can be shown that in this case the ribbon is metallic, i. e its energy spectrum is gapless, while otherwise the spectrum has a bandgap that scales inversely with W [25, 79, 80, 85]. We will therefore speak about 'metallic boundary conditions' for the cases in Eq. (2.62), and about 'semiconducting boundary conditions' otherwise, even when we consider only individual edges or more complicated structures.

Due to Kramers' theorem, $\mathcal{T}_0^2 = -1$ implies a degeneracy just as $\mathcal{T}_x$ does in the absence of intervalley coupling. In order to gain a better understanding of this degeneracy, we rotate the valleyspin space by $\pi/2$ around the x-direction such that $\tau_y \to \tau_z$, using the unitary transformation

$$\mathcal{R}_{zy} = \exp\left(\mathrm{i}\frac{\pi}{4}\tau_x\right)\,. \tag{2.64}$$

By rotating the valley space we have constructed a new *pseudovalley* structure and we obtain for the symmetries and the boundary matrix

$$\mathcal{T}_y^{zy} = \mathcal{R}_{zy}^\dagger \mathcal{T}_y \mathcal{R}_{zy} = \tau_y \otimes \sigma_y \mathcal{C}\,, \tag{2.65}$$

$$\mathcal{T}_x^{zy} = \mathcal{R}_{zy}^\dagger \mathcal{T}_x \mathcal{R}_{zy} = -\mathrm{i}\tau_0 \otimes \sigma_y \mathcal{C}\,, \tag{2.66}$$

$$\mathcal{T}_0^{zy} = \mathcal{R}_{zy}^\dagger \mathcal{T}_0 \mathcal{R}_{zy} = -\mathrm{i}\tau_x \otimes \sigma_y \mathcal{C}\,, \tag{2.67}$$

$$\mathcal{P}_{\mathrm{ac}}^{zy} = \mathcal{R}_{zy}^\dagger \mathcal{P}_{\mathrm{ac}} \mathcal{R}_{zy} = \frac{1}{2}\left(1 \pm \tau_z \mathrm{e}^{-2\mathrm{i}Kx_0\tau_y} \otimes \sigma_{\boldsymbol{t}}\right)\,. \tag{2.68}$$

From Eq. (2.68) we can read off that the metallic boundary conditions do not mix the pseudovalleys but the semiconducting boundary conditions do so: In the former case only τ_z valley matrices occur, while also in-plane valley matrices are present in the latter case. Furthermore, we find that the intervalley TRS $\mathcal{T}_y$ is invariant under the rotation. On the other hand, $\mathcal{T}_x^{zy}$ is now the effective intra(pseudo)valley TRS, but it is broken by all armchair edges. Finally, $\mathcal{T}_0^{zy}$ is preserved only for the metallic boundary conditions, ensuring the degeneracy of the pseudovalleys in this case. We discuss the consequences of this pseudovalley structure on the conductance of disordered nanoribbons in Sec. 7.1.

Infinite mass boundary conditions

While the boundary conditions for zigzag and armchair type edges are derived from microscopic lattice terminations, one can also think about confining Dirac electrons by means of a potential. For example semiconductor nanostructures like quantum dots, quantum wires, or

Aharonov-Bohm rings are usually realized by scalar potentials that are produced by voltages applied to top gates. These voltages deplete the the region in the 2DEG below the gates, since the Fermi energy is locally shifted into the band gap. For Dirac electrons, however, it is in principle not possible to confine them with a scalar potential. As mentioned before, the reason is the lack of a gap in the bulk band structure and the resulting Klein tunneling.

However, if instead of a scalar potential we consider a potential

$$V_m(\boldsymbol{x}) = \tau_z \otimes \sigma_z m(\boldsymbol{x})\,, \tag{2.69}$$

which has a different sign on each of the two sublattices (due to the Pauli matrix σ_z), the energy spectrum indeed has a (local) gap wherever $m(\boldsymbol{x})$ is non-zero. Physically, such a staggered potential can result e. g. from certain substrates, like boron nitride, that couple differently to A- and B-sites [88, 89]. Moreover, we study in Chap. 6 effects of magnetic ordering at zigzag edges, which in mean field approximation takes the form of a spin-dependent staggered potential. Considering the most simple case of a constant staggered potential, $m(\boldsymbol{x}) = m_0$, the Hamiltonian can be easily diagonalized and the resulting eigenenergies are

$$E = \pm\sqrt{v_F^2 p^2 + m_0^2}\,, \tag{2.70}$$

as for massive Dirac particles with a rest mass of m_0. Therefore a potential as in Eq. (2.69) is denoted as *mass term* or *mass potential*. Since it leads to a gap of $2m_0$ in the spectrum, such a mass potential can be used to effectively confine the Dirac electrons. We consider a slightly more complicated mass term, namely the staggered step potential

$$m(\boldsymbol{x}) = \begin{cases} 0, & \text{if } \boldsymbol{x} \in \mathcal{V}\,, \\ m_0, & \text{else}\ . \end{cases} \tag{2.71}$$

In this case, the boundary conditions on the spinors in the interior of the domain $\mathcal{V}$ have been derived by Berry and Mondragon almost 25 years ago [90], when they discussed the 2D Dirac equation in order to describe confined neutrinos. They have shown that the requirement of a vanishing particle current towards outside of the system leads to the relation

$$\Psi(\boldsymbol{\alpha}) = \gamma\, \tau_z \otimes \sigma_{\boldsymbol{t}_{\boldsymbol{\alpha}}} \Psi(\boldsymbol{\alpha})\,, \tag{2.72}$$

where $\boldsymbol{t}_{\boldsymbol{\alpha}}$ is the tangential direction at the boundary point $\boldsymbol{\alpha}$ and γ depends on m_0. Furthermore, they find for an infinitely large mass that

$$\gamma = \mp 1\,, \qquad \text{for} \quad m_0 \to \mp\infty\,, \tag{2.73}$$

leading to a boundary matrix

$$\mathcal{P}_{\text{im}} = \frac{1}{2}\left(1 \pm \tau_z \otimes \sigma_{\boldsymbol{t}}\right)\,. \tag{2.74}$$

The valleys are not mixed by the infinite mass edges and the effects on the antiunitary symmetries are exactly as for zigzag edges

$$0 = [\mathcal{T}_y, \mathcal{P}_{\text{im}}] = [\mathcal{T}_x, \mathcal{P}_{\text{im}}] \neq [\mathcal{T}_0, \mathcal{P}_{\text{im}}]\,. \tag{2.75}$$

This means that also for infinite mass edges the intervalley TRS and the valley degeneracy are preserved, while the intravalley TRS is broken.

2.3 Summary

In this introductory chapter we have discussed the basic properties of graphene that we need for our further work. We have sketched the derivation of the effective continuum Hamiltonian (2.17) that describes quasiparticles in graphene at low energies. It has the form of a Dirac equation for fermions with zero rest mass in two dimensions, where, however, the spin is replaced by a pseudospin corresponding to the sublattice degree of freedom. We have shown that a second pseudospin degree of freedom appears for graphene, namely the valley pseudospin, describing contributions from the vicinity of the two non-equivalent corner points of the first Brillouin zone. The Dirac Hamiltonian (2.17) is of central importance for the rest of this thesis. In the following chapter we derive the Green function of graphene structures based on Eq. (2.17). This Green function in turn will be used extensively in Chaps. 4-6.

Secondly, we have introduced the most important graphene boundary conditions for the Dirac Hamiltonian. We have presented them in a compact form in terms of a projection of the two pseudospin degrees of freedom into directions that depend on the boundary type [Eqs. (2.44), (2.55), (2.60), and (2.74)]. Also these projections will be used frequently in the remainder of this thesis. Finally we have discussed the different boundary types in view of the antiunitary symmetries of the Dirac Hamiltonian. In this respect the most important statements are that both zigzag and infinite mass type edges break the effective intravalley TRS $\mathcal{T}_0$ and that armchair edges break the valley degeneracy $\mathcal{T}_x$. On the other hand, the intervalley TRS $\mathcal{T}_y$ is preserved in all three cases. Further we have found that, even though the original valleys are mixed, certain (combinations of) armchair edges lead to a preserved pseudovalley structure, which we investigate further in Sec. 7.1.

CHAPTER 3

Green function for ballistic graphene structures

In this chapter we derive the Green function G of a ballistic graphene flake within the framework of the effective Dirac equation. For this purpose we follow in principle the route of Balian and Bloch, who derived expansions for the exact Green function and the density of states for the Helmholtz equation in a closed three-dimensional domain of arbitrary shape [91]. Each term in this expansion can be considered as the contribution from all Feynman paths that hit the boundary of the system a specific number of times. Later this method has been extended to various other types of systems and problems, including flexural vibrations in elastic plates [92, 93], Andreev billiards [94], and Schrödinger billiards with spin-orbit interaction [95, 96]. Also for the three-dimensional Dirac equation, a similar expansion has been presented for so-called MIT bag model boundary conditions [97]. We derive an analog expansion for graphene, including the two pseudospin degrees of freedom σ and τ, corresponding to the sublattice structure of the hexagonal lattice and the contributions from the two valleys. The exact Green function of a ballistic graphene flake is uniquely defined by the corresponding equation of motion, i. e. by the effective Dirac equation, and appropriate boundary conditions that have the form of local linear restrictions of the pseudospins at the boundaries in the effective theory for graphene, as discussed in Sec. 2.2.2.

The second and major part of this chapter is then concerned with the Green function in the *semiclassical limit*, i. e. for systems with a typical size L that is much larger than the Fermi wavelength $\sim 1/k_E$ ($k_E = E/\hbar v_F$). We derive an asymptotic expression for G, taking into account only contributions of leading order in $(k_E L)^{-1}$. The two dominating contributions to G originate from the *classical trajectories* that exist in the system and from *short-range singularities* due to quantum paths that hit the boundary several times close to the same boundary point. The latter can be resummed, so that we have to consider only the classical trajectories, but with renormalized reflections. Finally we obtain an expression for the graphene Green function in the semiclassical limit in terms of a sum over all classical trajectories, that is very similar to the well-known semiclassical Green function for the 2D Schrödinger equation. The main difference to the Schrödinger case is a matrix propagator, which describes the evolution of sublattice and valley pseudospin along each classical orbit. A similar object occurs also in the semiclassical Green function for Schrödinger billiards with spin-orbit interaction, where the dynamics of the real spin is described solely by a matrix propagator along classical trajectories [98, 99, 100, 101].

We focus on ballistic systems here, i. e. we assume that the graphene flake is rather clean

so that scattering from impurities, defects, etc., within the system can be neglected, and scattering occurs only at the boundaries. In App. A.6 we show how weak potential disorder in the interior of the flake affects the semiclassical result.

3.1 Multiple reflection expansion

We consider a graphene flake defined by the two-dimensional domain $\mathcal{V}$, without scattering potentials in the interior. Scattering of the charge carriers then occurs exclusively at the edges of the flake. The system is fully described by the Hamiltonian $\mathcal{H}$, Eq. (2.17), and the boundary conditions on the wavefunctions at $\partial\mathcal{V}$, see Eq. (2.38). The corresponding retarded Green function in configuration space $G(\boldsymbol{x}, \boldsymbol{x}')$ fulfills the equation of motion

$$\left[k_E + \mathrm{i}\eta - \frac{\mathcal{H}(\boldsymbol{x})}{\hbar v_F}\right] G(\boldsymbol{x}, \boldsymbol{x}') = \delta(\boldsymbol{x} - \boldsymbol{x}')\,, \tag{3.1}$$

in the interior of the system. Here we have introduced an infinitesimal positive imaginary part of the momentum, η. For convenience we mostly absorb η into k_E, rather than writing it explicitly. In order to find a solution of (3.1) that fulfills the boundary conditions as well, we write the Green function in terms of the eigenstate wavefunctions as

$$G(\boldsymbol{x}, \boldsymbol{x}') = \sum_n \frac{\Psi_n(\boldsymbol{x})\Psi_n^\dagger(\boldsymbol{x}')}{k_E + \mathrm{i}\eta - k_n}\,, \tag{3.2}$$

which obviously fulfills Eq. (3.1), since $\mathcal{H}\,\Psi_n = \hbar v_F k_n \Psi_n$ and the Ψ_n form a complete basis set. In this notation it becomes clear that the Green function has to obey the boundary condition

$$\mathcal{P}_{\boldsymbol{\alpha}} \lim_{\boldsymbol{x}\to\boldsymbol{\alpha}} G(\boldsymbol{x}, \boldsymbol{x}') = 0 \tag{3.3}$$

for every boundary point $\boldsymbol{\alpha}$. We now parametrize the exact retarded Green function G as the free retarded Green function G_0, i. e. the Green function of extended graphene without any boundary, plus a boundary correction that has the shape of a potential produced by a yet unknown Dirac charge layer μ [91, 97, 102]

$$G(\boldsymbol{x}, \boldsymbol{x}') = G_0(\boldsymbol{x}, \boldsymbol{x}') - \int\limits_{\partial\mathcal{V}} d\sigma_{\boldsymbol{\beta}}\, G_0(\boldsymbol{x}, \boldsymbol{\beta})\, \mathrm{i}\boldsymbol{\sigma}_{\boldsymbol{n}_{\boldsymbol{\beta}}}\, \mu(\boldsymbol{\beta}, \boldsymbol{x}')\,. \tag{3.4}$$

We have introduced the short notation $\sigma_{\boldsymbol{v}} \equiv \boldsymbol{\sigma}\cdot\boldsymbol{v}$ for an arbitrary vector $\boldsymbol{v}$, and $\boldsymbol{n}_{\boldsymbol{\beta}}$ is the normal vector at the boundary point $\boldsymbol{\beta}$. We note that the factor $\mathrm{i}\boldsymbol{\sigma}_{\boldsymbol{n}_{\boldsymbol{\beta}}}$ has been included for convenience only. The parametrization (3.4) fulfills Eq. (3.1) in the interior of $\mathcal{V}$ by construction: The free Green function G_0 does so by definition and the second term gives a delta function $\delta(\boldsymbol{x} - \boldsymbol{\beta})$ within the integral, which is always equal to zero, since $\boldsymbol{\beta}$ does not lie in the interior but on $\partial\mathcal{V}$. The function μ has to be determined such that Eq. (3.3) holds. For this purpose we have a closer look at the free Green function. G_0 is obtained by solving

Eq. (3.1) with the boundary condition $G(\boldsymbol{x},\boldsymbol{x}') \to 0$ as $\boldsymbol{x}-\boldsymbol{x}' \to \infty$. We formally invert the defining equation (3.1) to obtain

$$\begin{aligned} G_0(\boldsymbol{x},\boldsymbol{x}') &= \left[k_E - \frac{\mathcal{H}(\boldsymbol{x})}{\hbar v_F}\right]^{-1} \delta(\boldsymbol{x}-\boldsymbol{x}') = (k_E + \mathrm{i}\boldsymbol{\nabla}_{\boldsymbol{x}}\cdot\boldsymbol{\sigma})^{-1}\,\delta(\boldsymbol{x}-\boldsymbol{x}') \\ &= (k_E - \mathrm{i}\boldsymbol{\nabla}_{\boldsymbol{x}}\cdot\boldsymbol{\sigma})\,(k_E^2+\boldsymbol{\nabla}_{\boldsymbol{x}}^2)^{-1}\delta(\boldsymbol{x}-\boldsymbol{x}')\,. \end{aligned} \tag{3.5}$$

Now we realize that the term $(k_E^2+\boldsymbol{\nabla}_{\boldsymbol{x}}^2)^{-1}\delta(\boldsymbol{x}-\boldsymbol{x}')$ is nothing else but the free Green function of the Schrödinger equation in two dimensions g_0, i. e. the solution of

$$(k_E^2 + \mathrm{i}\tilde{\eta} + \boldsymbol{\nabla}_{\boldsymbol{x}}^2)\, g(\boldsymbol{x},\boldsymbol{x}') = \delta(\boldsymbol{x}-\boldsymbol{x}') \tag{3.6}$$

with the boundary condition $g(\boldsymbol{x},\boldsymbol{x}') \to 0$ as $\boldsymbol{x}-\boldsymbol{x}' \to \infty$. The free Green function g_0 is well-known (see e. g. Ref. [50]), namely

$$g_0(\boldsymbol{x},\boldsymbol{x}') = -\frac{\mathrm{i}}{4}H_0^+(k_E|\boldsymbol{x}-\boldsymbol{x}'|)\,, \tag{3.7}$$

where H_0^+ denotes the zeroth order Hankel function of the first kind. With this we obtain the following expression for the free graphene Green function

$$G_0(\boldsymbol{x},\boldsymbol{x}') = (k_E - \mathrm{i}\boldsymbol{\nabla}_{\boldsymbol{x}}\cdot\boldsymbol{\sigma})g_0(\boldsymbol{x},\boldsymbol{x}') = -\frac{\mathrm{i}}{4}(k_E - \mathrm{i}\boldsymbol{\nabla}_{\boldsymbol{x}}\cdot\boldsymbol{\sigma})H_0^+(k_E|\boldsymbol{x}-\boldsymbol{x}'|)\,. \tag{3.8}$$

The close relation of G_0 to g_0 will later prove very useful for the evaluation of the exact Green function G.

Now we feed the result (3.8) into the ansatz (3.4), and find that the integrand has a singularity at $\boldsymbol{\alpha}=\boldsymbol{\beta}$ in the limit $\boldsymbol{x}\to\boldsymbol{\alpha}$ [91], which has its origin in the logarithmic divergence of $H_0^+(\xi)$ as $\xi\to 0$. This singularity results in a finite discontinuity of G at the boundary, namely, as shown in App. A.1,

$$\lim_{\boldsymbol{x}\to\boldsymbol{\alpha}} G(\boldsymbol{x},\boldsymbol{x}') = G_0(\boldsymbol{\alpha},\boldsymbol{x}') - \int_{\partial\mathcal{V}} d\sigma_{\boldsymbol{\beta}}\, G_0(\boldsymbol{\alpha},\boldsymbol{\beta})\,\mathrm{i}\sigma_{\boldsymbol{n}_{\boldsymbol{\beta}}}\,\mu(\boldsymbol{\beta},\boldsymbol{x}') + \frac{1}{2}\mu(\boldsymbol{\alpha},\boldsymbol{x}')\,. \tag{3.9}$$

Together with the boundary condition (3.3) we obtain the inhomogeneous integral equation for the charge layer μ

$$\mathcal{P}_{\boldsymbol{\alpha}}\mu(\boldsymbol{\alpha},\boldsymbol{x}') = 2\mathcal{P}_{\boldsymbol{\alpha}}G_0(\boldsymbol{\alpha},\boldsymbol{x}') - 2\int_{\partial\mathcal{V}} d\sigma_{\boldsymbol{\beta}}\,\mathcal{P}_{\boldsymbol{\alpha}}G_0(\boldsymbol{\alpha},\boldsymbol{\beta})\,\mathrm{i}\sigma_{\boldsymbol{n}_{\boldsymbol{\beta}}}\,\mu(\boldsymbol{\beta},\boldsymbol{x}')\,. \tag{3.10}$$

First we make the assumption that the charge layer is already projected into the subspace given by the boundary condition, i. e. $\mathcal{P}_{\boldsymbol{\alpha}}\mu = \mu$ [102]. Then the integral equation becomes

$$\mu(\boldsymbol{\alpha},\boldsymbol{x}') = 2\mathcal{P}_{\boldsymbol{\alpha}}G_0(\boldsymbol{\alpha},\boldsymbol{x}') - 2\int_{\partial\mathcal{V}} d\sigma_{\boldsymbol{\beta}}\,\mathcal{P}_{\boldsymbol{\alpha}}G_0(\boldsymbol{\alpha},\boldsymbol{\beta})\,\mathrm{i}\sigma_{\boldsymbol{n}_{\boldsymbol{\beta}}}\,\mu(\boldsymbol{\beta},\boldsymbol{x}')\,. \tag{3.11}$$

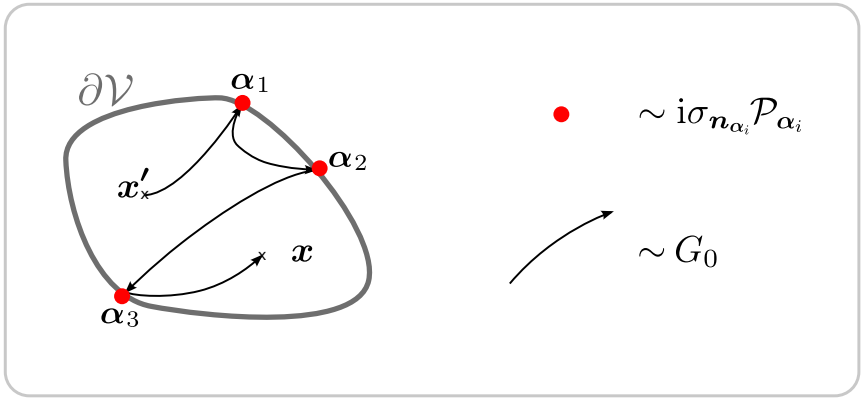

Figure 3.1: Schematic representation of a quantum path contributing to the Green function $G(\boldsymbol{x},\boldsymbol{x}')$. The black arrows stand for free propagations described by G_0, while each red disk represents a vertex of the form $\mathrm{i}\sigma_{\boldsymbol{n}_{\boldsymbol{\alpha}_i}}\mathcal{P}_{\boldsymbol{\alpha}_i}$.

Since $\mathcal{P}_{\boldsymbol{\alpha}}^2 = \mathcal{P}_{\boldsymbol{\alpha}}$, see Eq. (2.39), one realizes that a solution of Eq. (3.11) is automatically a solution of Eq. (3.10), too, since the right-hand side of (3.11) is unchanged by a multiplication with $\mathcal{P}_{\boldsymbol{\alpha}}$ from the left. The Green function is uniquely defined by the equation of motion, Eq. (3.1), and the boundary condition, Eq. (3.3). Therefore the solution of Eq. (3.11) already yields the correct Green function. The formal solution of Eq. (3.11) is obtained by iteration, resulting in

$$\mu(\boldsymbol{\alpha},\boldsymbol{x}') = 2\mathcal{P}_{\boldsymbol{\alpha}}G_0(\boldsymbol{\alpha},\boldsymbol{x}') - 4\int\limits_{\partial\mathcal{V}} d\sigma_{\boldsymbol{\beta}}\mathcal{P}_{\boldsymbol{\alpha}}G_0(\boldsymbol{\alpha},\boldsymbol{\beta})\mathrm{i}\sigma_{\boldsymbol{n}_{\boldsymbol{\beta}}}\mathcal{P}_{\boldsymbol{\beta}}G_0(\boldsymbol{\beta},\boldsymbol{x}') + \dots\,. \tag{3.12}$$

We insert this iterative solution into Eq. (3.4) and finally obtain the expansion for the exact Green function of a ballistic graphene flake with arbitrary types of edges

$$G(\boldsymbol{x},\boldsymbol{x}') = G_0(\boldsymbol{x},\boldsymbol{x}') + \sum_{N=1}^{\infty} G_N(\boldsymbol{x},\boldsymbol{x}')\,, \tag{3.13}$$

where

$$\begin{aligned} G_N(\boldsymbol{x},\boldsymbol{x}') = (-2)^N \int\limits_{\partial\mathcal{V}} d\sigma_{\boldsymbol{\alpha}_N}\dots d\sigma_{\boldsymbol{\alpha}_2}d\sigma_{\boldsymbol{\alpha}_1}G_0(\boldsymbol{x},\boldsymbol{\alpha}_N)\mathrm{i}\sigma_{\boldsymbol{n}_{\boldsymbol{\alpha}_N}}\mathcal{P}_{\boldsymbol{\alpha}_N} \\ \dots\mathrm{i}\sigma_{\boldsymbol{n}_{\boldsymbol{\alpha}_2}}\mathcal{P}_{\boldsymbol{\alpha}_2}G_0(\boldsymbol{\alpha}_2,\boldsymbol{\alpha}_1)\mathrm{i}\sigma_{\boldsymbol{n}_{\boldsymbol{\alpha}_1}}\mathcal{P}_{\boldsymbol{\alpha}_1}G_0(\boldsymbol{\alpha}_1,\boldsymbol{x}')\,. \end{aligned} \tag{3.14}$$

Following Balian and Bloch [91], we denote this result as *multiple reflection expansion* (MRE), since each term in this expansion can be considered as a series of free propagations, represented by the G_0, that are connected by reflections at the boundary. Every reflection is represented by a boundary-dependent projection $P_{\boldsymbol{\alpha}_i}$ and $\sigma_{\boldsymbol{n}_{\boldsymbol{\alpha}_i}}$, a reflection of the sublattice pseudospin across the normal axis. Note, however, that the reflections and the resulting paths are not classical in any sense at this level, but quantum (Feynman) paths. The integrals over

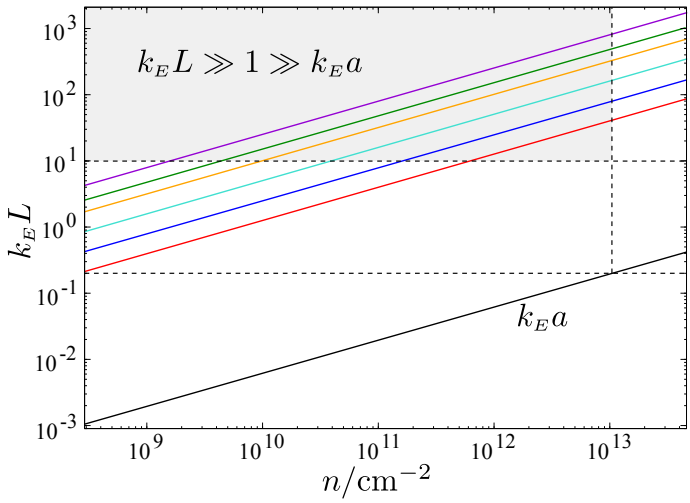

Figure 3.2: The colored lines show $k_E L$ as a function of the carrier density $n = k_E^2/2\pi$ for different typical system sizes (from bottom to top): $L = 50\,\mathrm{nm}$ (red), 100 nm (blue), 200 nm (turquoise), 400 nm (orange), 600 nm (green), and 1000 nm (violet). The solid black line is $k_E a$. The approximate region where both semiclassical approximation and Dirac equation are valid is shaded.

the boundary points correspond to a 'summation' over all quantum paths leading from $\boldsymbol{x}'$ to $\boldsymbol{x}$. Figure 3.1 shows schematically an example of a quantum path with three reflections at the boundary.

3.2 Green function in the semiclassical limit

With the MRE, Eq. (3.14), we have obtained a formalism that naturally relates the effects of the graphene edges to any property that involves single particle Green functions. As written in (3.14), the MRE is an exact expansion for the Green function of a graphene flake of arbitrary shape $\partial\mathcal{V}$. On the other hand, in a generic case the boundary integrals are extremely complicated and do not allow for a detailed analytical investigation into physical properties. However, often the experimentally realized structures are in the *mesoscopic* regime, i. e. their typical sizes lie between that of microscopic objects (e. g. atoms or molecules) and macroscopic bulk materials. The size L of these systems is usually large compared to the Fermi wavelength, and thus an adequate approximation is to work in the semiclassical limit and to consider physical properties only to leading order in $(k_E L)^{-1}$. On the other hand, the Fermi wavelength should be still large compared to the lattice constant a, to ensure the validity of the effective Dirac theory. For mesoscopic graphene systems both requirements, large $k_E L$ and small $k_E a$, are well fulfilled over several orders of magnitude of the carrier density, as shown in Fig. 3.2.

First we consider the free Green function between two successive reflections $G_0(\boldsymbol{\alpha}_{i+1}, \boldsymbol{\alpha}_i)$. Assuming that the distance between the arguments is of the order L, the scalar part of G_0,

i.e. the Hankel function, is in the semiclassical limit proportional to an exponential,

$$G_0(\boldsymbol{\alpha}_{i+1}, \boldsymbol{\alpha}_i) \sim H_0^+(k_E|\boldsymbol{\alpha}_{i+1} - \boldsymbol{\alpha}_i|) \sim \frac{\exp(\mathrm{i}k_E|\boldsymbol{\alpha}_{i+1} - \boldsymbol{\alpha}_i|)}{\sqrt{|\boldsymbol{\alpha}_{i+1} - \boldsymbol{\alpha}_i|}}\,. \tag{3.15}$$

Therefore each term in the expansion (3.13) can formally be written as

$$G_N(\boldsymbol{x}, \boldsymbol{x}') \approx \int^N \mathcal{A}(\boldsymbol{x}, \underline{\boldsymbol{\alpha}}_N, \boldsymbol{x}') \exp\left[\mathrm{i}k_E \mathcal{L}(\boldsymbol{x}, \underline{\boldsymbol{\alpha}}_N, \boldsymbol{x}')\right]\,, \tag{3.16}$$

where $\mathcal{A}$ contains the square root terms from Eq. (3.15) and all other scalar and matrix prefactors, while the phase term $\mathcal{L}$ consists of the sum of distances $|\boldsymbol{\alpha}_{i+1} - \boldsymbol{\alpha}_i|$. Furthermore, $\underline{\boldsymbol{\alpha}}_N$ is the supervector containing all boundary points

$$\underline{\boldsymbol{\alpha}}_N = (\boldsymbol{\alpha}_N, \boldsymbol{\alpha}_{N-1}, \ldots, \boldsymbol{\alpha}_2, \boldsymbol{\alpha}_1)\,. \tag{3.17}$$

In Ref. [103], the authors show that, if $\partial\mathcal{V}$ is smooth, there exist two classes of leading order contributions to the MRE. One is due to paths, for which all gradients of the phase term vanish

$$\boldsymbol{\nabla}_{\boldsymbol{\alpha}_i} \mathcal{L}(\boldsymbol{x}, \underline{\boldsymbol{\alpha}}_N, \boldsymbol{x}') = 0 \quad \forall i \in \{1, 2, \ldots, N\}\,. \tag{3.18}$$

We will see later that the corresponding paths are actually *classical* orbits in the sense that they obey Snell's classical law of reflection. These contributions are captured by evaluating the boundary integrals in stationary phase approximation, where $\mathcal{L}$ is expanded to second order around the stationary boundary points. We study these paths in Sec. 3.2.2. The other class of contributions is due to paths, where the prefactor $\mathcal{A}$ of the exponential diverges. From Eq. (3.15) we read off, that this is the case if and only if two consecutive reflection points come close, i. e. at the short-range singularities for which

$$\exists\, i \in \{1, 2, \ldots, N-1\} : |\boldsymbol{\alpha}_{i+1} - \boldsymbol{\alpha}_i| \to 0\,. \tag{3.19}$$

These contributions cannot be captured within stationary phase approximation, thus we have to treat them separately following a method described in Ref. [94]. The general idea is as follows: For a given boundary point $\boldsymbol{\alpha}$, we consider all quantum paths where one reflection occurs at $\boldsymbol{\alpha}$ and one or more additional reflections occur very close to $\boldsymbol{\alpha}$. Then we resum all these orbits by effectively renormalizing the free Green function or the boundary condition, respectively, so that only one renormalized reflection at $\boldsymbol{\alpha}$ has to be considered (see Fig. 3.3). We do this in Sec. 3.2.1. Afterwards we use the resummed MRE and evaluate the remaining boundary integrals in stationary phase approximation in Sec. 3.2.2. In this way we reduce the multiple boundary integrals to a sum over classical orbits with renormalized reflections that account for the short-range singularities, and thus we obtain the complete leading order contribution to the Green function G.

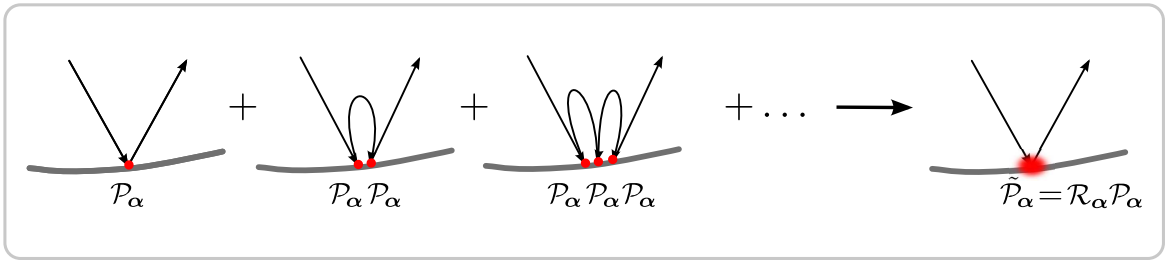

Figure 3.3: Schematic representation of the procedure to resum the short-range contributions to G. Successive reflections that occur all in close vicinity to one boundary point $\boldsymbol{\alpha}$ can give rise to singularities in the amplitude in (3.16), $\mathcal{A}$. The resummation results in only one effective reflection with a renormalized boundary matrix $\tilde{\mathcal{P}}_{\boldsymbol{\alpha}}$.

3.2.1 Resummation of short-range processes

First we isolate the short-range singularities formally [94]. For a function f we define the operator $\hat{\mathcal{I}}$ as follows

$$\hat{\mathcal{I}} f(\boldsymbol{\alpha}) = \int_{\partial\mathcal{V}} d\sigma_{\boldsymbol{\beta}}\, \mathcal{I}(\boldsymbol{\alpha},\boldsymbol{\beta}) f(\boldsymbol{\beta})\,, \tag{3.20}$$

$$\text{with} \quad \mathcal{I}(\boldsymbol{\alpha},\boldsymbol{\beta}) = 2\mathcal{P}_{\boldsymbol{\alpha}} G_0(\boldsymbol{\alpha},\boldsymbol{\beta})\, \mathrm{i}\sigma_{\boldsymbol{n}_{\boldsymbol{\beta}}}\,, \tag{3.21}$$

so that Eq. (3.11) reads

$$\mu(\boldsymbol{\alpha},\boldsymbol{x}') = 2\mathcal{P}_{\boldsymbol{\alpha}} G_0(\boldsymbol{\alpha},\boldsymbol{x}') - \hat{\mathcal{I}}\mu(\boldsymbol{\alpha},\boldsymbol{x}')\,. \tag{3.22}$$

Furthermore we divide $\mathcal{I}$ into a short-range part $\mathcal{I}_{\mathrm{s}}$, corresponding to an integration close to the singularity, and a long range part $\mathcal{I}_{\mathrm{l}}$ corresponding to an integration along the rest of the boundary:

$$\mathcal{I}_{\mathrm{s}}(\boldsymbol{\alpha},\boldsymbol{\beta}) = \mathcal{I}(\boldsymbol{\alpha},\boldsymbol{\beta})\,[1 - w(\boldsymbol{\alpha}-\boldsymbol{\beta})]\,, \tag{3.23}$$

$$\mathcal{I}_{\mathrm{l}}(\boldsymbol{\alpha},\boldsymbol{\beta}) = \mathcal{I}(\boldsymbol{\alpha},\boldsymbol{\beta}) w(\boldsymbol{\alpha}-\boldsymbol{\beta})\,, \tag{3.24}$$

where $w(\boldsymbol{\alpha}-\boldsymbol{\beta})$ is a smooth function that is zero, whenever $\boldsymbol{\alpha}$ is close to $\boldsymbol{\beta}$ and goes to one otherwise, so that integrating over $\boldsymbol{\beta}$ isolates the critical point $\boldsymbol{\beta} = \boldsymbol{\alpha}$. Note that this separation is only formal, in the sense that the specific form of w does not change the final result. Then Eq. (3.22) leads to

$$(1 + \hat{\mathcal{I}}_{\mathrm{s}})\,\mu(\boldsymbol{\alpha},\boldsymbol{x}') = 2\mathcal{P}_{\boldsymbol{\alpha}} G_0(\boldsymbol{\alpha},\boldsymbol{x}') - \hat{\mathcal{I}}_{\mathrm{l}}\,\mu(\boldsymbol{\alpha},\boldsymbol{x}')\,. \tag{3.25}$$

With the definition $\hat{\Gamma} = (\hat{1} + \hat{\mathcal{I}}_{\mathrm{s}})^{-1}$ we obtain

$$\mu(\boldsymbol{\alpha},\boldsymbol{x}') = 2\hat{\Gamma}\mathcal{P}_{\boldsymbol{\alpha}} G_0(\boldsymbol{\alpha},\boldsymbol{x}') - \hat{\Gamma}\,\hat{\mathcal{I}}_{\mathrm{l}}\,\mu(\boldsymbol{\alpha},\boldsymbol{x}')\,. \tag{3.26}$$

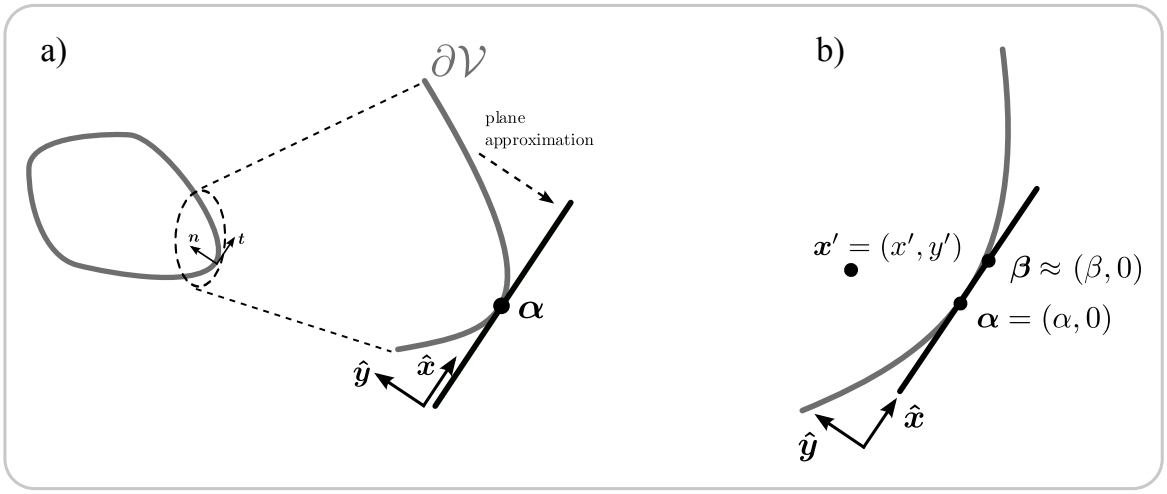

Figure 3.4: a) For the resummation of the short-range processes (and also for calculating the smooth density of states in Chap.4) we work in plane approximation: For a given point $\boldsymbol{\alpha}$ on the boundary $\partial\mathcal{V}$, we approximate the boundary locally by the tangent at $\boldsymbol{\alpha}$ and introduce a local coordinate system with x and y along the tangential and normal direction, respectively. b) Notation in the local coordinate system spanned by the tangent and the normal to the boundary at $\boldsymbol{\alpha}$. Corrections to the approximation $\boldsymbol{\beta} \approx (\beta, 0)$ are of subleading order in $k_E L$.

In integral representation this reads

$$\mu(\boldsymbol{\alpha}, \boldsymbol{x}') \;=\; 2\int\limits_{\partial V} d\sigma_{\boldsymbol{\beta}}\, \Gamma(\boldsymbol{\alpha}, \boldsymbol{\beta}) \mathcal{P}_{\boldsymbol{\beta}} G_0(\boldsymbol{\beta}, \boldsymbol{x}') - \int\limits_{\partial V} d\sigma_{\boldsymbol{\beta}'} \int\limits_{\partial V} d\sigma_{\boldsymbol{\beta}}\, \Gamma(\boldsymbol{\alpha}, \boldsymbol{\beta}) \mathcal{I}_1(\boldsymbol{\beta}, \boldsymbol{\beta}')\, \mu(\boldsymbol{\beta}', \boldsymbol{x}')\,. \tag{3.27}$$

Both terms in this expression have a very similar structure: By defining

$$\mathcal{Z}_{\boldsymbol{\alpha}}(\boldsymbol{\beta}, \boldsymbol{x}') = 2\Gamma(\boldsymbol{\alpha}, \boldsymbol{\beta}) \mathcal{P}_{\boldsymbol{\beta}} G_0(\boldsymbol{\beta}, \boldsymbol{x}')\,, \tag{3.28}$$

we can write

$$\mu(\boldsymbol{\alpha}, \boldsymbol{x}') = \int\limits_{\partial V} d\sigma_{\boldsymbol{\beta}}\, \mathcal{Z}_{\boldsymbol{\alpha}}(\boldsymbol{\beta}, \boldsymbol{x}') - \int\limits_{\partial V} d\sigma_{\boldsymbol{\beta}'} \int\limits_{\partial V} d\sigma_{\boldsymbol{\beta}}\, \mathcal{Z}_{\boldsymbol{\alpha}}(\boldsymbol{\beta}, \boldsymbol{\beta}') \mathrm{i}\sigma_{\boldsymbol{n}_{\boldsymbol{\beta}'}} w(\boldsymbol{\beta} - \boldsymbol{\beta}') \mu(\boldsymbol{\beta}', \boldsymbol{x}')\,. \tag{3.29}$$

Note that in both terms the arguments of $\mathcal{Z}$ can be assumed *not* to lie close to each other. For the left term this is evident because $\boldsymbol{x}'$ is located in the interior of the system and $\boldsymbol{\beta}$ lies on the boundary. For the right term, the separating function w ensures that the integral is zero when $\boldsymbol{\beta}$ and $\boldsymbol{\beta}'$ are close to each other. In this way we have separated all the short-range contributions that are now collected in Γ. We note that the main contributions to the integrals in Eq. (3.29) are due to points $\boldsymbol{\beta}$ that are close to $\boldsymbol{\alpha}$. To see this we write Γ formally as an infinite sum

$$\hat{\Gamma} = (\hat{1} + \hat{\mathcal{I}}_{\mathrm{s}})^{-1} = \sum_{n=0}^{\infty} (-\hat{\mathcal{I}}_{\mathrm{s}})^n\,. \tag{3.30}$$

Since $\hat{\mathcal{I}}_\mathrm{s}$ is short-ranged, i. e. it leads to integrals around $\boldsymbol{\alpha}$, the $\boldsymbol{\beta}$-integrals in Eq. (3.29) are also dominated by the contributions close to $\boldsymbol{\alpha}$. Therefore we replace the boundary for these integrals by a straight line along the tangent at $\boldsymbol{\alpha}$, see Fig. 3.4 a). This approximation, known as 'plane approximation', is adequate for sufficiently smooth boundaries. To be more precise, corrections to the plane approximation are of second or higher order in $(k_E R)^{-1}$, where R is the local radius of curvature at the considered boundary point $\boldsymbol{\alpha}$ [91, 94]. Considering smooth surfaces, R is in the order of the system size L, hence it is justified to neglect the curvature corrections. In a local coordinate system with the tangential and normal directions at $\boldsymbol{\alpha}$ denoted as x- and y-directions respectively, we write in plane approximation for a point $\boldsymbol{\beta}$ close to $\boldsymbol{\alpha}$, $\boldsymbol{\beta} \approx (\beta, 0)$, and for a point $\boldsymbol{x}'$ far away from $\boldsymbol{\alpha}$ we have $\boldsymbol{x}' = (x', y')$, see Fig. 3.4 b). Since $\boldsymbol{\beta}$ is close to $\boldsymbol{\alpha}$, we can also replace $w(\boldsymbol{\beta} - \boldsymbol{\beta}')$ by $w(\boldsymbol{\alpha} - \boldsymbol{\beta}')$ in the second term in Eq. (3.29), so that in plane approximation we get

$$\mu(\boldsymbol{\alpha}, \boldsymbol{x}') \approx \int_{-\infty}^{\infty} d\beta\, \mathcal{Z}_{\boldsymbol{\alpha}}(\boldsymbol{\beta}, \boldsymbol{x}') - \int_{\partial V} d\sigma_{\boldsymbol{\beta}'}\, w(\boldsymbol{\alpha} - \boldsymbol{\beta}') \int_{-\infty}^{\infty} d\beta\, \mathcal{Z}_{\boldsymbol{\alpha}}(\boldsymbol{\beta}, \boldsymbol{\beta}') \mathrm{i}\sigma_{\boldsymbol{n}_{\boldsymbol{\beta}'}} \mu(\boldsymbol{\beta}', \boldsymbol{x}')\,. \tag{3.31}$$

Now we make use of the homogeneity of the boundary close to $\boldsymbol{\alpha}$. Introducing the partial Fourier transform of a function f along the x-axes and its inverse as

$$f(k, y) = \int_{-\infty}^{\infty} dx\, \mathrm{e}^{-\mathrm{i}kx} f(x, y)\,, \quad f(x, y) = \int_{-\infty}^{\infty} \frac{dk}{2\pi}\, \mathrm{e}^{\mathrm{i}kx} f(k, y)\,, \tag{3.32}$$

we can work in the resulting mixed representation, where we keep the spatial dependence in the local y-direction, i. e. in the direction normal to the boundary at $\boldsymbol{\alpha}$, and replace the spatial dependence on the local x-direction, i. e. along the tangent to the boundary, by a momentum dependence. Then we have to calculate

$$\int_{-\infty}^{\infty} d\beta\, \mathcal{Z}_{\boldsymbol{\alpha}}(\boldsymbol{\beta}, \boldsymbol{x}') = \int_{-\infty}^{\infty} dk\, \mathrm{e}^{\mathrm{i}k(\alpha - x')}\, \mathcal{Z}_{\boldsymbol{\alpha}}(k, -y')\,, \tag{3.33}$$

with

$$\mathcal{Z}_{\boldsymbol{\alpha}}(k, -y') = 2\Gamma(k) \mathcal{P}_{\boldsymbol{\alpha}} G_0(k, -y')\,. \tag{3.34}$$

Here we employed the convolution theorem and used the homogeneity of the boundary, namely that

$$\Gamma(\boldsymbol{\alpha}, \boldsymbol{\beta}) = \Gamma(\alpha - \beta, 0)\,, \quad G_0(\boldsymbol{\beta}, \boldsymbol{x}') = G_0(\beta - x', -y')\,. \tag{3.35}$$

Starting from the free Green function in full momentum representation

$$G_0(\boldsymbol{k}') = \left(k_E - \boldsymbol{\sigma} \cdot \boldsymbol{k}'\right)^{-1} = \frac{k_E + \boldsymbol{\sigma} \cdot \boldsymbol{k}'}{k_E^2 - k'^2}\,, \tag{3.36}$$

we calculate the free Green function in mixed representation:

$$G_0(k,y') = \int_{-\infty}^{\infty} dx'\, \mathrm{e}^{-\mathrm{i}kx'}\, G_0(\boldsymbol{x}') = \int_{-\infty}^{\infty} dx'\, \mathrm{e}^{-\mathrm{i}kx'} \int \frac{d\boldsymbol{k}'}{(2\pi)^2}\, \mathrm{e}^{\mathrm{i}\boldsymbol{k}'\cdot\boldsymbol{x}'}\, G_0(\boldsymbol{k}') \tag{3.37}$$

$$= \int \frac{d\boldsymbol{k}'}{(2\pi)^2} \underbrace{\int_{-\infty}^{\infty} dx'\, \mathrm{e}^{\mathrm{i}(k'_x-k)x'}}_{2\pi\delta(k'_x-k)}\, \mathrm{e}^{\mathrm{i}k'_y y'}\, \frac{k_E+\boldsymbol{\sigma}\cdot\boldsymbol{k}'}{k_E^2-k'^2} = \int_{-\infty}^{\infty} \frac{dk'_y}{2\pi}\, \mathrm{e}^{\mathrm{i}k'_y y'}\, \frac{k_E+k\sigma_{\boldsymbol{t_\alpha}}+k'_y\sigma_{\boldsymbol{n_\alpha}}}{k_E^2-k^2-k_y'^2}\,.$$

The remaining integral is solved by means of the residue theorem and we obtain

$$G_0(k,y') = -\frac{\mathrm{e}^{-a(k)|y'|}}{2a(k)}\left[k_E + k\sigma_{\boldsymbol{t_\alpha}} + \mathrm{i}\,\mathrm{sgn}(y')\,a(k)\,\sigma_{\boldsymbol{n_\alpha}}\right]\,, \tag{3.38}$$

with

$$a(k) = \sqrt{k^2-k_E^2}\,. \tag{3.39}$$

Due to the infinitesimal imaginary part of k_E, the square root has always a finite real part. The branch has to be chosen such that $\mathfrak{Re}\, a(k) > 0$. We note that the expression (3.38) for G_0 in mixed representation also holds true for $y' = 0$, when we identify $\mathrm{sgn}(0) = 0$, in this case leading to

$$G_0(k,0) = -\frac{(k_E + k\sigma_{\boldsymbol{t_\alpha}})}{2a(k)}\,. \tag{3.40}$$

With that we can write for $\Gamma^{-1} = 1 + \mathcal{I}_s$ in Eq. (3.34)

$$\Gamma^{-1}(k) = 1 - \mathrm{i}2\mathcal{P}_{\boldsymbol{\alpha}}\frac{(k_E + k\sigma_{\boldsymbol{t_\alpha}})}{2a(k)}\sigma_{\boldsymbol{n_\alpha}}\,. \tag{3.41}$$

In order to evaluate Eq. (3.33), we have to perform the inversion in Eq. (3.41). To this end we use the explicit form of the boundary condition at the point $\boldsymbol{\alpha}$. Here we perform the calculation for the three most common boundary conditions, namely those for armchair edges, infinite mass type boundaries, and zigzag edges. In App. A.2.2 we perform the corresponding calculation for a model that describes zigzag edges in the presence of next-nearest-neighbor hopping.

Armchair and infinite mass boundaries

Starting with armchair edges, we consider the boundary matrix of Eq. (2.60)

$$\mathcal{P}_{\boldsymbol{\alpha}} = \frac{1}{2}\left(1 \pm \tau_y \mathrm{e}^{2\mathrm{i}Kx_{\boldsymbol{\alpha}}\tau_z} \otimes \sigma_{\boldsymbol{t_\alpha}}\right)\,. \tag{3.42}$$

For the sake of simplicity, we omit the subscript $\boldsymbol{\alpha}$ during the course of the calculation and assume $x_{\boldsymbol{\alpha}} = 0$, which does not change the results. Then we have

$$\begin{aligned}\Gamma^{-1}(k) &= 1 - \frac{\mathrm{i}}{2a(k)}\left(1 \pm \tau_y \otimes \sigma_{\boldsymbol{t}}\right)(k_E + k\sigma_{\boldsymbol{t}})\sigma_{\boldsymbol{n}} \\ &= 1 - \frac{\mathrm{i}}{2a(k)}[k_E\sigma_{\boldsymbol{n}} + \mathrm{i}k\sigma_z \pm \tau_y \otimes (k\sigma_{\boldsymbol{n}} + \mathrm{i}k_E\sigma_z)]\,.\end{aligned} \tag{3.43}$$

For the inversion we make use of the formula for block matrices

$$\begin{pmatrix} A & B \\ -B & A \end{pmatrix}^{-1} = \begin{pmatrix} Q^{-1} & -Q^{-1}BA^{-1} \\ A^{-1}BQ^{-1} & A^{-1} - A^{-1}BQ^{-1}BA^{-1} \end{pmatrix}, \tag{3.44}$$

with $Q = A + BA^{-1}B$. This relation holds for arbitrary quadratic blocks A and B, as long as A has an inverse, as can be checked by matrix multiplication. In our case the blocks are given by

$$A = 1 - \frac{\mathrm{i}}{2a(k)}(k_E\sigma_{\boldsymbol{n}} + \mathrm{i}k\sigma_z)\,, \quad B = \frac{\mp 1}{2a(k)}(k\sigma_{\boldsymbol{n}} + \mathrm{i}k_E\sigma_z)\,, \tag{3.45}$$

leading to

$$\Gamma(k) = 1 + \frac{\mathrm{i}}{2a(k)}[k_E\sigma_{\boldsymbol{n}} + \mathrm{i}k\sigma_z \pm \tau_y \otimes (k\sigma_{\boldsymbol{n}} + \mathrm{i}k_E\sigma_z)]\,. \tag{3.46}$$

This can be further simplified yielding

$$\Gamma(k) = 1 + \frac{\mathrm{i}}{2a(k)}(k_E\sigma_{\boldsymbol{n}} + \mathrm{i}k\sigma_z)(1 \mp \tau_y \otimes \sigma_{\boldsymbol{t}}) = 1 + \frac{\mathrm{i}}{a(k)}(k_E\sigma_{\boldsymbol{n}} + \mathrm{i}k\sigma_z)(1 - \mathcal{P}_{\boldsymbol{\alpha}})\,. \tag{3.47}$$

Since in $\mathcal{Z}_{\boldsymbol{\alpha}}$, Eq. (3.34), the matrix Γ is multiplied by $\mathcal{P}_{\boldsymbol{\alpha}}$ from the right, only the 1 in the expression (3.47) contributes, because of the projection property $\mathcal{P}_{\boldsymbol{\alpha}}^2 = \mathcal{P}_{\boldsymbol{\alpha}}$. Hence we get

$$\mathcal{Z}_{\boldsymbol{\alpha}}(k, -y) = 2\mathcal{P}_{\boldsymbol{\alpha}}G_0(k, -y') \tag{3.48}$$

$$\Rightarrow \int_{-\infty}^{\infty} d\beta\, \mathcal{Z}_{\boldsymbol{\alpha}}(\boldsymbol{\beta}, \boldsymbol{x}') = 2\mathcal{P}_{\boldsymbol{\alpha}}G_0(\boldsymbol{\alpha}, \boldsymbol{x}')\,, \tag{3.49}$$

where we have used the identity (3.33). Now we insert (3.49) into Eq. (3.31) to obtain

$$\mu(\boldsymbol{\alpha}, \boldsymbol{x}') \approx 2\mathcal{P}_{\boldsymbol{\alpha}}G_0(\boldsymbol{\alpha}, \boldsymbol{x}') - 2\int_{\partial V} d\sigma_{\boldsymbol{\beta}}\, \mathcal{P}_{\boldsymbol{\alpha}}G_0(\boldsymbol{\alpha}, \boldsymbol{\beta})\, \mathrm{i}\, \sigma_{\boldsymbol{n}_{\boldsymbol{\beta}}}\mu(\boldsymbol{\beta}, \boldsymbol{x}')\, w(\boldsymbol{\alpha} - \boldsymbol{\beta})\,. \tag{3.50}$$

In comparison to the original integral equation for μ, Eq. (3.11), the only difference is the isolating function w in (3.50). This means that, while all quantum paths contribute to Eq. (3.11), the short-range processes are completely removed in Eq. (3.50), i. e. they do not contribute for armchair edges to leading order in $(k_E L)^{-1}$. Mathematically this can be understood by realizing that the boundary matrix commutes with the free propagation between two adjacent reflection points, but not with the $\sigma_{\boldsymbol{n}_{\boldsymbol{\alpha}}}$. Rather, commutation leads to two projections in opposite directions and thus the corresponding term in the Green function vanishes. Expressed in formulas, we have for two successive reflections at the same armchair edge [cf. Eqs. (3.40) and (3.42)]

$$\frac{\sigma_{\boldsymbol{n}_{\boldsymbol{\alpha}}}\mathcal{P}_{\boldsymbol{\alpha}}(k_E + k\sigma_{\boldsymbol{t}_{\boldsymbol{\alpha}}})\sigma_{\boldsymbol{n}_{\boldsymbol{\alpha}}}\mathcal{P}_{\boldsymbol{\alpha}}}{|\boldsymbol{\alpha} - \boldsymbol{\beta}|} = \frac{(k_E - k\sigma_{\boldsymbol{t}_{\boldsymbol{\alpha}}})(1 - \mathcal{P}_{\boldsymbol{\alpha}})\mathcal{P}_{\boldsymbol{\alpha}}}{|\boldsymbol{\alpha} - \boldsymbol{\beta}|} = 0\,. \tag{3.51}$$

The same holds true also for infinite mass type edges where, according to Eq. (2.74), we have $\mathcal{P}_{\boldsymbol{\alpha}} = (1 \pm \tau_z \otimes \sigma_{\boldsymbol{t}_{\boldsymbol{\alpha}}})/2$, and we show now that indeed also in this case the short-range

processes do not contribute. Since now the boundary condition, and therefore also Γ^{-1}, is diagonal in valley space, we can invert the valley subblocks separately:

$$\Gamma^{-1} = \begin{pmatrix} \Gamma_{+1}^{-1} & 0 \\ 0 & \Gamma_{-1}^{-1} \end{pmatrix} \quad \Rightarrow \quad \Gamma = \begin{pmatrix} \Gamma_{+1} & 0 \\ 0 & \Gamma_{-1} \end{pmatrix}. \tag{3.52}$$

Just as before we get

$$\Gamma_\tau^{-1}(k) = 1 - \frac{\mathrm{i}}{2a(k)}[(k_E \pm \tau k)\sigma_{\boldsymbol{n}} + \mathrm{i}(k \pm \tau k_E)\sigma_z]\,. \tag{3.53}$$

Now we have to invert only a 2×2 matrix. To this end we make use of the relation

$$(b + \boldsymbol{\sigma}\cdot\boldsymbol{v})^{-1} = (b - \boldsymbol{\sigma}\cdot\boldsymbol{v})(b - \boldsymbol{\sigma}\cdot\boldsymbol{v})^{-1}(b + \boldsymbol{\sigma}\cdot\boldsymbol{v})^{-1} = \frac{b - \boldsymbol{\sigma}\cdot\boldsymbol{v}}{b^2 - \boldsymbol{v}\cdot\boldsymbol{v}}\,, \tag{3.54}$$

which holds for an arbitrary three component vector $\boldsymbol{v}$ and a scalar b. With this we obtain

$$\begin{aligned} \Gamma_\tau(k) &= \frac{1 + \frac{\mathrm{i}}{2a(k)}[(k_E \pm \tau k)\sigma_{\boldsymbol{n}} + \mathrm{i}(k \pm \tau k_E)\sigma_z]}{1 + \frac{(k_E \pm \tau k)^2}{4a^2(k)} - \frac{(k \pm \tau k_E)^2}{4a^2(k)}} = 1 + \frac{\mathrm{i}}{2a(k)}[(k_E \pm \tau k)\sigma_{\boldsymbol{n}} + \mathrm{i}(k \pm \tau k_E)\sigma_z] \\ &= 1 + \frac{\mathrm{i}}{2a(k)}(k_E\sigma_{\boldsymbol{n}} + \mathrm{i}k\sigma_z)(1 \mp \tau\sigma_{\boldsymbol{t}}) = 1 + \frac{\mathrm{i}}{a(k)}(k_E\sigma_{\boldsymbol{n}} + \mathrm{i}k\sigma_z)(1 - \mathcal{P}_{\boldsymbol{\alpha}})_\tau, \end{aligned} \tag{3.55}$$

leading again to Eq. (3.48) and in consequence also to Eq. (3.50), as claimed.

Zigzag boundaries

We now turn to the case of reflections at zigzag type edges, i. e. according to Eq. (2.44) we use $\mathcal{P}_{\boldsymbol{\alpha}} = (1 \pm \tau_z \otimes \sigma_z)/2$. Here the situation if different from the previous cases, namely the the analog to Eq. (3.51) for zigzag edges reads

$$\frac{\sigma_{\boldsymbol{n}_{\boldsymbol{\alpha}}}\mathcal{P}_{\boldsymbol{\alpha}}(k_E + k\sigma_{\boldsymbol{t}_{\boldsymbol{\alpha}}})\sigma_{\boldsymbol{n}_{\boldsymbol{\alpha}}}\mathcal{P}_{\boldsymbol{\alpha}}}{|\boldsymbol{\alpha} - \boldsymbol{\beta}|} = -\frac{k\sigma_{\boldsymbol{t}_{\boldsymbol{\alpha}}}\mathcal{P}_{\boldsymbol{\alpha}}}{|\boldsymbol{\alpha} - \boldsymbol{\beta}|} \overset{\boldsymbol{\alpha}\to\boldsymbol{\beta}}{\longrightarrow} \infty\,. \tag{3.56}$$

Thus the short-range singularities remain and we show in the following that they give rise to an effective renormalization of the reflection. Due to the diagonal valley structure of $\mathcal{P}_{\boldsymbol{\alpha}}$ for zigzag edges, we can do the calculation again within the individual valley blocks and consider

$$\Gamma_\tau^{-1}(k) = 1 - \frac{\mathrm{i}}{2a(k)}(1 \pm \tau\sigma_z)(k_E + k\sigma_{\boldsymbol{t}})\sigma_{\boldsymbol{n}} = 1 \pm \frac{\tau k}{2a(k)} - \frac{1}{2a(k)}(\pm\tau k_E\sigma_{\boldsymbol{t}} + \mathrm{i}k_E\sigma_{\boldsymbol{n}} - k\sigma_z)\,. \tag{3.57}$$

Again we make use of the formula (3.54) to perform the inversion

$$\begin{aligned} \Gamma_\tau(k) &= \frac{1}{1 \pm \tau k/a(k)}\left[1 \pm \frac{\tau k}{2a(k)} + \frac{1}{2a(k)}(\pm\tau k_E\sigma_{\boldsymbol{t}} + \mathrm{i}k_E\sigma_{\boldsymbol{n}} - k\sigma_z)\right] \\ &= \frac{1}{1 \pm \tau k/a(k)}\left[1 + \frac{\mathrm{i}}{2a(k)}(k_E\sigma_{\boldsymbol{n}} + \mathrm{i}k\sigma_z)(1 \mp \tau\sigma_z)\right] \\ &= -\frac{a(k)}{k_E^2}[a(k) \mp \tau k]\left[1 + \frac{\mathrm{i}}{2a(k)}(k_E\sigma_{\boldsymbol{n}} + \mathrm{i}k\sigma_z)(1 - \mathcal{P}_{\boldsymbol{\alpha}})_\tau\right]. \end{aligned} \tag{3.58}$$

Here we see that, although the right term again does not contribute to $\mathcal{Z}_{\boldsymbol{\alpha}}$ because of the appearance of $(1-\mathcal{P}_{\boldsymbol{\alpha}})$, the remaining left term is not just unity as for the cases of armchair and infinite mass boundaries. Rather we obtain

$$\mathcal{Z}_{\boldsymbol{\alpha}}(k,-y') = -2\frac{a(k)}{k_E}[a(k) \mp \tau_z k]\mathcal{P}_{\boldsymbol{\alpha}} G_0(k,-y')\,. \tag{3.59}$$

We now define the renormalized Green function as

$$\tilde{G}_0(k,-y') = -2\frac{a(k)}{k_E}[a(k) \mp \tau_z k] G_0(k,-y')\,, \tag{3.60}$$

$$\tilde{G}_0(\boldsymbol{\alpha},\boldsymbol{x}') = \int_{-\infty}^{\infty} \frac{dk}{2\pi}\, \mathrm{e}^{\mathrm{i}k(\alpha-x')} \tilde{G}_0(k,-y')\,. \tag{3.61}$$

With that Eq. (3.33) reads

$$\int_{-\infty}^{\infty} d\beta\, \mathcal{Z}_{\boldsymbol{\alpha}}(\boldsymbol{\beta},\boldsymbol{x}') = 2\mathcal{P}_{\boldsymbol{\alpha}} \tilde{G}_0(\boldsymbol{\alpha},\boldsymbol{x}')\,, \tag{3.62}$$

so that we finally get for the charge layer (3.31)

$$\mu(\boldsymbol{\alpha},\boldsymbol{x}') \approx 2\mathcal{P}_{\boldsymbol{\alpha}}\tilde{G}_0(\boldsymbol{\alpha},\boldsymbol{x}') - 2\int_{\partial\mathcal{V}} d\sigma_{\boldsymbol{\beta}}\, \mathcal{P}_{\boldsymbol{\alpha}}\tilde{G}_0(\boldsymbol{\alpha},\boldsymbol{\beta})\, \mathrm{i}\sigma_{\boldsymbol{n_\beta}}\, \mu(\boldsymbol{\beta},\boldsymbol{x}')\, w(\boldsymbol{\alpha}-\boldsymbol{\beta})\,. \tag{3.63}$$

Up to the exchange of G_0 with $\tilde{G}_0$, this is the same as Eq. (3.50). This means that we have formally removed the short-range singularities (due to w), and their contributions are implicitly contained in the renormalized Green function. However, until now we have an explicit expression for $\tilde{G}_0$ only in the mixed position-momentum representation. In order to obtain an expression for $\tilde{G}_0(\boldsymbol{\alpha},\boldsymbol{x}')$, we have to carry out the inverse Fourier transform in Eq. (3.61).

Since we are working in plane approximation, i. e. we consider the leading order contributions in $1/k_E L$, it is consistent to perform also the inverse Fourier transform within the stationary phase approximation in the limit $k_E L \gg 1$. We thus define the angle

$$\theta(k) = \arctan\left(k/\sqrt{k_E^2-k^2}\right)\,, \tag{3.64}$$

which allows to write the momentum k and $a(k)$ as

$$k = |k_E|\sin\theta(k)\,, \quad a(k) = -\mathrm{i}|k_E|\cos\theta(k)\,. \tag{3.65}$$

Now we solve the integral

$$\int_{-\infty}^{\infty} dk\, \mathrm{e}^{\mathrm{i}k(\alpha-x')}\tilde{G}_0(k,-y') = \int_{-\infty}^{\infty} dk\, \mathrm{e}^{\mathrm{i}k(\alpha-x')}\cos\theta(k)\, \mathrm{e}^{\mp\mathrm{i}\theta(k)\tau_z}\, G_0(k,-y')$$

in stationary phase approximation. The θ-dependent prefactors of G_0 are slowly varying functions of k, so we evaluate them at the stationary phase point k_0, which is defined by

$$\frac{d}{dk}\left[k(\alpha - x') + \sqrt{k_E^2 - k^2}\,|y'|\right]_{k_0} = 0\,, \tag{3.66}$$

$$\Rightarrow \quad \frac{k_0}{\sqrt{k_E^2 - k_0^2}} = \tan\theta(k_0) = \frac{\alpha - x'}{|y'|}\,. \tag{3.67}$$

This means that the stationary phase point k_0 is such that the angle $\theta(k_0)$ is equal to the angle between the vector $\boldsymbol{x}' - \boldsymbol{\alpha}$ and the normal at $\boldsymbol{\alpha}$, i. e. the classical angle of incidence, as depicted in Fig. 3.5. Expanding the phase to second order in k around k_0, we can compute the remaining Gaussian integral and finally get

$$\tilde{G}_0^{\mathrm{sc}}(\boldsymbol{\alpha}, \boldsymbol{x}') = -\frac{\mathrm{i}}{4}\sqrt{\frac{2k_E}{\pi|\boldsymbol{\alpha} - \boldsymbol{x}'|}}\cos(\theta_{\boldsymbol{\alpha}})\,\mathrm{e}^{\mp\mathrm{i}\theta_{\boldsymbol{\alpha}}\tau_z}\left(1 + \sigma_{\boldsymbol{\alpha},\boldsymbol{x}'}\right)\mathrm{e}^{\mathrm{i}k_E|\boldsymbol{\alpha}-\boldsymbol{x}'|-\mathrm{i}\pi/4}\,, \tag{3.68}$$

with $\theta_{\boldsymbol{\alpha}} = \theta(k_0)$ and the short notation

$$\sigma_{\boldsymbol{\alpha},\boldsymbol{x}'} = \boldsymbol{\sigma}\cdot\frac{\boldsymbol{\alpha} - \boldsymbol{x}'}{|\boldsymbol{\alpha} - \boldsymbol{x}'|}\,. \tag{3.69}$$

This result can be written in a compact form as

$$\tilde{G}_0^{\mathrm{sc}}(\boldsymbol{\alpha}, \boldsymbol{x}') = \mathcal{R}_{\boldsymbol{\alpha}} G_0^{\mathrm{sc}}(\boldsymbol{\alpha}, \boldsymbol{x}')\,, \tag{3.70}$$

with the renormalization matrix for zigzag edges

$$\mathcal{R}_{\boldsymbol{\alpha}} = \cos(\theta_{\boldsymbol{\alpha}})\,e^{\mp\mathrm{i}\theta_{\boldsymbol{\alpha}}\tau_z}\,. \tag{3.71}$$

In Eq. (3.70), G_0^{sc} is free Green function in the semiclassical limit

$$G_0^{\mathrm{sc}}(\boldsymbol{\alpha}, \boldsymbol{\beta}) = -\frac{\mathrm{i}}{4}\sqrt{\frac{2k_E}{\pi|\boldsymbol{\alpha} - \boldsymbol{\beta}|}}\mathrm{e}^{\mathrm{i}k_E|\boldsymbol{\alpha}-\boldsymbol{\beta}|-\mathrm{i}\pi/4}\left(1 + \sigma_{\boldsymbol{\alpha},\boldsymbol{\beta}}\right)\,. \tag{3.72}$$

To see this, we replace the Hankel function in Eq. (3.8) by its asymptotic form for large arguments

$$H_0^+(\xi) \overset{\xi\gg 1}{\longrightarrow} \sqrt{\frac{2}{\pi\xi}}\mathrm{e}^{\mathrm{i}\xi-\mathrm{i}\pi/4}\,, \tag{3.73}$$

to get

$$\begin{aligned} G_0(\boldsymbol{\alpha}, \boldsymbol{\beta}) &\approx -\frac{\mathrm{i}}{4}(k_E - \mathrm{i}\boldsymbol{\nabla}_{\boldsymbol{\alpha}}\cdot\boldsymbol{\sigma})\sqrt{\frac{2}{\pi k_E|\boldsymbol{\alpha} - \boldsymbol{\beta}|}}\mathrm{e}^{\mathrm{i}k_E|\boldsymbol{\alpha}-\boldsymbol{\beta}|-\mathrm{i}\pi/4} \\ &\approx -\frac{\mathrm{i}}{4}\sqrt{\frac{2k_E}{\pi|\boldsymbol{\alpha} - \boldsymbol{\beta}|}}(1 + \sigma_{\boldsymbol{\alpha},\boldsymbol{\beta}})\mathrm{e}^{\mathrm{i}k_E|\boldsymbol{\alpha}-\boldsymbol{\beta}|-\mathrm{i}\pi/4}\,. \end{aligned} \tag{3.74}$$

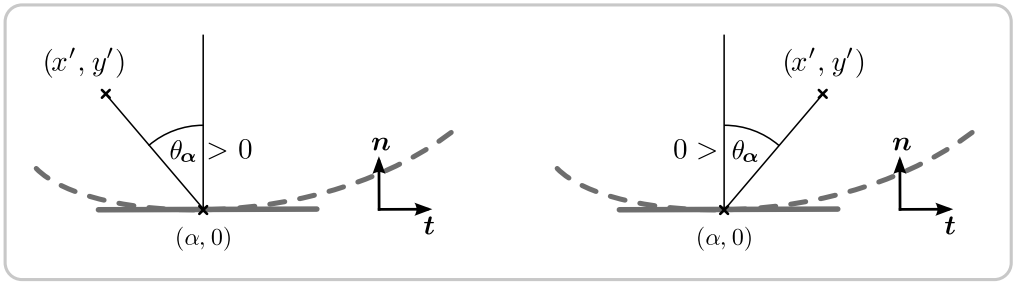

Figure 3.5: The stationary phase condition, Eq. (3.66), selects the critical momentum k_0 such that the angle $\theta(k_0)$ is equivalent to the angle $\theta_{\boldsymbol{\alpha}}$ as shown here. The sign of the reflection angle will be defined according to Eq. (3.66) from now on, namely $\mathrm{sgn}(\theta_{\boldsymbol{\alpha}}) = \mathrm{sgn}\left[(\boldsymbol{x}' - \boldsymbol{\alpha}) \cdot \boldsymbol{t}_{\boldsymbol{\alpha}}\right]$.

In the last step we neglected the term containing the gradient of the square root, since it is of subleading order in $(k_E L)^{-1}$. In this semiclassical approximation to G_0, the encoding of the chirality of charge carriers in graphene becomes particularly transparent. The matrix prefactor in Eq. (3.72) is a projection because $\sigma^2_{\boldsymbol{\alpha},\boldsymbol{\beta}} = 1$. It projects the sublattice pseudospin in the direction of the vector $\boldsymbol{\alpha} - \boldsymbol{\beta}$, which is - in the semiclassical limit - equivalent to the direction of propagation. This fixed relation of the pseudospin and the propagation direction is the chirality we have discussed in Sec. 2.1.

In order to understand the physical origin of the short-range singularities in the zigzag case, we go one step back to the renormalized Green function in mixed representation, Eq. (3.60). In the limit of small energies, $k_E \to 0$, the renormalization factor becomes

$$\frac{a(k)}{k_E}[a(k) \mp \tau_z k] \approx \frac{k^2}{k_E}[1 \mp \mathrm{sgn}(k)\tau_z]\,. \tag{3.75}$$

Considering the upper sign, this expression diverges in the valley $\tau = +1$ for negative k and in the valley $\tau = -1$ for positive k, as k_E goes to zero. For the lower sign it is the other way around. This divergence is due to the low energy states that are localized at graphene zigzag edges [25, 79, 81, 82, 83]. At a single zigzag edge, this state exists at $k_E = 0$, for exactly those combinations of τ and $\mathrm{sgn}(k)$, where (3.75) diverges. In each valley this obviously causes a strong asymmetry in the energy spectrum and breaks the effective TRS $\mathcal{T}_0$. However, one can see that $\mathcal{T}_0$ is broken also at finite energies, because the renormalization factor $\mathcal{R}_{\boldsymbol{\alpha}}$ causes different phases for different propagation directions, similar to the phases accumulated by a particle moving in a vector potential. We will discuss the effect of this phase on the energy spectrum and the conductance of graphene systems in detail in Chaps. 4 and 5, respectively.

Note that we have neglected nnn hopping so far. As discussed in Subsec. 2.2.2, nnn hopping has important effects on the properties of the zigzag edge states, e. g. they are not located at exactly zero energy anymore and obtain a finite velocity. In App. A.2 we derive an effective boundary condition to account for finite nnn hopping, and also discuss the renormalization procedure.

Defining $\mathcal{R}_{\boldsymbol{\alpha}} = 1$ for infinite mass and armchair edges, we can now rewrite the MRE for the Green function, Eqs. (3.13) and (3.14), in such a way that the short-range singularities

are formally removed, namely we obtain

$$G(\boldsymbol{x},\boldsymbol{x}') \approx G_0(\boldsymbol{x},\boldsymbol{x}') - 2\int\limits_{\partial\mathcal{V}} d\sigma_{\boldsymbol{\alpha}_1} G_0(\boldsymbol{x},\boldsymbol{\alpha}_1)\mathrm{i}\sigma_{\boldsymbol{n}_{\boldsymbol{\alpha}_1}}\mathcal{R}_{\boldsymbol{\alpha}_1}\mathcal{P}_{\boldsymbol{\alpha}_1} G_0(\boldsymbol{\alpha}_1,\boldsymbol{x}') \tag{3.76}$$

$$+\ 4\int\limits_{\partial\mathcal{V}}\int\limits_{\partial\mathcal{V}} d\sigma_{\boldsymbol{\alpha}_2} d\sigma_{\boldsymbol{\alpha}_1} w(\boldsymbol{\alpha}_1-\boldsymbol{\alpha}_2) G_0(\boldsymbol{x},\boldsymbol{\alpha}_2)\mathrm{i}\sigma_{\boldsymbol{n}_{\boldsymbol{\alpha}_2}}\mathcal{R}_{\boldsymbol{\alpha}_2}\mathcal{P}_{\boldsymbol{\alpha}_2} G_0(\boldsymbol{\alpha}_2,\boldsymbol{\alpha}_1)\mathrm{i}\sigma_{\boldsymbol{n}_{\boldsymbol{\alpha}_1}}\mathcal{R}_{\boldsymbol{\alpha}_1}\mathcal{P}_{\boldsymbol{\alpha}_1} G_0(\boldsymbol{\alpha}_1,\boldsymbol{x}')$$

$$-\ \ldots\,.$$

This result allows to evaluate the boundary integrals in stationary phase approximation, to get an asymptotic expression for the Green function in the limit of large $k_E L$. We emphasize again, that the resummation of the short-range singularities is an essential step in order to describe a generic system. Since they are of the same order as the contributions from classical trajectories, neglecting them would lead to inconsistent results for observables calculated in the semiclassical limit.

3.2.2 From quantum paths to classical trajectories

Now that we have resummed the short-range singularities and collected their contribution in the renormalization factors $\mathcal{R}_{\boldsymbol{\alpha}}$, we proceed with the second leading order contribution to the boundary integrals, namely their stationary phase points (3.18).

The free graphene Green function in the semiclassical limit (3.72) is again closely related to the semiclassical free Green function g_0^{sc} for the Schrödinger equation, namely

$$G_0^{\mathrm{sc}}(\boldsymbol{\alpha},\boldsymbol{\beta}) = k_E\,(1+\sigma_{\boldsymbol{\alpha},\boldsymbol{\beta}})\,g_0^{\mathrm{sc}}(\boldsymbol{\alpha},\boldsymbol{\beta})\,. \tag{3.77}$$

With that we can write a general term in the renormalized MRE (3.76) involving N (renormalized) reflections in the semiclassical limit as

$$G_N^{\mathrm{sc}}(\boldsymbol{x},\boldsymbol{x}') = (-2)^N \prod_{i=1}^{N}\int\limits_{\partial\mathcal{V}} d\sigma_{\boldsymbol{\alpha}_i}\tilde{K}_N(\underline{\boldsymbol{\alpha}})\,k_E g_0^{\mathrm{sc}}(\boldsymbol{x},\boldsymbol{\alpha}_N)\ldots\mathrm{i}k_E g_0^{\mathrm{sc}}(\boldsymbol{\alpha}_2,\boldsymbol{\alpha}_1)\,\mathrm{i}k_E g_0^{\mathrm{sc}}(\boldsymbol{\alpha}_1,\boldsymbol{x}')W(\underline{\boldsymbol{\alpha}})\,, \tag{3.78}$$

with the *pseudospin propagator* $\tilde{K}_N(\underline{\boldsymbol{\alpha}})$. The latter contains the graphene specific physics, in particular edge-related effects. The pseudospin propagator is given by

$$\tilde{K}_N(\underline{\boldsymbol{\alpha}}) = (1+\sigma_{\boldsymbol{x},\boldsymbol{\alpha}_N})\left[\prod_{i=N}^{2}\sigma_{\boldsymbol{n}_{\boldsymbol{\alpha}_i}}\mathcal{R}_{\boldsymbol{\alpha}_i}\mathcal{P}_{\boldsymbol{\alpha}_i}\left(1+\sigma_{\boldsymbol{\alpha}_i,\boldsymbol{\alpha}_{i-1}}\right)\right]\sigma_{\boldsymbol{n}_{\boldsymbol{\alpha}_1}}\mathcal{R}_{\boldsymbol{\alpha}_1}\mathcal{P}_{\boldsymbol{\alpha}_1}\left(1+\sigma_{\boldsymbol{\alpha}_1,\boldsymbol{x}'}\right)\,. \tag{3.79}$$

Note that the index i in the product *decreases* from N to 2. In Eq. (3.79) the renormalization matrices $\mathcal{R}_{\boldsymbol{\alpha}_i}$ take care of possible short-range singularities. Due to the separation function

$$W(\underline{\boldsymbol{\alpha}}) = \prod_{i=1}^{N-1} w(\boldsymbol{\alpha}_{i+1}-\boldsymbol{\alpha}_i) \tag{3.80}$$

in Eq. (3.78), we do not have to take them explicitly into account for the evaluation of the boundary integrals. The MRE for the Helmholtz equation that has been derived by Balian and Bloch [91] for different boundary conditions is similar to the scalar part of the MRE (3.78). In fact, the scalar part of (3.78) differs from the MRE of Balian and Bloch for Dirichlet boundary conditions in the semiclassical limit only in one point. Namely (3.78) contains factors $\mathrm{i}k_E$ in front of the $g_0^{\mathrm{sc}}(\boldsymbol{\alpha}_{i+1}, \boldsymbol{\alpha}_i)$, while in the MRE with Dirichlet boundary conditions in Ref. [91], these factors are replaced by normal derivatives acting on the first argument of the $g_0^{\mathrm{sc}}(\boldsymbol{\alpha}_{i+1}, \boldsymbol{\alpha}_i)$. However, the latter produce factors $\mathrm{i}k_E \cos(\theta_{i+1})$, with θ_{i+1} the incident angle at $\boldsymbol{\alpha}_{i+1}$. This means that instead of evaluating the boundary integrations in Eq. (3.78) explicitly within stationary phase approximation, we can immediately deduce

$$G_N^{\mathrm{sc}}(\boldsymbol{x}, \boldsymbol{x}') = k_E K_N(\underline{\boldsymbol{\alpha}})\, g_N^{\mathrm{sc}}(\boldsymbol{x}, \boldsymbol{x}')\,, \tag{3.81}$$

with

$$K_N(\underline{\boldsymbol{\alpha}}) = \tilde{K}_N(\underline{\boldsymbol{\alpha}}) \left(\prod_{i=1}^{N} \cos\theta_i \right)^{-1} . \tag{3.82}$$

We make use of the well-known expression for $g_N^{\mathrm{sc}}(\boldsymbol{x}, \boldsymbol{x}')$ [49, 103], and with $K_\gamma = K_{N_\gamma}(\underline{\boldsymbol{\alpha}})$ we finally obtain $G^{\mathrm{sc}}(\boldsymbol{x}, \boldsymbol{x}')$ expressed in terms of a sum over classical trajectories γ that connect the initial point $\boldsymbol{x}'$ to the final point $\boldsymbol{x}$

$$G^{\mathrm{sc}}(\boldsymbol{x}, \boldsymbol{x}') = \frac{\hbar v_F}{2} \sum_{\gamma(\boldsymbol{x}, \boldsymbol{x}')} \frac{|D_\gamma|}{\sqrt{2\pi\hbar^3}} \mathrm{e}^{\mathrm{i}k_E L_\gamma + \mathrm{i}\mu_\gamma \pi/2}\, K_\gamma\,. \tag{3.83}$$

Mathematically this results from the evaluation of the boundary integrals in stationary phase approximation. For G_N, the stationary phase condition selects a set of N points that minimizes the total phase occurring in Eq. (3.78). We introduced this phase as $\mathcal{L}$ in Eq. (3.16). The condition for stationary $\mathcal{L}$ is met if every reflection angle is equal to the angle of incidence θ_i, which is exactly the definition of a classical path, according to the Hamilton principle of stationary action [104]. The slowly varying prefactors are then evaluated at these stationary boundary points and the remaining integrals are performed approximately by expanding $\mathcal{L}$ to second order in the reflection points around the set of stationary points.

In Eq. (3.83), L_γ is the length of the classical orbit γ and μ_γ is the number of conjugate points along γ. For an interpretation and discussion of the latter we refer to Refs. [51, 105, 106]. D_γ is the determinant of a particular element of the stability matrix of the orbit γ. It is basically given by the variation in the final position $\boldsymbol{x}$, when the initial momentum $\boldsymbol{p}'$ is slightly changed:

$$D = \frac{1}{v_F} \det \left[\left(\frac{\partial \boldsymbol{x}}{\partial \boldsymbol{p}'} \right)_{\perp\gamma}^{-1} \right]^{1/2} = \frac{1}{v_F} \left(\frac{\partial x_\perp}{\partial p'_\perp} \right)_\gamma^{-1/2} . \tag{3.84}$$

The $\perp$ indicates that the derivative involves only the projections perpendicular to the trajectory, which are scalars in two dimensions, and therefore the determinant becomes redundant. The pseudospin propagator K_γ in Eq. (3.83) is evaluated at the *classical* reflection points.

	zigzag	armchair	infinite mass
$\boldsymbol{\nu}$	$\hat{\boldsymbol{z}}$	$-\sin(2Kx_{\boldsymbol{\alpha}})\hat{\boldsymbol{x}}+\cos(2Kx_{\boldsymbol{\alpha}})\hat{\boldsymbol{y}}$	$\hat{\boldsymbol{z}}$
$\boldsymbol{\eta}$	$\pm\hat{\boldsymbol{z}}$	$\pm\hat{\boldsymbol{t}}_{\boldsymbol{\alpha}}$	$\pm\hat{\boldsymbol{t}}_{\boldsymbol{\alpha}}$

Table 3.1: The vectors $\boldsymbol{\nu}$ and $\boldsymbol{\eta}$ for zigzag, armchair, and infinite mass type boundaries, as they occur in Eq. (3.86).

Expression (3.83) represents the main result of the present chapter: The semiclassical charge dynamics for electrons and holes in a ballistic graphene system is very similar to the case of electrons in Schrödinger billiards with Dirichlet boundary conditions. The graphene specific, in particular edge-related, physics is incorporated in the pseudospin dynamics described by K_γ. We note that semiclassical Green functions for the Dirac equation [99] and for bulk graphene [107] have been derived earlier, without taking into account the edges, which are in fact crucial for the description of ballistic nanostructures.

Using geometrical relations for the classical reflection points, Eq. (3.79) can be simplified considerably. We begin with an orbit that contains only a single reflection at a boundary point $\boldsymbol{\alpha}$. Then the pseudospin propagator becomes

$$\tilde{K}_1 \;=\; (1+\sigma_{\boldsymbol{x\alpha}})\sigma_{\boldsymbol{n_\alpha}}\mathcal{R}_{\boldsymbol{\alpha}}\mathcal{P}_{\boldsymbol{\alpha}}(1+\sigma_{\boldsymbol{\alpha x'}})\,. \tag{3.85}$$

According to our discussion in Subsec. 2.2.2, the boundary matrices for zigzag, armchair, and infinite mass type can be written as

$$\mathcal{P}_{\boldsymbol{\alpha}} = \frac{1}{2}\left(1+\boldsymbol{\nu}\cdot\boldsymbol{\tau}\otimes\boldsymbol{\eta}\cdot\boldsymbol{\sigma}\right)\,, \tag{3.86}$$

where the vectors $\boldsymbol{\nu}$ and $\boldsymbol{\eta}$ are given in Table 3.1. We adapt here the notation of Ref. [87]. For zigzag edges, the lower sign in Table 3.1 is valid for A-terminated edges, while the upper sign holds for B-termination. For the armchair case, the lower sign corresponds to the case of A-B ordered dimers along the tangential direction $\hat{\boldsymbol{t}}_{\boldsymbol{\alpha}}$, and the upper sign holds for B-A ordering. For infinite mass edges, the lower sign is valid for (infinitely large) positive mass potential outside the system and the upper for (infinitely large) negative mass. If not stated otherwise, we will use these sign conventions throughout the thesis. For the further evaluation of $\tilde{K}_1$, we make use of the following geometrical relations:

$$\sigma_{\boldsymbol{x\alpha}}\sigma_{\boldsymbol{n_\alpha}} \;=\; -\sigma_{\boldsymbol{n_\alpha}}\sigma_{\boldsymbol{\alpha x'}}\,, \tag{3.87}$$

$$\sigma_{\boldsymbol{\alpha x'}}\sigma_{\boldsymbol{t_\alpha}} \;=\; \sigma_{\boldsymbol{t_\alpha}}\sigma_{\boldsymbol{x\alpha}}\,, \tag{3.88}$$

$$\mathrm{e}^{\mathrm{i}\theta\sigma_z}\sigma_{\boldsymbol{\alpha x'}}\,\mathrm{e}^{-\mathrm{i}\theta\sigma_z} \;=\; -\sigma_{\boldsymbol{x\alpha}}\,. \tag{3.89}$$

Incorporating Eq. (3.87), $\sigma^2_{\boldsymbol{\alpha x'}}=1$, and the valley isotropic structure of $\mathcal{R}_{\boldsymbol{\alpha}}$, we obtain

$$\tilde{K}_1 = \frac{1}{2}\boldsymbol{\nu}\cdot\boldsymbol{\tau}\,\mathcal{R}_{\boldsymbol{\alpha}}\otimes\sigma_{\boldsymbol{n_\alpha}}(1-\sigma_{\boldsymbol{\alpha x'}})\boldsymbol{\eta}\cdot\boldsymbol{\sigma}(1+\sigma_{\boldsymbol{\alpha x'}})\,. \tag{3.90}$$

Now we restrict the vector $\boldsymbol{\eta}$ to the cases in Table 3.1, i. e. $\boldsymbol{\eta} = \eta_t\,\hat{\boldsymbol{t}} + \eta_z\,\hat{\boldsymbol{z}}$. For the term with η_t, we use Eq. (3.88) and rotate the pseudospin according to Eq. (3.89), namely

$$\begin{aligned}(1-\sigma_{\boldsymbol{x}\boldsymbol{\alpha}})(1+\sigma_{\boldsymbol{\alpha}\boldsymbol{x}'}) &= (1+\mathrm{e}^{\mathrm{i}\theta\sigma_z}\sigma_{\boldsymbol{\alpha}\boldsymbol{x}'}\,\mathrm{e}^{-\mathrm{i}\theta\sigma_z})(1+\sigma_{\boldsymbol{\alpha}\boldsymbol{x}'}) \\ &= (1+\mathrm{e}^{2\mathrm{i}\theta\sigma_z}\sigma_{\boldsymbol{\alpha}\boldsymbol{x}'})(1+\sigma_{\boldsymbol{\alpha}\boldsymbol{x}'}) = 2\cos(\theta)\mathrm{e}^{\mathrm{i}\theta\sigma_z}(1+\sigma_{\boldsymbol{\alpha}\boldsymbol{x}'})\,. \end{aligned} \tag{3.91}$$

With that we get for the pseudospin propagator of a classical orbit with only one reflection at a zigzag (zz), armchair (ac), or infinite mass (im) edge

$$\tilde{K}_1 = \mathrm{i}\boldsymbol{\nu}\cdot\boldsymbol{\tau}\,\mathcal{R}_{\boldsymbol{\alpha}} \otimes \left(\eta_z\,\sigma_{\boldsymbol{t}_{\boldsymbol{\alpha}}} - \eta_t\,\cos(\theta)\sigma_z\mathrm{e}^{\mathrm{i}\theta\sigma_z}\right)(1+\sigma_{\boldsymbol{\alpha}\boldsymbol{x}'})\,. \tag{3.92}$$

In Eq. (3.92), the combination of the original pseudospin direction and the boundary-dependent rotations and projections of the pseudospin, implicitly contains information about the final pseudospin direction. This allows for an iterative construction of the pseudospin propagator for an orbit with arbitrary number of reflections from edges as listed in Table 3.1, namely we find

$$K_\gamma = \prod_{i=N}^{1} \check{K}_i\left(1+\sigma_{\boldsymbol{\alpha}_1,\boldsymbol{x}'}\right)\,, \tag{3.93}$$

with

$$\check{K}_i = \mathrm{i}\begin{cases} \pm\tau_z\mathrm{e}^{\mp\mathrm{i}\theta_i\tau_z}\otimes\sigma_{\boldsymbol{t}_i} & \text{for zz}\,, \\ \mp\tau_y\mathrm{e}^{\mathrm{i}2Kx_i\tau_z}\otimes\sigma_z\mathrm{e}^{\mathrm{i}\theta_i\sigma_z} & \text{for ac}\,, \\ \mp\tau_z\otimes\sigma_z\mathrm{e}^{\mathrm{i}\theta_i\sigma_z} & \text{for im}\,. \end{cases} \tag{3.94}$$

We will use these expressions frequently in the following chapters, when we evaluate the traces of (products of) Green functions and thus the traces of (products of) pseudospin propagators that are related to the spectral and transport properties of graphene flakes. Note that all factors $\cos(\theta_i)$ in the product of the definition (3.82) are actually canceled by those occurring e. g. in Eq. (3.92). This is an important point, since otherwise the scalar weight of the classical orbits in the sum (3.83) would be altered significantly. For armchair and infinite mass edges, these factors come from the reorganization of the sublattice Pauli matrices, cf. Eq. (3.91). For zigzag edges however, we point out that the cosine factors originate from the renormalization factors $\mathcal{R}_{\boldsymbol{\alpha}}$, emphasizing again the importance of the short-range contributions.

3.3 Summary

In this chapter we have derived the Green function of a ballistic graphene flake with generic shape and boundaries in the effective Dirac theory. We did this in two steps. First we adapted the multiple reflection expansion of Balian and Bloch [91] for the exact Green function G in Sec. 3.1, by combining the specific form of the boundary conditions for the Dirac Hamiltonian, Eq. (2.38), with a parametrization of the Green function in terms of a Dirac charge density at the boundary, Eq. (3.4). This led to an exact formal expansion for G, Eq. (3.13), where each

term can be interpreted as the contribution from all quantum paths that include a specific number of reflections from the system boundary.

Second, in Sec. 3.2 we focused on the contributions that dominate the Green function in the semiclassical limit, i. e. that are of leading order in $(k_E L)^{-1}$. Evaluating the boundary integrals in the MRE in the limit of large $k_E L$, we have obtained the semiclassical graphene Green function in terms of a sum over all classical orbits in the system, representing one class of leading order contributions to G. The resulting expression, Eq. (3.83), is closely related to the semiclassical Green function of a Schrödinger system, but also contains the graphene specific physics, such as the charge carrier chirality and the effects of the edges. While the scalar part that each classical orbit contributes to (3.83) is basically identical to the Schrödinger case, the pseudospin propagator K_γ is the most important object in view of the graphene physics. Apart from the classical orbits, there is a second leading order contribution to G, namely multiple reflections close to the same boundary point at zigzag edges. It is essential to include these contributions into the semiclassical Green function. We have shown in Subsec. 3.2.1 that resumming the corresponding short-range singularities effectively renormalizes the zigzag boundary matrix, so that Eq. (3.83) is valid also in the presence of zigzag edges. The semiclassical Green function, Eq. (3.83), with the (renormalized) pseudospin propagator, Eqs. (3.93) and (3.94), represent the main results of this chapter.

The Green function derived here serves as a starting point for our investigations into the spectral density of states and the transport properties of graphene nanostructures in Chaps. 4-6. The results of this chapter have been published in Ref. [108].

CHAPTER 4

Density of states of closed graphene flakes

The energy spectrum of a closed quantum system, for example a finite graphene flake, is given by a set of discrete energy levels. Thus the density of states (DOS) of a closed graphene flake is given by a series of δ-functions[1]

$$\rho(k_E) = \sum_n \delta\left(k_E - k_n\right) , \tag{4.1}$$

where n labels the eigenenergies $E_n = \hbar v_F k_n$. Although the DOS depends in general on the very details of the system under consideration, some of its aspects are rather general. In particular, the statistical distribution of the energy levels provides insight into various interesting properties. For a mesoscopic graphene flake with an area of about $(200\,\mathrm{nm})^2$ there are several thousands of levels in the interval $0 < k_E a < 0.2$, as one can estimate from the DOS of bulk graphene. This means that ρ can in principle be considered as a very rapidly oscillating function of k_E. However, the DOS can always be decomposed into a smooth part $\bar{\rho}$ and an oscillating part ρ_{osc} in a well defined way [49, 51]. The smooth part, i. e. the average number of levels per unit k_E-interval, contains mainly information about the geometrical properties of the system, e. g. the area and the length of (certain parts of) the boundary in the two-dimensional case. The oscillating part on the other hand reflects the underlying classical dynamics, i. e. whether the corresponding classical system shows regular or chaotic dynamics, and can also provide information about symmetries like (effective) TRS and subtle inter-relations between them.

Consider a small energy interval that is still large enough to contain several DOS quantum oscillations. If one performs a local averaging over this window in the whole relevant energy range, one obtains a smoothed density of states, namely $\bar{\rho}$. Another way to think about the smoothing is to start from the sequence of delta functions (4.1) and broaden the levels, e. g. by convolution with a Lorentzian. For strong broadening the levels overlap completely, eventually resulting in $\bar{\rho}$ [91]. By definition, the difference between $\bar{\rho}$ and the full DOS is then the oscillating density ρ_{osc}.

During the course of this chapter we will address both parts of ρ and focus thereby on the particularities that arise due to the pseudospin degrees of freedom of the Dirac quasiparticles and the effect of the edges on them. First we focus on the smoothed DOS $\bar{\rho}$, approximated in

[1] This definition is related to the common definition of the spectral density $D(E) = \sum_n \delta\left(E - E_n\right)$ via $\rho(k_E) = \hbar v_F D(E)$.

the semiclassical limit by the so-called Weyl expansion [49, 91, 109]. We derive the two leading contributions to this expansion and find that the edge structure of a graphene flake strongly affects the smooth DOS. In fact, our results suggest that the relative amount of zigzag edges can be estimated from low energy features in $\bar{\rho}$. Then we turn to the oscillating part of ρ. We derive semiclassical trace formulae for chaotic and regular graphene billiards, which relate ρ_{osc} to sums over periodic classical orbits, analog to the known expressions, namely the Gutzwiller [49] and the Berry-Tabor [110] trace formulae. For graphene, the occurrence of the pseudospin propagator (3.93) leads to additional effects of pseudospin interference and thus to edge specific modifications of ρ_{osc}. We discuss these effects for two representative regular shapes, namely the graphene rectangle and the graphene disk billiard. With 'billiards' we denote here and in the remainder of this thesis two-dimensional systems where particles are confined to a closed domain, but can move freely within the domain. Finally we study the oscillating part of the DOS of chaotic graphene flakes in more detail by investigating correlations in the spectrum. To this end we consider the spectral form factor, i. e. the Fourier transform of the spectral two-point correlator. We find that the leading order and the next-to-leading order contributions are strongly influenced by the edges. The total amount of armchair edges is the relevant quantity that determines the size of the correlations. Our results suggest that evidence for partial (effective) breaking of the TRS is visible in the spectral correlations at scales of many mean level spacings.

For all our studies within this chapter we start from the relation between the DOS and the Green function

$$\rho(k_E) = -\frac{1}{\pi}\mathfrak{Im}\int_{\mathcal{V}} d\boldsymbol{x}\,\mathrm{Tr}\left[G(\boldsymbol{x},\boldsymbol{x})\right]\,, \tag{4.2}$$

which follows directly from the expansion of G in eigenstates, Eq. (3.2), since for real ξ, $\lim_{\eta\to 0}\mathfrak{Im}(\xi+\mathrm{i}\eta)^{-1} = -\pi\delta(\xi)$.

4.1 Smooth density of states - Weyl expansion

In this section we derive the leading order contributions to the smooth density of states, $\bar{\rho}$. In Schrödinger billiards with quadratic energy dispersion, $E = \hbar^2 k_E^2/2m$, as they are realized e. g. in 2DEGs in semiconductor heterostructures, $\bar{\rho}$ can be expanded in (inverse) powers of $k_E L$

$$\frac{\hbar^2 k_E}{2m}\bar{D}(E) = \bar{\rho}(k_E) = \sum_{i=0}^{\infty}\bar{\rho}_i(k_E)\,, \qquad \text{with } \bar{\rho}_i \sim (k_E L)^{1-i}\,. \tag{4.3}$$

The leading order term is linear, $\bar{\rho}_0 \sim k_E$, followed by a constant $\bar{\rho}_1$ and so forth. In the large $k_E L$ limit $\bar{\rho}$ is dominated by the first term, which does not depend on the shape of the system but only on its total area. This theorem goes back to Hermann Weyl [109], and thus the series (4.3) is known as the Weyl expansion for the smoothed density of states. Each of the terms in this expansion can be obtained from the MRE (3.13). The leading order term $\bar{\rho}_0$ originates from the zero-reflection term (simply G_0), while $\bar{\rho}_1$ is due to surface contributions evaluated

in plane approximation (cf. Fig. 3.4). The next term, $\bar{\rho}_2$, stems from curvature and corner corrections to the plane approximation and so on. Therefore the individual contributions usually scale with the geometric properties of the billiard: $\bar{\rho}_0$ scales with the area as mentioned above, $\bar{\rho}_1$ with the length of the boundary (the system's surface) and so forth. These contributions are of qualitatively different origin than the oscillating part of the DOS that we treat in Secs. 4.2 and 4.3. While the latter originates from orbits for which the total phase that occurs in Eq. (4.2) is stationary, the smooth DOS is due to trajectories of 'zero-length', for which the amplitudes diverge. This is very similar to the leading order contributions to the Green function itself, as we have discussed in the previous chapter. Indeed, we will see that the calculation of $\bar{\rho}_1$ is closely related to the issue of resumming the short-range singularities, which we have addressed in Subsec. 3.2.1. We find that for graphene the bulk term in the Weyl expansion is similar to the Schrödinger case, but the formerly constant surface term behaves strikingly different and depends on the edge structure. At this point we also refer to a discussion of the Weyl expansion for Schrödinger billiards with Rashba spin-orbit coupling in Ref. [111].

4.1.1 Bulk term

We begin with the zero-reflection term in the MRE, namely $G_0(\boldsymbol{x}, \boldsymbol{x})$. From Eq. (3.8) we can directly read off

$$\mathrm{Tr}\left[G_0(\boldsymbol{x}, \boldsymbol{x'})\right] = -\mathrm{i}k_E H_0^+(k_E|\boldsymbol{x} - \boldsymbol{x'}|)\,. \tag{4.4}$$

According to Eq. (4.2), we have to consider the limit $\boldsymbol{x'} \to \boldsymbol{x}$, where the Hankel function diverges logarithmically. In order to see that the imaginary part of G_0 is nevertheless finite, we write the trace in momentum representation [112]

$$-\mathrm{i}k_E H_0^+(k_E|\boldsymbol{x} - \boldsymbol{x}'|) = \frac{k_E}{\pi^2}\int d\boldsymbol{k}\,\frac{\mathrm{e}^{\mathrm{i}\boldsymbol{k}(\boldsymbol{x'}-\boldsymbol{x})}}{k_E^2 - \boldsymbol{k}^2}\,, \tag{4.5}$$

so that we can perform the limit straightforwardly and get

$$\mathfrak{Im}\mathrm{Tr}\left[G_0(\boldsymbol{x}, \boldsymbol{x})\right] = -|k_E|\,. \tag{4.6}$$

Here we made use of the fact that k_E has an infinitesimal positive imaginary part and used the well-known relation

$$\lim_{\eta\to 0}\mathfrak{Im}\frac{1}{\xi + \mathrm{i}\eta} = -\lim_{\eta\to 0}\frac{\eta}{\xi^2 - \eta^2} = -\pi\delta(\xi)\,, \tag{4.7}$$

for real ξ and η. Since there is no $\boldsymbol{x}$-dependence left in (4.6), the spatial integration in Eq. (4.2) gives just the area $|\mathcal{V}|$, and we get for the first term in the Weyl expansion for a graphene billiard

$$\bar{\rho}_0(k_E) = \frac{|\mathcal{V}|}{\pi}|k_E|\,. \tag{4.8}$$

Since the zero reflection term 'does not know' about any boundaries, $\bar{\rho}_0$ is equivalent to the DOS of a bulk system. It scales with the total area of the billiard, just as in the Schrödinger

case. Therefore $\bar{\rho}_0$ is usually referred to as *bulk-, volume-* or *area-term* of the DOS. Note that for Schrödinger billiards the expression for the bulk term $\bar{\rho}_0(k_E)$ is exactly one half times the result (4.8), and therefore $\bar{D}_0(E)$ has no energy dependence in this case. It is a particularity of graphene, more precisely its constant Fermi velocity, that $\bar{D}_0(E)$ and $\bar{\rho}_0(k_E)$ are equal up to a constant factor. In terms of $\bar{\rho}_0(k_E)$ the graphene result is larger by a factor of two due to the contributions from both valleys, which are independent degenerate subsystems in clean bulk graphene.

4.1.2 Surface term

Now we go one step further in the Weyl expansion and evaluate the surface term. As stated above, in Schrödinger billiards this term gives rise to a contribution to $\bar{\rho}(k_E)$ that has no dependence on the Fermi momentum [49] and scales with the total length of the system's boundary, i. e. its total surface. We will show below that for graphene $\bar{\rho}_1$ depends on k_E as well as on the boundary length of the system in a manner distinctly different from that of Schrödinger billiards. In fact in the graphene case $\bar{\rho}_1$ shows a strong dependence on k_E in the low energy regime, and the scaling is linear in the zigzag part of the boundary only. The reason is that *exclusively* zigzag edge states give rise to a surface term in graphene.

In order to evaluate $\bar{\rho}_1$ we assume that the Fermi momentum has a finite imaginary part ξ. This formally broadens the energy levels, where the linewidth is set by the magnitude of ξ. If ξ is comparable to the mean level spacing, the energy levels overlap and for even larger values of ξ, the DOS is completely smeared out and a smooth function, namely $\bar{\rho}$. Technically, the finite imaginary part ξ makes $G_0(\boldsymbol{x}, \boldsymbol{x'})$ an exponentially decaying function of the distance $|\boldsymbol{x} - \boldsymbol{x'}|$, with a decay length $1/\xi$. Then G_0 is a short-ranged function and we can use the same approximation as in Subsec. 3.2.1, i. e. we replace the boundary locally by its tangent (cf. Fig. 3.4), which is justified for sufficiently smooth surfaces, in that corrections to the plane approximation are of higher order in $(k_E L)^{-1}$ [91].

Our starting point is Eq. (3.4). We omit the free Green propagation term G_0 that led to $\bar{\rho}_0$, so that Eq. (4.2) gives

$$\delta\bar{\rho}(k_E) = \bar{\rho}(k_E) - \bar{\rho}_0(k_E) = \frac{1}{\pi}\mathfrak{Im}\int\limits_{\mathcal{V}} d\boldsymbol{x} \int\limits_{\partial\mathcal{V}} d\sigma_{\boldsymbol{\alpha}}\,\mathrm{Tr}\left[G_0(\boldsymbol{x},\boldsymbol{\alpha})\mathrm{i}\sigma_{\boldsymbol{n}_{\boldsymbol{\alpha}}}\mu(\boldsymbol{\alpha},\boldsymbol{x})\right] \tag{4.9}$$

$$= \frac{1}{\pi}\mathfrak{Im}\sum_i \int\limits_{\partial\mathcal{V}_i} d\sigma_{\boldsymbol{\alpha}} \int\limits_{\mathcal{V}} d\boldsymbol{x}\,\mathrm{Tr}\left[G_0(\boldsymbol{x},\boldsymbol{\alpha})\mathrm{i}\sigma_{\boldsymbol{n}_{\boldsymbol{\alpha}}}\mu_i(\boldsymbol{\alpha},\boldsymbol{x})\right]\,. \tag{4.10}$$

Here we replaced the boundary integration by a sum of integrations over boundary pieces $\mathcal{V}_i$, where the boundary condition is constant for each i. Furthermore, μ_i is the solution of Eq. (3.11) for $\boldsymbol{\alpha} \in \partial\mathcal{V}_i$. Since G_0 is short-ranged, the dominant contribution to the integrals in Eq. (4.10) comes from configurations where $\boldsymbol{x}$ is near the boundary point $\boldsymbol{\alpha}$. Thus we approximate the integral over $\boldsymbol{x}$ by an integral along the approximately straight boundary close to $\boldsymbol{\alpha}$ and an integral in perpendicular direction to the boundary. Further we note that the boundary integral in Eq. (3.11) is dominated by contributions where $\boldsymbol{\beta}$ is close to $\boldsymbol{\alpha}$.

Therefore we approximate the boundary by a straight line in the direction of the tangent to $\partial\mathcal{V}_i$ at $\boldsymbol{\alpha}$, also in Eq. (3.11). We now take advantage of the homogeneity of the approximate surface at $\boldsymbol{\alpha}$ and use Fourier transformation along the direction of the tangent to get for the surface term $\delta\bar{\rho} \approx \bar{\rho}_1$

$$\bar{\rho}_1(k_E) = \sum_i \bar{\rho}_{1,i}(k_E) = \sum_i \frac{|\partial\mathcal{V}_i|}{\pi}\, \mathfrak{Im} \int_0^\infty dy_i \int_{-\infty}^{\infty} \frac{dk}{2\pi}\, \mathrm{Tr}\left[\delta G_i(k, y_i)\right] , \tag{4.11}$$

with

$$\delta G_i(k, y_i) = G_0(k, y_i)\mathrm{i}\sigma_{\boldsymbol{n}_\alpha}\mu_i(k, y_i)\,. \tag{4.12}$$

As mentioned before, the corrections to this approximation are of higher order in the Weyl expansion for smooth boundaries. Since G_0 is short-ranged, i. e. $\xi L \gg 1$, we have extended the limits of the y_i-integrations to infinity. To obtain Eq. (4.11), we further assumed that $\boldsymbol{\alpha}$ is away from the corners, where the boundary condition changes. The corrections due to such points are of order $(k_E L)^{-1}$ smaller than the boundary term [91]. The charge layer $\mu_i(k, y_i)$ is given by the Fourier transform of Eq. (3.11)

$$\mu_i(k, y_i) = 2\mathcal{P}_{\boldsymbol{\alpha}} G_0(k, -y_i) - 2\mathcal{P}_{\boldsymbol{\alpha}} G_0(k, 0)\mathrm{i}\sigma_{\boldsymbol{n}_\alpha}\mu_i(k, y_i)\,. \tag{4.13}$$

The virtue of this equation is that it does not contain any integrals and we can solve it for μ_i

$$\mu_i(k, y_i) = \left[1 + 2\mathcal{P}_{\boldsymbol{\alpha}} G_0(k, 0)\mathrm{i}\sigma_{\boldsymbol{n}_\alpha}\right]^{-1} 2\mathcal{P}_{\boldsymbol{\alpha}} G_0(k, -y_i)\,, \tag{4.14}$$

so that the remaining problem is basically to perform the matrix inversion in Eq. (4.14). In fact, we have already performed this inversion when we resummed the short-range singularities in Subsec. 3.2.1, see Eq. (3.41). More precisely the results for armchair, infinite mass, and zigzag type edges without nnn hopping are given by Eqs. (3.47), (3.55) and (3.58), respectively. For finite nnn hopping we perform the inversion in App. A.2, see Eq. (A.21). Using these results, Eq. (4.12) reads

$$\delta G_i(k, y_i) = 2\,\mathcal{R}_{\boldsymbol{\alpha}}(k) G_0(k, y_i)\,\mathrm{i}\sigma_{\boldsymbol{n}_\alpha}\,\mathcal{P}_{\boldsymbol{\alpha}}\, G_0(k, -y_i)\,. \tag{4.15}$$

Here we define the momentum representation of the renormalization matrix $\mathcal{R}_{\boldsymbol{\alpha}}(k) = 1$ for armchair and infinite mass type edges, and for zigzag edges including the effect of possible nnn hopping, $\mathcal{R}_{\boldsymbol{\alpha}}(k)$ is given by Eq. (A.23).

From Eq. (4.15), we see that the boundary term in the Weyl expansion is closely related to the short-range singularities, which we have discussed in Subsec. 3.2.1. In fact δG_i is given by the one-reflection term of the *renormalized* MRE (3.76) in mixed position-momentum representation.

Next we study the contributions to the surface term from the different types of edges.

Armchair and infinite mass boundaries

We begin with armchair and infinite mass type edges, where $\mathcal{R}_{\boldsymbol{\alpha}}(k) = 1$, and calculate δG_i for this case. For the free Green function we have found earlier [cf. Eq. (3.38)]

$$G_0(k,y) = -\frac{\mathrm{e}^{-a(k)|y|}}{2a(k)}\left[k_E + k\sigma_{\boldsymbol{t}_{\boldsymbol{\alpha}}} + \mathrm{i}\,\mathrm{sgn}(y)a(k)\sigma_{\boldsymbol{n}_{\boldsymbol{\alpha}}}\right] . \tag{4.16}$$

In view of Eq. (4.15) we note further that for positive y

$$\begin{aligned} G_0(k,y)\,\mathrm{i}\sigma_{\boldsymbol{n}_{\boldsymbol{\alpha}}} G_0(k,-y) &\sim \sigma_{\boldsymbol{n}_{\boldsymbol{\alpha}}}\left[k_E - k\sigma_{\boldsymbol{t}_{\boldsymbol{\alpha}}} + \mathrm{i}\,a(k)\sigma_{\boldsymbol{n}_{\boldsymbol{\alpha}}}\right]\left[k_E + k\sigma_{\boldsymbol{t}_{\boldsymbol{\alpha}}} - \mathrm{i}\,a(k)\sigma_{\boldsymbol{n}_{\boldsymbol{\alpha}}}\right] \\ &= \sigma_{\boldsymbol{n}_{\boldsymbol{\alpha}}}\left[k_E^2 - k^2 + a^2(k)\right] = 0\,, \end{aligned} \tag{4.17}$$

so that we have to consider only the second term of $\mathcal{P}_{\boldsymbol{\alpha}} = (1 + \boldsymbol{\nu}\cdot\boldsymbol{\tau}\otimes\boldsymbol{\eta}\cdot\boldsymbol{\sigma})/2$ to evaluate δG_i. For armchair edges, according to Table 3.1, this results in

$$\delta G_i(k,y_i) = \pm\tau_y \exp(2\mathrm{i}Kx_{\boldsymbol{\alpha}}\tau_z)\, G_0(k,y)\sigma_z G_0(k,-y)\,. \tag{4.18}$$

Since $G_0 \sim \tau_0$ and $\mathrm{Tr}\left[\tau_y \exp(2\mathrm{i}Kx_{\boldsymbol{\alpha}}\tau_z)\right] = 0$, it follows that

$$\mathrm{Tr}\left[\delta G_i(k,y_i)\right] = 0 \quad \Rightarrow \quad \bar{\rho}_{1,i} = 0\,, \tag{4.19}$$

if $\partial\mathcal{V}_i$ is an armchair edge. This means that armchair edges do not contribute to the surface term of the smooth DOS (4.11).

For infinite mass type edges, we also find that the surface term vanishes. In this case we have (cf. Table 3.1)

$$\delta G_i(k,y_i) = \pm\tau_z \otimes G_0(k,y)\sigma_z G_0(k,-y_i)\,, \tag{4.20}$$

leading to Eq. (4.19) as well, because $\mathrm{Tr}(\tau_z) = 0$. However, this appears somehow curious, because it suggests that the surface contributions to the DOS from the two valleys $\tau = 1$ and $\tau = -1$ cancel each other. Apart from the fact that a negative DOS does not exist, the contributions from both valleys cannot be opposite, due to the valley degeneracy of a system with a boundary that consists exclusively of infinite mass type edges. Therefore, the contribution from each valley has to vanish individually. It has been shown by Berry and Mondragon that this is actually the case, when they introduced the infinite mass boundary condition for neutrino billiards [90]. Within our framework one can understand this, continuing the calculation within an individual valley, for instance for the $\tau = 1$ subblock of δG_i:

$$\mathrm{Tr}\left[(\delta G_i)_{\tau=1}(k,y_i)\right] = \pm\mathrm{Tr}\left[G_0(k,y_i)\sigma_z G_0(k,-y_i)\right] = \mp\frac{k}{2a(k)}\mathrm{e}^{-2a(k)y_i}\,. \tag{4.21}$$

This means that indeed the contribution of each individual valley is zero, because (4.21) is an odd function of k, and thus the momentum integration in Eq. (4.11) vanishes.

Zigzag boundaries

For zigzag edges the renormalization matrix $\mathcal{R}_{\boldsymbol{\alpha}}(k)$ is more complicated, namely including nnn hopping we find in App. A.2 [Eq. (A.23)]

$$\mathcal{R}_{\boldsymbol{\alpha}}(k) = a(k)\frac{a(k) - t'k_E \mp \tau_z k}{[a(k) - t'k_E]^2 - k^2}\,, \tag{4.22}$$

with the relative strength of the nnn hopping t'. For the case without nnn hopping ($t' = 0$), this is equivalent to the expression (3.59) we found in Subsec. 3.2.1, so that we can treat both cases at once. With Eq. (4.15) we find

$$\bar{\rho}_{1,i} = \frac{|\partial\mathcal{V}_i|}{2\pi^2}\,\mathfrak{Im}\int_{-\infty}^{\infty} dk\,\frac{k^2}{a(k)^2}\frac{t'^2 - 1}{k_E + 2a(k)t' - k_E t'^2}\,. \tag{4.23}$$

First we neglect the effect of nnn hopping and consider the case $t' = 0$, resulting in

$$\bar{\rho}_{1,i} = -\frac{|\partial\mathcal{V}_i|}{2\pi^2}\,\mathfrak{Im}\int_{-\infty}^{\infty} dk\frac{k^2}{a(k)^2 k_E}\,. \tag{4.24}$$

To perform the momentum integral, we split it into two terms and shift the integration variable by k_E in one term and by $-k_E$ in the other term to get

$$\int dk\frac{k^2}{a(k)^2} = \int dk\,\frac{k + k_E}{2k} + \int dk\,\frac{k - k_E}{2k} = \int dk = 2k_{\max}\,, \tag{4.25}$$

where we defined the cut-off momentum $k_{\max}$. Physically this cut-off corresponds to the finite size of the first Brillouin zone, due to the discreteness of the graphene lattice. In the effective continuum theory the momentum space is infinite, thus we had to introduce $k_{\max} \sim 1/a$. The contribution to the surface term is exclusively due to the nontrivial $\mathcal{R}_{\boldsymbol{\alpha}}$, and thus due to the zigzag edge states, see Eq. (3.75) and the discussion thereafter. Therefore we can estimate $k_{\max}$ from the total momentum space that is occupied by the edge states in an atomistic tight-binding model, which is $K/2 = 2\pi/3a$ [61]. This means, for the cut-off we expect $k_{\max} \approx K/4 = \pi/3a$. Recalling that the imaginary part of k_E is ξ, we end up with the surface contribution to the smooth density of states from a zigzag edge neglecting the effect of nnn hopping

$$\bar{\rho}_{1,i} = \frac{|\partial\mathcal{V}_i|}{\pi}k_{\max}\,\delta_\xi(k_E)\,, \tag{4.26}$$

with the Lorentzian

$$\delta_\xi(k_E) = \frac{1}{\pi}\frac{\xi}{\xi^2 + k_E^2}\,. \tag{4.27}$$

Before we discuss this result further, we consider the case of a small nnn hopping term, keeping terms up to linear order in t' in Eq. (4.23). To this end, we make use of the fact that for edge states we have according to Eq. (A.15)

$$\frac{k_E^2}{k^2} = 4t'^2 + \mathcal{O}(t'^3) \ll 1\,. \tag{4.28}$$

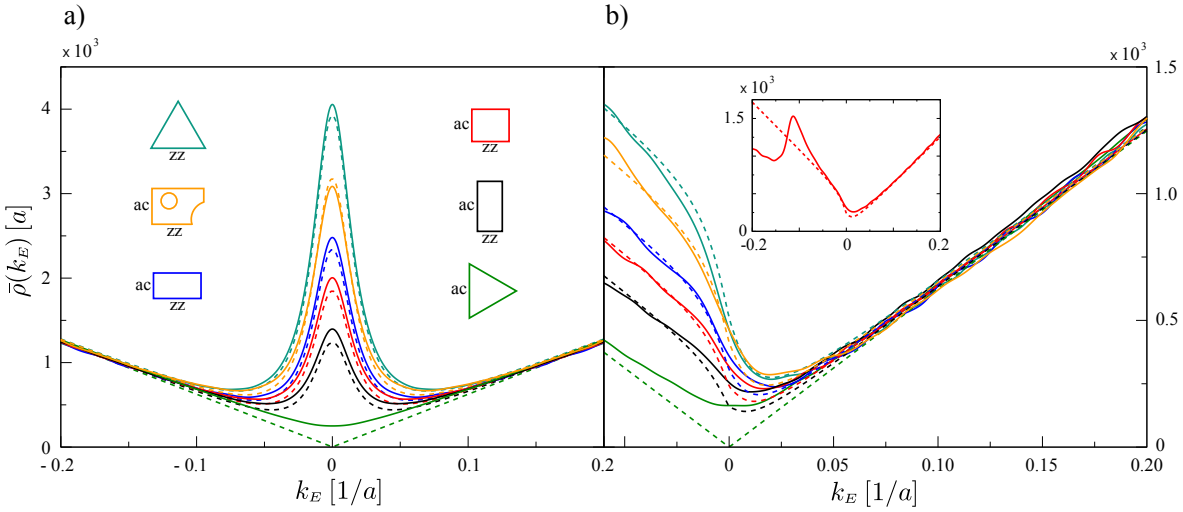

Figure 4.1: a) Smooth part of the density of states for several graphene billiards with approximately the same area $|\mathcal{V}| \approx (140a)^2$, calculated numerically using a tight-binding code with only nearest neighbor coupling (solid lines). The numerical curves are obtained by first calculating exact eigenenergies and successive smoothing by replacing each energy level by a Lorentzian with a half width at half maximum of $0.017\,1/a$. The dashed lines are the predictions of our theory, Eq. (4.32). From top to bottom: $|\partial\mathcal{V}_{zz}|/|\partial\mathcal{V}| = 1$ (grey, zigzag triangle), $|\partial\mathcal{V}_{zz}|/|\partial\mathcal{V}| \approx 1/1.6$ (orange, Sinai shape), $|\partial\mathcal{V}_{zz}|/|\partial\mathcal{V}| \approx 1/1.5$ (blue, rectangle), $|\partial\mathcal{V}_{zz}|/|\partial\mathcal{V}| \approx 1/1.9$ (red, rectangle), $|\partial\mathcal{V}_{zz}|/|\partial\mathcal{V}| \approx 1/1.3$ (black, rectangle), $|\partial\mathcal{V}_{zz}|/|\partial\mathcal{V}| = 0$ (green, armchair triangle). b) Smooth part of the density of states for the same systems as in a), but with a relative next-nearest neighbor hopping strength $t' = 0.1$. Solid lines show the numerical tight-binding results and dashed lines the predictions from Eq. (4.33). For the smoothing we used Lorentzians with a half width at half maximum of $0.012\,1/a$. We used the same color coding as in a). Inset: The tight-binding model exhibits a van Hove singularity at $k_E = -0.1\,t/\hbar v_F \approx -0.115\,1/a$. As a result the smoothed DOS shows a peak at the corresponding position (solid).

We neglect terms with such scaling, since only edge states are relevant for the surface contribution. This enables us to calculate the approximate surface contribution analytically also for finite nnn hopping

$$\bar{\rho}_{1,i} \approx \frac{|\partial\mathcal{V}_i|}{\pi^2}\int_0^\infty dk\,\frac{\xi}{(k_E+2kt')^2+\xi^2} = \frac{|\partial\mathcal{V}_i|}{\pi}\frac{1-\Theta_\xi(k_E)}{2t'}\,, \tag{4.29}$$

where we defined the smooth step function

$$\Theta_\xi(k_E) = \frac{1}{\pi}\arctan(k_E/\xi) + \frac{1}{2}\,. \tag{4.30}$$

In the limit $\xi \to 0$, Θ_ξ becomes the Heaviside step function.

We can summarize our results for the surface contribution to the smooth density of states

of a graphene billiard as

$$\bar{\rho}_1(k_E) \approx \frac{|\partial\mathcal{V}_{\mathrm{zz}}|}{\pi} \begin{cases} k_{\max}\delta_\xi(k_E) & \text{if } t' = 0\,, \\ \left[1-\Theta_\xi(k_E)\right]/(2t') & \text{otherwise}\ . \end{cases} \tag{4.31}$$

As opposed to Schrödinger billiards, for graphene $\bar{\rho}_1(k_E)$ does not scale with the total length of the system's boundary $|\partial\mathcal{V}|$, but only with the length of the zigzag part of the boundary, which we denote by $|\partial\mathcal{V}_{\mathrm{zz}}|$. Armchair and infinite mass type edges do not give rise to a surface term. The zigzag contribution depends qualitatively on the nnn hopping strength t': While for zero t', it is strongly peaked at zero energy and symmetric around the Dirac point, it has the shape of a smooth step for finite values of t'. The step gives rise to an enhancement of $\bar{\rho}$ for negative energies and is a clear manifestation of electron-hole symmetry breaking due to the nnn hopping. The step height is inversely proportional to the hopping strength. The smaller t' gets, the flatter also the edge state band becomes in momentum space, and therefore its density becomes larger.

Comparison with numerical simulations

In summary, our result for the smooth part of the density of states of a generic graphene billiard, neglecting the effect of nnn hopping, is represented by the the first two terms of the Weyl expansion

$$\bar{\rho}(k_E) \approx \frac{|\mathcal{V}|}{\pi}k_E + \frac{|\partial\mathcal{V}_{\mathrm{zz}}|}{\pi}k_{\max}\delta_\xi(k_E)\,. \tag{4.32}$$

Moreover, with nnn hopping we have found

$$\bar{\rho}(k_E) \approx \frac{|\mathcal{V}|}{\pi}k_E + \frac{|\partial\mathcal{V}_{\mathrm{zz}}|}{2t'\pi}\left[1-\Theta_\xi(k_E)\right]\ . \tag{4.33}$$

In the following we compare these predictions with the smooth DOS obtained by numerical solution of an atomistic tight-binding model for graphene. To this end we set up a discrete Hamiltonian according to the desired shape of the billiard, and then directly calculate its eigenvalues using standard algorithms [56, 81]. In this way we obtain a number of discrete levels k_n^{tb}. For smoothing, we convolute the levels with a Lorentzian function that is broad enough that the fine structure of the levels is completely eliminated. The resulting curves are then compared to Eqs. (4.32) and (4.33).

Figure 4.1 a) shows the analytical result for $t' = 0$ (dashed lines) and the corresponding numerical simulations for various graphene billiards (solid lines). All the billiards are chosen to have approximately the same area, $|\mathcal{V}| \approx (140\,a)^2$. This is reflected in the common slope of $\bar{\rho}$ for larger $|k_E|$, confirming the leading order contribution in the Weyl expansion, i. e. the bulk term. The different shapes and orientations of the billiards give rise to different fractions of the total zigzag boundary $|\partial\mathcal{V}_{\mathrm{zz}}|/|\partial\mathcal{V}|$. While the boundaries of the equilateral triangles consist completely of either zigzag (grey) or armchair (green) edges, both edge types are present in the rectangles (blue, red and black) and in the non-integrable (modified) Sinai

billiard (orange). The smooth DOS of the grey triangle shows a very pronounced peak around $k_E = 0$ due to the edge states. For the Sinai billiard and the rectangles the height of the peak decreases as $|\partial\mathcal{V}_{\mathrm{zz}}|$ becomes smaller, and for the green triangle the peak eventually vanishes. We find very good agreement with our analytic prediction. We point out that the dashed lines for the triangles and the rectangles do not involve any fitting, rather we have used the estimation from tight-binding theory, $k_{\max} = \pi/3a$. For the Sinai billiard, our theory allows to determine the total effective zigzag length $|\mathcal{V}_{\mathrm{zz}}| \approx 516\,a$. We note that Libisch and coworkers have numerically investigated the averaged DOS of graphene billiards and found a $\bar{\rho}(k_E)$ profile similar to that in Fig. 4.1 a) [44].

For the case of finite nnn hopping ($t' = 0.1$), Fig. 4.1 b) shows the comparison between theory and simulations for the same billiards. The lineshape of $\bar{\rho}(k_E)$ is a smooth step with a height that scales with the total length of the zigzag boundary, as predicted by Eq. (4.33). Also here we find good agreement close to the Dirac point and in the electron regime $k_E > 0$, without any additional fitting [for the Sinai billiard we use $|\partial\mathcal{V}_{\mathrm{zz}}| = 516\,a$, as obtained from the fit in Fig. 4.1 a)]. Further towards the hole regime, i. e. towards more negative energies, the tight-binding model has a van Hove singularity due to the edge state band edge at $k_E = -0.1\,t/\hbar v_F \approx -0.115\,1/a$, as depicted in the inset of Fig. 4.1 b) (solid line). This peak is missing in our calculation, since in the effective Dirac theory the edge state dispersion is always linear for finite t', cf. Eq. (A.15). At more negative energies the simulations give again a linear k_E dependence like for positive energies, since no edge states are present anymore. For a related study on edge states in graphene quantum dots, we refer to Ref. [81].

Equations (4.32) and (4.33) are the main results of this section. From our discussion it becomes clear that in principle the structure of a graphene flake's boundary, i. e. the ratio between zigzag and armchair type edges, can be estimated from the behavior of the smoothed density of states at low energies. The level broadening due to room temperature is of the order $10^{-2}\,1/a$, just as the values that we have used for ξ in Figs. 4.1 a) and 4.1 b). In view of the specific lineshape, Eq. (4.33) is the more realistic prediction, since nnn hopping exists in a real sample. Furthermore, not only nnn hopping, but also edge potentials, e. g. due to impurities, lead to a boundary condition like in Eq. (A.7) and thus to Eq. (4.33). On the other hand, Eq. (4.32) is nevertheless very useful for the estimation of the zigzag edge length, since it predicts the total spectral weight of the edge states

$$\int_{-\infty}^{\infty} dk_E \bar{\rho}_1(k_E) = \frac{|\partial\mathcal{V}_{\mathrm{zz}}|}{3}\,, \tag{4.34}$$

which is model independent, since the number of edge states is conserved [81]. This means that the part of the smooth DOS that scales with the length of the boundary is always exclusively due to the zigzag edges.

4.2 Density of states oscillations - trace formulae

Having derived the leading order contributions to the smoothed DOS, we now concern ourselves with the oscillating part of the DOS. For $k_E L \gg 1$, ρ_{osc} is associated with the classical periodic orbits of the system, in contrast to $\bar{\rho}$. This means that the nature of the classical dynamics, i. e. whether it is regular or chaotic, influences the result for ρ_{osc} significantly. For a detailed introduction to the physics of regular and chaotic systems in classical and quantum mechanics, see e. g. Refs. [49, 51, 65, 113]

For two-dimensional billiards, two conserved quantities are needed to ensure integrability. Consider for example a classical particle in a circular billiard without any time dependent potentials. Then the total energy is conserved, and in addition the angular momentum is conserved due to the rotational invariance of the system. Another example is the classical rectangular billiard. Again the total energy is conserved, which is equivalent to the conservation of the absolute value of the total momentum. But in addition the absolute values of both x- and y-component of the momentum are conserved individually, making the rectangle a classically integrable system as well. The symmetries that are associated to the integrals of motion allow to classify the classical orbits of a regular system in terms of invariant tori in phase space, on which the (canonical) classical action is constant. In this context, one speaks about the EBK (Einstein, Brillouin and Keller) quantization of regular systems [114, 115, 116]. The DOS oscillations of quantum systems with regular classical counterpart are given by a sum over orbit families, each corresponding to an invariant torus. This is expressed in the Berry-Tabor trace formula [110, 117]. In Subsec. 4.2.2 we consider the trace formulae for two representative regular shapes, disk and rectangle, in the graphene case.

Chaotic classical systems on the other hand are non-integrable, i. e. less integrals of motion than degrees of freedom exist. Classical trajectories in chaotic systems explore the whole energetically available phase space (ergodicity), in contrast to the regular case where they are restricted to a certain part of the phase space. Moreover, the distance between trajectories that differ slightly in initial position and momentum increases exponentially with time. The rates of proliferation are given by the *Lyapunov exponents* of the system. However, one should not be mislead by this and conclude that chaotic dynamics is in general very unstable. Consider a long trajectory with given initial and final position. If initial and final position are slightly changed, there exists a second trajectory that comes exponentially close to the original one [118]. These correlations between classical orbits have turned out to be essential for the semiclassical description of spectral and transport properties of chaotic systems. In Sec. 4.2.1 we present a graphene version of the Gutzwiller trace formula [49] for the oscillating part of the DOS, which we use later in Sec.4.3 to study the spectral correlations of chaotic graphene billiards.

4.2.1 Gutzwiller trace formula for chaotic graphene billiards

We begin with the chaotic systems and provide a version of the Gutzwiller trace formula for the oscillating part of the DOS of chaotic graphene billiards. Our starting point is the relation

between DOS and retarded Green function, Eq. (4.2), in the semiclassical limit $k_E L \gg 1$. As discussed in the previous section, short orbits give rise to $\bar{\rho}$, so that we focus on long orbits here. The Green function in the semiclassical limit has been derived in Sec. 3.2 in terms of a sum over all classical trajectories, Eq. (3.83). From this expression for G^{sc} we know already that the final result for ρ_{osc} can only differ from the oscillating DOS for chaotic Schrödinger billiards by effects from the trace of the pseudospin propagator. Thus we have to work out how the spatial integral in Eq. (4.2) depends on this trace. However, instead of inserting the orbit sum (3.83) directly into Eq. (4.2), we go one step back to Eq. (3.78), where we have already replaced the free Green function by its asymptotic form for large $k_E L$, but not yet performed the boundary integrals [103]. Then the N-reflection term of the DOS,

$$\rho_N(k_E) = -\frac{1}{\pi}\Im\mathfrak{m}\int\limits_{\mathcal{V}} d\boldsymbol{x}\,\mathrm{Tr}\left[G_N(\boldsymbol{x},\boldsymbol{x})\right]\,, \tag{4.35}$$

contains the spatial integral

$$I_N = \int\limits_{\mathcal{V}} d\boldsymbol{x}\,\frac{(1+\sigma_{\boldsymbol{\alpha}_1\boldsymbol{x}})(1+\sigma_{\boldsymbol{x}\boldsymbol{\alpha}_N})}{\sqrt{|\boldsymbol{x}-\boldsymbol{\alpha}_N||\boldsymbol{\alpha}_1-\boldsymbol{x}|}}\mathrm{e}^{\mathrm{i}k_E(|\boldsymbol{x}-\boldsymbol{\alpha}_N|+|\boldsymbol{\alpha}_1-\boldsymbol{x}|)}\,. \tag{4.36}$$

We parametrize the integration variable as $\boldsymbol{x} = l\,\hat{\boldsymbol{l}} + t\,\hat{\boldsymbol{t}}$, where $\hat{\boldsymbol{l}}$ is the direction from $\boldsymbol{\alpha}_N$ to $\boldsymbol{\alpha}_1$ and $\hat{\boldsymbol{t}}$ is the direction perpendicular to $\hat{\boldsymbol{l}}$, such that a right-handed coordinate system results, as sketched in Fig. 4.2. The origin $l = t = 0$ lies at the point $\boldsymbol{\alpha}_N$, and we denote the distance between the first and the last reflection point by $l_{N1} = |\boldsymbol{\alpha}_N - \boldsymbol{\alpha}_1|$. Then we can rewrite the phase in (4.36), assuming $t \ll l$ and $t \ll l - l_{N1}$, as

$$\varphi(l,t) = k_E|\boldsymbol{x}-\boldsymbol{\alpha}_N| + k_E|\boldsymbol{\alpha}_1-\boldsymbol{x}| \approx k_E l_{N1}\left(1+\frac{t^2}{2l[l_{N1}-l]}\right)\,, \tag{4.37}$$

and evaluate the t-integral in stationary phase approximation, assuming $k_E l_{N1} \gg 1$. The stationary phase point is given by

$$\frac{\partial\varphi(l,t_0)}{\partial t} = \frac{k_E\,l_{N1}t_0}{l(l_{N1}-l)} = 0 \quad \Rightarrow \quad t_0 = 0\,. \tag{4.38}$$

This means (cf. Fig. 4.2) that the dominant contributions to ρ_{osc} indeed originate from the periodic classical orbits. The stationary phase method then yields

$$I_N = \sqrt{\frac{2\pi}{k_E\,l_{N1}}}\mathrm{e}^{\mathrm{i}k_E l_{N1}}\int\limits_0^{l_{N1}} dl\;\left[(1+\sigma_{\boldsymbol{\alpha}_1\boldsymbol{x}})(1+\sigma_{\boldsymbol{x}\boldsymbol{\alpha}_N})\right]_{t=0}\,. \tag{4.39}$$

The only position dependence that could be left, is due to the chiral projections. However, for $t = 0$ they do not depend on the longitudinal coordinate l, since (cf. Fig. 4.2)

$$\sigma_{\boldsymbol{\alpha}_1\boldsymbol{x}}|_{t=0} = \sigma_{\boldsymbol{x}\boldsymbol{\alpha}_N}|_{t=0} = \sigma_{\boldsymbol{\alpha}_1\boldsymbol{\alpha}_N}\,. \tag{4.40}$$

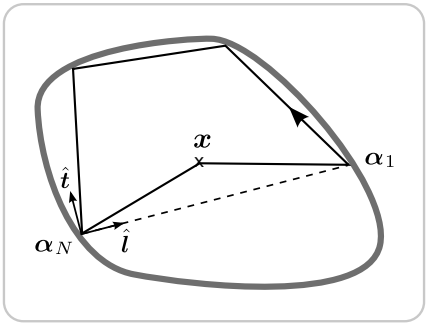

Figure 4.2: Sketch of the geometry and notations for the integration in Eq. (4.35).

The remaining integral over l can be performed exactly and we get

$$I_N = \sqrt{\frac{2\pi l_{N1}}{k_E}} \mathrm{e}^{\mathrm{i}k_E l_{N1}} 2(1 + \sigma_{\boldsymbol{\alpha}_1 \boldsymbol{\alpha}_N}) \,. \tag{4.41}$$

The important result here is that we can essentially read off ρ_{osc} for the graphene case directly from the corresponding Dirichlet problem for the Schrödinger equation [51, 103, 106], since the pseudospin does not affect the stationary phase points. Thus we find

$$\rho_{\mathrm{osc}}(k_E) = \frac{v_F}{2\pi} \mathfrak{Re} \sum_{\gamma} \mathrm{Tr}(K_\gamma) A_\gamma \, \mathrm{e}^{\mathrm{i}k_E L_\gamma} \,. \tag{4.42}$$

Here the sum runs over all, infinitely many *periodic classical orbits* γ. The classical amplitudes A_γ depend on the period T_{γ_p} of the corresponding primitive (non-recurring) orbit γ_p and the stability of the orbit γ via the stability matrix M_γ [49, 51]

$$A_\gamma = \frac{T_{\gamma_p}}{\sqrt{|\det(M_\gamma - 1)|}} \mathrm{e}^{-\mathrm{i}\tilde{\mu}_\gamma \pi/2} \,. \tag{4.43}$$

The Maslov index $\tilde{\mu}_\gamma$ contains the number of conjugated points μ_γ that occurred already in the semiclassical Green function (3.83) and the additional phases from the spatial integration in Eq. (4.35). In contrast to μ_γ, the Maslov index $\tilde{\mu}_\gamma$ is always independent of the starting point of γ [119]. The trace formula (4.42) for ρ_{osc} is only valid for systems with isolated orbits, a prerequisite to evaluate the integral perpendicular to $\boldsymbol{\alpha}_N - \boldsymbol{\alpha}_1$ in stationary phase approximation. This is particularly fulfilled for chaotic systems, while for regular systems one has to consider whole families of degenerate periodic orbits as described in Subsec. 4.2.2. We note that in Ref. [107] a semiclassical trace formula for graphene is presented, which however is not taking into account the boundaries required to obtain chaotic dynamics (see also Ref. [99] for a trace formula for the Dirac equation).

The term *trace formula* for a representation of ρ_{osc} in terms of the periodic classical orbits of a system has been coined by Gutzwiller, who first presented the trace formula for isolated orbits in Ref. [106]. Later Berry and Tabor derived a trace formula that is valid for regular

systems with degenerate orbits [110, 117]. It is remarkable that except for $\hbar$ and the trace of K_γ that takes care of the graphene specific pseudospin interference, the trace formula (4.42) contains only classical quantities and still describes a pure quantum property, the oscillating part of the DOS.

In principle, the trace formula Eq. (4.42) allows to compute semiclassical approximations for energy levels in chaotic graphene billiards. Since the classical dynamics of a graphene billiard is the same as that of a Schrödinger billiard, the convergence properties of Eq. (4.42) are expected to be similar to those of Gutzwiller's trace formula, i. e. convergence problems arise due to the exponential increase of the total number of periodic orbits with their length [51]. However, residual disorder scattering (cf. App. A.6), giving rise to a finite life time of the quantum states, or finite temperature lead to a damping of longer orbits in the trace formula, improving its convergence. We study the case of such damping in the context of graphene billiards with regular dynamics in the following subsection.

As the Gutzwiller trace formula for the case of quantum chaotic Schrödinger dynamics, the trace formula (4.42) represents a suitable starting point to consider the statistical properties of energy levels for chaotic graphene cavities. In particular it allows to study universal spectral features of ρ_{osc}. Based on Eq. (4.42) we perform a semiclassical analysis of spectral statistics of graphene billiards in Sec. 4.3, focusing in particular on edge-related effects.

4.2.2 Regular billiards - trace formulae and shell effects

In the following we give two representative examples for trace formulae describing the oscillating part of the density of states in graphene billiards that have classically integrable dynamics. In the previous subsection we have found that for chaotic billiards the sum over all classical orbits in the semiclassical Green function (3.83) is reduced to the periodic classical orbits that exist in the system in the trace formula for ρ_{osc}. This result carries over to the case of the regular billiards. However, the (spatial) symmetries in many regular cases cause orbit degeneracies, thus the orbits are organized in families on classical invariant tori [114, 115, 116]. All members of a family possess the same classical properties such as length, stability, number of reflections, and Maslov index. An example of a periodic orbit family in the circular billiard is given in Fig. 4.3 a): The triangular orbit can be rotated by an arbitrary angle resulting in another equivalent periodic orbit. All orbits constructed in this way constitute one family. In order to compute the oscillatory part of the DOS from the semiclassical Green function, it is convenient to organize the trajectories in terms of tori, respectively families f, in the trace-integral Eq. (4.2):

$$\rho(k_E) = -\frac{1}{\pi}\mathfrak{Im}\sum_f \int_{\mathcal{V}_f} d\boldsymbol{x}\,\mathrm{Tr}\left[G_f(\boldsymbol{x},\boldsymbol{x})\right] . \tag{4.44}$$

Here $\mathcal{V}_f$ is the part of $\mathcal{V}$ that is covered by the family f. This can be the whole domain $\mathcal{V}$, as for the diametral orbits in the circle or the families of the rectangular billiard, or only part of it, as for all other families in the circle (cf. Figs. 4.3 and 4.6). Restricting oneself to a specific

orbit family f, the spatial integral over $\mathcal{V}_f$ can be performed exactly for many geometries (see Ref.[51] and references therein).

As we have discussed above for the chaotic case, the semiclassical pseudospin propagator for graphene does not alter the resonance condition, and the pseudospin trace of periodic classical orbits does not depend on the coordinates of the starting and end point. Therefore, the integrals over $\mathcal{V}_f$ are the same as for Schrödinger billiards with Dirichlet boundary conditions. Hence we can adapt the corresponding results by explicitly including the correct pseudospin trace for each orbit family. The collective effect of orbit families giving rise to constructive interference due to action degeneracies lead to pronounced signatures in the DOS of integrable systems known as shell effects [51]. We analyze below how such features are modified due to graphene edge effects.

After the spatial integrals in Eq. (4.44) are performed, the result is a semiclassical Berry-Tabor type trace formula for $\rho_{\rm osc}$ in terms of sums over families of periodic orbits organized on resonant tori [110]

$$\rho^{\rm sc}_{\rm osc}(k_E) = \sum_f R_f(k_E) \mathrm{e}^{ik_E L_f} \,. \tag{4.45}$$

We have already mentioned that for chaotic billiards the convergence of such sums is an issue, and in order to obtain the quantum levels of a billiard, one has to take into account in principle all orbits. However, even if the sum converges, as it is the case for many integrable geometries, the quantum levels are in general reproduced by semiclassics only with an accuracy of the mean level spacing. On the other hand, many physical properties like the stability of finite fermion systems or also the conductance fluctuations in quantum dots, do not depend on the exact spectrum, but only on the gross-shell effects, i. e. the contributions from the shortest periodic orbits [51]. In order to investigate these, we consider broadened energy levels, e. g. by convoluting the DOS with a Gaussian

$$\rho_\xi(k_E) = \frac{1}{\xi\sqrt{\pi}} \int\limits_{-\infty}^{\infty} dk'_E \mathrm{e}^{-(k_E-k'_E)^2/\xi^2} \rho(k'_E) = \frac{1}{\xi\sqrt{\pi}} \sum_n \mathrm{e}^{-(k_E-k_n)^2/\xi^2} \,. \tag{4.46}$$

For the trace formula (4.45), this level broadening results in an effective damping of long orbits and therefore improves convergence of the periodic orbit sum

$$\begin{aligned}
\rho^{\rm sc}_{\xi,{\rm osc}}(k_E) &= \frac{1}{\xi\sqrt{\pi}} \sum_\gamma \int\limits_{-\infty}^{\infty} dk'_E \mathrm{e}^{-(k_E-k'_E)^2/\xi^2} R_\gamma(k'_E) \mathrm{e}^{\mathrm{i}k'_E L_\gamma} \\
&\approx \frac{1}{\xi\sqrt{\pi}} \sum_\gamma R_\gamma(k_E) \mathrm{e}^{\mathrm{i}k_E L_\gamma} \int\limits_{-\infty}^{\infty} dk'_E \mathrm{e}^{-(k'_E-k_E)^2/\xi^2} \mathrm{e}^{\mathrm{i}(k'_E-k_E)L_\gamma} \\
&= \sum_f R_f(k_E) \mathrm{e}^{\mathrm{i}k_E L_f} \mathrm{e}^{-(\xi L_f/2)^2} \,.
\end{aligned} \tag{4.47}$$

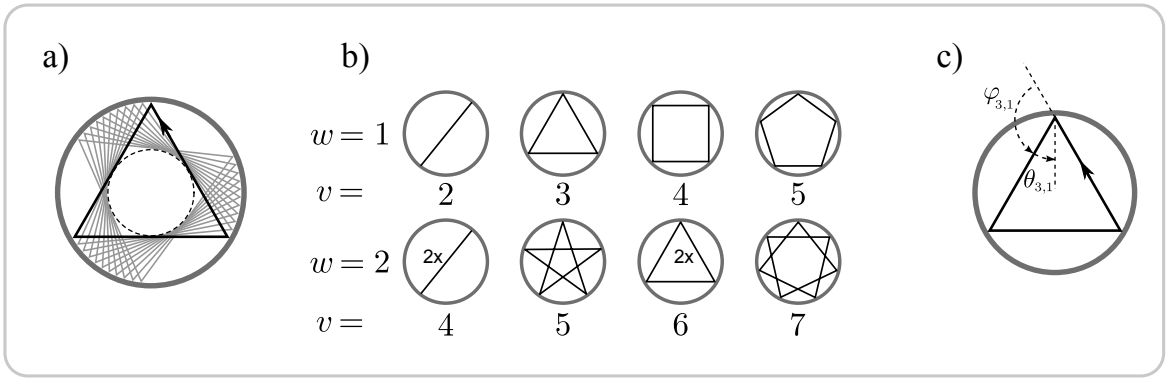

Figure 4.3: a) Example of a family of degenerate classical orbits in the circular billiard. The black triangular orbit can be rotated by an arbitrary angle without the length being changed. All resulting orbits give the same contribution to the density of states. (After Ref. [120].) b) Families of periodic classical orbits in the circular billiard, with v the total number of reflections along the orbit and w the winding number. (After reference [103].) If (v, w) are not coprime, then the orbits are repetitions of some primitive orbits. For example members of (4,2) are repetitions of (2,1) and members of (6,2) are repetitions of (3,1). c) Angles of rotation, φ, and reflection, θ, for a reflection of a member of the family $(3, 1)$.

Circular billiard with infinite mass edges

We begin with the circular billiard with infinite mass type edges. The sign of the mass term is considered constant so that we can choose the boundary matrix $P_{\boldsymbol{\alpha}} = (1 - \tau_z \otimes \sigma_{\boldsymbol{t_\alpha}})/2$ for all boundary points $\boldsymbol{\alpha}$. The exact quantum energy eigenvalues $E_{nm} = \hbar v_F k_{nm}$ are given by Bessel functions of the first kind [90]

$$J_m(k_{nm}R) = \tau J_{m+1}(k_{nm}R)\,, \tag{4.48}$$

where R is the radius of the billiard, $\tau = \pm 1$ labels the two valleys, and $n, |m| \in \mathbb{N}$. In Eq. (4.48), $k_{nm}R$ is then the n-th intersection of the Bessel functions J_m and J_{m+1}.

In Fig. 4.3 b) we show members of a few periodic orbit families that exist in the circle. In order to label them, we introduce the total number of reflections, v, and the winding number, w. Obviously the number of reflections is always equal or greater than twice the winding number, i. e. $v \geq 2w$. The orbits of the families in the first row of Fig. 4.3 b) where $w = 1$, are regular polygons that do not intersect themselves. For larger winding numbers, the orbits are star-like self-intersecting polygons, with the exception of repetitions of the $w = 1$ families. In general a family is a repeated version of another one if v and w are not coprime, i. e. if positive integer numbers $r \geq 2$, a and b exist, such that $(v, w) = (ra, rb)$. In this case, v and w describe orbits with total number of reflections a and winding number b that are repeated r times. In Fig. 4.3 b) we have $(v, w) = (4, 2)$ and $(v, w) = (6, 2)$ as examples. In the following we allow for negative winding numbers and define the sign such that $w > 0$ for clockwise and $w < 0$ for anti-clockwise going orbits. Using simple geometrical relations, one can derive the

length

$$L_{v,w} = 2vR\sin(|\varphi_{v,w}|) \tag{4.49}$$

and the angle of rotation at every reflection

$$\varphi_{v,w} = \pi\frac{w}{v}\,. \tag{4.50}$$

Therefore the reflection angles read [cf. Fig. 4.3 c)]

$$\theta_{v,w} = \mathrm{sgn}(w)\frac{\pi}{2} - \varphi_{v,w} = \left(\frac{\mathrm{sgn}(w)}{2} - \frac{w}{v}\right)\pi\,. \tag{4.51}$$

With that we proceed calculating the trace of the pseudospin propagator, through which graphene physics enters. According to Eq. (3.94), the pseudospin propagator $K_{v,w}$ obtains a factor $\mathrm{i}\tau_z \otimes \sigma_z$ for every reflection, so that the trace for an orbit (v, w) is

$$\mathrm{Tr}\,(K_{v,w}) = \mathrm{i}^v\,\mathrm{Tr}\left(\tau_z^v \otimes \sigma_z^v \mathrm{e}^{\mathrm{i}v\theta_{v,w}\sigma_z}\right)\,. \tag{4.52}$$

In the following we will frequently have to evaluate traces of this form. First we rewrite

$$\sigma_z = -\mathrm{i}\mathrm{e}^{\mathrm{i}\sigma_z\pi/2} \Rightarrow \sigma_z^v = (-\mathrm{i})^v \mathrm{e}^{\mathrm{i}\sigma_z v\pi/2}\,, \tag{4.53}$$

so that the trace can then be evaluated using the rule

$$\mathrm{Tr}\left(\mathrm{e}^{\mathrm{i}\sigma_z\Theta}\right) = \mathrm{Tr}\,(\sigma_0\cos\Theta + \sigma_z \mathrm{i}\sin\Theta) = 2\cos\Theta\,. \tag{4.54}$$

The same of course holds true for the Pauli matrices of the valley pseudospin, so that Eq. (4.52) gives

$$\begin{aligned}\mathrm{Tr}\,(K_{v,w}) &= \mathrm{i}^{3v}\,\mathrm{Tr}\left(\mathrm{e}^{\mathrm{i}\tau_z v\pi/2} \otimes \mathrm{e}^{\mathrm{i}\sigma_z[v\,\theta_{v,w}+v\pi/2]}\right) = (-\mathrm{i})^v 4\cos(v\pi/2)\cos(v\,\theta_{v,w} + v\pi/2) \\ &= (-1)^w \times \begin{cases} 4 & \text{for even } v\,, \\ 0 & \text{for odd } v\,. \end{cases}\end{aligned} \tag{4.55}$$

This result reflects the Berry phase that the quasiparticles in graphene pick up along periodic orbits. Interestingly, orbits with an odd number of reflections do not contribute to the oscillating part of the DOS, since the pseudospins interfere destructively in this case. One can already see this in Eq. (4.52), because $\mathrm{Tr}\,\tau_z^v = \mathrm{Tr}\,\tau_z = 0$ for odd v. However, similar as for the surface term of $\bar{\rho}$, valley degeneracy requires that we have to get the very same result for both K-points individually. Since orbits with odd v do not contribute, this has to hold also if we neglect the valley structure. Thus we reconsider the sublattice part of Eq. (4.52). If v is odd, we have

$$\mathrm{Tr}\left(\sigma_z^v \mathrm{e}^{\mathrm{i}v\theta_{v,w}\sigma_z}\right) = (-\mathrm{i})^v(-1)^{(v+1)/2}\sin\theta_{v,w}\,. \tag{4.56}$$

However, for each orbit family (v, w) with $\theta_{v,w} \neq 0$, i. e. for all except for the diametral orbits $(2w, w)$, we have a 'time reversed' family[2] $(v, -w)$ with orbits that have the same scalar part, but differ in the pseudospin part, namely according to Eq. (4.51)

$$\theta_{v,-w} = -\theta_{v,w}\,, \tag{4.57}$$

and thus the contributions from orbits with odd v cancel each other even within a single valley.

For the circular Schrödinger billiard with Dirichlet boundary conditions, the semiclassical trace formula has been derived already about thirty years ago [120, 121, 122]

$$D^{\mathrm{S}}_{\mathrm{osc}}(E) = \frac{2}{\hbar v_F}\sqrt{\frac{k_E R^3}{\pi}} \sum_{w=1}^{\infty}\sum_{v=2w}^{\infty} \frac{f_{v,w}}{\sqrt{v}} \sin^{3/2}(\varphi_{v,w}) \cos\left(k_E L_{v,w} + \frac{v}{2}\pi + \frac{\pi}{4}\right)\,. \tag{4.58}$$

Here $f_{v,w} = 1$ for the diametral orbits $(2w, w)$ and $f_{v,w} = 2$ otherwise, which accounts for the fact that the diametral orbits are their own time reversed partners and do not have to be counted twice. Taking into account the graphene specific modifications due to the pseudospin, Eq. (4.55), we obtain the semiclassical trace formula for a graphene disk billiard with infinite mass type edges

$$\rho^{\mathrm{sc}}_{\mathrm{osc}}(k_E) = 4\sqrt{\frac{k_E R^3}{\pi}} \sum_{w=1}^{\infty}\sum_{\substack{v=2w \\ \text{even}}}^{\infty} \frac{f_{v,w}}{\sqrt{v}} (-1)^{w+v/2} \sin^{3/2}(\varphi_{v,w}) \cos\left(k_E L_{v,w} + \frac{\pi}{4}\right) \mathrm{e}^{-(\xi L_{v,w}/2)^2}\,. \tag{4.59}$$

Since for families with even v the contribution to ρ_{osc} does not depend on the sign of the winding number, the sum is restricted to positive w. We also included the exponential damping of longer orbits due to the Gaussian convolution according to Eq. (4.47).

In Fig. 4.4 we show the results for the oscillating part of the density of states, calculated with the semiclassical trace formula (4.59) for different values of the broadening ξ, and compare them with the results obtained from the exact quantum energy levels. In order to obtain the latter, we solve Eq. (4.48) numerically and convolute the resulting discrete energy spectrum with a Gaussian of width ξ. We find that the gross-shell structure, i. e. the short orbit contributions to ρ_{osc}, of the graphene billiard with infinite mass edges is approximated very well by the semiclassical theory, see panels a) and b). For comparison, panel c) shows the same energy range for the corresponding Schrödinger disk billiard. For panel d) we have used the undamped trace formula ($\xi = 0$) and summed over many orbits with up to several hundred reflections. In this case even the exact quantum levels (blue circles) are reproduced with remarkable accuracy by the semiclassical theory (black line). For every level, we have a sharp peak in the semiclassical result. An exception are the two levels close to $k_E R = 6$, for which the semiclassical trace formula yields only one peak, though twice as high as the others, meaning that in the semiclassical expression the two levels are nearly degenerate.

[2] In the sense that the propagation direction is reversed. The physical time reversal operation for the Dirac particles involves operations on the pseudospins, see Sec. 2.2.

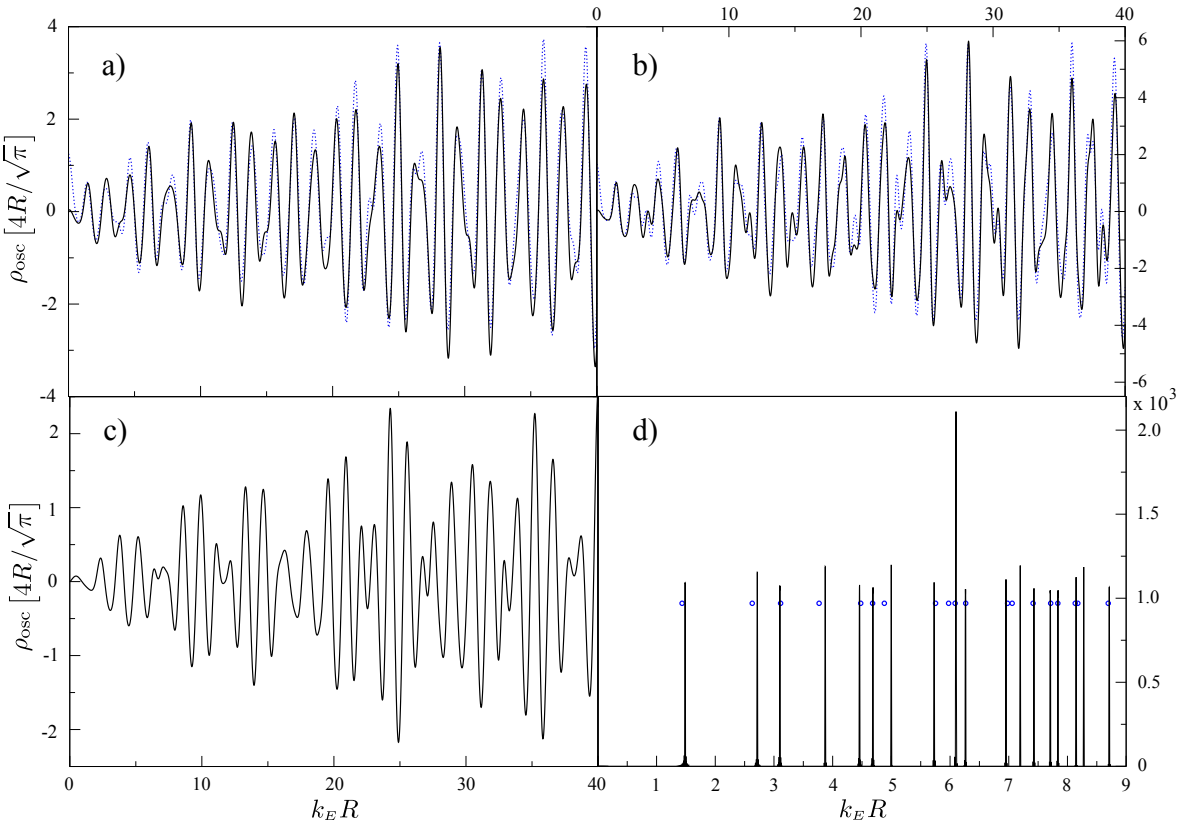

Figure 4.4: Oscillating part $\rho_{\rm osc}$ of the density of states of a circular billiard as a function of $k_E R$. a), b) Gaussian convoluted $\rho_{\rm osc}(k_E)$ for graphene billiards with infinite mass edges for $\xi = 0.4/R$ and $\xi = 0.3/R$ respectively. The full (dotted) curves show the semiclassical (quantum mechanical) results. c) Corresponding result (for $\xi = 0.4/R$) for a circular Schrödinger billiard with Dirichlet boundary conditions. d) Peaks are obtained from the semiclassical expression (4.59) for $\xi = 0$ by summing up orbit families up to $v, w = 400$. Blue circles mark the positions of the exact quantum mechanical levels obtained from Eq. (4.48).

In Fig. 4.5 we have a closer look at the frequency content of the oscillations. In fact one can see from panel c) that the two shortest non-vanishing orbit families, $(2,1)$ and $(4,1)$, already give a good approximation to the shell structure for $\xi = 0.4/R$. To obtain the power spectrum of the exact quantum result, see panel d), we have broadened the levels with Gaussians ($\xi = 0.3/R$) and then took the Fourier transform of the resulting DOS oscillations. Evidently, only families with an even number of vertices v are contained in the spectrum, as semiclassically predicted. For example the triangular orbits $(3,1)$ that would give a peak at $l/R = 5.2$ and also the pentagram orbits $(5,2)$ ($l/R = 9.5$) do not contribute. The inset shows the same plot on a logarithmic scale, where the absence of the orbits with odd v is even more evident.

For some regular geometries it is in fact possible to obtain analytic semiclassical approximations to the quantum levels by summing the trace formula approximately, and indeed the

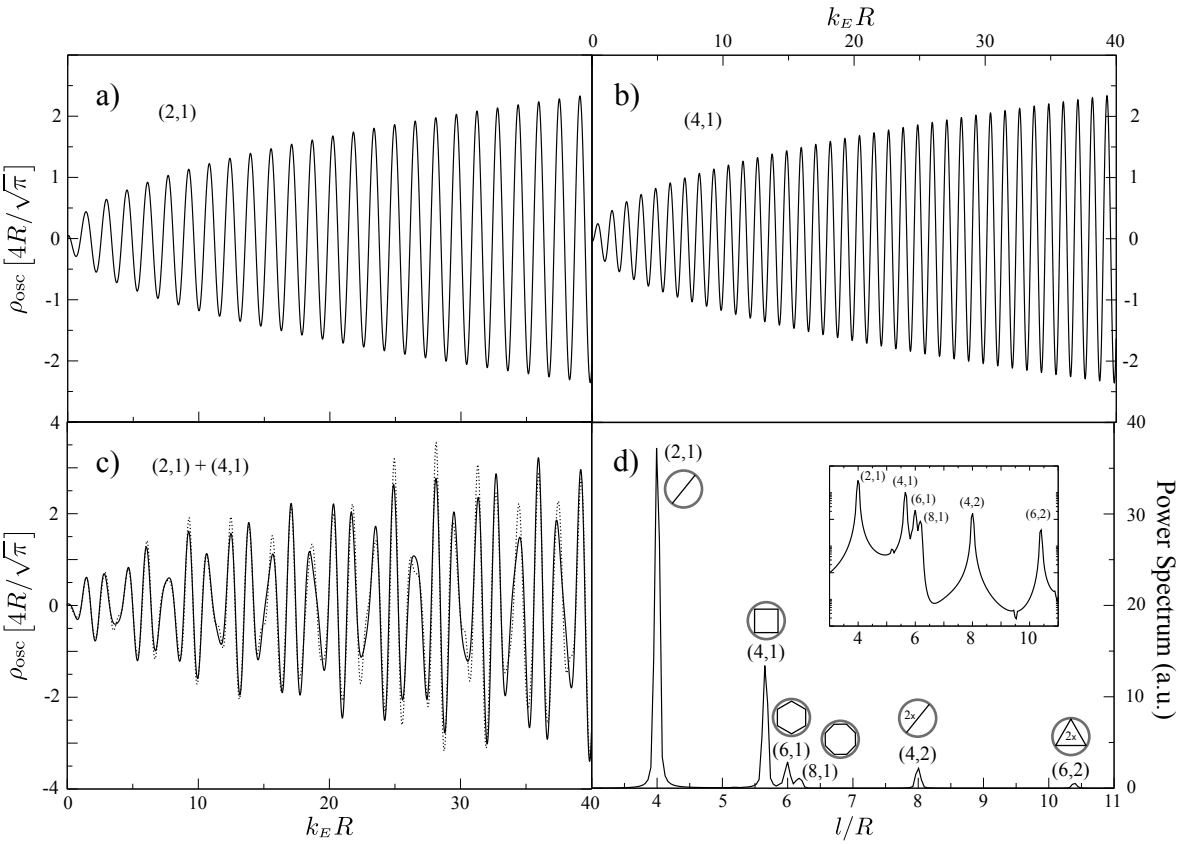

Figure 4.5: Most important constituents of the Gaussian convoluted $\rho_{\rm osc}$ of the circular graphene billiard. a), b) Semiclassical contributions from the two shortest contributing orbit families $(2,1)$ and $(4,1)$, respectively. c) Comparison of the full semiclassical orbit sum (dotted) with the contribution from the two shortest orbit families $(2,1)$ and $(4,1)$ (solid) for $\xi = 0.4/R$. d) Power spectrum of the Gaussian convoluted ($\xi = 0.3/R$) quantum DOS. Peaks can be uniquely assigned to periodic orbit families (v,w). Inset: Logarithmic representation.

circle is such a case. Therefore we use the Poisson sum rule in the form

$$\sum_{w=1}^{\infty} F(w) = \sum_{W=-\infty}^{\infty} \int_0^{\infty} dx F(x) \mathrm{e}^{2\pi \mathrm{i} x W} - \frac{1}{2} F(0) \tag{4.60}$$

for the sum over the winding number w in Eq. (4.59). Then we can rewrite the trace formula as

$$\rho_{\rm osc}(k_E) = 4\sqrt{\frac{2k_E R^3}{\pi}} \mathfrak{Re} \sum_{W=-\infty}^{\infty} \sum_{v=-\infty}^{\infty} \frac{\mathrm{e}^{\mathrm{i}\pi v}}{\sqrt{v}} \int_0^{\infty} dx\, \Theta(v-x) \sin^{3/2}\left(\frac{\pi}{2}\frac{x}{v}\right) \mathrm{e}^{\mathrm{i}\pi x} \mathrm{e}^{\mathrm{i}\Phi(x)}\,, \tag{4.61}$$

with

$$\Phi(x) = 4vk_E R \sin\left(\frac{\pi}{2}\frac{x}{v}\right) + 2\pi W x\,, \tag{4.62}$$

and Θ the Heaviside step function. We evaluate the integral in Eq. (4.61) approximately using the method of stationary phase. To this end, we consider all terms other than the exponential with Φ as slowly varying and obtain

$$\rho_{\mathrm{osc}}(k_E) \sim \mathfrak{Re} \sum_{W=0}^{\infty} \sum_{v=-\infty}^{\infty} \Theta(v) \sqrt{k_E^2 R^2 - W^2}\, \mathrm{e}^{2\pi \mathrm{i} v V_0(W)}\,, \tag{4.63}$$

with

$$V_0(W) = 2W - \frac{3}{2} + \frac{1-2W}{\pi}\left[1 - \arccos\left(\frac{W}{k_E R}\right)\right] - \frac{2k_E R}{\pi}\sqrt{1 - \frac{W^2}{k_E^2 R^2}}\,. \tag{4.64}$$

This equation implicitly defines the semiclassical approximations to the quantum levels of the graphene disk with infinite mass boundaries, since the sum in Eq. (4.63) is singular if and only if $V_0(W) = V$ for given integers V and W. This defines the approximate eigenenergies in terms of $k_E R$. To see this, we consider the Poisson formula now for v

$$\sum_{v=-\infty}^{\infty} F(v) = \sum_{V=-\infty}^{\infty} \int_{-\infty}^{\infty} dy\, F(y) \mathrm{e}^{2\pi \mathrm{i} y V} \tag{4.65}$$

and note that the real part of the Fourier transformed Heaviside function is given by a Dirac delta function

$$\mathfrak{Re} \int_{-\infty}^{\infty} dy\, \Theta(y)\, \mathrm{e}^{2\pi \mathrm{i} y (V+V_0)} = \frac{1}{2}\delta(V + V_0)\,. \tag{4.66}$$

In Table 4.1, we compare several energy levels obtained from the trace formula (4.59) by summing over many orbits [see also black peaks in Fig. 4.4 d)], with the numerical solutions of $V = V_0(W)$, i. e. Eq.(4.64), and the exact quantum levels from Eq. (4.48) [blue circles in Fig. 4.4 d)]. Also here we find that the semiclassical results agree very well with the quantum levels (see also relative errors in Table 4.1)

In conclusion we find that the results of our semiclassical theory for the graphene disk with infinite mass edges agree very well with the exact quantum mechanical solution of the Dirac equation with corresponding boundary conditions.

Rectangular billiard with zigzag and armchair edges

Next we study the the rectangular billiard, representing another prominent classically integrable geometry. While for the Schrödinger equation with Dirichlet boundary conditions, finding the eigenvalues of the 2D box is a simple textbook problem [$E_{nm} \sim (n^2 + m^2)$], the graphene rectangle is a much more subtle problem. For instance, the eigenvalue problem of a graphene rectangle with infinite mass type edges (see also App. A.4) has, to the best of our knowledge, not been solved analytically so far. Here we consider the more realistic case

a) circular infinite mass billiard			b) square billiard ('semiconducting')		c) square billiard ('metallic')	
TF	TF (P)	QM	TF	QM	TF	QM
1.49 (4.2)	1.57 (9.8)	1.43	6.85 (0.6)	6.81	6.86 (0.2)	6.85
2.72 (3.4)	2.78 (5.7)	2.63	7.85 (0.1)	7.84	7.30 (0.3)	7.28
3.10 (0.3)	3.14 (1.0)	3.11	7.93 (0.8)	7.87	7.92 (0.9)	7.85
3.87 (2.7)	3.92 (4.0)	3.77	8.11 (0.7)	8.05	8.15 (0.7)	8.09
4.46 (0.4)	4.49 (0.2)	4.48	8.97 (0.6)	8.92	8.41 (0.2)	8.39
4.69 (0.2)	4.71 (0.6)	4.68	9.11 (0.1)	9.10	8.84 (0.5)	8.80
5.00 (2.5)	5.04 (3.3)	4.88	9.26 (0.2)	9.24	9.43 -	-
5.73 (0.4)	5.75 (0.0)	5.75	9.35 (0.3)	9.32	9.54 (0.4)	9.50
6.10 (2.0)	6.12 (2.3)	5.98	10.47 -	-	9.85 (0.0)	9.85
6.10 (0.2)	6.14 (0.8)	6.09	10.86 (0.0)	10.86	10.06 (0.1)	10.05
6.26 (0.2)	6.28 (0.2)	6.27	10.92 (0.2)	10.90	10.59 (0.3)	10.56
6.95 (0.4)	6.98 (0.0)	6.98	11.05 (0.4)	11.01	11.04 (0.4)	11.00
7.20 (2.0)	7.23 (2.4)	7.06	11.18 (0.4)	11.14	11.04 (0.1)	11.03
7.43 (0.3)	7.45 (0.5)	7.41	11.29 (0.2)	11.27	11.21 (0.5)	11.16
7.71 (0.0)	7.72 (0.1)	7.71	11.52 -	-	11.71 (0.2)	11.69
7.84 (0.1)	7.85 (0.3)	7.83	11.80 (0.3)	11.76	11.74 (0.3)	11.70
8.15 (0.3)	8.17 (0.5)	8.13	11.97 (0.1)	11.96	12.23 (0.3)	12.20
8.28 (1.2)	8.31 (1.6)	8.18	12.02 (0.0)	12.02	12.57 -	-
8.71 (0.2)	8.73 (0.5)	8.69	12.13 (0.3)	12.10	12.83 (0.2)	12.81
9.08 (0.1)	9.09 (0.0)	9.09	13.31 (0.2)	13.29	12.90 (0.0)	12.90

Table 4.1: a) Energy levels $k_n R$ of the circular billiard with infinite mass type edges obtained from the semiclassical trace formula, Eq. (4.59), by summing over many classical orbits with $\xi = 0$ (TF) and by means of the Poisson resummation [TF (P)], Eq. (4.64), compared to the quantum mechanical result (QM) from Eq. (4.48). The relative error of the semiclassical result with respect to the quantum mechanics in percent is given in brackets. b), c) Energy levels $k_n L$ for square graphene billiards with $KL \bmod 2\pi = 2\pi/3$ ($L = 200\,a$ 'semiconducting') and $KL \bmod 2\pi = 0$ ($L = 201\,a$ 'metallic'), respectively. Again we compare the result from the semiclassical trace formula (4.77) at $\xi = 0$ with the quantum mechanical result (4.69).

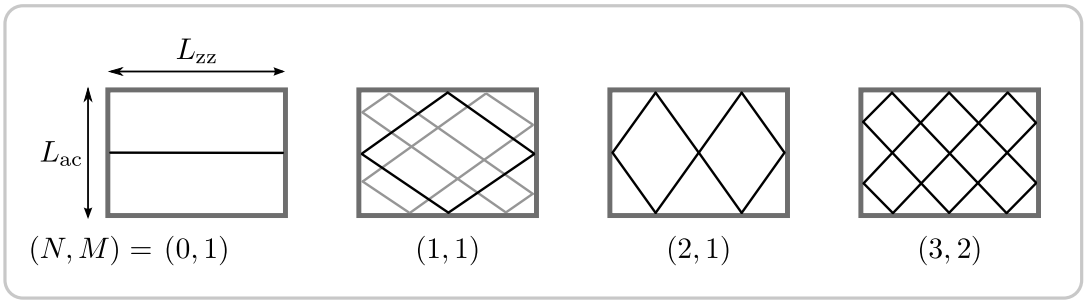

Figure 4.6: Families of periodic classical orbits in the rectangular billiard. N (M) is the number of reflections at each zigzag (armchair) edge. For the (1,1) family we show three degenerate members.

of a rectangle with two zigzag and two armchair edges of lengths L_{zz} and L_{ac}, respectively. Even though for this case a closed formula for the eigenvalues in terms of a transcendental equation can be derived, an explicit expression for the eigenvalues does not exist, due to coupling of the momenta in different directions. In App. A.3 we show that the energy eigenvalues $E_{nm} = \hbar v_F k_{nm}$ are given by

$$k_{nm} = \pm\sqrt{p_{nm}^2 + q_m^2}\,, \tag{4.67}$$

where p_{nm} and q_m are the components of the momentum in the direction along the armchair and zigzag edges, respectively. The latter is quantized according to

$$q_m = \frac{m\pi}{L_{zz}} - K \quad m \in \mathbb{N}\,, \tag{4.68}$$

and both momenta are connected via the transcendental equation

$$p_{nm} = \frac{1}{L_{ac}} \arctan(q_m/p_{nm}) - \frac{\pi}{L_{ac}}\left(n + \frac{1}{2}\right), \quad n \in \mathbb{N}\,. \tag{4.69}$$

In the following we show that our semiclassical theory provides a very good approximation to the quantum DOS of the graphene rectangle, in spite of the nontrivial momentum coupling.

As for the circle, the periodic orbit families in the rectangle can be labeled with two integer indices. By N and M we denote the numbers of reflections that occur at each zigzag edge (N) and each armchair edge (M), respectively (cf. Fig. 4.6), i. e. the total number of reflections, $2(N + M)$, is always even. The shortest families, $(N, 0)$ and $(0, M)$, consist of the so-called bouncing ball orbits, where the reflections occur only at two opposite edges and the reflection angle is zero. For the other cases, the ratio of N and M fixes the absolute values of the reflection angles. Every reflection at a zigzag edge occurs under a reflection angle θ_{zz} and every reflection at an armchair edge under a reflection angle θ_{ac} with

$$|\theta_{zz}| = \arctan\left(\frac{ML_{zz}}{NL_{ac}}\right), \tag{4.70}$$

$$|\theta_{ac}| = \frac{\pi}{2} - |\theta_{zz}| = \arctan\left(\frac{NL_{ac}}{ML_{zz}}\right). \tag{4.71}$$

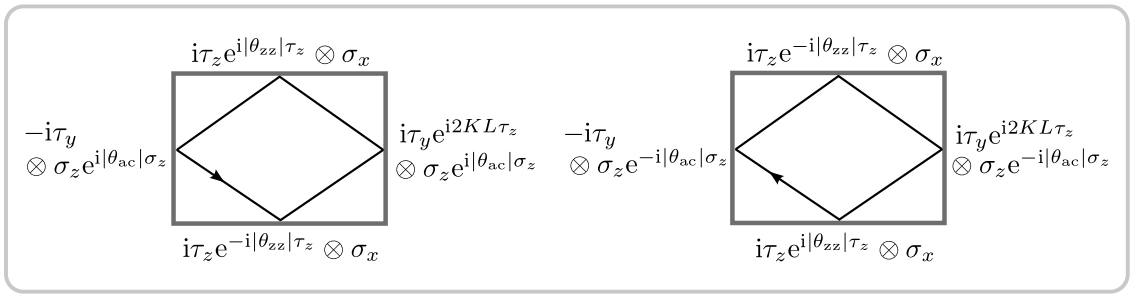

Figure 4.7: Matrix factors obtained along orbits of the (1,1) family. For counterclockwise propagation (left) reflection angles are positive, for clockwise propagation they are negative.

Furthermore, the length of an orbit (N, M) is given by

$$L_{NM} = 2\sqrt{M^2 L_{\mathrm{zz}}^2 + N^2 L_{\mathrm{ac}}^2}\,. \tag{4.72}$$

From Eq. (3.94) we can read off the specific matrix factors for reflections from each of the four sides, namely

$$\begin{aligned}
\mathrm{i}\tau_z \mathrm{e}^{-\mathrm{i}\theta_{\mathrm{zz}}\tau_z} \otimes \sigma_x \qquad & \text{at lower zigzag edge}\,, \\
\mathrm{i}\tau_z \mathrm{e}^{\mathrm{i}\theta_{\mathrm{zz}}\tau_z} \otimes \sigma_x \qquad & \text{at upper zigzag edge}\,, \\
-\mathrm{i}\tau_y \otimes \sigma_z \mathrm{e}^{\mathrm{i}\theta_{\mathrm{ac}}\sigma_z} \qquad & \text{at left armchair edge}\,, \\
\mathrm{i}\tau_y \mathrm{e}^{\mathrm{i}2KL_{\mathrm{zz}}\tau_z} \otimes \sigma_z \mathrm{e}^{\mathrm{i}\theta_{\mathrm{ac}}\sigma_z} \qquad & \text{at right armchair edge}\,.
\end{aligned} \tag{4.73}$$

As discussed in Subsec. 3.2.1 (see Fig. 3.5) the sign of the reflection angles is positive for counter clockwise reflections and negative for clockwise reflections. As an example we show the corresponding factors for an orbit $(1, 1)$ in Fig. 4.7. Stringing together the four terms above, we find for the pseudospin propagator of the $(1, 1)$ family

$$\mathrm{Tr} K_{11} = -4\cos(2KL_{\mathrm{zz}} - 2|\theta_{\mathrm{zz}}|)\,, \tag{4.74}$$

irrespective of the propagation direction of the orbits. We point out that the zigzag reflection angle θ_{zz} occurs in Eq. (4.74) due to the fact that the rectangle has different zigzag edges at the top and the bottom edges (A- and B-terminated, respectively), otherwise the corresponding phases would cancel, as for the armchair reflections. In the same way we obtain the trace also for the general case (N, M), namely (see also Sec.4.3, in particular Eq. (4.99) and its derivation)

$$\mathrm{Tr} K_{NM} = (-1)^N 4\cos(2MKL_{\mathrm{zz}} - 2N|\theta_{\mathrm{zz}}|)\,. \tag{4.75}$$

For rectangular Schrödinger billiards with Dirichlet boundary conditions and side lengths L_1 and L_2, the semiclassical trace formula reads [51, 123]

$$D_{\mathrm{osc}}^{\mathrm{S}}(E) = \frac{L_1 L_2}{\hbar v_{_F}} \sqrt{\frac{2k_{_E}}{\pi^3}} \sum_{N=1}^{\infty} \sum_{M=1}^{\infty} \frac{f_{NM}}{\sqrt{\tilde{L}_{NM}}} \cos\left(k_{_E} \tilde{L}_{NM} - \frac{\pi}{4}\right)\,, \tag{4.76}$$

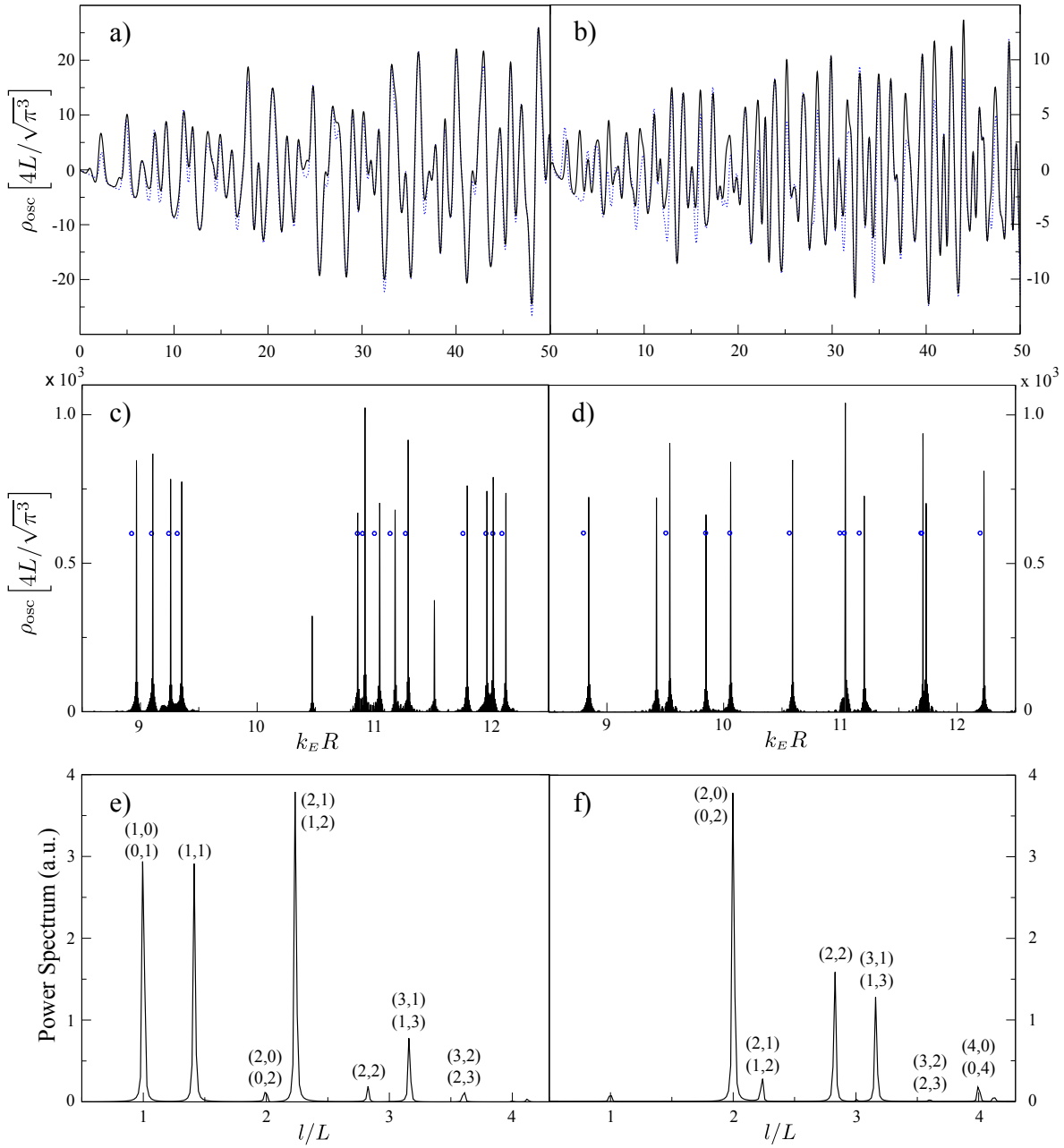

Figure 4.8: Oscillating part of the density of states of square graphene billiards with two armchair edges and two zigzag edges ($L_{\rm zz} = L_{\rm ac} = L$). The left panels (a, c, e) show the results for a square with $KL \mod 2\pi = 2\pi/3$ ('semiconducting') and the right panels (b, d, f) are for a square with $KL \mod 2\pi = 0$ ('metallic'). Panels a) and b) show the Gaussian convoluted $\rho_{\rm osc}(k_E)$ for $\xi = 0.3/L$. The blue dotted curves represent the exact quantum mechanical results calculated with Eq. (4.69) and broadened correspondingly (we consider only real p_{nm} here, i. e. no zigzag edge states). Panels c) and d) show $\rho_{\rm osc}(k_E)$ without broadening ($\xi = 0$). For the latter we take all orbit families with $M, N \leq 400$ in the sum (4.77). Blue circles mark the positions of the exact quantum energy levels obtained from Eq. (4.69). Panel e) and f) show the quantum mechanical power spectra for $\xi = 0.3$. The peaks can be uniquely assigned to classical orbit families (N, M).

with $f_{NM} = 1$ for the bouncing ball orbits, i. e. if $N = 0$ or $M = 0$, and $f_{NM} = 2$ otherwise, and the orbit length $\tilde{L}_{NM} = 2\sqrt{M^2 L_1^2 + N^2 L_2^2}$. The factors f_{NM} again account for the fact that members of the families $(N, 0)$ and $(0, M)$ are their own time reversed partners. Combining Eqs. (4.75) and (4.76) we eventually obtain the semiclassical trace formula for the graphene rectangle with armchair and zigzag edges

$$\begin{aligned} \rho_{\mathrm{osc}}(k_E) &= L_{\mathrm{zz}} L_{\mathrm{ac}} \sqrt{\frac{8k_E}{\pi^3}} \sum_{N=1}^{\infty} \sum_{M=1}^{\infty} \frac{(-1)^N f_{NM}}{\sqrt{\tilde{L}_{NM}}} \cos\left(k_E \tilde{L}_{NM} - \frac{\pi}{4}\right) \\ &\quad \times \cos(2MKL_{\mathrm{zz}} - 2N|\theta_{\mathrm{zz}}|) \mathrm{e}^{-(\xi \tilde{L}_{NM}/2)^2} \,. \end{aligned} \tag{4.77}$$

Also here we have included the exponential damping according to Eq. (4.47).

It is interesting to note that the frequency content of ρ_{osc} depends sensitively on the size of the billiard. As an example we consider a square with $L_{\mathrm{ac}} = L_{\mathrm{zz}} = L$. Since the distance between the two armchair sides can only take discrete values, namely multiples of half of the lattice constant $a/2$ [see e. g. Fig. 2.1 a)], the quantity KL is always a multiple of $2\pi/3$. In particular if $2L/3a \in \mathbb{N}$, one has $KL \bmod 2\pi = 0$. This corresponds to the 'metallic' distances as introduced in Subsec. 2.2.2. In this case the families with odd $N = M$, i. e. $(1, 1)$, $(3, 3)$, and so on do not contribute to the oscillating part of the DOS, because then $|\theta_{\mathrm{zz}}| = \pi/4$ and thus the cosine in Eq. (4.77) vanishes. More generally, in the metallic case orbit families $(N, NL_{\mathrm{ac}}/L_{\mathrm{zz}})$ with odd N do not contribute due to the destructive interference of pseudospins, provided $NL_{\mathrm{ac}}/L_{\mathrm{zz}} \in \mathbb{N}$. We point out that also if the latter ratio is not integer, the families $(N, [NL_{\mathrm{ac}}/L_{\mathrm{zz}}])$ with odd N are suppressed with respect to the semiconducting case. Here the square brackets denote the closest integer. In a sense, this destructive pseudospin interference is eventually a consequence of the short-range singularities at the zigzag edges (see Subsec. 3.2.1), since θ_{zz} in the trace formula originates from these singularities. This means that, in contrast to the smooth part of the DOS, the oscillating part, ρ_{osc}, is affected by the short-range singularities at all energies, not only around $k_E = 0$. Another example for destructive pseudospin interference in the square are the families $(M, 0)$ and $(0, N)$ for odd N and M respectively. They cancel each other exactly for metallic armchair distances.

In Fig. 4.8 we compare the results from the semiclassical trace formula Eq. (4.77) for $L_{\mathrm{ac}} = L_{\mathrm{zz}} = L$ with the quantum result obtained by solving Eq. (4.69) numerically. Again we find very good agreement with quantum mechanics, both for the Gaussian convoluted ρ_{osc} in panels a) and b), and the exact quantum energy levels in c) and d). This is rather remarkable in view of the complicated structure of the quantization condition (4.68). The semiclassical predictions concerning frequency content of the DOS oscillations and peak heights, in particular the absence/presence of whole orbit families, are confirmed in panels e) and f), where we plot the power spectra of the quantum DOS. For example the shortest orbits $(1, 0)$, $(0, 1)$ and $(1, 1)$ do not contribute for the system in f) ($KL \bmod 2\pi = 0$), while they are rather important in e) ($KL \bmod 2\pi = 2\pi/3$). In Table 4.1 we give also the numerical values of several levels.

Note that in Fig. 4.8 c) and d) (and Table 4.1) we find some additional peaks from the semiclassical trace formula, which are not associated with quantum energy levels of the rectangle.

Rather these peaks occur at positions that fulfill the quantization condition of a fictitious 1D quantum well of width L with armchair boundary conditions. It is well-known [51] that this is an effect of subleading order [$(k_E L)^{-1/2}$ with respect to leading order] that is produced by orbits that 'graze' along the edges. Semiclassically these orbits have the same weight as the other bouncing ball orbits. Quantum, mechanically however, the particles have to 'feel' also the boundary that is not hit by the grazing classical orbits.

4.3 Density of states oscillations - spectral statistics of chaotic billiards

The random matrix theory (RMT) for statistical properties of the level density has been shown to accurately describe the spectra, in particular the repulsion of levels, of complex many-particle systems such as heavy atom nuclei [124] as well as neutral and ionized rare earth atoms [125]. For the description of single-particle systems it was initially not clear whether RMT could be a suitable tool. In fact it has been shown that the spectra of regular systems with more than one degree of freedom are uncorrelated [117] (apart from the case of a harmonic oscillator). In 1984, however, Bohigas, Giannoni, and Schmit conjectured that also the single particle energy spectra of classically chaotic systems are universally described by RMT[3] [70]. Many subsequent works suggest the validity of their statement, see e. g. Ref. [118] and references therein.

In this section we investigate the statistical properties of the spectral fluctuations of classically chaotic graphene billiards. To this end we study the spectral two-point correlator

$$R(\eta) = \frac{1}{\bar{\rho}(k_E)} \langle \rho_{\mathrm{osc}}(k_E + \eta/2) \rho_{\mathrm{osc}}(k_E - \eta/2) \rangle_{k_E} \,, \tag{4.78}$$

where $\langle\rangle_{k_E}$ denotes averaging over a small window of the Fermi momentum k_E. Roughly speaking, R measures the average density of level pairs separated by a distance η. To be more precise, we consider the Fourier transform of $R(\eta)$, the spectral form factor

$$F(t) = \int_{-\infty}^{\infty} d\eta \, R(\eta) \mathrm{e}^{\mathrm{i}2\pi\eta t \bar{\rho}(k_E)} \,. \tag{4.79}$$

For $0 < t < 1$, RMT for the Hamiltonian predicts for the spectral form factor [65]

$$F(t) = \begin{cases} 2t - t\ln(1+2t) & \text{for GOE}\,, \\ t & \text{for GUE}\,, \\ \frac{1}{2}t - \frac{1}{4}t\ln(1-t) & \text{for GSE}\,, \end{cases} \tag{4.80}$$

[3] The original formulation from reference [70] is: "Spectra of time-reversal invariant systems whose classical analogs are K systems show the same fluctuation properties as predicted by GOE."

which we expand for small t up to second order as

$$F(t) = \begin{cases} 2t - 2t^2 + \mathcal{O}(t^3) & \text{for GOE}, \\ t & \text{for GUE}, \\ \frac{1}{2}t + \frac{1}{4}t^2 + \mathcal{O}(t^3) & \text{for GSE}. \end{cases} \tag{4.81}$$

Here, GOE, GUE and GSE stand for the Gaussian orthogonal, unitary, and symplectic ensemble respectively, i. e. the appropriate matrix ensembles for the Hamiltonian, according to its symmetry class or (effective) time reversal symmetries, respectively (cf. Sec. 2.2). Since for uncorrelated spectra the form factor is unity $F(t) = 1$, while according to Eq. (4.80), $F(t) < 1$ for the correlated spectra of random matrices, it can be considered as a measure of the correlation strength.

For chaotic quantum systems described by the 2D Schrödinger equation, the properties of classical orbits have been connected to $F(t)$, and the RMT form factor (4.81) has been derived using the original Gutzwiller trace formula [126, 127, 128]. We start from our trace formula for the oscillating part of the graphene DOS, Eq. (4.42), in order to extend the existing theory to the case of chaotic graphene systems. For graphene, the universal predictions of RMT are only reproduced as limiting cases. In general we find that the edge characteristics have significant effects and the statistics follow a mixture of GOE and GUE. The reason is that graphene actually consists of two subsystems, namely the two valleys, that can be coupled to different extent, depending on the edge structure of the graphene billiard.

Following reference [127], we insert the semiclassical trace formula for ρ_{osc} from Eq. (4.42) into the definition of $F(t)$, Eq. (4.79), and obtain the approximate expression

$$F(t) \approx \frac{1}{4T_{\text{H}}} \left\langle \sum_{\gamma,\gamma'} A_\gamma A^*_{\gamma'} Z_{\gamma,\gamma'} \, \mathrm{e}^{\mathrm{i}k_E \delta L_{\gamma,\gamma'}} \, \delta\left(T - \frac{T_\gamma + T_{\gamma'}}{2}\right) \right\rangle_{k_E} . \tag{4.82}$$

We have introduced the time variable $T = t\,T_{\text{H}}$ with the Heisenberg time $T_{\text{H}} = 2\pi\bar{\rho}(k_E)/v_F$, the period of an orbit $T_\gamma = L_\gamma/v_F$, and the length difference $\delta L_{\gamma,\gamma'} = L_\gamma - L_{\gamma'}$. Furthermore we defined the short notation for the product of pseudospin traces

$$Z_{\gamma,\gamma'} = \operatorname{Tr} K_\gamma \operatorname{Tr} K^\dagger_{\gamma'} . \tag{4.83}$$

We show in App. A.6, how the expression (4.82) is changed in the presence of weak bulk disorder. As stated earlier, the number of the periodic orbits of chaotic systems grows exponentially with the orbit length [51], leading also to an exponentially increasing number of orbit pairs that in principle contribute to F. However, when γ and γ' are an arbitrary, uncorrelated pair of orbits, $\exp(\mathrm{i}k_E\delta L_{\gamma,\gamma'})$ is in the semiclassical limit a rapidly oscillating function of k_E. Thus the contributions of most of the orbit pairs in the sum (4.82) vanish after the energy average. Hence, the major contributions to F are due to classes of orbit pairs which have a length difference that is comparable to $1/k_E$ or smaller. This means that the lengths of the orbits have to be classically correlated. The most obvious class of correlated orbit pairs is captured by the so-called diagonal approximation, where only pairs (γ, γ') are

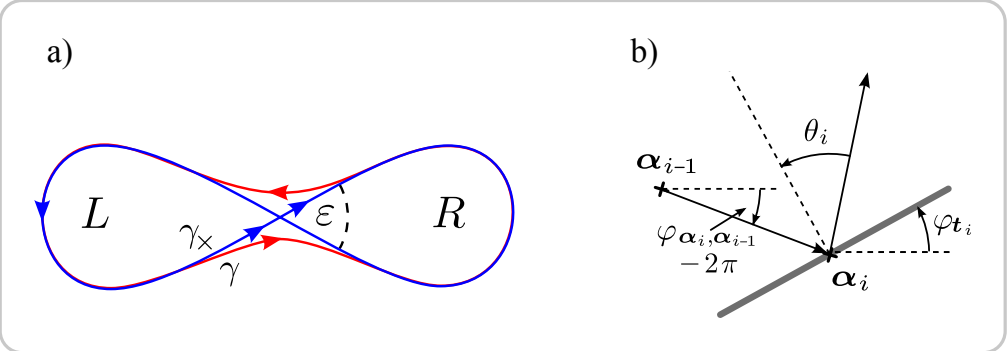

Figure 4.9: a) Scheme of the most important orbit pairs that contribute to the spectral form factor beyond the diagonal approximation. The orbit $\gamma_\times$ intersects itself with an angle ε, while the orbit γ avoids this crossing. Apart from this, the orbits follow each other closely, with the same propagation direction in the L part and the opposite direction in the R part. Note that the real trajectories consist of a series of many straight pieces and classical reflections at the system boundary between them. b) Definition of several angles at a classical reflection.

considered that are identical ($\gamma' = \gamma$) or identical up to the propagation direction ($\gamma' = \gamma^{-1}$). Then the length difference is zero, $\delta L_{\gamma,\gamma'} = 0$. These orbit pairs give rise to the leading order terms ($\sim t$) in the expansion for $F(t)$ [126]. The second order terms ($\sim t^2$) are connected to another class of periodic orbit pairs, which we will refer to as *loop pairs* in the following, cf. Fig. 4.9 a). The two orbits follow each other closely for the most part, but one of them has a self-crossing ($\gamma_\times$) while the other one 'avoids' this crossing (γ). Therefore the propagation directions of γ and $\gamma_\times$ are the same in one part of the orbits (L) and opposite in the other part (R) [127]. We show now that for graphene both diagonal and loop contribution depend on the structure of the edges due to the inter-relation of the boundary conditions and the (effective) TRS of a graphene flake.

First we calculate the trace of K_γ for a given periodic classical orbit γ, taking into account reflections from infinite mass (im), armchair (ac), and zigzag (zz) type edges. Since in the boundary matrices for single reflections, Eq. (3.94), sublattice and valley pseudospin are not entangled, also the total pseudospin propagator can be separated into a valley part and a sublattice part, $K_\gamma = K_\gamma^\tau \otimes K_\gamma^\sigma$. First we consider the valley part K_γ^τ. According to Eq. (3.94), every ac reflection contributes a purely off-diagonal valley spin matrix, and every reflection at a zz or an im edge contributes a purely diagonal valley spin matrix. Since any product with an odd number of off-diagonal and an arbitrary number of diagonal matrices is off-diagonal, it follows that $\mathrm{Tr} K_\gamma^\tau = 0$ if N_{ac}, the total number of ac reflections along the orbit γ, is odd. On the other hand, if N_{ac} is even we can organize the contributions from ac reflections in $N_{\mathrm{ac}}/2$ pairs, where each of them is of the form

$$\tau_y \mathrm{e}^{2\mathrm{i}Kx_i\tau_z} \tau_y \mathrm{e}^{2\mathrm{i}Kx_{i-1}\tau_z} = \mathrm{e}^{2\mathrm{i}K(x_{i-1}-x_i)\tau_z} \,. \tag{4.84}$$

This means that the effect of an even number of ac reflections along γ on K_γ is a phase

(operator), measuring the differences in the x-coordinate of pairs of subsequent ac reflections. Further, each zz reflection contributes a factor $\sim \tau_z \exp(\pm \mathrm{i}\theta_i \tau_z)$, where the sign depends on the sublattice at the edge, and finally im reflections contribute factors $\sim \tau_z$. Altogether, we obtain for the valley pseudospin propagator for an orbit γ with $N_\gamma = N$ reflections in the case of even N_{ac}

$$K_\gamma^\tau = \pm \tau_z^N \mathrm{e}^{\mathrm{i}(2K\Lambda_\gamma + \vartheta_\gamma)\tau_z}\,, \tag{4.85}$$

and thus for its trace

$$\mathrm{Tr} K_\gamma^\tau = \pm \mathrm{i}^N 2\cos(2K\Lambda_\gamma + \vartheta_\gamma - N\pi/2)\,. \tag{4.86}$$

Here we have defined the sum of the corresponding differences in the x-coordinate of subsequent ac reflections

$$\Lambda_\gamma = \sum_{i=1}^{N_{\mathrm{ac}}/2} (x_{2i-1} - x_{2i})\,, \tag{4.87}$$

where the summation is performed only over the subset of ac reflection points. Further we have introduced the sum of zz reflection angles with appropriate signs

$$\vartheta_\gamma = \sum_{i=1}^{N_{\mathrm{zz}}} (-1)^{s_i} \vartheta_i\,, \tag{4.88}$$

where s_i is the number of ac reflections that occur *after* the specific zz reflection i. This is due to the fact that τ_z anticommutes with the off-diagonal matrices from ac reflections. Furthermore, $\vartheta_i = +\theta_i$ for reflections at A-edges and $\vartheta_i = -\theta_i$ for reflections at B-edges. In Eq. (4.88) the sum runs over the subset of zz reflection points. The overall signs in Eqs. (4.85) and (4.86) depend on the exact sequence, i. e. the ordering of zz, ac, and im reflections and the individual signs in Eq. (3.94).

For the sublattice part of the pseudospin propagator K_γ^σ, we first assume that only a single reflection along γ is at a zz edge, without loss of generality the very first one, and afterwards an even number of ac reflections and an arbitrary number of im reflections occur. Then we can cast the sublattice pseudospin propagator into the form

$$K_\gamma^\sigma \;=\; \mathrm{i}^N \sigma_z^{N-1} \mathrm{e}^{\mathrm{i}(\theta_\gamma - \theta_1)\sigma_z} \sigma_{\boldsymbol{t}_1} (1 + \sigma_{\boldsymbol{\alpha}_1, \boldsymbol{\alpha}_N})\,, \tag{4.89}$$

with the sum of all reflection angles along the orbit γ

$$\theta_\gamma = \sum_{i=1}^{N} \theta_i\,, \tag{4.90}$$

and $\boldsymbol{t}_1 = \boldsymbol{t}_{\boldsymbol{\alpha}_1}$. Taking the trace yields

$$\mathrm{Tr} K_\gamma^\sigma = \mathrm{i}^{2N-1} 2\cos\left(\theta_\gamma - \theta_1 + \varphi_{\boldsymbol{\alpha}_1, \boldsymbol{\alpha}_N} - \varphi_{\boldsymbol{t}_1} - [N-1]\pi/2\right)\,. \tag{4.91}$$

We make use of the geometric relation [cf. Fig. 4.9 b)]

$$(\theta_1 - \varphi_{\boldsymbol{\alpha}_1,\boldsymbol{\alpha}_N} + \varphi_{\boldsymbol{t}_1} - \pi/2) \mod 2\pi = 0\,, \tag{4.92}$$

and thus we get

$$\mathrm{Tr}K_\gamma^\sigma = \mathrm{i}^{2N-1} 2\cos\left(\theta_\gamma - N\pi/2\right)\,. \tag{4.93}$$

Similarly we can write for the case of two zz reflections

$$K_\gamma^\sigma = \mathrm{i}^N \sigma_z^{N^{(2)}} \mathrm{e}^{\mathrm{i}\theta_\gamma^{(2)}\sigma_z} \sigma_{\boldsymbol{t}_2} \sigma_z^{N^{(1)}} \mathrm{e}^{\mathrm{i}\theta_\gamma^{(1)}\sigma_z} \sigma_{\boldsymbol{t}_1} (1 + \sigma_{\boldsymbol{\alpha}_1,\boldsymbol{\alpha}_N})\,. \tag{4.94}$$

The meaning of this is the following: The first reflection is at a zz edge as before. Afterwards there is a series of $N^{(1)}$ reflections at ac and im edges with summed reflection angles $\theta_\gamma^{(1)}$. Then we have another zz reflection followed again by a series of $N^{(2)}$ ac and im reflections with total reflection angle $\theta_\gamma^{(2)}$. This leads to

$$\mathrm{Tr}K_\gamma^\sigma = \mathrm{i}^{2N-2} 2\cos\left(\theta_\gamma^{(2)} - \theta_\gamma^{(1)} + \varphi_{\boldsymbol{t}_1} - \varphi_{\boldsymbol{t}_2} + [N^{(1)} - N^{(2)}]\pi/2\right)\,. \tag{4.95}$$

From Fig. 4.9 b) we can read off another geometric relation, namely the angle of rotation at an individual reflection is given by the reflection angle via

$$\varphi_{\boldsymbol{\alpha}_i,\boldsymbol{\alpha}_{i-1}} + \pi\ \mathrm{sign}\,\theta_i - 2\,\theta_i = \varphi_{\boldsymbol{\alpha}_{i+1},\boldsymbol{\alpha}_i}\,. \tag{4.96}$$

Using this together with Eq. (4.92) and the analog relation for the second zz reflection, we find

$$\mathrm{Tr}K_\gamma^\sigma = \mathrm{i}^{2N-2} 2\cos\left(\theta_\gamma - N\pi/2\right)\,, \tag{4.97}$$

which is up to phase factors equal to the result for one zz reflection. The treatment of these two special cases can be combined to find the sublattice pseudospin trace for an arbitrary number of zz reflections

$$\mathrm{Tr}K_\gamma^\sigma = \mathrm{i}^{2N-N_{\mathrm{zz}}} 2\cos\left(\theta_\gamma - N\pi/2\right)\,. \tag{4.98}$$

Collecting all phase factors that occur in Eqs. (4.86) and (4.98) in p_γ, we finally obtain for the trace of the pseudospin propagator of an orbit γ with an even number of ac reflections N_{ac}

$$\mathrm{Tr}K_\gamma = 4p_\gamma \cos(2K\Lambda_\gamma + \vartheta_\gamma - N\pi/2)\cos(\theta_\gamma - N\pi/2)\,. \tag{4.99}$$

This results holds also for $N_{\mathrm{ac}} = 0$; then we identify $\Lambda_\gamma = 0$. We note that the trace of the time reversed orbit γ^{-1}, which differs from γ only in that the propagation direction is reversed, is the same as for the original orbit γ.

4.3.1 Diagonal contribution

First we focus on the leading order contributions to $F(t)$ that are connected to the diagonal orbit pairs in the double sum (4.82). We thus calculate the product of traces for $\gamma' = \gamma$, namely from Eq. (4.99) we get

$$Z_\gamma = Z_{\gamma,\gamma} = Z_{\gamma,\gamma^{-1}} = |\mathrm{Tr}K_\gamma|^2 = 16\cos^2(2K\Lambda_\gamma + \vartheta_\gamma - N\pi/2)\cos^2(\theta_\gamma - N\pi/2)\,, \tag{4.100}$$

if N_{ac} is even, and $Z_\gamma = 0$ for odd N_{ac}. To simplify this further, we note that for a periodic classical orbit γ, the total rotation angle is given by the integer winding number, defined as

$$w_\gamma = \frac{1}{2\pi}\sum_{i=1}^{N}(\pi\ \mathrm{sgn}\,\theta_i - 2\,\theta_i) \in \mathbb{Z}\,. \tag{4.101}$$

Introducing the numbers of reflections with positive and negative angles of reflection, respectively,

$$N_\pm = \frac{1}{2}\left(N \pm \sum_{i=1}^{N}\mathrm{sgn}\,\theta_i\right)\,, \tag{4.102}$$

we get for the total reflection angle

$$\theta_\gamma = (N_+ - N_-)\frac{\pi}{2} - w_\gamma\pi\,. \tag{4.103}$$

This leads to

$$\cos^2(\theta_\gamma - N\pi/2) = \cos^2[(N_- + w_\gamma)\pi] = 1\,, \tag{4.104}$$

and thus we finally get for the pseudospin contribution of a diagonal orbit pair to the spectral form factor

$$Z_\gamma = \begin{cases} 16\cos^2\left(2K\Lambda_\gamma + \vartheta_\gamma - N\pi/2\right) & \text{for even } N_{\mathrm{ac}}\,, \\ 0 & \text{for odd } N_{\mathrm{ac}}\,. \end{cases} \tag{4.105}$$

In order to perform the orbit sum in Eq. (4.82), we need to average Z_γ accordingly. To this end we make use of the fact that classically chaotic billiards exhibit ergodic dynamics, i. e. we assume that a long orbit hits any boundary point with the same probability. Therefore we average Z_γ for orbits of a given length over the possible edge types or boundary conditions, respectively. Then the diagonal contribution to the spectral form factor reads

$$F_D(t) \approx \frac{1}{2T_{\mathrm{H}}}\sum_\gamma \langle Z_\gamma\rangle |A_\gamma|^2 \delta\left(T - T_\gamma\right)\,, \tag{4.106}$$

where an additional factor of two accounts for the contribution of the orbit pairs (γ, γ^{-1}). To evaluate the average of Z_γ, we consider three different situations. First we study the limiting cases of zero and very strong valley coupling, respectively. Afterwards we turn to the generic case of intermediate coupling.

No ac scattering - valley conservation

To put the foundation for systems with general boundaries that we treat below, we first consider the simpler case of billiards whose boundaries consist only of a combination of zz and im type edges, i. e. $N_{\mathrm{ac}} = 0$ for all orbits γ, so that there is no valley coupling at all.

If $N_{\rm ac} = 0$, also Λ_γ vanishes and ϑ_γ is either zero (if no zz edges are present) or randomly distributed between zero and 2π. In the latter case the averaging yields

$$\langle Z_\gamma \rangle = 16 \langle \cos^2 (\vartheta_\gamma - N\pi/2) \rangle = 8 \,. \tag{4.107}$$

On the other hand, for $\vartheta_\gamma = 0$ we get $Z_\gamma = 0$ for odd N and $Z_\gamma = 16$ for even N, leading to $\langle Z_\gamma \rangle = 8$ as well. Thus, in the absence of intervalley coupling we can pull $\langle Z_\gamma \rangle$ out of the sum in Eq. (4.106), which then reduces to

$$F_D(t) \approx \frac{4}{T_{\rm H}} \sum_\gamma |A_\gamma|^2 \delta \left(T - T_\gamma \right) \,. \tag{4.108}$$

Now $F_D(t)$ can be evaluated as for the Schrödinger equation. The Hannay-Ozorio de Almeida sum rule [129] replaces the sum over classical orbits of a chaotic system by an integral over orbit periods with an appropriate density. Considering two-dimensional chaotic systems with uniformly hyperbolic dynamics, i. e. systems where the classical dynamics is described by one positive Lyapunov exponent λ, the density of long classical orbits with period T_γ is increasing exponentially

$$D(T_\gamma) = \frac{{\rm e}^{\lambda T_\gamma}}{T_\gamma} \,. \tag{4.109}$$

On the other hand, the stability of the orbits decays exponentially

$$|A_\gamma|^2 \approx T_\gamma^2 {\rm e}^{-\lambda T_\gamma} \,, \tag{4.110}$$

so that the resulting integral yields

$$F_D(t) \approx \frac{4}{T_{\rm H}} \int_0^\infty dT' D(T') |A(T')|^2 \, \delta \left(T - T' \right) = \frac{4T}{T_{\rm H}} = 4t \,. \tag{4.111}$$

According to Eq. (4.81), this result can be interpreted as four times the GUE prediction for the linear term of $F(t)$. To understand this we recall the antiunitary symmetries of the problem. Since there is no intervalley scattering, RMT has to be applied to both decoupled subsystems separately. The physical TRS, $\mathcal{T}_y$, would lead to the orthogonal symmetry class. However, due to the lack of intervalley coupling and because $\mathcal{T}_y$ connects states from different valleys, it is basically irrelevant. The effective intravalley TRS, $\mathcal{T}_0$, which would drive the system into the symplectic symmetry class, is broken by both zigzag and infinite mass type edges, as we have discussed in Subsec. 2.2.2. This means that there is no TRS within the individual subsystems, and thus GUE is the correct ensemble. However, due to the remaining symmetry $\mathcal{T}_x$, both subsystems are Kramers degenerate partners, so that the DOS is given by $\rho = 2\rho_1$, where ρ_1 is the DOS of one subsystem. Then Eqs. (4.78) and (4.79) yield $F(t) = 2F_1(2t)$, with the form factor of one individual subsystem F_1, leading to $F_D(t) = 4t$. Below we find that the loop contribution supports this argumentation, and excludes an interpretation of the result as 2×GOE or 8×GSE, since F_L vanishes for the unitary class but is finite for the other cases.

Ac billiards - complete valley mixing

Next we focus on the opposite situation, i. e. when the ac part of the boundary is large enough that the valleys are completely mixed. Hence we consider the limiting case where all reflections happen at ac edges, so that $\vartheta_\gamma = 0$ for all orbits, and $N = N_{\mathrm{ac}}$. Then Eq. (4.105) leads to

$$\langle Z_\gamma \rangle = \frac{1}{2}\left(16\langle\cos^2(2K\Lambda_\gamma)\rangle + 0\right) = 8\langle\cos^2(2K\Lambda_\gamma)\rangle\,. \tag{4.112}$$

As discussed earlier already, the argument of the cosine cannot take arbitrary values, since it originates from the microscopic ac lattice terminations. Since the difference in the x-coordinates of two subsequent armchair reflection points can only be a multiple of $a/2$, the quantity $K\Lambda_\gamma$ for even N is always a multiple of $2\pi/3$, and

$$2K\Lambda_\gamma = \frac{4\pi}{3}m\,, \quad m \in \mathbb{Z}\,. \tag{4.113}$$

For generic systems, every m occurs with the same probability, so that

$$\langle\cos^2(2K\Lambda_\gamma)\rangle = \lim_{M\to\infty}\sum_{m=1}^{M}\frac{\cos^2(m\,4\pi/3)}{M} = \frac{1}{3}\left[\cos^2\left(\frac{\pi}{3}\right) + \cos^2\left(\frac{2\pi}{3}\right) + \cos^2(0)\right] = \frac{1}{2}\,, \tag{4.114}$$

as for averaging over the continuous interval $[0, 2\pi]$. It follows that $\langle Z_\gamma\rangle = 4$ and the orbit summation is performed exactly as for decoupled valleys, resulting in

$$F_D(t) = 2t\,. \tag{4.115}$$

In terms of RMT, there is no valley substructure left due to the complete mixing. Additionally, the valley coupling has re-enabled the TRS $\mathcal{T}_y$, in the sense that it provides a mechanism to connect time reversed partner states. Therefore the semiclassical theory yields the RMT prediction for one single GOE.

Before we go ahead and focus on the more complicated generic situation of mixed boundaries, we first consider the peculiar case that all ac edges of the system have 'metallic distances', i. e. for every i in the sum (4.87) we have

$$\frac{2}{3a}(x_{2i-1} - x_{2i}) \in \mathbb{Z}\,. \tag{4.116}$$

Then Eq. (4.113) reads

$$2K\Lambda_\gamma = 4\pi m'\,, \quad m' \in \mathbb{Z}\,. \tag{4.117}$$

In this case the cosine in Eq. (4.112) is equal to one, leading to $\langle Z_\gamma\rangle = 8$, and therefore $F_D(t) = 4t$, as for systems without any armchair scattering. This is very surprising at first glance, since indeed every ac edge couples the valleys K and K′, irrespective of the distances between different ac edges [cf. Eq. (3.94)]. The reason for the effective TRS breaking in this case is the 'pseudovalley' structure associated with $\mathcal{T}_0$ that we have discussed in Subsec. 2.2.2. Since we have assumed that all the distances are metallic, Eq. (4.116), the boundary matrices

can always be chosen to contain only τ_y but not τ_x. Then the symmetry $\mathcal{T}_0$ is preserved, giving rise to a substructure very similar to the original valleys. In fact the 'pseudovalleys' are rotated versions of the original valleys. Since there is no TRS within each individual pseudovalley, and $\mathcal{T}_y$ again connects states from different pseudovalleys, the effective symmetry class is GUE also here. While in connection with chaotic billiards this is rather an academic case, since there is no real chaotic graphene cavity that would fulfill the condition (4.116) for all i, we will see in Chap. 7 that the pseudovalley substructure is responsible for very interesting quantum transport properties of disordered armchair nanoribbons.

Mixed boundaries - generic case

In a realistic situation the boundary consists of both, edge segments that conserve the valleys, and such that lead to intervalley scattering. Therefore we generalize our discussion to the general case of a boundary that is built from ac, zz, and im type edges. In view of averaging Z_γ, we consider classical orbits that hit ac edges and those that do not hit ac edges separately. For the latter case, i. e. if only reflections from zz and im edges are involved, we have already found $\langle Z_\gamma \rangle = 8$, see Eq. (4.107). On the other hand if ac reflections and an arbitrary number of zz and im reflections occur, the result is the same as for the pure ac case, because the additional ϑ_γ does not alter the the result of the averaging (4.114). This means we have $\langle Z_\gamma \rangle = 8$ for even $N_{\rm ac}$ and $\langle Z_\gamma \rangle = 0$ for odd $N_{\rm ac}$, i. e. in general

$$\langle Z_\gamma \rangle = 8 P^{\rm e}_{\rm ac}(T_\gamma)\,, \tag{4.118}$$

where $P^{\rm e}_{\rm ac}(T_\gamma)$ is the probability that a classical orbit with period T_γ undergoes an even number of reflections at armchair edges (including the possibility of zero ac reflections). To express this probability directly in terms of the properties of the system, we consider the relevant time scales of the problem. The first one is the *Heisenberg time*, that we have already introduced below Eq. (4.82) as a unit for the time variable t. It is basically given by the inverse mean level spacing or the mean DOS, respectively, namely

$$T_{\rm H} = 2\pi\hbar\,\bar{D}(E) = \frac{2\pi}{v_{_F}}\bar{\rho}(k_{_E})\,. \tag{4.119}$$

In view of the Heisenberg uncertainty principle, $\Delta E \Delta t \sim \hbar$, $T_{\rm H}$ is the 'observation time' needed to resolve the energy spectrum down to one level spacing. The second time scale is the typical time between two reflections at armchair edges, $T_{\rm ac}$, which depends on the relative amount of armchair edges at the boundary. Assuming that individual reflections are independent of each other and uniformingly distributed on the boundary, the probability that an orbit has hit ac edges exactly n times after N reflections is given by the binomial distribution

$$p_n(N) = \binom{N}{n}\left(\frac{W_{\rm ac}}{|\partial V|}\right)^n\left[1-\frac{W_{\rm ac}}{|\partial V|}\right]^{N-n}\,, \tag{4.120}$$

with the total length of ac edges of the billiard, $W_{\rm ac} = |\partial\mathcal{V}_{\rm ac}|$. To get the probability to hit ac edges an even (odd) number of times we sum over all even (odd) n and, using the binomial

identity, obtain

$$\begin{aligned} P_{\rm ac}^{\rm e/o}(N) &= \sum_{\substack{n=0 \\ \text{even/odd}}}^{\infty} p_n(N) = \frac{1}{2}\sum_{n=0}^{\infty}\binom{N}{n}\left[\left(\frac{W_{\rm ac}}{|\partial V|}\right)^n \pm \left(-\frac{W_{\rm ac}}{|\partial V|}\right)^n\right]\left[1-\frac{W_{\rm ac}}{|\partial V|}\right]^{N-n} \\ &= \frac{1}{2}1^N \pm \frac{1}{2}\left(1-\frac{2W_{\rm ac}}{|\partial V|}\right)^N = \frac{1}{2}\left[1 \pm \left(1-\frac{2W_{\rm ac}}{|\partial V|}\right)^N\right], \end{aligned} \tag{4.121}$$

where the upper sign holds for the even case and the lower for the odd case. The number of reflections N is connected to the period T of an orbit by the average time between two reflections, $T_{\rm of}$ ('time of flight'). For chaotic billiards we have [130]

$$T_{\rm of} = \frac{T}{N} = \frac{\pi|\mathcal{V}|}{v_F|\partial\mathcal{V}|}\,. \tag{4.122}$$

Inserting this into Eq. (4.121) and assuming $W_{\rm ac} < |\partial\mathcal{V}|/2$, we get for the probability to hit ac edges an even (odd) number of times after a time T

$$P_{\rm ac}^{\rm e/o}(T) = \frac{1}{2}\left(1 \pm {\rm e}^{-2T/T_{\rm ac}}\right), \tag{4.123}$$

with

$$T_{\rm ac}^{-1} = -\frac{v_F|\partial\mathcal{V}|}{2\pi|\mathcal{V}|}\ln\left(1-\frac{2W_{\rm ac}}{|\partial\mathcal{V}|}\right). \tag{4.124}$$

If the total ac length is small compared to the boundary length, $T_{\rm ac}^{-1}$ can be identified as escape rate into a fictitious lead of width $W_{\rm ac}$ (see Ref. [131] and references therein)

$$T_{\rm ac}^{-1} = \frac{v_F W_{\rm ac}}{\pi|\mathcal{V}|} + \mathcal{O}\left(\frac{W_{\rm ac}^2}{|\partial\mathcal{V}|^2}\right) \tag{4.125}$$

In the limiting cases of very small and very large ratios $T/T_{\rm ac}$, $P_{\rm ac}^{\rm e}$ becomes 1 (no reflection at ac edges) and 1/2 (equal chance of even and odd number of ac reflections) and Eq. (4.118) reproduces the previous results $\langle Z_\gamma\rangle = 8$ and $\langle Z_\gamma\rangle = 4$, respectively. For the general case, the diagonal contribution to the form factor is obtained as in (4.111)

$$\begin{aligned} F_D(t) &\approx \frac{4}{T_{\rm H}}\int_0^\infty dT' D(T') P_{\rm ac}^{\rm e}(T)(T')|A(T')|^2\,\delta\left(T-T'\right) \\ &= \frac{2T}{T_{\rm H}}\left(1+{\rm e}^{-2\,T/T_{\rm ac}}\right) = 2t\left(1+{\rm e}^{-2t\,T_{\rm H}/T_{\rm ac}}\right). \end{aligned} \tag{4.126}$$

This formula describes the crossover between the two limiting cases of completely decoupled and totally mixed valleys, respectively. For the asymptotic limits $T_{\rm H}/T_{\rm ac} \to 0$ and $T_{\rm H}/T_{\rm ac} \to \infty$ we recover Eqs. (4.111) and (4.115), respectively. A big advantage of Eq. (4.126) is that the crossover parameter does not have to be introduced phenomenologically, but can be directly related to the microscopic properties of the system, namely the total length of

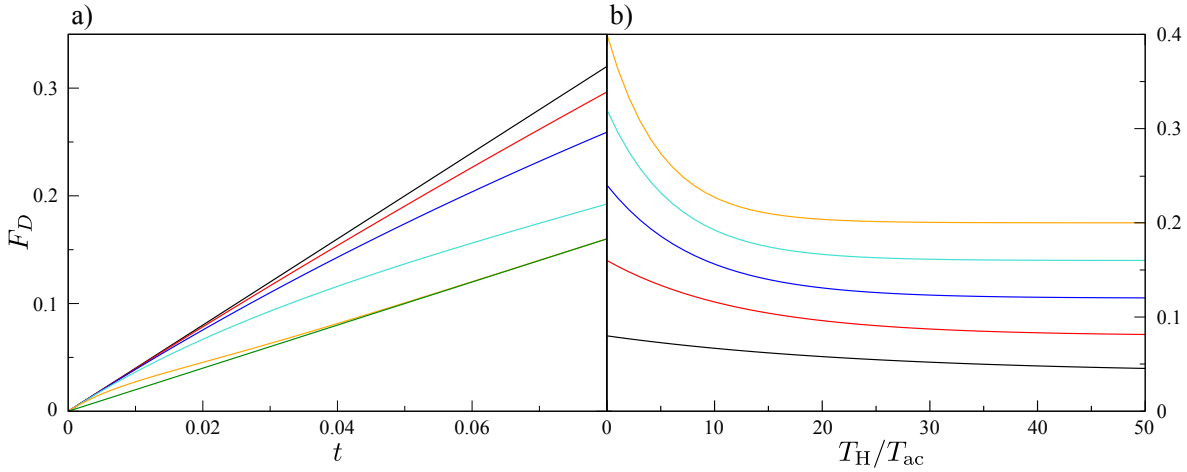

Figure 4.10: a) Diagonal contribution to the spectral form factor, F_D, as a function of $t = T/T_H$ for a generic graphene cavity for different values of the intervalley scattering strength, cf. Eq. (4.126). From top to bottom: $T_H/T_{ac} = 0$ (black), 1 (red), 3 (blue), 10 (turquoise), 50 (orange) and ∞ (green). While in the limiting cases of $T_H/T_{ac} \to 0$ and $T_H/T_{ac} \to \infty$ the t-dependence of F_D is purely linear, this is not the case in general. Even for large values of T_H/T_{ac}, F_D shows signatures of unitary correlations at small t. This becomes even more clear in the rescaled plot Fig. 4.11 a). b) F_D as a function of T_H/T_{ac} at (from bottom to top) $t = 0.02$ (black), 0.04 (red), 0.06 (blue), 0.08 (turquoise) and 0.1 (orange). The curves describe an exponential crossover from four times the GUE to the GOE result.

intervalley scattering ac boundary W_{ac}, see Eq. (4.124). For small $W_{ac}/|\partial\mathcal{V}|$ the ratio of the relevant time scales that occurs in Eq. (4.126) is directly proportional to the total length of ac boundary:

$$\frac{T_H}{T_{ac}} = -\frac{k_E}{\pi}|\partial\mathcal{V}| \ln\left(1 - \frac{2W_{ac}}{|\partial\mathcal{V}|}\right) = 2k_E W_{ac}/\pi + \mathcal{O}\left(\frac{W_{ac}^2}{|\partial\mathcal{V}|^2}\right), \tag{4.127}$$

in other words, T_H/T_{ac} is proportional to the number of channels associated with the fictitious ac lead of width W_{ac}.

Figure 4.10 a) shows $F_D(t)$ for small $t = T/T_H$ and the parametric crossover between the limiting RMT symmetry classes, namely GOE [lowest line, Eq. (4.115)] and 4×GUE [uppermost line, Eq. (4.111)]. In the general case of finite T_H/T_{ac}, F_D is not purely linear as in both limiting cases. Note that even for a considerable amount of ac scattering (consider e. g. the (turquoise) curve for $T_H/T_{ac} = 10$) we still find rather strong deviations from the GOE statistics. In Fig. 4.10 b) the crossover is represented as a function of T_H/T_{ac}. In Fig. 4.11 a) we plot $F_D(t)$ rescaled by t, to make the deviation from the linear t-dependence more clear.

Further we point out that the crossover from 4×GUE to GOE is rather particular: Usually transitions between GUE and GOE result from a symmetry *breaking* mechanism, e. g. due to a magnetic field. Here the armchair edges and the resulting intervalley scattering act as a symmetry *restoring* mechanism. Moreover, the correlations in the unitary limit are *weaker* than in the orthogonal case, in contrast to the usual GOE-GUE transition.

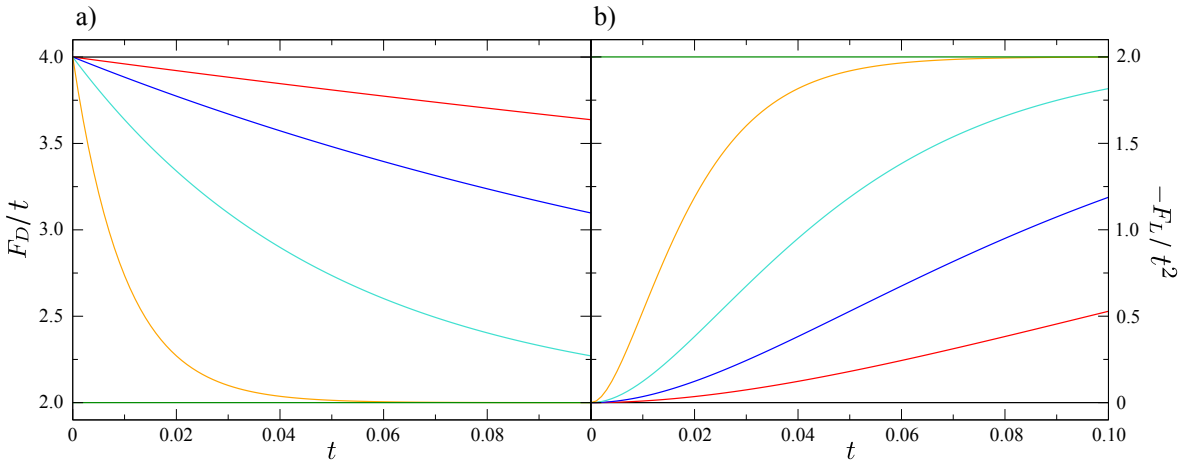

Figure 4.11: a) Rescaled diagonal contribution to the spectral form factor, $F_D(t)/t$, for different values of the intervalley scattering strength, cf. Eq. (4.126). From top to bottom: $T_{\rm H}/T_{\rm ac} = 0$ (black), 1 (red), 3 (blue), 10 (turquoise), 50 (orange) and ∞ (green). b) Rescaled loop contribution to the spectral form factor, $-F_L(t)/t^2$, for different values of the intervalley scattering strength, cf. Eq. (4.155). From bottom to top: $T_{\rm H}/T_{\rm ac} = 0$ (black), 5 (red), 10 (blue), 20 (turquoise), 50 (orange) and ∞ (green).

4.3.2 Loop contribution

After Berry had obtained the linear terms in the form factor for Schrödinger systems from the diagonal orbit pairs in 1985 [126], it remained unclear for quite some time, what kind of correlated classical orbits give rise to the higher order terms in Eq. (4.81). Only more than fifteen years later, Sieber and Richter found that the loop pairs, sketched in Fig. 4.9 a), are responsible for the quadratic terms [127]. Subsequently it has also been achieved to account for terms of cubic [132] and even arbitrary order [133], by considering more than one or more complex (avoided) self-crossings.

We continue our discussion now with the loop contribution to the spectral form factor of graphene billiards. As depicted in Fig. 4.9 a) we separate the orbits into the left part L, where the propagation directions are parallel, and the right part R, where they are antiparallel. All quantities will be labeled correspondingly by L and R. Outside of the crossing region (encounter), the two trajectories are exponentially close to each other, hence we can assume that the sequences of reflections along γ and $\gamma_\times$ are exactly equal in the L-part while they are equal but with opposite order in the R-part. Orbit pairs which differ in their number of reflections do not contribute in the semiclassical limit.

We begin with the calculation of the pseudospin trace $Z_{\gamma,\gamma_\times}$. From the discussion of F_D, we know already that $\mathrm{Tr}K_\gamma = \mathrm{Tr}K_{\gamma_\times} = 0$, if the total number of armchair reflections is odd, so we can concentrate on the opposite case of even (or zero) $N_{\rm ac}$. Then Eq. (4.99) gives

$$\begin{aligned} Z_{\gamma,\gamma_\times} &= 16\cos(2K\Lambda_\gamma + \vartheta_\gamma - N\pi/2)\cos(2K\Lambda_{\gamma_\times} + \vartheta_{\gamma_\times} - N\pi/2) \\ &\quad \times \cos(\theta_\gamma - N\pi/2)\cos(\theta_{\gamma_\times} - N\pi/2)\,. \end{aligned} \tag{4.128}$$

For the total reflection angles we have

$$\theta_\gamma = \theta_L + \theta_R\,, \quad \theta_{\gamma_\times} = \theta_L - \theta_R\,. \tag{4.129}$$

Furthermore, making use of the expression for the pieces L and R analog to Eq. (4.103)

$$\theta_L \mod \pi = (N_{+,L} - N_{-,L} + 1)\frac{\pi}{2} \mod \pi + \mathcal{O}(\varepsilon)\,, \tag{4.130}$$

$$\theta_R \mod \pi = (N_{+,R} - N_{-,R} - 1)\frac{\pi}{2} \mod \pi + \mathcal{O}(\varepsilon)\,, \tag{4.131}$$

we get for the last two factors in (4.128)

$$\cos(\theta_\gamma - N\pi/2)\cos(\theta_{\gamma_\times} - N\pi/2) = (-1)^{N_R+1} + \mathcal{O}(\varepsilon^2)\,. \tag{4.132}$$

With this we obtain for orbit pairs $(\gamma, \gamma_\times)$ with an even number of ac reflections

$$Z_{\gamma,\gamma_\times} \approx (-1)^{N_R+1} 16 \cos\left(2K\Lambda_\gamma + \vartheta_\gamma - N\pi/2\right) \cos\left(2K\Lambda_{\gamma_\times} + \vartheta_{\gamma_\times} - N\pi/2\right)\,, \tag{4.133}$$

where we have neglected terms of higher order in ε, because the loop contribution to the orbit sum (4.82) is dominated by pairs with very small crossing angles, since the length difference $\delta L_{\gamma,\gamma_\times}$ scales quadratically with ε [127].

No ac scattering - valley conservation

As for the diagonal contribution, we consider the case of decoupled valleys first, i. e. no intervalley scattering ac edges. Then, with

$$\vartheta_\gamma = \vartheta_L + \vartheta_R\,, \quad \vartheta_{\gamma_\times} = \vartheta_L - \vartheta_R\,, \tag{4.134}$$

equation (4.133) reads

$$Z_{\gamma,\gamma_\times} = (-1)^{N_R+1} 16 \left[\cos^2\left(\vartheta_L - N\pi/2\right)\cos^2\left(\vartheta_R\right) - \sin^2\left(\vartheta_L - N\pi/2\right)\sin^2\left(\vartheta_R\right)\right]\,. \tag{4.135}$$

If zz edges are involved, the angles ϑ_L and ϑ_R are independent of each other and have to be be averaged separately. Since the sines and cosines all average to 1/2, the total average is zero in this case, $\langle Z_{\gamma,\gamma_\times}\rangle = 0$. On the other hand, if no zz reflections occur either, but only im edges are involved, $\vartheta_L = \vartheta_R = 0$, and thus $Z_{\gamma,\gamma_\times}$ is identically zero for odd N. For even N we have $Z_{\gamma,\gamma_\times} = (-1)^{N_L+1}$, which averages to zero as well, because for long orbits the probability for even N_L is the same as for odd N_L. That means

$$\langle Z_{\gamma,\gamma_\times}\rangle = 0 \tag{4.136}$$

holds if there is no valley coupling, and hence it follows that there is *no loop contribution* to the spectral form factor in this case, i. e.

$$F_L(t) = 0\,, \tag{4.137}$$

in agreement with the RMT prediction (4.81) for the unitary symmetry class. This supports our interpretation of the diagonal contribution F_D as 4×GUE, since all other symmetry classes would have led to a finite loop contribution.

Ac billiards - complete valley mixing

According to the discussion of F_D, the loop contribution to the form factor should be $F_D(t) = -2t^2$, corresponding to the orthogonal symmetry class, if only ac edges are present and the valleys are completely mixed. An exception is again the special case when the ac edges have exclusively metallic distances, so that $K\Lambda_\gamma$ and $K\Lambda_{\gamma_\times}$ are multiples of 2π [cf. Eq. (4.117)]. This means we have the same situation as for decoupled valleys with $\vartheta_L = \vartheta_R = 0$ and therefore obtain $F_L(t) = 0$ also here, as expected. We focus on the generic case of arbitrary distances now.

As we have seen before, the total number of (ac) reflections has to be even to obtain non-vanishing pseudospin traces. In this case, Eq. (4.133) reads

$$Z_{\gamma,\gamma_\times} \approx (-1)^{N_R+1} 16 \cos\left(2K\Lambda_\gamma\right) \cos\left(2K\Lambda_{\gamma_\times}\right) . \tag{4.138}$$

Since we assume even $N_{\mathrm{ac}} = N = N_R + N_L$, the contributing orbits either have an even number of reflections in both parts, L and R, or they have an odd number of reflections in both parts. For the former case of even N_L and N_R, Λ_L and Λ_R are well defined by restricting the sum (4.87) to the corresponding subset of reflections. Then we have

$$\Lambda_\gamma = \Lambda_L + \Lambda_R \,, \quad \Lambda_{\gamma_\times} = \Lambda_L - \Lambda_R \,, \tag{4.139}$$

and therefore

$$Z_{\gamma,\gamma_\times} \approx -16 \cos^2\left(2K\Lambda_L\right) \cos^2\left(2K\Lambda_R\right) + 16 \sin^2\left(2K\Lambda_L\right) \sin^2\left(2K\Lambda_R\right) . \tag{4.140}$$

However, this is zero on average, because Λ_L and Λ_R are averaged independently, so that each of the sines and cosines averages to $1/2$ individually. On the other hand, for N_L and N_R both odd, it is straightforward to show that

$$\cos(2K\Lambda_{\gamma_\times}) = \cos(2K\Lambda_\gamma) \,, \tag{4.141}$$

and therefore

$$Z_{\gamma,\gamma_\times} = 16 \cos^2(2K\Lambda_\gamma) \,. \tag{4.142}$$

For the overall average we get finally for systems with exclusively ac edges (with arbitrary distances)

$$\langle Z_{\gamma,\gamma_\times} \rangle = 2 \,, \tag{4.143}$$

where we have used that for long periods, one quarter of the orbits has N_L and N_R both odd. This means that the graphene specific pseudospin trace enters merely with an overall prefactor of two. Hence we can in this case adapt the evaluation of the loop contribution to the semiclassical form factor in Ref. [127]. The length difference of $\delta L_{\gamma,\gamma_\times}$ scales quadratically with the crossing angle ε [127]

$$\delta L_{\gamma,\gamma_\times} = \delta L(\varepsilon) = \frac{v_F}{2\lambda} \varepsilon^2 \,. \tag{4.144}$$

The entire form factor contribution of the pairs $(\gamma, \gamma_\times)$ is obtained by summing over all γ and for each γ counting the number of self encounters, i. e. self-intersections with a small crossing angle ε. We implicitly assume here that for every self-intersection there is actually a partner orbit with a corresponding avoided self-crossing. The existence of these pairs in classically chaotic systems has been demonstrated in Ref. [127]. As before, we write the sum over γ as an integral with a density $D(T)$. Assuming that the classical properties that are contained in A_γ, i. e. stability and the Maslov indices, are equal for both orbits, we get

$$F_L(t) \approx \frac{2}{T_\mathrm{H}} \mathfrak{Re} \int_0^\pi d\varepsilon \, \mathrm{e}^{\mathrm{i}k_E \delta L(\varepsilon)} D(T) |A(T)|^2 P_F(\varepsilon, T) \,, \tag{4.145}$$

where we have included again a factor of two to account for time reversed orbits γ^{-1} and another factor of two from the averaged pseudospin trace (4.143). Further, we evaluate twice the real part of the expression, because for every pair $(\gamma, \gamma_\times)$, the orbit double sum contains also its complex conjugate due to the opposite pairing $(\gamma_\times, \gamma)$. In Eq. (4.145), $P_F(\varepsilon, T)$ is the density of self-crossings of an orbit with period T, given by the integral over the period of the part R [127]

$$P_F(\varepsilon, T_\gamma) \approx \frac{v_F^2 \, \varepsilon}{\pi |\mathcal{V}|} \int_{T_{\min}(\varepsilon)}^{T_\gamma - T_{\min}(\varepsilon)} dT_R \, (T_\gamma - T_R) = \frac{v_F^2 \, \varepsilon}{\pi |\mathcal{V}|} T \left[\frac{T}{2} - T_{\min}(\varepsilon) \right] . \tag{4.146}$$

The lower integration limit, $T_{\min}(\varepsilon)$, is the minimal time to form a closed loop, which depends logarithmically on the crossing angle

$$T_{\min}(\varepsilon) = -\frac{2}{\lambda} \ln(c \, \varepsilon) \,, \tag{4.147}$$

with the Lyapunov exponent λ and a constant of order unity c [127]. Since the second loop, L, also has the same minimal period, the upper limit of the integral must be $T_\gamma - T_{\min}$. For given T_R, the probability for a crossing is proportional to the period of the remaining trajectory, $T_\gamma - T_R$. The inclusion of the minimum time is crucial to obtain the correct value for F_L, since the $T_{\min}$-independent term in (4.146) does not contribute to the real part of the integral in (4.145). The second term in (4.146) however gives a contribution, namely with [127]

$$\mathfrak{Re} \int_0^\pi d\varepsilon \, \mathrm{e}^{\mathrm{i}k_E \delta L(\varepsilon)} \varepsilon \, T_{\min}(\varepsilon) \approx \frac{\pi}{2 v_F k_E} \,, \tag{4.148}$$

and using Eqs. (4.119), (4.145), and (4.146), we get

$$F_L(t) \approx -\frac{2}{T_\mathrm{H}} T^2 \frac{v_F}{2 k_E |\mathcal{V}|} = -2t^2 \,, \tag{4.149}$$

in agreement with the RMT prediction for the GOE, cf. Eq. (4.81).

Mixed boundaries - generic case

We now consider the general case, where all three types of edges - ac, zz, and im - are present. From the previous discussion we know that the contribution to F_L is exclusively due to such classical orbits γ and $\gamma_\times$, that undergo odd numbers of ac reflections along both, the L ($N_{\mathrm{ac},L}$) and the R ($N_{\mathrm{ac},L}$) part of γ. This holds true also in the presence of reflections from zz and im type edges. In fact for these orbits we have [cf. also Eq. (4.141)]

$$\cos(2K\Lambda_{\gamma_\times} + \vartheta_{\gamma_\times} - N\pi/2) = (-1)^{N_R - N_{R,\mathrm{ac}}} \cos(2K\Lambda_\gamma + \vartheta_\gamma - N\pi/2)\,, \tag{4.150}$$

which inserted into Eq. (4.133) gives

$$\langle Z_{\gamma,\gamma_\times}\rangle \;=\; 16\langle\cos^2(2K\Lambda_\gamma + \vartheta_\gamma - N\pi/2)\rangle = 8\,, \tag{4.151}$$

while $\langle Z_{\gamma,\gamma_\times}\rangle = 0$ for all other orbits. In order to compute F_L we write therefore, analog to Eq. (4.145),

$$F_L(t) \approx 8t\,\mathfrak{Re}\int_0^\pi d\varepsilon\, \mathrm{e}^{\mathrm{i}k_E\delta L(\varepsilon)}\tilde{P}_F(\varepsilon,T)\,, \tag{4.152}$$

where $\tilde{P}_F(\varepsilon,T)$ is the corresponding density of self-crossings of orbits with period T, that fulfill the additional condition that the number of ac reflections is odd along both parts, L and R. To obtain $\tilde{P}_F$ we start from the integral expression for the unrestricted density (4.146), and incorporate the probability $P^{\mathrm{o}}_{\mathrm{ac}}(T)$, Eq. (4.123), to hit ac edges an odd number of times after a time T, namely

$$\tilde{P}_F(\varepsilon,T) \approx \frac{v_F^2\,\varepsilon}{\pi|\mathcal{V}|}\int_{T_{\min}(\varepsilon)}^{T-T_{\min}(\varepsilon)} dT_R\,(T-T_R)\,P^{\mathrm{o}}_{\mathrm{ac}}[T_R - T_{\min}(\varepsilon)]\,P^{\mathrm{o}}_{\mathrm{ac}}[T - T_R - T_{\min}(\varepsilon)]\,. \tag{4.153}$$

Here the factors $P^{\mathrm{o}}_{\mathrm{ac}}[T_R - T_{\min}(\varepsilon)]$ and $P^{\mathrm{o}}_{\mathrm{ac}}[T - T_R - T_{\min}(\varepsilon)]$ measure the probability for an odd number of ac reflections along R and L, respectively, as a function of T_R. The minimal time $T_{\min}$ has to be subtracted in the arguments of $P^{\mathrm{o}}_{\mathrm{ac}}$, since the orbit pieces are correlated during the encounter. That means if the orbit hits an ac edge the first time it comes close to the self-crossing, it will hit the same ac edge again when it comes back, i. e. the number of ac reflections within the encounter is always even. Now we assume that (in the RMT limit) $T_{\min}$ is much shorter than the other time scales, T and T_{ac}, and therefore evaluate the T_R integral to leading order in $T_{\min}$ to obtain

$$\tilde{P}_F(\varepsilon,T_\gamma) \approx \frac{v_F^2\,\varepsilon}{\pi|V|}\frac{T}{8}\left(T - T_{\mathrm{ac}} + (T+T_{\mathrm{ac}})e^{-2T/T_{\mathrm{ac}}} - 2T_{\min}(\varepsilon)\left[1 - \left(1 + \frac{2T}{T_{\mathrm{ac}}}\right)e^{-2T/T_{\mathrm{ac}}}\right]\right). \tag{4.154}$$

As mentioned before, the $T_{\min}$-independent terms of $\tilde{P}_F$ do not contribute to the real part of the integral in (4.152), so that with Eq. (4.148) we get

$$F_L(t) \approx -2t^2\left(1 - \left(1 + \frac{2tT_{\mathrm{H}}}{T_{\mathrm{ac}}}\right)e^{-2tT_{\mathrm{H}}/T_{\mathrm{ac}}}\right). \tag{4.155}$$

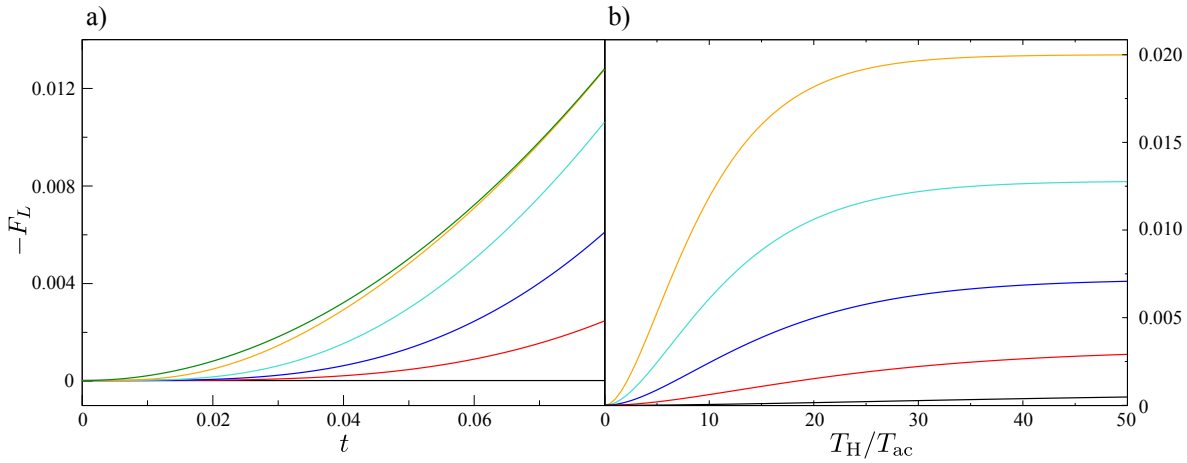

Figure 4.12: a) Absolute value of the leading off-diagonal contribution, $-F_L$, to the form factor as a function of $t = T/T_H$ for different values of the ac scattering strength, cf. Eq. (4.155). From bottom to top: $T_H/T_{ac} = 0$ (black), 5 (red), 10 (blue), 20 (turquoise), 50 (orange) and ∞ (green). At $T_H/T_{ac} = 0$, F_L is vanishing, in agreement with GUE, while for larger values the curve approaches the quadratic behavior of the GOE prediction, see also Fig. 4.11 b). b) Exponential crossover of the absolute value of F_L as a function of T_H/T_{ac} at $t = 0.02$ (black), 0.04 (red), 0.06 (blue), 0.08 (turquoise) and 0.1 (orange).

Also here we recover the asymptotic limits (4.137) and (4.149) for vanishing, $T_H/T_{ac} \to 0$, and very strong ac scattering, $T_H/T_{ac} \to \infty$, respectively.

Figure 4.12 a) shows the dependence of $-F_L$ on t for various effective ac scattering strengths T_H/T_{ac}. It displays the range of small t, where F_L is the dominant off-diagonal contribution to the form factor. The parameter T_H/T_{ac} controls the crossover between the two RMT limits, as shown in Fig. 4.12 b): $F_L = 0$ for $T_H/T_{ac} \to 0$ and $F_L = -2t^2$ for $T_H/T_{ac} \to \infty$. In Fig. 4.11 b) we plot $-F_L(t)$ rescaled by t^2, to emphasize the deviation from the quadratic t-dependence.

Eqs. (4.126) and (4.155) are the main results of this section. They rather generally describe the spectral correlations of chaotic graphene billiards with a boundary that consists of an arbitrary combination of ac, zz, and im type edges. The total length of intervalley scattering ac edges sets the time scale T_{ac}, which represents the control parameter for a 4×GUE to GOE crossover.

4.3.3 Explicit time reversal symmetry breaking

We generalize our results by incorporating explicit TRS breaking, e. g. by including a small magnetic flux Φ through the billiard that is produced by a magnetic field of strength B, oriented perpendicular to the graphene plane. Due to the flux induced Aharonov-Bohm type phase differences, this causes a breaking of both, the TRS $\mathcal{T}_y$ and the valley symmetry $\mathcal{T}_x$, leading to another crossover for fixed T_H/T_{ac}. Considering a weak magnetic field B, we neglect the bending of the classical orbits and effects on the pseudospin, i. e. we only take

into account the phases produced by the resulting magnetic flux through the cavity Φ. Every orbit γ obtains a phase shift $\exp(\mathrm{i}\pi BA_\gamma/\Phi_0)$, where A_γ is the directed area enclosed by γ and the magnetic flux quantum is defined as $\Phi_0 = h/e$.

We begin with the diagonal contribution to the spectral form factor. For pairs of identical orbits, the phase shifts cancel exactly, but for the pairs (γ, γ^{-1}), the resulting phase difference is $2\pi BA_\gamma/\Phi_0$. For chaotic systems the distribution of the A_γ is known to be approximately Gaussian [134]

$$P_A(A_\gamma, T_\gamma) \approx \frac{1}{\sqrt{2\pi\alpha T_\gamma}} \exp\left(-\frac{A_\gamma^2}{2\alpha T_\gamma}\right), \tag{4.156}$$

with a system specific parameter α. Integrating the Aharonov-Bohm type phase shift over the enclosed areas with the density P_A results in an exponential suppression of the contribution of the corresponding orbit pairs

$$\int_{-\infty}^{\infty} dA_\gamma P_A(A_\gamma, T_\gamma) \mathrm{e}^{2\pi \mathrm{i} BA_\gamma/\Phi_0} = \mathrm{e}^{-T_\gamma/T_\mathrm{B}}, \tag{4.157}$$

that multiplies the integrand in Eq. (4.126) (see also Ref. [135]). Here a third timescale occurs, namely the magnetic dephasing time

$$T_\mathrm{B} = \frac{|\mathcal{V}|^2}{2\pi^2\alpha}\frac{\Phi_0^2}{\Phi^2} = \zeta\frac{\Phi_0^2}{\Phi^2}. \tag{4.158}$$

Since the pairs with identical orbits are not affected, we obtain for the diagonal contribution to the spectral form factor

$$F_D(t) = t\left(1 + \mathrm{e}^{-2tT_\mathrm{H}/T_\mathrm{ac}}\right)\left(1 + \mathrm{e}^{-tT_\mathrm{H}/T_\mathrm{B}}\right), \tag{4.159}$$

which turns into Eq. (4.126) for $T_\mathrm{B} \to \infty$, i. e. for zero magnetic field. For very strong ac scattering, $T_\mathrm{ac} \to 0$, we recover the known formula [135] for the GOE to GUE crossover, $F_D(t) = 2t \to t$, describing the breaking of the full TRS $\mathcal{T}_y$. In the opposite case of very weak ac scattering, $T_\mathrm{ac} \to \infty$, the magnetic field leads to a crossover $F_D(t) = 4t \to 2t$. This corresponds to a crossover from two degenerate unitary ensembles, 4×GUE, to two non-degenerate unitary ensembles, 2×GUE, reflecting the breaking of the valley symmetry $\mathcal{T}_x$.

For the loop contribution the calculation is in principle very similar. Here an orbit pair $(\gamma, \gamma_\times)$ obtains a phase difference $2\pi BA_R/\Phi_0$, so that the T_R integration in Eq. (4.153) is modified by an exponential as in Eq. (4.157). However, one has to be more careful here when taking into account orbit pairs like $(\gamma, \gamma_\times^{-1})$, since they have the same propagation direction along R and the opposite direction along L in contrast to the pairs $(\gamma, \gamma_\times)$. Without magnetic field, this difference was not important, but for finite B, we have to distinguish these contributions [135]. Namely for the pairs $(\gamma, \gamma_\times)$ the T_R integral has to be modified by a factor

$$\int_{-\infty}^{\infty} dA_R P_A[A_R, T_R - T_\mathrm{min}(\varepsilon)] \mathrm{e}^{2\pi \mathrm{i} BA_R/\Phi_0} = \mathrm{e}^{-[T_R - T_\mathrm{min}(\varepsilon)]/T_\mathrm{B}}, \tag{4.160}$$

and for the pairs $(\gamma, \gamma_\times^{-1})$ by a factor

$$\int_{-\infty}^{\infty} dA_L P_A[A_L, T_\gamma - T_R - T_{\min}(\varepsilon)] \mathrm{e}^{2\pi \mathrm{i} B A_L/\Phi_0} = \mathrm{e}^{-[T_\gamma - T_R - T_{\min}(\varepsilon)]/T_\mathrm{B}} . \tag{4.161}$$

The minimum time has to be subtracted here due to the correlated motion within the encounter region, where no phase difference is accumulated [135]. Performing the same calculational steps as before for the case without magnetic field, we obtain for the loop contribution to the spectral form factor

$$F_L(t) \approx \frac{-4t^2 T_\mathrm{B}}{2T_\mathrm{B} + T_\mathrm{ac}} \left(\mathrm{e}^{-tT_\mathrm{H}/T_\mathrm{B}} - \left[\mathrm{e}^{-tT_\mathrm{H}/T_\mathrm{B}} + \frac{2T_\mathrm{B}}{T_\mathrm{ac}} \left(1 - \mathrm{e}^{-tT_\mathrm{H}/T_\mathrm{B}} \right) \right] \mathrm{e}^{-2tT_\mathrm{H}/T_\mathrm{ac}} \right) . \tag{4.162}$$

For zero magnetic field, $T_\mathrm{B} \to \infty$, this formula turns into the former expression (4.155), while for finite magnetic field and very strong ac scattering, $T_\mathrm{ac} \to 0$, we obtain again the known expression for the GOE to GUE crossover as in a Schrödinger billiard [135]

$$F_L(t) \approx -2t^2 \mathrm{e}^{-tT_\mathrm{H}/T_\mathrm{B}} . \tag{4.163}$$

In the opposite case of decoupled valleys $T_\mathrm{ac} \to \infty$, the loop contribution vanishes, $F_L(t) \to 0$, as expected.

4.4 Summary

In this chapter we have investigated the DOS of graphene billiards in the semiclassical limit. First we separated the DOS into a smooth part and an oscillating part.

For the smooth part we derived the two leading terms in the corresponding Weyl expansion in Sec. 4.1, the results are summarized in Eqs. (4.32) and (4.33). We found that the bulk term scales with the total area of the graphene billiard, as for the Schrödinger case. On the other hand, the surface term does not, as in Schrödinger billiards, scale with the total length of the system boundary, since the contributions from armchair and infinite mass edges are zero. Zigzag edges, or more precisely zigzag edge states, however, give rise to a characteristic feature in the smooth DOS at low energies. The size of the surface contribution to $\bar{\rho}$ scales linearly with the length of the zigzag part of the boundary, and thus the number of zigzag edge states, as we have analyzed in detail. The comparison of our theory with numerical simulations shows very good agreement. Therefore our method allows for an analytical calculation of the zigzag edge state contribution. For graphene nanostructures with unknown amount of zigzag type boundary segments, one can estimate the effective zigzag edge length from the smooth DOS.

For the oscillating part ρ_osc we have presented extensions of the semiclassical trace formulae for two representative regular graphene billiards, the disk with infinite mass edges, and the rectangle with zigzag and armchair edges, Eqs. (4.59) and (4.77), respectively. We have discussed ρ_osc for these systems in detail and found that the modifications due to the interference of pseudospins have significant effects on the frequency content. Further we have

provided semiclassical approximations to the quantum energy levels. For chaotic billiards we have presented the graphene version of the Gutzwiller trace formula for isolated orbits, Eq. (4.42), including effects from edge scattering explicitly. Since edge effects enter the trace formulae exclusively via the pseudospin propagator, while the orbital dynamics is the same as for Schrödinger billiards, edge-related phenomena are accessible in our theory in a particularly clear way. The results of Secs. 4.1 and 4.2 have been published in Ref. [108].

In the second part of this chapter we used the trace formula (4.42) to study the oscillating part of the DOS of chaotic graphene billiards in more detail. Due to the complex nature of ρ_{osc} in such systems, we have investigated its universal statistical properties in terms of the spectral form factor, i. e. the Fourier transform of the two-point correlator. We found that the sizes of both, the diagonal and the leading off-diagonal contribution, depend strongly on the edge structure, see our main results Eqs. (4.126) and (4.155). The total length of armchair boundary segments represents a symmetry enabling parameter for a crossover between the different relevant symmetry classes, namely the unitary (GUE) and the orthogonal class (GOE). Due to the intervalley coupling, mediated by armchair edges, an increasing armchair scattering rate drives the system from two degenerate unitary subsystems to one orthogonal system, effectively re-enabling the TRS. However, even for a significant amount of intervalley scattering ac edges, we predict that the small t correlations deviate significantly from the GOE result. Finally, we generalized our results for the form factor to include a weak magnetic field. The presented results suggest that partial (effective) breaking of the TRS should be visible in the spectral correlations at scales of many mean level spacings, corresponding to small times $t \ll 1$, rather than in the nearest neighbor level spacing distribution, which is predominantly governed by the orthogonal symmetry class, even for rather weak armchair scattering [43]. In a mesoscopic graphene billiard, the ratio $T_{\mathrm{H}}/T_{\mathrm{ac}}$ can be tuned by changing the Fermi energy. Since our theory is valid in a wide range of k_E, the transitions in Figs. 4.10 b) and 4.12 b) should be accessible in a real system. For a concrete example we consider for the perimeter $|\partial\mathcal{V}| = 500\,\mathrm{nm}$ and for the ac length $W_{\mathrm{ac}} = 100\,\mathrm{nm}$. For an energy range $0.1 \lesssim k_E a \lesssim 0.2$ (cf. Fig. 3.2), we get from Eq. (4.127) $3 \lesssim T_{\mathrm{H}}/T_{\mathrm{ac}} \lesssim 66$. The results of Sec. 4.3 have been published in Ref. [136].

CHAPTER 5

Quantum transport through open graphene cavities

Following the discussion of the DOS of closed graphene billiards, this chapter is devoted to quantum transport properties of open systems. Our main focus is the conductance of graphene cavities with two attached leads, from which the charge carriers enter and leave the system, as depicted e. g. in Figs. 5.1 b) and 5.2 a). In particular we consider cavities with chaotic classical dynamics and develop a semiclassical theory of transport. We address the question of how the edge characteristics of the system influences the quantum conductance. We show that the crossover between the different effective symmetry classes that we have discussed in the previous chapter for the spectral form factor, is reflected also in the quantum transport properties, which are experimentally more directly accessible compared to the DOS.

Since for chaotic graphene cavities the conductance is, like the DOS oscillations, a very complex quantity, we study universal statistical transport properties in the following. In Fig. 5.1 a) we show an example of the conductance of the chaotic graphene cavity depicted in Fig. 5.1 b) as a function of the Fermi momentum k_E for a fixed number of propagating channels in the leads. The orange curve is the conductance for zero magnetic field, while the blue curve corresponds to a flux of $\Phi \approx 1.5\,\Phi_0$ through the cavity. We also plot the corresponding conductance averages over the shown energy range (dash-dotted horizontal lines). The average conductance in the field free case is reduced by $\sim 0.21\,g_0$. This phenomenon is known as *weak localization* (WL), a suppression of the average conductance with respect to its classical value, and a purely quantum mechanical effect. The magnetic flux leads to dephasing and destroys the quantum interference.

Originally the WL correction was studied in weakly disordered electron gases in semiconductor heterostructures. Considering the Drude formula, where the resistivity is directly proportional to the total scattering rate, the resistivity is expected to decrease with decreasing temperature, since inelastic scattering processes, such as electron-phonon scattering, are reduced. The residual resistivity at very low temperatures is then solely due to impurities, defects, or other sources of elastic scattering. However, in experiments one finds that the resistivity increases again for temperatures below a certain value, see e. g. Ref. [139]. This increase is due to coherent quantum interference at low temperatures, namely the weak localization effect. Its origin is an enhanced probability for a quantum particle to return to its original position. Assume there is one possible Feynman path with a probability amplitude $\mathcal{A}$ for a particle to return to its starting point. If the system has a time reversal symmetry, then also a second path returning exists, namely the counter propagating path with amplitude $\bar{\mathcal{A}}$.

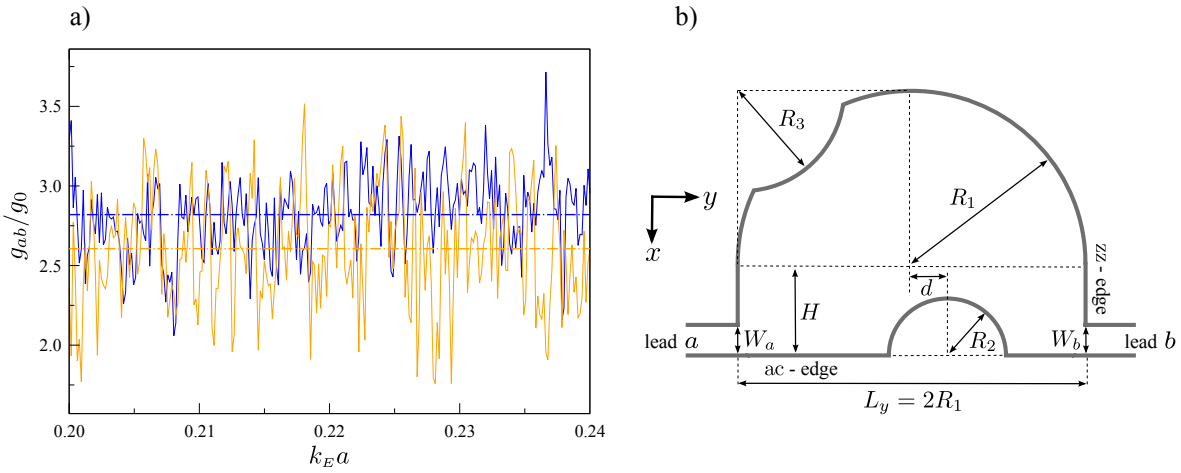

Figure 5.1: a) Conductance of a chaotic graphene cavity [for the shape see panel b)] computed numerically using tight-binding simulations [56]. The solid lines show the conductance g_{ab} as a function of k_E without magnetic flux (orange) and with a flux of $\Phi \approx 1.5\,\Phi_0$ through the cavity (blue), respectively. The dash-dotted lines represent the average conductance in the shown range of k_E. The increase of the average conductance upon applying a magnetic flux reflects the weak localization. b) Scheme of the geometry of the used cavity [134]. The basic shape is a half stadium, which is known to exhibit largely chaotic classical dynamics [137, 138]. Additionally we introduced a stopper at the bottom, to prevent so-called direct paths that connect the leads without being scattered at the boundary, and a desymmetrization at the top left to break all mirror symmetries. We show exemplarily the location of a zz and an ac boundary piece (cf. Fig. 2.4). Note that for convenience we chose the y-axis to lie in the horizontal. This basic shape is used for all numerical transport simulations in the present chapter and in Chap. 6.

If no other Feynman paths exist, the return probability is

$$R = |\mathcal{A} + \bar{\mathcal{A}}|^2 = |\mathcal{A}|^2 + |\bar{\mathcal{A}}|^2 + \mathcal{A}\bar{\mathcal{A}}^* + \mathcal{A}^*\bar{\mathcal{A}}\,. \tag{5.1}$$

The first two terms in this sum constitute the classical return probability, the mixed terms are due to quantum interference. However, for time reversal symmetric systems the amplitudes $\mathcal{A}$ and $\bar{\mathcal{A}}$ are equal, leading to $R = 4|\mathcal{A}|^2$, i. e. twice the classical value. On the other hand, if TRS is broken the amplitudes are different. Consider for example a small magnetic flux. Then the classical probabilities, i. e. the absolute values of the amplitudes, remain approximately unchanged, but there is a phase difference between the time reversed partner paths, which we denote by $\Delta\phi$. Then we have $R = 2|\mathcal{A}|^2[1 + \cos(\Delta\phi)]$, which is in general smaller than $4|\mathcal{A}|^2$. If we average over many random phase differences, the interference terms vanish and we have $R = 2|\mathcal{A}|^2 = |\mathcal{A}|^2 + |\bar{\mathcal{A}}|^2$, i. e. the classical return probability. In a conductor, the enhanced return probability in the case of intact TRS leads to an enhanced resistivity, in other words to a 'weak localization'. This is of course a very crude explanation of the physics behind WL, but it can provide a rough understanding. Theoretically WL was first addressed using diagrammatic perturbation theory [140, 141]. In the presence of spin-orbit interaction, the sign of the effect can be reversed due to an additionally accumulated phase difference of

π, leading to a resistivity that is smaller than the classical value. In this case one speaks of *weak antilocalization* (WAL). For reviews on these topics see e. g. Refs. [142, 143, 144, 145]. Since the charge carrier dynamics in disordered systems can be considered chaotic in a sense, it was only natural to search for analog effects like the WL also in the transport properties of chaotic ballistic conductors. Baranger and coworkers gave a first theoretical description of the WL correction in ballistic microstructures in 2DEGs, described by an effective Schrödinger equation [134, 146]. They derived semiclassically the quantum correction to the resistance due to time reversed pairs of classical orbits, known as coherent backscattering. Furthermore, they showed that the magnetoresistance has different line shapes, depending on whether the system has regular or chaotic classical dynamics. While the predictions concerning the different line shapes have been confirmed experimentally [147], the size of the quantum correction was too large in the semiclassical theory. In addition, since time reversed pairs of classical orbits exist only if the orbits start and end in the same lead, but not if they connect different leads, the semiclassical theory was known to be incomplete. While RMT calculations soon yielded the correct size of the WL correction in resistance and transmission [148, 149], a semiclassical description was not available until 2002, when Richter and Sieber recognized the importance of certain correlations of classical orbits [150]. The responsible orbit pairs are closely related to the loop pairs that we have discussed in the context of spectral correlations in Subsec. 4.3.2. For diffusive bulk graphene, the dependence of the weak (anti)localization correction on various scattering mechanisms has been theoretically derived by McCann and coworkers [63] and further investigated theoretically [151, 152, 153] and experimentally [64, 154, 155, 156, 157]. Numerical studies include simulations of disordered graphene nanoribbons [158, 159] as well as ballistic graphene cavities [43], however an analytical description of WL in chaotic ballistic graphene cavities was still missing. In this chapter we provide such a theory, generalizing the existing semiclassical approach.

Apart from the average conductance, we see from Fig. 5.1 a) that $g_{ab}(k_E)$ fluctuates strongly around its average value. These fluctuations are also a quantum effect; they are reproducible and must not be confused with noise. Since the size of the conductance fluctuations is always of the order of the conductance quantum, $g_0 = e^2/h$, irrespective of the system size or the average conductance, they are usually denoted as *universal conductance fluctuations* (UCF). UCF also occur in the transport through disordered systems [160, 161], as well as in ballistic microstructures [134]. In the case of disordered graphene, several experimental studies [154, 162, 163, 164], numerical simulations [165] and analytical investigations [166, 167] have focused on UCF. For ballistic graphene cavities on the other hand, numerical simulations have been performed [43], but an analytic theory that explains the results in detail, as presented here, was not available.

In the following we provide a theory for quantum transport in ballistic graphene samples and show that the edge structure has important consequences on the quantum interference phenomena. We focus mainly on the aforementioned statistical properties of the conductance, i. e. the average conductance including the WL correction and the UCF. Finally we also briefly discuss the *shot noise* of ballistic graphene cavities, i. e. temporal fluctuations of the current

due to charge quantization. For graphene ribbons with rather large width to length ratio, where transport at very low energies may be dominated by evanescent modes, shot noise has been studied theoretically [168, 169, 170] and experimentally [171, 172].

Conductance of graphene cavities

One well-known way to obtain the conductance of a mesoscopic quantum system is via the Landauer formula [173, 174], which relates the conductance from lead b to lead a, g_{ab}, to the transmission probability through the system

$$g_{ab} = \frac{e^2}{h} \sum_{nm} \left| t_{nm}^{(ab)} \right|^2 . \tag{5.2}$$

Here n and m are the propagating channels in lead a and b, respectively, and $t_{nm}^{(ab)}$ is the scattering amplitude for charge carriers to be transmitted from channel m in lead b to channel n in lead a. In App. A.5.2 we derive the generalized Fisher-Lee relation [175] for graphene for the transmission amplitudes in terms of the retarded Green function

$$t_{nm}^{(ab)} = \mathrm{i}v_F \int\limits_{C_a} dy_a \int\limits_{C_b} dy_b' \, \Psi_n^{+\dagger}(\boldsymbol{x}_a) \, \sigma_{\boldsymbol{a}} \, G(\boldsymbol{x}_b, \boldsymbol{x}_a') \, \sigma_{\boldsymbol{b}} \, \Psi_m^{-}(\boldsymbol{x}_b') \, , \tag{5.3}$$

where C_a and C_b denote the cross-sections of the leads, and the $\Psi^{\pm}$ are the lead wavefunctions for outgoing $(+)$ and incoming $(-)$ quasiparticles in the corresponding channel, respectively. The vectors $\boldsymbol{a}$ and $\boldsymbol{b}$ are unit vectors in the direction of the corresponding lead and point into the interior of the system, as depicted in Fig. 5.2 a). However, a disadvantage of this approach is the necessity to directly include the lead wavefunctions, and thus the boundary conditions of the leads, which is rather unpractical, since in principle one has to perform all calculations for different (combinations of) lead boundary types.

Thus we follow a different approach in this work, where the lead boundaries do not have to be included explicitly, namely we start from the linear response Kubo formula for the conductance. Both methods are in fact equivalent, as has been shown by Baranger and Stone using the Schrödinger equation [176]. We show in App. A.5.2 that this is true also for graphene. The Kubo formula for the conductance from lead b to lead a reads [176]

$$g_{ab} = - \int\limits_{C_a} dy \int\limits_{C_b} dy' \; \sigma_{ab}(\boldsymbol{x}, \boldsymbol{x'}) \, , \tag{5.4}$$

where the non-local conductivity for graphene is given by

$$\sigma_{ab}(\boldsymbol{x}, \boldsymbol{x'}) = \frac{e^2}{2\pi\hbar} \mathrm{Tr} \left[\sigma_{\boldsymbol{a}} G(\boldsymbol{x}, \boldsymbol{x'}) \sigma_{\boldsymbol{b}} G^{\dagger}(\boldsymbol{x}, \boldsymbol{x'}) \right] . \tag{5.5}$$

We derive this formula in App. A.5.1, see Eq. (A.61). Our discussion in the present chapter is focused on the semiclassical limit. On the one hand that means we assume large cavities, so

that $k_E L \gg 1$ and we can approximate the Green functions that occur in (5.5) by the semiclassical graphene Green function (3.83). On the other hand, we consider many propagating lead channels, which allows to compare the semiclassical results with the leading order (in the inverse channel numbers of the leads, $M_{a/b}^{-1}$) terms of the corresponding RMT expressions. Inserting G^{sc} from Eq. (3.83) into Eq. (5.5), we obtain a double sum over classical orbits γ and γ', similar as for the spectral form factor (4.82)

$$\sigma_{ab}(\boldsymbol{x}, \boldsymbol{x'}) \approx \left(\frac{e v_F}{4\pi\hbar}\right)^2 \sum_{\gamma\gamma'} Y_{\gamma,\gamma'} D_\gamma D_{\gamma'} \exp\left(\mathrm{i} k_E \delta L_{\gamma,\gamma'}\right) . \tag{5.6}$$

However, while we summed over periodic orbits for the spectral form factor, here the arguments of the conductivity in Eq. (5.4) lie on the lead cross sections $C_{a/b}$, and thus the classical orbits contributing to (5.6) connect the point $\boldsymbol{x'}$ in lead b to the point $\boldsymbol{x}$ in lead a. In Eq. (5.6) we have absorbed the phases due to the conjugate points into the stability prefactors D_γ, and the pseudospin part for each orbit pair (γ, γ') is given by the trace

$$Y_{\gamma,\gamma'} = \mathrm{Tr}\left(\sigma_{\boldsymbol{a}} K_\gamma \sigma_{\boldsymbol{b}} K_{\gamma'}^\dagger\right) . \tag{5.7}$$

While the pseudospin independent part of Eq. (5.6) is rather similar to the one in Eq. (4.82) for the spectral form factor in the semiclassical limit, the pseudospin part is different here, since the pseudospin propagators have to be multiplied *before* tracing. This has important consequences on the pseudospin interference, e. g. it leads to the independence of the classical conductance on the edge type, as we show below.

5.1 Average conductance

First we consider the average conductance, $\langle g_{ab}\rangle_{k_E} = \langle g_{ab}\rangle$, where as before the averaging is performed over an energy window that is classically small, in particular the number of lead channels must be constant within the window, but still contains several quantum fluctuations. Semiclassical calculations for the Schrödinger equation [101, 146, 150, 177, 178] and RMT for the scattering matrix [148, 149] predict for the average conductance the universal values

$$\frac{\langle g_{ab}\rangle}{g_0} = \frac{M_a M_b}{M_a + M_b - 1 + 2/\beta} . \tag{5.8}$$

Here β depends on the universality class, namely $\beta = 1$ for the orthogonal class (circular orthogonal RMT ensemble, COE), $\beta = 2$ for the unitary class (circular unitary ensemble, CUE), and $\beta = 4$ for the symplectic class (circular symplectic ensemble, CSE). As for the spectral statistics in Sec. 4.3, the relevant antiunitary symmetries can drive the system into different universality classes (cf. also Sec. 2.2). If some of the symmetries are partially broken or restored, this leads to crossovers between the symmetry classes. The conductance quantum is defined as

$$g_0 = \frac{e^2}{2\pi\hbar} \tag{5.9}$$

and $M_{a/b}$ is the number of propagating channels in the corresponding lead. We expand (5.8) for large $M_{a/b}$ as

$$\frac{\langle g_{ab}\rangle}{g_0} = \frac{M_a M_b}{M_a + M_b} + \left(1 - \frac{2}{\beta}\right) \frac{M_a M_b}{(M_a + M_b)^2} + \mathcal{O}\left(M_{a/b}^{-1}\right) . \tag{5.10}$$

Semiclassically, just as for the spectral form factor, relevant contributions to the average conductance are due to orbit pairs that have a small or vanishing length difference $\delta L_{\gamma,\gamma'}$. Again, as we shall see, the diagonal and the leading off-diagonal terms in the orbit sum (5.6) give rise to the leading order ($\sim M_{a/b}^1$) and the next-to-leading order ($\sim M_{a/b}^0$) terms in the expansion (5.10) [134, 150].

5.1.1 Diagonal contribution

We begin with the diagonal contribution, where $\gamma' = \gamma$ and $\delta L_{\gamma,\gamma'} = 0$. Since in the boundary matrices for single reflections, Eq. (3.94), sublattice and valley pseudospin are not entangled, we can separate the pseudospin propagator into a valley part and a sublattice part $K_\gamma = K_\gamma^\tau \otimes K_\gamma^\sigma$. Then the pseudospin trace for diagonal terms becomes

$$Y_\gamma = Y_{\gamma,\gamma} = Y_\gamma^\tau \otimes Y_\gamma^\sigma = \mathrm{Tr}\left(K_\gamma^\tau K_\gamma^{\tau\dagger}\right) \mathrm{Tr}\left(\sigma_{\boldsymbol{a}} K_\gamma^\sigma \sigma_{\boldsymbol{b}} K_\gamma^\sigma\right) = 2\, Y_\gamma^\sigma . \tag{5.11}$$

Since K_γ^τ is a product of valley Pauli matrices and thus unitary, we can directly trace out the valley part, giving a factor of two. This means that, in diagonal approximation, the total number of ac reflections is not important for whether or not an orbit contributes to the conductance, in contrast to the diagonal contribution to the spectral form factor, where only orbits with an even number of ac reflections enter. As mentioned above, the origin of this difference is that Y_γ^τ is a trace of products and the valley part of Z_γ, Eq. (4.83), is a product of traces of unitary pseudospin propagators.

For the sublattice part Y_γ^σ, we first consider orbits with $N_\gamma = N$ reflections that hit only ac and im type edges. According to Eq. (3.94), each reflection then effectively contributes a term $\sigma_z \mathrm{e}^{\mathrm{i}\theta_i \sigma_z}$, and thus we get with the sum of reflection angles θ_γ, as defined in Eq. (4.90),

$$\begin{aligned} Y_\gamma &= 2\,\mathrm{Tr}\left[\sigma_{\boldsymbol{a}} \sigma_z^N \mathrm{e}^{\mathrm{i}\theta_\gamma \sigma_z} (1 + \sigma_{\boldsymbol{\alpha}_1 \boldsymbol{x}'}) \sigma_{\boldsymbol{b}} (1 + \sigma_{\boldsymbol{\alpha}_1 \boldsymbol{x}'}) \mathrm{e}^{-\mathrm{i}\theta_\gamma \sigma_z} \sigma_z^N\right] \\ &= (-1)^N 2\,\mathrm{Tr}\left[\mathrm{e}^{-2\mathrm{i}\theta_\gamma \sigma_z} (\sigma_{\boldsymbol{a}} \sigma_{\boldsymbol{b}} + \sigma_{\boldsymbol{a}} \sigma_{\boldsymbol{\alpha}_1 \boldsymbol{x}'} \sigma_{\boldsymbol{b}} \sigma_{\boldsymbol{\alpha}_1 \boldsymbol{x}'})\right] \\ &= (-1)^N 8 \cos(2\theta_\gamma + \varphi_{\boldsymbol{a}} - \varphi_{\boldsymbol{\alpha}_1 \boldsymbol{x}'}) \cos(\varphi_{\boldsymbol{b}} - \varphi_{\boldsymbol{\alpha}_1 \boldsymbol{x}'}) , \end{aligned} \tag{5.12}$$

where $\varphi_{\boldsymbol{a}}$, $\varphi_{\boldsymbol{b}}$, and $\varphi_{\boldsymbol{\alpha}_1 \boldsymbol{x}'}$ are the polar angles of the vectors $\boldsymbol{a}$, $\boldsymbol{b}$, and $(\boldsymbol{\alpha}_1 - \boldsymbol{x}')$ respectively. We define the angles of the incoming (θ_b) and outgoing (θ_a) segment of the orbit γ relative to the lead orientation [cf. Fig. 5.2 a)]

$$\theta_a = \varphi_{\boldsymbol{x}\boldsymbol{\alpha}_N} - \varphi_{\boldsymbol{a}} + \pi , \tag{5.13}$$

$$\theta_b = \varphi_{\boldsymbol{\alpha}_1 \boldsymbol{x}'} - \varphi_{\boldsymbol{b}} . \tag{5.14}$$

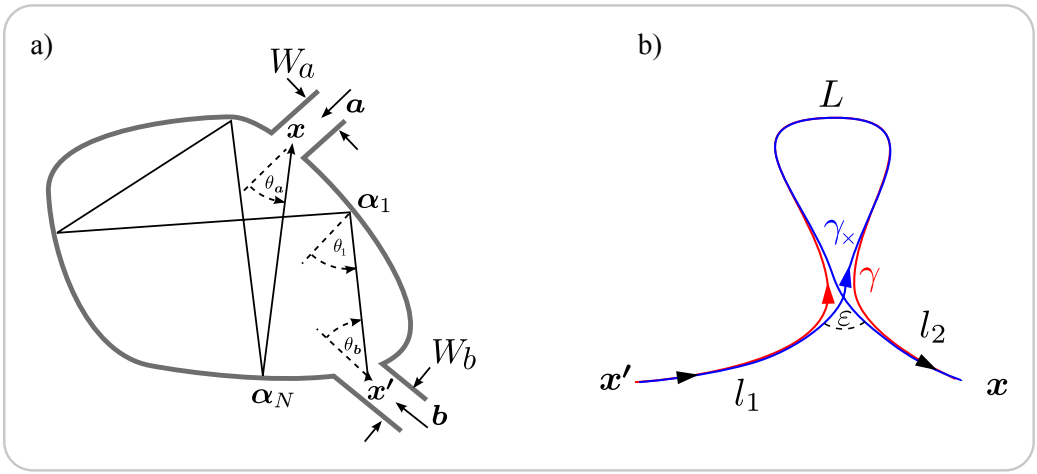

Figure 5.2: a) Sketch of an open cavity with two leads, a and b. The lead openings have widths W_a and W_b. The angles that the incoming and the outgoing trajectory segments include with the lead directions are θ_b and θ_a, respectively. b) Schematic representation of a loop pair that contributes to the weak localization correction to the average conductance [150]. One of the orbits crosses itself with an angle ε, the other orbit 'avoids' this crossing, but apart from this follows the first one exponentially closely.

Further we use the relation

$$(2\theta_\gamma - N\pi - \varphi_{\boldsymbol{\alpha}_1\boldsymbol{x'}} + \varphi_{\boldsymbol{x}\boldsymbol{\alpha}_N}) \mod 2\pi = 0\,, \tag{5.15}$$

which is obtained by repeatedly making use of Eq. (4.96) [cf. also Fig. 4.9 b)], to obtain finally

$$Y_\gamma = -8\cos(\theta_a)\cos(\theta_b)\,. \tag{5.16}$$

Note that for the conductance between two different leads, we do not have to take into account time reversed orbits γ^{-1}: If the orbit γ starts from lead b and ends in lead a, the opposite holds for γ^{-1}, thus it does not contribute to (5.6).

In the same way as in Sec. 4.3, one shows that Eq. (5.16) holds also if reflections from zz edges are involved. As an example, we assume that the first reflection is at a zz edge and the remaining $N-1$ reflections are at ac and im type edges. Then we have

$$\begin{aligned} Y_\gamma &= 2\,\mathrm{Tr}\left[\sigma_{\boldsymbol{a}}\sigma_z^{N-1}\mathrm{e}^{\mathrm{i}(\theta_\gamma-\theta_1)\sigma_z}\sigma_{\boldsymbol{t}_1}(1+\sigma_{\boldsymbol{\alpha}_1\boldsymbol{x'}})\sigma_{\boldsymbol{b}}(1+\sigma_{\boldsymbol{\alpha}_1\boldsymbol{x'}})\sigma_{\boldsymbol{t}_1}\mathrm{e}^{-\mathrm{i}(\theta_\gamma-\theta_1)\sigma_z}\sigma_z^{N-1}\right] \\ &= (-1)^{N-1}2\mathrm{Tr}\left[\mathrm{e}^{-2\mathrm{i}(\theta_\gamma-\theta_1)\sigma_z}(\sigma_{\boldsymbol{a}}\sigma_{\boldsymbol{t}_1}\sigma_{\boldsymbol{b}}\sigma_{\boldsymbol{t}_1}+\sigma_{\boldsymbol{a}}\sigma_{\boldsymbol{t}_1}\sigma_{\boldsymbol{\alpha}_1\boldsymbol{x'}}\sigma_{\boldsymbol{b}}\sigma_{\boldsymbol{\alpha}_1\boldsymbol{x'}}\sigma_{\boldsymbol{t}_1})\right] \\ &= (-1)^{N-1}8\cos(2\theta_\gamma - 2\theta_1 + \varphi_{\boldsymbol{a}} + \varphi_{\boldsymbol{\alpha}_1\boldsymbol{x'}} - 2\varphi_{\boldsymbol{t}_1})\cos(\varphi_{\boldsymbol{b}} - \varphi_{\boldsymbol{\alpha}_1\boldsymbol{x'}})\,. \end{aligned} \tag{5.17}$$

Adapting Eq. (4.92) appropriately yields

$$(2\theta_1 - 2\varphi_{\boldsymbol{\alpha}_1,\boldsymbol{x'}} + 2\varphi_{\boldsymbol{t}_1} - \pi) \mod 2\pi = 0\,, \tag{5.18}$$

which inserted into Eq. (5.17) together with Eqs. (5.13) - (5.15) finally gives the result (5.16) again. In this way, one obtains Eq. (5.16) also for the general case with an arbitrary number of zz reflections.

Therefore the result for the pseudospin trace in diagonal approximation is indeed independent of the specific edge types involved in the various reflections along γ, in contrast to the diagonal contribution to the spectral form factor. As we discuss below, beyond diagonal approximation edge effects become essential also for $\langle g_{ab}\rangle$. First, however, we proceed summing up the diagonal orbit pairs. To this end we rewrite the diagonal part of the orbit sum (5.6) as a sum over orbits with fixed outgoing and incoming angles employing the classical sum rule [179]

$$\sum_{\gamma(\theta_a,\theta_b)} |D_\gamma|^2\, \delta(T-T_\gamma) = \frac{\hbar k_E^2}{v_F \Sigma(k_E)} d\theta_a d\theta_b \mathrm{e}^{-T/T_\mathrm{d}}\,, \tag{5.19}$$

to transform the sum into a triple integral over the time the particle spends in the cavity, and entrance and exit angles. Here, Σ is the available energy surface and T_d is the dwell time, the first characteristic time scale for the transport problem. The dwell time is the time a classical particle typically spends within the cavity before it leaves by hitting one of the lead openings, in other words it is the inverse classical escape rate. The term $\mathrm{e}^{-T/T_\mathrm{d}}$ in Eq. (5.19) represents the classical survival probability. We denote the lead widths by W_a and W_b, so that for $W_{a/b} \ll |\partial\mathcal{V}|$, the dwell time is approximately given by the time between two reflections, i. e. the time of flight (4.122), and the ratio of total boundary length and the width of the lead openings (see Ref. [131] and references therein)

$$T_\mathrm{d} \approx \frac{\pi|\mathcal{V}|}{v_F|\partial\mathcal{V}|}\frac{|\partial\mathcal{V}|}{W_a+W_b} = \frac{\pi|\mathcal{V}|}{v_F(W_a+W_b)}\,. \tag{5.20}$$

Additionally we find for the energy surface of the cavity

$$\Sigma(k_E) = \int d^2x \int d^2k\, \delta(k_E-k) = 2\pi|\mathcal{V}|k_E\,. \tag{5.21}$$

With Eqs. (5.19) - (5.21) and Eq. (5.6), we get for the averaged diagonal contribution to the non-local conductivity

$$\begin{aligned}\langle\sigma_D(\boldsymbol{x},\boldsymbol{x}')\rangle &= -\left(\frac{ev_F}{4\pi\hbar}\right)^2 \int_{-\pi/2}^{\pi/2} d\theta_a \int_{-\pi/2}^{\pi/2} d\theta_b\, 8\cos(\theta_a)\cos(\theta_b)\frac{\hbar k_E}{v_F 2\pi|\mathcal{V}|}\int_0^\infty dT\, \mathrm{e}^{-T/T_\mathrm{d}} \\ &= -\frac{2k_E}{\pi}\frac{g_0}{W_a+W_b}\,.\end{aligned} \tag{5.22}$$

After the integration over the lead openings in Eq. (5.4), we obtain the universal, edge independent diagonal conductance of a ballistic graphene cavity

$$\langle g_D\rangle/g_0 = \frac{2k_E}{\pi}\frac{W_aW_b}{W_a+W_b} \approx \frac{M_aM_b}{M_a+M_b}\,, \tag{5.23}$$

in agreement with the leading order term in the expansion (5.10), and also with the numerical findings of Refs. [43, 60]. We have approximated the numbers of propagating lead channels M_a and M_b by

$$M_{a/b} \approx \frac{2k_E}{\pi} W_{a/b}\,, \tag{5.24}$$

accounting for the two valleys. For identical leads ($M_a = M_b = M$) we have $\langle g_D \rangle / g_0 = M/2$, half of the maximum possible conductance. This is what one expects for a classical particle: It enters the cavity and is randomly scattered. After many random scattering events, the 'memory' of the particle is erased, i. e. both lead openings are in fact equivalent and thus leaving through either of them is equally probable.

5.1.2 Loop contributions - weak localization

We turn now to the leading order off-diagonal contributions to the average conductance, namely the loop contributions that are responsible for the WL correction. The corresponding orbit pairs $(\gamma, \gamma_\times)$, sketched in Fig. 5.2 b), are similar to the ones considered in Sec. 4.3 for the off-diagonal contributions to the spectral form factor. However, here the orbits are not periodic but lead connecting. One can think of the orbits in Fig. 5.2 b) as versions of the periodic orbits from Fig. 4.9 a), where the counter propagating loop is left intact and the other loop is 'cut open'. As depicted in Fig. 5.2 b), we divide the orbits into the legs l_1 and l_2, where γ and $\gamma_\times$ both have the same propagation direction, and the loop part L, where the propagation directions are opposed, and label all quantities correspondingly.

We begin with the calculation of the pseudospin trace $Y_{\gamma,\gamma_\times}$ for the pairs $(\gamma, \gamma_\times)$. For the sum of reflection angles we have

$$\theta_\gamma = \theta_{l_1} + \theta_L + \theta_{l_2}\,, \tag{5.25}$$

$$\theta_{\gamma_\times} = \theta_{l_1} - \theta_L + \theta_{l_2}\,. \tag{5.26}$$

As before, we first focus on orbits with reflections from ac and im edges. In this case we obtain with Eq. (3.94) for the sublattice part

$$\begin{aligned} Y^\sigma_{\gamma,\gamma_\times} &= \mathrm{Tr}\left[\sigma_{\boldsymbol{a}}\sigma_z^N \mathrm{e}^{\mathrm{i}\theta_\gamma\sigma_z}(1+\sigma_{\boldsymbol{\alpha}_1\boldsymbol{x}'})\sigma_{\boldsymbol{b}}(1+\sigma_{\boldsymbol{\alpha}_1\boldsymbol{x}'})\mathrm{e}^{-\mathrm{i}\theta_{\gamma_\times}\sigma_z}\sigma_z^N\right] \\ &= (-1)^N \mathrm{Tr}\left[\mathrm{e}^{-2\mathrm{i}(\theta_\gamma-\theta_L)\sigma_z}(\sigma_{\boldsymbol{a}}\sigma_{\boldsymbol{b}} + \sigma_{\boldsymbol{a}}\sigma_{\boldsymbol{\alpha}_1\boldsymbol{x}'}\sigma_{\boldsymbol{b}}\sigma_{\boldsymbol{\alpha}_1\boldsymbol{x}'})\right] \\ &= -4\cos(\theta_a + 2\theta_L)\cos(\theta_b) = (-1)^{N_L} 4\cos(\theta_a)\cos(\theta_b) + \mathcal{O}(\varepsilon)\,. \end{aligned} \tag{5.27}$$

Here we have used Eqs. (5.13) - (5.15) and the geometric relation similar to Eq. (4.103)

$$2\theta_L \mod 2\pi = (N_L+1)\pi \mod 2\pi + \mathcal{O}(\varepsilon)\,. \tag{5.28}$$

As for the spectral form factor, we neglect terms of higher order in ε, since in the semiclassical limit the contributions from small ε dominate [150]. The combination of the calculations in

(5.17) and (5.27) shows that the result of Eq. (5.27) is not changed in the presence of zz reflections. For the valley part we have

$$Y^{\tau}_{\gamma,\gamma_\times} \;=\; \mathrm{Tr}\left(K^{\tau}_{l_2}K^{\tau}_{L}K^{\tau}_{l_1}K^{\tau\dagger}_{l_1}K^{\tau\dagger}_{L^{-1}}K^{\tau\dagger}_{l_2}\right) = \mathrm{Tr}\left[(K^{\tau}_{L})^2\right]\,. \tag{5.29}$$

This means that the edge type at reflections along the legs l_1 and l_2 are irrelevant, as for the diagonal contribution. For the loop part L we directly take into account reflections from zz, ac, and im type edges. Namely with Eq. (3.94) we get

$$\begin{aligned} Y^{\tau}_{\gamma,\gamma_\times} &= \begin{cases} (-1)^{N_L+1}\,\mathrm{Tr}(\tau_0) & \text{for odd } N_{\mathrm{ac},L}\,, \\ \mathrm{Tr}\left[\exp(4\mathrm{i}K\Lambda_L\tau_z + 2\mathrm{i}\vartheta_L\tau_z)\right] & \text{for even } N_{\mathrm{ac},L}\,, \end{cases} \\ &= 2\begin{cases} (-1)^{N_L+1} & \text{for odd } N_{\mathrm{ac},L}\,, \\ \cos(4K\Lambda_L + 2\vartheta_L) & \text{for even } N_{\mathrm{ac},L}\,. \end{cases} \end{aligned} \tag{5.30}$$

Here Λ_L is defined as in Eq. (4.87), where the sum runs only over ac reflections along the loop part L. In the same manner ϑ_L is defined as in Eq. (4.88) with the sum running only over zz reflections of the loop part. Putting together Eqs. (5.27) and (5.30), we get for the total pseudospin trace for the loop contribution to the conductance, including reflections from ac, zz, and im type edges

$$Y_{\gamma,\gamma_\times} \approx 8\cos(\theta_a)\cos(\theta_b)\begin{cases} -1 & \text{for odd } N_{\mathrm{ac},L}\,, \\ (-1)^{N_L}\cos(4K\Lambda_L + 2\vartheta_L) & \text{for even } N_{\mathrm{ac},L}\,. \end{cases} \tag{5.31}$$

The next step is to average the trace $Y_{\gamma,\gamma_\times}$ according to the edge characteristics of the graphene cavity, in order to perform the loop part of the orbit sum (5.6). To this end we distinguish the different regimes of uncoupled, totally coupled and intermediately coupled valleys.

No ac scattering - valley conservation

In the absence of valley coupling due to ac edges, we have $\Lambda_L = 0$, and consequently $\langle Y_{\gamma,\gamma_\times}\rangle = 0$. To see this, we consider first a pure infinite mass boundary, i. e. no zz edges are present either and $\vartheta_L = 0$. In this case we have $Y_{\gamma,\gamma_\times} = (-1)^{N_L}$. Since the probability for even and odd N_L is the same for long orbits, see e. g. Eq. (4.123), it follows that $\langle Y_{\gamma,\gamma_\times}\rangle$ vanishes in this case. When zz reflections are involved, then ϑ_L is distributed randomly between 0 and 2π, so that $\langle\cos(2\vartheta_L)\rangle = 0$ and therefore again $\langle Y_{\gamma,\gamma_\times}\rangle = 0$. This means that for uncoupled valleys there is no loop correction to the conductivity and thus *no weak localization*

$$\langle g_L\rangle = 0\,. \tag{5.32}$$

The physical reason is the absence of an effective intravalley TRS, since the symmetry $\mathcal{T}_0$ is broken by both im and zz type edges. Note that because of this effective symmetry breaking, also *no weak antilocalization* occurs, as would be the case for diffusive bulk graphene in the absence of intervalley scattering [63]. The semiclassical explanation for the fact that we do

not get the symplectic class here, even though graphene's Berry phase of π suggests this in principle, is that the effective phase difference $2\theta_L$ in Eq. (5.27) is given by the sum of *reflection angles*, Eq. (5.28), and *not the rotation angles*. One can see e. g. from Fig. 5.2 a) or Fig. 4.9 b) that the rotation at each individual reflection is $\pm\pi - 2\theta_i$ [see also Eq. (4.96)]. This means that $2\theta_L$ contains the total Berry phase (half of the total rotation angle) plus an additional phase of $\pm\pi$ for every reflection [90]. This additional phase shift leads to the sign $(-1)^{N_L}$ in Eq. (5.27), which destroys the effect of the Berry phase, resulting in an absence of W(A)L.

Ac billiards - complete valley mixing

For the opposite case of complete valley mixing, we assume that all reflections occur at ac edges, such that $\vartheta_L = 0$. Since the microscopic ac boundary condition implies that $K\Lambda_L = m\,2\pi/3$ with $m \in \mathbb{Z}$ (see Eq. (4.113) and the discussion in Subsec. 2.2.2), the cosine in Eq. (5.31) averages to zero:

$$\langle\cos(4K\Lambda_L)\rangle = \lim_{M\to\infty}\frac{1}{M}\sum_{m=1}^{M}\cos\left(m\,\frac{2\pi}{3}\right)=\frac{1}{3}\left[\cos\left(\frac{2\pi}{3}\right)+\cos\left(\frac{4\pi}{3}\right)+\cos(2\pi)\right]=0\,. \quad (5.33)$$

This means that the averaged pseudospin trace for the loop pairs in the case of complete valley mixing is given by [cf. Eq. (5.31)]

$$\langle Y_{\gamma,\gamma_\times}\rangle = -4\cos(\theta_a)\cos(\theta_b)\,, \quad (5.34)$$

giving rise to a finite weak localization correction in this case. Note that, as for the spectral form factor, also here a special situation arises if all distances fulfill the 'metallic' condition, cf. Subsec. 2.2.2. Then $K\Lambda_L \bmod 2\pi = 0$ and therefore $\langle Y_{\gamma,\gamma_\times}\rangle = 0$, as discussed for the pure im type boundary. Consequently the WL correction vanishes, indicating unitary symmetry. In Sec. 7.1 we show that indeed the WL is strongly suppressed in metallic graphene nanoribbons with weak bulk disorder. Here we exclude this case from the further discussion.

In order to calculate the loop contribution to the non-local conductivity, we use the classical sum rule (5.19) and replace the γ-sum (5.6) by integrations over T, θ_a, θ_b, and the crossing angles ε. Then we get (cf. also Subsec. 4.3.2)

$$\langle\sigma_L(\boldsymbol{x},\boldsymbol{x}')\rangle = -\frac{g_0}{W_a+W_b}\frac{2k_E}{\pi T_\mathrm{d}}\mathfrak{Re}\int_0^\pi d\varepsilon\int_{2T_\mathrm{min}(\varepsilon)}^\infty dT\,\mathrm{e}^{-[T-T_\mathrm{min}(\varepsilon)]/T_\mathrm{d}}P_g(\varepsilon,T)\mathrm{e}^{\mathrm{i}k_E\delta L_{\gamma,\gamma_\times}}\,, \quad (5.35)$$

where we took twice the real part, since every orbit pair in the sum has a partner pair, where γ and $\gamma_\times$ are interchanged leading to the complex conjugated term. The lower cut-off in the T-integral is due to the fact that a minimal time, T_min [see Eq. (4.147)], is needed to form a closed loop. Also for the legs a minimal time in necessary, in this case $T_\mathrm{min}/2$ for each of them (for details see Ref. [52]). Therefore the period of the full orbit has to be at least $2T_\mathrm{min}$. The minimum time T_min has also been subtracted from the argument of the survival probability,

because the trajectory segments close to the crossing are correlated. That means the orbit either leaves the cavity when it traverses the encounter region close to the crossing point for the first time, or it does not leave the cavity at all in the encounter region. This leads to the modification of the survival probability [52]. In Eq. (5.35), P_g denotes the density of loop pairs with crossing angle ε, which is to leading order in ε given by [52, 150]

$$P_g(\varepsilon, T) \approx \frac{v_F^2 \varepsilon}{\pi |\mathcal{V}|} \int\limits_{T_{\min}(\varepsilon)}^{T - T_{\min}(\varepsilon)} dT_L [T - T_L - T_{\min}(\varepsilon)] = \frac{v_F^2 \varepsilon}{2\pi |\mathcal{V}|} [T - 2T_{\min}(\varepsilon)]^2 \,. \tag{5.36}$$

The integration limits are set by the minimal periods of the loop part and the legs, respectively. For given T_L, the probability for a crossing is proportional to the period of the remaining trajectory, $T_\gamma - T_L - T_{\min}$. We insert Eq. (5.36) into Eq. (5.35) and use further that for

$$T_{\mathrm{d}} \gg T_{\mathrm{E}} = \frac{1}{\lambda} \ln \left(\frac{v_F k_E}{\lambda} \right) \tag{5.37}$$

we have according to Refs. [52, 150]

$$\mathfrak{Re} \int\limits_0^\pi d\varepsilon \, \varepsilon \, \mathrm{e}^{\mathrm{i} k_E \delta L_{\gamma,\gamma_\times}} \int\limits_{2T_{\min}(\varepsilon)}^\infty dT \, \mathrm{e}^{-[T - T_{\min}(\varepsilon)]/T_{\mathrm{d}}} P_g(\varepsilon, T) \approx -\frac{v_F}{2k_E |\mathcal{V}|} T_{\mathrm{d}}^2 \,. \tag{5.38}$$

Then we get for the non-local conductivity

$$\langle \sigma_L(\boldsymbol{x}, \boldsymbol{x}') \rangle \approx \frac{g_0}{(W_a + W_b)^2} \,, \tag{5.39}$$

and integrating over the lead openings [see Eq. (5.4)] together with Eq. (5.24) finally yields

$$\langle g_L \rangle / g_0 \approx -\frac{M_a M_b}{(M_a + M_b)^2} \,, \tag{5.40}$$

in agreement with the second term in the RMT expansion (5.10) for the orthogonal symmetry class ($\beta = 1$). The complete valley mixing due to the scattering from ac edges has effectively restored the TRS $\mathcal{T}_y$, and we find that the weak localization correction to the average conductance has the same size as in the Schrödinger case. In Eq. (5.37), T_{E} is the *Ehrenfest time*, the time scale after which a wave packet has spread over the whole system, so that quantum interference is possible. While we have neglected T_{E} here, we discuss the effect of finite Ehrenfest time briefly for the generic case of mixed boundaries below.

Mixed boundaries - generic case

Finally we turn to the general case of intermediate valley coupling, i. e. a boundary that consists of ac, zz, and im type edges. In view of our results for the spectral form factor, we expect the size weak localization correction to lie between that of the limiting cases, Eqs. (5.40) and

(5.32), and that the total amount of ac edges determines $\langle g_L \rangle$. From the discussion of the limiting cases above, we have learned that the pseudospin trace $Y_{\gamma,\gamma_\times}$ vanishes on average for orbits that hit an even number of ac edges or none at all during the loop part L. This carries over also to the general case, since a finite ϑ_L does not alter the result of the average (5.33). On the other hand, for orbits with an odd number of ac reflections along L we have according to Eq. (5.31)

$$\langle Y_{\gamma,\gamma_\times} \rangle = -8 \cos(\theta_a) \cos(\theta_b) \,. \tag{5.41}$$

Analogous to the calculation in Subsec. 4.3.2, cf. Eq. (4.152), we take this into account by modifying the density of self crossings accordingly with the probability for an odd number of ac reflections, so that in the general case the loop contribution to the non-local conductivity reads

$$\langle \sigma_L(\boldsymbol{x}, \boldsymbol{x}') \rangle = -\frac{g_0}{W_a + W_b} \frac{4k_E}{\pi T_\mathrm{d}} \mathfrak{Re} \int_0^\pi d\varepsilon \int_{2T_\mathrm{min}(\varepsilon)}^\infty dT \, \mathrm{e}^{-[T - T_\mathrm{min}(\varepsilon)]/T_\mathrm{d}} \tilde{P}_g(\varepsilon, T) \mathrm{e}^{\mathrm{i}k_E \delta L_{\gamma,\gamma_\times}} \,. \tag{5.42}$$

Here $\tilde{P}_g(\varepsilon, T)$ is the density of self crossings, where the corresponding orbit hits an odd number of ac edges along the loop part L, namely

$$\tilde{P}_g(\varepsilon, T) \approx \frac{v_F^2 \varepsilon}{\pi |\mathcal{V}|} \int_{T_\mathrm{min}(\varepsilon)}^{T - T_\mathrm{min}(\varepsilon)} dT_L [T - T_L - T_\mathrm{min}(\varepsilon)] P_\mathrm{ac}^\mathrm{o}[T_L - T_\mathrm{min}(\varepsilon)] \,. \tag{5.43}$$

In Eq. (5.43), P_ac^o is the probability to hit ac edges an odd number of times during the time T, as defined in Eq. (4.123). As for the survival probability in Eq. (5.42), we subtract the minimal time T_min in the argument of P_ac^o due to the correlation of the orbit segments during the encounter. If the orbit hits an ac edge the first time it comes close to the self crossing, it will hit the same ac edge again when it comes back, i. e. the number of ac reflections within the encounter is always even. For vanishing T_E and $T_\mathrm{d} \gg T_\mathrm{min}$, the integrals in Eq. (5.42) can be performed approximately using [52, 150]

$$\begin{aligned} \mathfrak{Re} \int_0^\pi d\varepsilon \, \varepsilon \, \mathrm{e}^{\mathrm{i}k_E \delta L_{\gamma,\gamma_\times}} \int_{2T_\mathrm{min}(\varepsilon)}^\infty dT \, \mathrm{e}^{-[T - T_\mathrm{min}(\varepsilon)]/T_\mathrm{d}} \int_{T_\mathrm{min}(\varepsilon)}^{T - T_\mathrm{min}(\varepsilon)} dT_L \, [T - T_L - T_\mathrm{min}(\varepsilon)] \mathrm{e}^{-(T_L - T_\mathrm{min}(\varepsilon))/T_0} \\ \approx \; -\frac{\pi}{2k_E v_F} \frac{T_\mathrm{d}^2}{1 + T_\mathrm{d}/T_0} \,. \end{aligned} \tag{5.44}$$

In our case the T_0 comes from the probability P_ac^o, i. e. according to Eq. (4.123) we have one term where formally $T_0 \to \infty$ and a second term with $T_0 = T_\mathrm{ac}/2$, leading to

$$\langle g_L \rangle / g_0 \approx -\frac{M_a M_b}{(M_a + M_b)^2} \left(1 - \frac{1}{1 + 2\, T_\mathrm{d}/T_\mathrm{ac}} \right) \,. \tag{5.45}$$

This formula relates the leading order quantum correction for the average conductance, the weak localization, to the total length of intervalley scattering ac boundary segments. The

ratio of the relevant time scales, namely the dwell time T_d, and the characteristic ac scattering time T_ac, Eq. (4.124), determines the size of the WL signal. It acts as a TRS restoring parameter, thus describing a crossover from the unitary to the orthogonal symmetry class with increasing ac scattering rate. With the approximate expressions for T_ac and T_d, Eqs. (4.125) and (5.20), respectively, the crossover parameter becomes

$$\frac{T_\mathrm{d}}{T_\mathrm{ac}} \approx \frac{W_\mathrm{ac}}{W_a + W_b} \,. \tag{5.46}$$

In experiments, the off-diagonal contributions to $\langle g \rangle$ are usually measured indirectly, as difference between the conductances at zero and finite magnetic field. For finite field, all (effective) TRS are broken and the system is in the unitary symmetry class. Quantum interference is washed out due to dephasing and only the diagonal (classical) conductance is left. Therefore a semiclassical expression for the magnetoconductance is desirable. The generalization of Eq. (5.45) to include a magnetic flux is straightforward, assuming that the magnetic field is small enough that it affects only the phases in Eq. (5.6), and we can neglect bending of the classical orbits as well as effects on the pseudospin. We consider a magnetic field of strength B, oriented perpendicular to the graphene plane. As discussed in Subsec. 4.3.3, the magnetic field induces a phase difference of $2\pi B A_L/\Phi_0$ between the orbits γ and $\gamma_\times$, where A_L is the directed area that the orbits enclose along the loop part L. This dephasing leads to an exponential suppression of long loops on a time scale T_B, defined in Eq. (4.158), so that the integral in Eq. (5.43) is modified as [cf. also Eqs. (4.156) and (4.157)]

$$\tilde{P}_g(\varepsilon, T) \approx \frac{v_F^2 \varepsilon}{\pi |\mathcal{V}|} \int\limits_{T_\mathrm{min}(\varepsilon)}^{T - T_\mathrm{min}(\varepsilon)} dT_L [T - T_L - T_\mathrm{min}(\varepsilon)] P_\mathrm{ac}^\mathrm{o}[T_L - T_\mathrm{min}(\varepsilon)] \mathrm{e}^{-[T_L - T_\mathrm{min}(\varepsilon)]/T_\mathrm{B}} \,. \tag{5.47}$$

Also here the minimum time has to be subtracted in the exponent, due to the correlation of the orbits within the encounter region, where no magnetic phase difference is accumulated. Since

$$P_\mathrm{ac}^\mathrm{o}(T)\, \mathrm{e}^{-T/T_\mathrm{B}} = \frac{1}{2} \left(\mathrm{e}^{-T/T_\mathrm{B}} - \mathrm{e}^{-T/T_\mathrm{B} - 2T/T_\mathrm{ac}} \right) , \tag{5.48}$$

we use Eq. (5.44) once with $T_0 = T_\mathrm{B}$ and once with $T_0 = (1/T_\mathrm{B} + 2/T_\mathrm{ac})^{-1}$ to get

$$\langle g_L \rangle / g_0 \approx - \frac{M_a M_b}{(M_a + M_b)^2} \left(\frac{1}{1 + T_\mathrm{d}/T_\mathrm{B}} - \frac{1}{1 + T_\mathrm{d}/T_\mathrm{B} + 2T_\mathrm{d}/T_\mathrm{ac}} \right) . \tag{5.49}$$

This central result represents the leading order (in inverse channel number) WL correction to the average magnetoconductance of a ballistic graphene cavity. Three competing timescales govern $\langle g_L \rangle$, namely the ac scattering time T_ac, Eq. (4.124), the dwell time T_d, Eq. (5.20), and the magnetic time T_B, Eq. (4.158). Equation (5.49) describes both, the crossover of $\langle g_L \rangle$ as a function of the armchair scattering rate, and the magnetodependence of the average conductance. In contrast to the crossover in the spectral form factor, Eq. (4.155), there is no

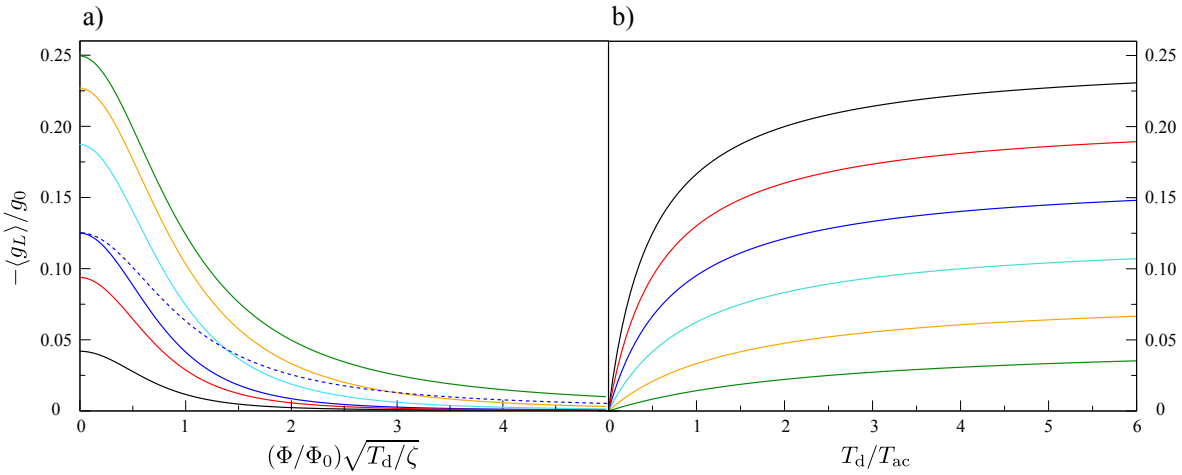

Figure 5.3: Absolute value of the WL correction obtained from our semiclassical theory for identical leads, Eq. (5.49). a) $-\langle g_L\rangle$ as a function of the magnetic flux Φ through the system. The curves correspond to different values of the effective armchair scattering strength $T_\mathrm{d}/T_\mathrm{ac}$ (from bottom to top): 0.1 (black), 0.3 (red), 0.5 (blue), 1.5 (turquoise), 5 (orange) and ∞ (green). The dashed blue line shows a Lorentzian curve $\sim \left[1+(\Phi^2 T_\mathrm{d})/(\Phi_0^2\zeta)\right]^{-1}$ for comparison. b) Crossover as a function of $T_\mathrm{d}/T_\mathrm{ac}$ for different values of $T_\mathrm{d}/T_\mathrm{B}$ (from top to bottom): 0 (black), 0.2 (red), 0.5 (blue), 1 (turquoise), 2 (orange) and 4 (green).

dependence on the Fermi momentum k_E (for fixed numbers of propagating lead channels). The total size of the WL signal is given by the value of $\langle g_L\rangle$ at zero magnetic field

$$\lim_{\Phi\to 0}\langle g_L\rangle/g_0 \approx -\frac{M_a M_b}{(M_a+M_b)^2}\frac{1}{1+T_\mathrm{ac}/(2T_\mathrm{d})}\,, \tag{5.50}$$

which reproduces our former results (5.32) and (5.40) for the limiting cases of infinite and zero $T_\mathrm{ac}/T_\mathrm{d}$, respectively.

For very strong ac scattering, $T_\mathrm{ac}\ll T_\mathrm{d}$, Eq. (5.49) yields the well-known Lorentzian magnetodependence [134, 150]

$$\lim_{T_\mathrm{ac}\to 0}\langle g_L\rangle/g_0 \approx -\frac{M_a M_b}{(M_a+M_b)^2}\frac{1}{1+T_\mathrm{d}/T_\mathrm{B}}\,, \tag{5.51}$$

describing the usual field induced symmetry breaking and the resulting COE $\to$ CUE transition. For identical leads the total WL signal in the limit of large channel numbers has then a size of approximately $-g_0/4$. On the other hand, for very weak ac scattering, $T_\mathrm{ac}\gg T_\mathrm{d}$, Eq. (5.49) becomes

$$\langle g_L\rangle/g_0 = -\frac{M_a M_b}{(M_a+M_b)^2}\frac{1}{(1+T_\mathrm{d}/T_\mathrm{B})^2}\frac{2T_\mathrm{d}}{T_\mathrm{ac}} + \mathcal{O}\left[(T_\mathrm{d}/T_\mathrm{ac})^2\right]\,. \tag{5.52}$$

This means we get a squared Lorentzian magnetodependence, linearly suppressed in $T_\mathrm{d}/T_\mathrm{ac}$. The magnetoconductance curves described by Eq. (5.52) are thus steeper and more narrow

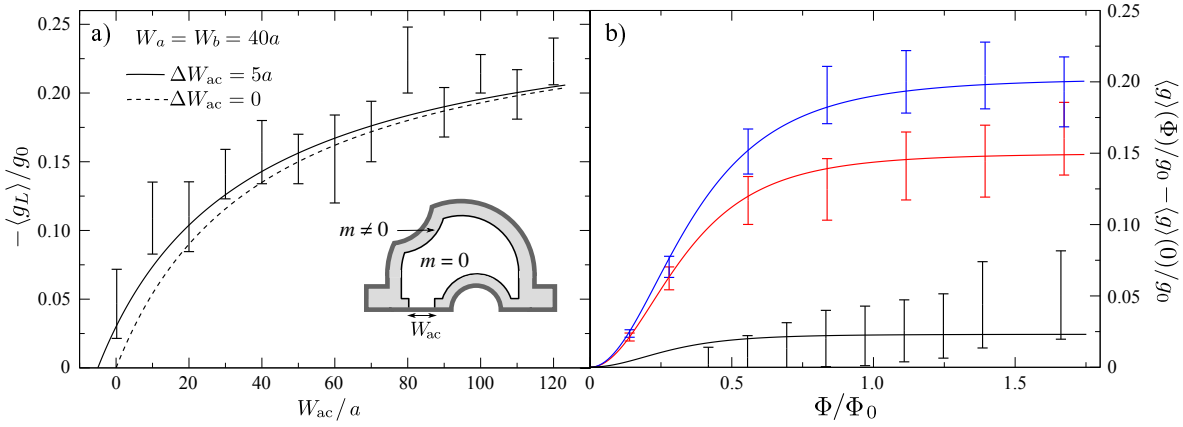

Figure 5.4: Comparison of the semiclassical theory for weak localization (solid and dashed lines) with numerical tight-binding simulations (error bars). For the numerics we use a system with a smooth mass edge, modeling infinite mass boundaries, and open this mass boundary in order to tune W_{ac} (cf. inset and text). For the geometrical parameters, as given in Fig. 5.1 b), we have used $R_1 = 300\,a, R_2 = 120\,a, R_3 = 180\,a, H = 110\,a$ and $d = 30\,a$, and for the mass parameters $\omega = 0.05\sqrt{t}/a$ and $W_m = 20\,a$. The two leads of the systems are identical with $W_a = W_b = 40\,a$. Panel b) shows three examples of the numerically calculated magnetoconductance for $W_{ac} = 0$ (black), $50\,a$ (red) and $110\,a$ (blue) (error bars). We find $\zeta = 0.17\,T_d$ and for the limiting value $\langle g_L \rangle(\Phi = 0, T_{ac} \to 0) = 0.27\,g_0$ from a fit of Eq. (5.49) to the numerical results for a system without mass boundary, that shows very strong intervalley scattering. Solid lines are fits to the semiclassical formula (5.49). Panel b) shows the absolute value of the WL correction as a function of W_{ac}. The numerical values (error bars) are obtained from the difference of $\langle g \rangle$ at zero flux and $\Phi \approx 1.4 - 1.7\,\Phi_0$. The solid (dashed) line displays the crossover as a function of W_{ac} obtained from the semiclassical theory, Eq. (5.50), including an offset $\Delta W_{ac} = 5\,a$ ($\Delta W_{ac} = 0$).

than Lorentzians with the same height. This means that the magnetic dephasing is essentially assisted by the partial TRS breaking. We stress once more that $\langle g_L \rangle$ is suppressed but not positive, i. e. there is no weak antilocalization, as discussed above for the case of vanishing ac scattering.

Figure 5.3 a) shows the dependence of the WL correction on the magnetic flux through the system for different values of the ratio T_d/T_{ac}. Note that we plot the WL correction as a function of $\sqrt{T_d/T_B} = \sqrt{T_d/\zeta}\,\Phi/\Phi_0$. Also in the regime of intermediate ac scattering, the Φ-dependence deviates from the Lorentzian shape [for comparison see dashed blue line in Fig. 5.3 a)]. As the ac scattering becomes stronger, the magnetoconductance gets closer to the Lorentzian behavior known from usual 2DEGs. Panel b) shows the crossover as a function of T_d/T_{ac} for the different values of the dephasing parameter T_d/T_B.

As mentioned, the Ehrenfest time T_E [see Eq. (5.37)] has been neglected in Eqs. (5.38) and (5.44). The Ehrenfest time is the typical time, after which a wave packet has spread over the whole cavity, so that it cannot be described by a classical particle anymore. After this time, quantum interference is possible [180]. Therefore T_E can be considered as time scale that separates the regime of classical dynamics, which typically lasts for times corresponding

to a few reflections from the boundary [52], from the regime of quantum interference. For Schrödinger systems it was first shown by means of field theoretical methods [181], that a finite Ehrenfest time leads to suppression of the WL correction. Semiclassical calculations for the Schrödinger equation that take into account finite T_E in the integral (5.44) yield for the loop contribution to the average conductance an exponential suppression [182, 183, 184, 185]

$$\frac{\langle g_L^\mathrm{S}\rangle}{g_0} \approx -\frac{M_a M_b}{(M_a+M_b)^2}\frac{\mathrm{e}^{-T_\mathrm{E}/T_\mathrm{d}}}{1+T_\mathrm{d}/T_\mathrm{B}}\,. \tag{5.53}$$

Since for graphene, the ac scattering time enters the integrals in a similar way as the magnetic dephasing time, the semiclassical calculation to include T_E is unchanged. Thus the WL is suppressed in the same way also here, namely we get an overall factor $\exp(-T_\mathrm{E}/T_\mathrm{d})$ in all our results for the WL, namely Eqs. (5.40), (5.45), and (5.49) - (5.52).

Comparison with numerical simulations

In Fig. 5.4 we compare our analytical results with the conductance obtained from numerical tight-binding simulations. We consider a graphene cavity with the shape of a desymmetrized half stadium, as depicted in the inset of Fig. 5.4 a) and in Fig. 5.1 b). In order to check our semiclassical predictions we tune the length of the ac boundary W_ac and thus T_ac. We model infinite mass type boundaries by adding a smooth mass term close to the edges of the system. In the tight-binding model, this corresponds to a staggered potential, i. e. an on-site potential $m(\boldsymbol{x})$ on sites of one sublattice and an on-site potential $-m(\boldsymbol{x})$ on the other sublattice. The mass is zero in the interior of the cavity and has a quadratic profile within a distance W_m from the boundary [see inset in Fig. 5.4 a)]

$$m(\boldsymbol{x}) = \frac{1}{2}\omega^2(\delta_b(\boldsymbol{x})-W_m)^2\,. \tag{5.54}$$

Here $\delta_b(\boldsymbol{x})$ is the shortest distance of the point $\boldsymbol{x}$ from the boundary (for details see Refs. [43, 60, 61]). In order to tune W_ac we cut a hole into the smooth mass so that locally a small region with ac edges is present [see Fig. 5.1 b) and inset in Fig. 5.4 a)]. Then we calculate the magnetoconductance numerically using an adaptive recursive Green function method [56] (Fig. 5.4 b) shows three examples) and obtain the numerical value of the WL correction from the difference of $\langle g\rangle$ at zero flux and $\Phi \approx 1.4 - 1.7\,\Phi_0$. On the other hand our semiclassical theory predicts the total height of the WL signal, see Eq. (5.50). In Fig. 5.4 a) we compare the absolute value of the WL correction obtained in both ways. We find that the numerical data reproduces our semiclassical theory well (dashed line). The agreement is even better if we assume an effective offset in W_ac of five lattice constants, $\Delta W_\mathrm{ac} = 5a$ (solid line). This offset can be explained by the fact that our smooth mass edges cannot completely avoid intervalley scattering from ac edges or sharp corners at the boundary, e. g. at the lead mouths [43, 60].

5.2 Universal conductance fluctuations

So far we have considered the averaged conductance, i. e. the smooth part of g. Now we address the quantum fluctuations around this average value, which are usually denoted as universal conductance fluctuations, because their order of magnitude does not scale with the average conductance or the system size, respectively. To quantify the size of the UCF, we calculate the variance of the conductance g_{ab}, which is identical to the covariance of the resistances g_{aa} and g_{bb} [185]:

$$\mathrm{var}(g_{ab}) = \langle g_{ab}^2 \rangle - \langle g_{ab} \rangle^2 = \mathrm{covar}(g_{aa}, g_{bb}) \tag{5.55}$$

$$\mathrm{covar}(g_{aa}, g_{bb}) = \langle g_{aa} g_{bb} \rangle - \langle g_{aa} \rangle \langle g_{bb} \rangle \,. \tag{5.56}$$

Here the RMT prediction and its expansion for many propagating lead channels reads [69, 148, 149]

$$\begin{aligned} \mathrm{var}(g_{ab})/g_0^2 &= \frac{2M_aM_b\,(M_a - 1 + 2/\beta)(M_b - 1 + 2/\beta)}{\beta(M_a + M_b - 2 + 2/\beta)(M_a + M_b - 1 + 4/\beta)(M_a + M_b - 1 + 2/\beta)^2} \\ &= \frac{2M_aM_b}{\beta(M_a + M_b)^4} + \mathcal{O}\left(M_{a/b}^{-1}\right) , \end{aligned} \tag{5.57}$$

which has been confirmed semiclassically for Schrödinger systems [134, 185, 186].

We consider the first term in Eq. (5.56), the averaged product of resistances. According to Eq. (5.6), multiplication of two non-local resistivities results in the fourfold sum over classical orbits

$$\sigma_{aa}\sigma_{bb} = \left(\frac{e^2 v_F^2}{16\pi^2\hbar^2}\right)^2 \sum_{\gamma\gamma'(a)} \sum_{\rho\rho'(b)} X_{\gamma,\gamma',\rho,\rho'} D_\gamma D_{\gamma'} D_\rho D_{\rho'} \exp\left(\mathrm{i}k_E \delta L_{\gamma,\gamma'} + \mathrm{i}k_E \delta L_{\rho,\rho'}\right) , \tag{5.58}$$

with the pseudospin-dependent term

$$X_{\gamma,\gamma',\rho,\rho'} = \mathrm{Tr}\left(\sigma_{\boldsymbol{a}} K_\gamma \sigma_{\boldsymbol{a}} K_{\gamma'}^\dagger\right) \mathrm{Tr}\left(\sigma_{\boldsymbol{b}} K_\rho \sigma_{\boldsymbol{b}} K_{\rho'}^\dagger\right) . \tag{5.59}$$

In the sums of Eq. (5.58), the orbits γ and γ' originate from the same point $\boldsymbol{x}_a'$ in lead a and end at the same point $\boldsymbol{x}_a$ also in lead a, as can be seen from the arguments of the Green functions in Eq. (5.5). The orbits ρ and ρ', on the other hand, both begin at $\boldsymbol{x}_b'$ in lead b and end at $\boldsymbol{x}_b$ in lead b. For the expression (5.58), the averaging procedure gives only a significant result when the *sum of the length differences* $\delta L_{\gamma,\gamma'}$ and $\delta L_{\rho,\rho'}$ is small or vanishing. One possible combination of orbits that fulfills this is, when the two orbits from each lead are correlated, i. e. the pairs (γ, γ') and (ρ, ρ'), and both have small length differences, while orbits from different leads are uncorrelated. In other words, when $\delta L_{\gamma,\gamma'}$ and $\delta L_{\rho,\rho'}$ are both small individually. However, these contributions are fully contained in the second term in Eq. (5.56), namely the product of averaged resistances, and thus cancel. This also means that there is no diagonal contribution to the UCF, since the diagonal terms correspond to $\gamma' = \gamma$ and $\rho' = \rho$. Combinations like $\gamma' = \rho$ and $\rho' = \gamma$ are not possible, since

the orbits begin and end in different leads. Therefore the UCF are a pure quantum effect, like the weak localization. Consequently we have to consider orbit quadruplets in which only the complete phase in Eq. (5.58) is small, but not the individual phases. It is known for Schrödinger systems that the variance of g_{ab} is independent of the Ehrenfest time [185], and since our discussion of the WL has shown that the semiclassical calculations for graphene are identical to the Schrödinger case in this respect, we neglect the Ehrenfest time here. The leading order contribution is then due to orbit quadruplets as sketched in Fig. 5.5 [185]. For example in panel a) two orbits from different leads, say γ and ρ, cross each other with a crossing angle ε_1 and then cross each other again, now with a crossing angle ε_2. The two other orbits follow the first ones exponentially closely, but avoid the crossings. For instance γ' follows γ to the first crossing, then it follows ρ to the second crossing and finally again γ back to the lead [see Fig. 5.5 a) and b)]. We label the individual pieces with m, n, o, p, q, r as marked in Fig. 5.5 a) and denote the combination of the pieces r and q^{-1}, which is q traversed in opposite direction, by the loop part L. The parts m, n, o and p are denoted as legs. We point out that also quadruplets where two orbits from different leads cross first and then avoid the second crossing (or vice versa) while the two other orbits avoid the first crossing and cross then (or vice versa) give rise to a contribution to the UCF in leading order [see Fig. 5.5 c) and d)]. The difference between the quadruplets in Fig. 5.5 a) and b) is the parallel and antiparallel propagation direction of the blue and the red orbit segments, respectively, along the loop part. The same holds for panels c) and d). For Schrödinger billiards this difference is only important in the presence of a magnetic field, since only for the quadruplets in b) and d) there is an overall Aharonov-Bohm phase difference. For graphene billiards, however, the pseudospin-dependent phases differ also at zero field.

We calculate now the product of pseudospin traces $X_{\gamma,\gamma',\rho,\rho'}$. As for $Y_{\gamma,\gamma'}$ before, we first consider quadruplets where all orbits hit only ac and im type edges. Then we have for the sublattice part of the first trace in (5.59) according to Eq. (3.94)

$$\begin{aligned}
\mathrm{Tr}\left(\sigma_{\boldsymbol{a}} K_\gamma^\sigma \sigma_{\boldsymbol{a}} K_{\gamma'}^{\sigma\dagger}\right) &= \mathrm{Tr}\left(\sigma_{\boldsymbol{a}} \sigma_z^{N_\gamma} \mathrm{e}^{\mathrm{i}\theta_\gamma \sigma_z} (1+\sigma_{\boldsymbol{\alpha}_1 \boldsymbol{x}'_a}) \sigma_{\boldsymbol{a}} (1+\sigma_{\boldsymbol{\alpha}_1 \boldsymbol{x}'_a}) \mathrm{e}^{-\mathrm{i}\theta_{\gamma'}\sigma_z} \sigma_z^{N_{\gamma'}}\right) \\
&= (-1)^{N_\gamma} \mathrm{i}^{N_\gamma + N_{\gamma'}} \mathrm{Tr}\left[\mathrm{e}^{-\mathrm{i}(\theta_\gamma + \theta_{\gamma'} + N_\gamma \pi/2 + N_{\gamma'}\pi/2)\sigma_z} \left(1 + [\sigma_{\boldsymbol{a}} \sigma_{\boldsymbol{\alpha}_1 \boldsymbol{x}'_a}]^2\right)\right] \\
&= (-1)^{N_\gamma} \mathrm{i}^{N_\gamma + N_{\gamma'}} 4 \cos(\theta'_a) \cos(\theta'_a - \theta_\gamma - \theta_{\gamma'} - (N_\gamma + N_{\gamma'})\pi/2)\,, \qquad (5.60)
\end{aligned}$$

where $\theta'_a = \varphi_{\boldsymbol{\alpha}_1 \boldsymbol{x}'_a} - \varphi_a$ is the angle of the incoming trajectory segment of the orbits γ and γ', relative to lead a [cf. Eq. (5.13)]. Next we make use of the identities

$$\begin{aligned}
\theta_\gamma + \theta_{\gamma'} &= 2\theta_\gamma + \theta_q - \theta_r\,, & (5.61)\\
\theta_q - \theta_r &= (N_{q,+} - N_{q,-} - N_{r,+} + N_{r,-})\frac{\pi}{2} - w_q\pi + w_r\pi + \mathcal{O}(\varepsilon_{1,2})\,, & (5.62)\\
\text{and} \qquad 0 &= (\theta'_a - \theta_a - 2\theta_\gamma + (N_\gamma + 1)\pi) \mod 2\pi\,, & (5.63)
\end{aligned}$$

with the angle of outgoing trajectory segments of the orbits γ and γ' relative to lead a, $\theta_a = \varphi_{\boldsymbol{x}_a \boldsymbol{\alpha}_N} - \varphi_a + \pi$ [cf. Eq. (5.14)]. The winding numbers of the parts q and r are denoted by w_q and w_r, and the signs in the subscripts of the reflection numbers stand for reflections

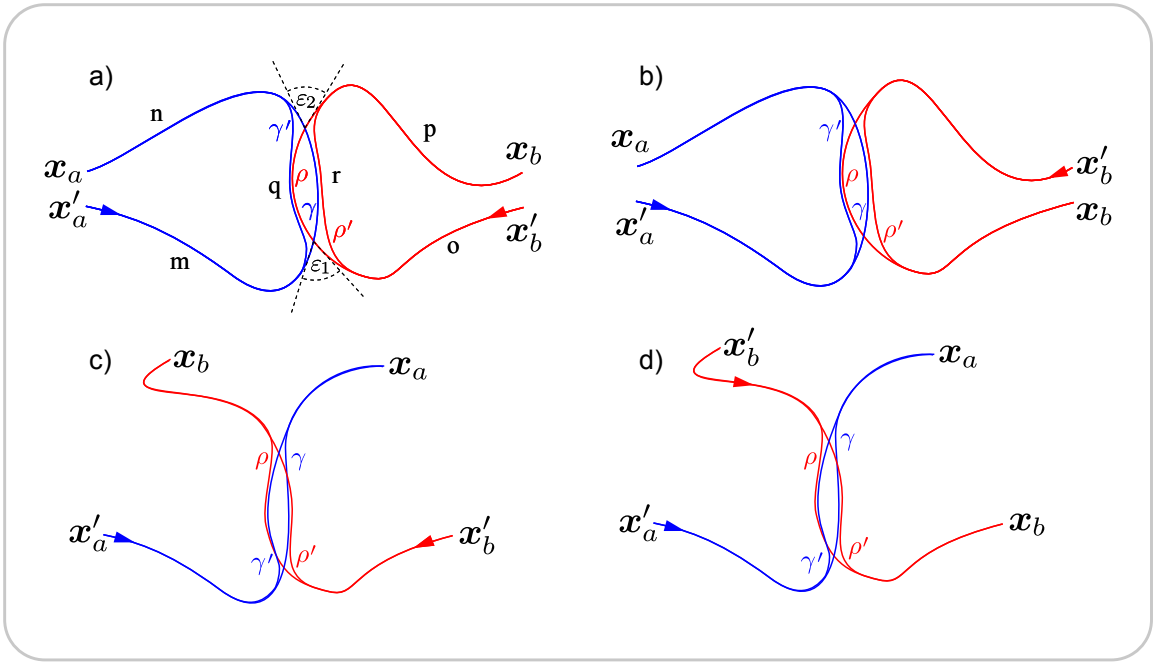

Figure 5.5: Schematic view of orbit quadruplets that give rise to the covariance (5.56) in leading order. Each quadruplet has two (avoided) crossings of orbits from different leads. The pieces of the orbits before, after, and between the crossings are labeled with letters m to r (cf. text). In the quadruplets of panels a) and b) the orbits γ and ρ cross twice, while γ' and ρ' avoid both crossings. In c) and d) both pairs have one crossing. In panels a) and c) the propagation direction along the part r (q) of the orbits is the same for γ (γ') and ρ' (ρ), while it is opposite in panels b) and d).

with positive and negative reflection angles θ_i, respectively [cf. Eq. (4.103)]. With Eqs. (5.60) - (5.63) we obtain

$$\mathrm{Tr}\left(\sigma_{\boldsymbol{a}} K^{\sigma}_{\gamma} \sigma_{\boldsymbol{a}} K^{\sigma\dagger}_{\gamma'}\right) = 4\,(-1)^{w_q+w_r+N_{q,+}+N_{r,-}+1}\,\mathrm{i}^{N_q+N_r}\cos(\theta_a)\cos(\theta'_a)\,. \tag{5.64}$$

Note that the phase factors depend only on properties of the loop part but not on the legs. For the second trace we perform an analogous calculation to get

$$\mathrm{Tr}\left(\sigma_{\boldsymbol{a}} K^{\sigma}_{\rho} \sigma_{\boldsymbol{a}} K^{\sigma\dagger}_{\rho'}\right) = 4\,(-1)^{w_q+w_r+N_{q,\mp}+N_{r,\pm}+1}\,\mathrm{i}^{N_q+N_r}\cos(\theta_b)\cos(\theta'_b)\,, \tag{5.65}$$

where the upper signs hold if the propagation directions of ρ and ρ' along the corresponding parts of the loop, i. e. q and r, respectively, are equal to the propagation directions of γ and γ' (panels a) and c) in Fig. 5.5), while the lower signs hold in the opposite case (panels b) and d) in Fig. 5.5). In the following we speak about parallel and antiparallel propagation in this context. This means we get for the total sublattice part of the pseudospin contribution

$$X^{\sigma}_{\gamma,\gamma',\rho,\rho'} = (\pm 1)^{N_L}\,16\cos(\theta_a)\cos(\theta'_a)\cos(\theta_b)\cos(\theta'_b)\,, \tag{5.66}$$

where the upper sign holds for parallel propagation of γ (γ') and ρ' (ρ) in the loop and the lower sign for antiparallel propagation. Using the same relations as for the pseudospin traces for the spectral form factor, see Sec. 4.3, and the average conductance, cf. Eqs. (5.17) and (5.18), one shows that the result (5.66) remains unchanged if reflections from zz edges are involved.

Next we calculate the valley part $X^{\tau}_{\gamma,\gamma',\rho,\rho'}$. Also here we have to distinguish the cases of parallel and antiparallel loop propagation. From Eq. (3.94) we get that $X^{\tau}_{\gamma,\gamma',\rho,\rho'} = 0$ if the loop part L contains an odd number of ac reflections, while for an even number of ac reflections along L we get for the parallel case

$$X^{\tau}_{\gamma,\gamma',\rho,\rho'} = \left|\mathrm{Tr}\left(K^{\tau}_{r} K^{\tau\dagger}_{q}\right)\right|^2 = 4\cos^2(2K\Lambda_L + \vartheta_L + N_L\,\pi/2) \tag{5.67}$$

and for the antiparallel case

$$X^{\tau}_{\gamma,\gamma',\rho,\rho'} = \mathrm{Tr}\left(K^{\tau}_{r} K^{\tau\dagger}_{q}\right)\mathrm{Tr}\left(K^{\tau}_{q^{-1}} K^{\tau\dagger}_{r^{-1}}\right) = 4(-1)^{N_L}\cos^2(2K\Lambda_L + \vartheta_L + N_L\,\pi/2)\,. \tag{5.68}$$

Finally we combine the results for sublattice and valley part, Eqs. (5.66) - (5.68), to get for the complete pseudospin contribution

$$X_{\gamma,\gamma',\rho,\rho'} = 64\cos(\theta_a)\cos(\theta'_a)\cos(\theta_b)\cos(\theta'_b)\cos^2(2K\Lambda_L + \vartheta_L + N_L\pi/2)\,, \tag{5.69}$$

if $N_{\mathrm{ac},L}$ is even, and $X_{\gamma,\gamma',\rho,\rho'} = 0$ otherwise. As for the average conductance and the spectral form factor, we distinguish different degrees of valley coupling when calculating $\mathrm{var}(g)$.

No ac scattering - valley conservation

Assuming that all reflections occur at zz or im edges, i. e. $N_{\mathrm{ac},L} = 0$ and thus always even, all quadruplets contribute to the UCF, and with $\Lambda_L = 0$ we get from Eq. (5.69) for the averaged pseudospin contribution

$$\begin{aligned}\langle X_{\gamma,\gamma',\rho,\rho'}\rangle &= 64\cos(\theta_a)\cos(\theta'_a)\cos(\theta_b)\cos(\theta'_b)\langle\cos^2(\vartheta_L + N_L\pi/2)\rangle \\ &= 32\cos(\theta_a)\cos(\theta'_a)\cos(\theta_b)\cos(\theta'_b)\,.\end{aligned} \tag{5.70}$$

We proceed as for the loop contribution to the average conductance. That means we use the sum rule (5.19), now twice, and replace the orbit sums in Eq. (5.58) by integrals over orbit periods, crossing angles, and integrals over the incoming and outgoing angles. Further we make use of the fact that the two orbit intersections are independent and thus their contributions factorize [177, 185], so that we can treat the ε-integrals separately. For zero magnetic field Eq. (5.58) then leads to

$$\mathrm{var}(\sigma_{ab}) \approx \left(\frac{g_0 W_a W_b}{W_a + W_b}\frac{4k_E}{\pi T_{\mathrm{d}}}\,\mathfrak{Re}\int_0^{\pi} d\varepsilon \int_{2T_{\min}(\varepsilon)}^{\infty} dT\,\mathrm{e}^{-[T-T_{\min}(\varepsilon)]/T_{\mathrm{d}}} P_g(\varepsilon,T)\,\mathrm{e}^{\mathrm{i}k_E\delta L(\varepsilon)}\right)^2 . \tag{5.71}$$

We have evaluated the real parts twice and included a factor of two due to the time reversed quadruplets (parallel and antiparallel loop propagation, cf. Fig. 5.5). Up to a constant factor, we had exactly the same expression already for the average conductance, namely in Eq. (5.35), so that with Eq. (5.38) we obtain directly

$$\mathrm{var}(\sigma_{ab}) \approx 4\frac{M_a^2 M_b^2}{(M_a+M_b)^4}\,, \tag{5.72}$$

in agreement with four times the leading order RMT result (5.57) for the unitary ensemble (CUE). As for the corresponding results for the spectral form factor, Eqs. (4.111) and (4.137), the factor of four is due to the Kramers degeneracy of the uncoupled valleys, which originates from the preserved symmetry $\mathcal{T}_x$ (at zero magnetic field). From Eq. (5.56), we see that the degeneracy of the two subsystems leads to a fourfold enhanced variance, compared to the variance of only one subsystem.

Ac billiards - complete valley mixing

In the opposite limit of complete valley mixing, we assume that all reflections occur at ac edges, so that $\vartheta_L = 0$, $N_L = N_{\mathrm{ac},L}$, and thus only orbit quadruplets with even N_L have a non-vanishing pseudospin contribution. Using Eq. (4.114), we find that the squared cosine in Eq (5.69) averages to 1/2 for the remaining quadruplets, and altogether we get

$$\langle X_{\gamma,\gamma',\rho,\rho'}\rangle = 16\cos(\theta_a)\cos(\theta_a')\cos(\theta_b)\cos(\theta_b')\,. \tag{5.73}$$

The conductance variance is thus half as large as in the previous case,

$$\mathrm{var}(\sigma_{ab}) \approx 2\frac{M_a^2 M_b^2}{(M_a+M_b)^4}\,, \tag{5.74}$$

in agreement with the leading order RMT prediction (5.57) for COE ($\beta = 1$), as expected from our earlier results. The valley coupling has effectively re-enabled the TRS $\mathcal{T}_y$.

Mixed boundaries - generic case

Finally we consider the general case of intermediate valley coupling, taking into account orbit quadruplets with reflections from ac, zz, and im type edges. From our earlier discussion, we know that the averaged pseudospin traces are zero if $N_{\mathrm{ac},L}$ is odd, and otherwise the pseudospin contribution is given by Eq. (5.70). For the correct evaluation of the orbit sums (5.58), we have to account for the fact that an even number of ac reflections along the loop part $L = r + q^{-1}$ corresponds to either an even number of ac reflections in both parts, r and q, or an odd number of ac reflections in both of them. Since the two crossings are nevertheless

independent, we get similar to Eq. (5.71)

$$\begin{aligned}\mathrm{var}(\sigma_{ab}) \;\approx\; & \left(\frac{g_0 W_a W_b}{W_a+W_b}\frac{4k_E}{\pi T_\mathrm{d}}\right)^2 \mathfrak{Re}\int\limits_0^\pi d\varepsilon_1 \int\limits_{2T_\mathrm{min}(\varepsilon_1)}^\infty dT_1\, \mathrm{e}^{-[T_1-T_\mathrm{min}(\varepsilon_1)]/T_\mathrm{d}}\mathrm{e}^{\mathrm{i}k_E\delta L_1} \\ & \times\mathfrak{Re}\int\limits_0^\pi d\varepsilon_2 \int\limits_{2T_\mathrm{min}(\varepsilon_2)}^\infty dT_2\, \mathrm{e}^{-[T_2-T_\mathrm{min}(\varepsilon_2)]/T_\mathrm{d}}\, \mathrm{e}^{\mathrm{i}k_E\delta L_1}\breve{P}_g(\varepsilon_1,\varepsilon_2,T_1,T_2)\,, \qquad (5.75)\end{aligned}$$

where $\breve{P}_\mathrm{ac}(\varepsilon_1,\varepsilon_2,T_1,T_2)$ is the density of two uncorrelated crossings, such that ac edges are hit either an even number of times during both the r and the q part of the loop, or an odd number of times during both parts,

$$\begin{aligned}\breve{P}_g(\varepsilon_1,\varepsilon_2,T_1,T_2) \;\approx\; & \left(\frac{v_F^2\varepsilon}{\pi|\mathcal{V}|}\right)^2 \int\limits_{T_\mathrm{min}(\varepsilon_1)}^{T_1-T_\mathrm{min}(\varepsilon_1)} dT_q \int\limits_{T_\mathrm{min}(\varepsilon_2)}^{T_2-T_\mathrm{min}(\varepsilon_2)} dT_r [T_1-T_q-T_\mathrm{min}(\varepsilon_1)][T_2-T_r-T_\mathrm{min}(\varepsilon_2)] \\ & \times P_\mathrm{ac}^\mathrm{e}[T_q+T_r-T_\mathrm{min}(\varepsilon_1)-T_\mathrm{min}(\varepsilon_2)]\,. \qquad (5.76)\end{aligned}$$

Here we have used that [cf. Eq. (4.123)]

$$P_\mathrm{ac}^\mathrm{o}(T)P_\mathrm{ac}^\mathrm{o}(T') + P_\mathrm{ac}^\mathrm{e}(T)P_\mathrm{ac}^\mathrm{e}(T') = P_\mathrm{ac}^\mathrm{e}(T+T')\,. \qquad (5.77)$$

Once more we make use of the formula (5.44), to find for the conductance variance of a ballistic graphene cavity with ac, zz, and im type edges for zero magnetic field

$$\frac{\mathrm{var}(g_{ab})}{g_0^2} \approx \frac{2M_a^2M_b^2}{(M_a+M_b)^4}\left[1+\frac{1}{(1+2\,T_\mathrm{d}/T_\mathrm{ac})^2}\right]. \qquad (5.78)$$

The crossover described by this equation is different from the one for the average conductance, Eq. (5.50). Also here we have no explicit dependence on k_E, but, as for the spectral form factor, degeneracies due to the valley symmetry are reflected in Eq. (5.78). For identical leads we get for $\mathrm{var}(g_{ab})/g_0^2$ a crossover from 1/4 to 1/8 for an increasing ac scattering rate $1/T_\mathrm{ac}$. This corresponds to a transition from two degenerate unitary subsystems (4×CUE) to one orthogonal system (COE).

For a finite magnetic flux through the cavity we have to modify the densities accordingly, as in the previous cases. However, as mentioned in the beginning of this section, not all quadruplets are affected by the magnetic field, because there is only a flux induced phase difference, if the loop part is propagated in opposite directions by the different orbits. Thus for the variance we get one half of the zero flux result, namely from quadruplets as in Fig. 5.5 a) and c), plus the contribution from the quadruplets that are affected by the magnetic dephasing, i. e. such of Fig. 5.5 b) and d). Technically, the inclusion of the magnetic field is identical to the case of the average conductance, cf. Eqs. (5.47) - (5.49), leading to

$$\frac{\mathrm{var}(g_{ab})}{g_0^2} = \frac{M_a^2M_b^2}{(M_a+M_b)^4}\left[1+\frac{1}{(1+2T_\mathrm{d}/T_\mathrm{ac})^2}+\frac{1}{(1+T_\mathrm{d}/T_\mathrm{B})^2}+\frac{1}{(1+T_\mathrm{d}/T_\mathrm{B}+2T_\mathrm{d}/T_\mathrm{ac})^2}\right], \qquad (5.79)$$

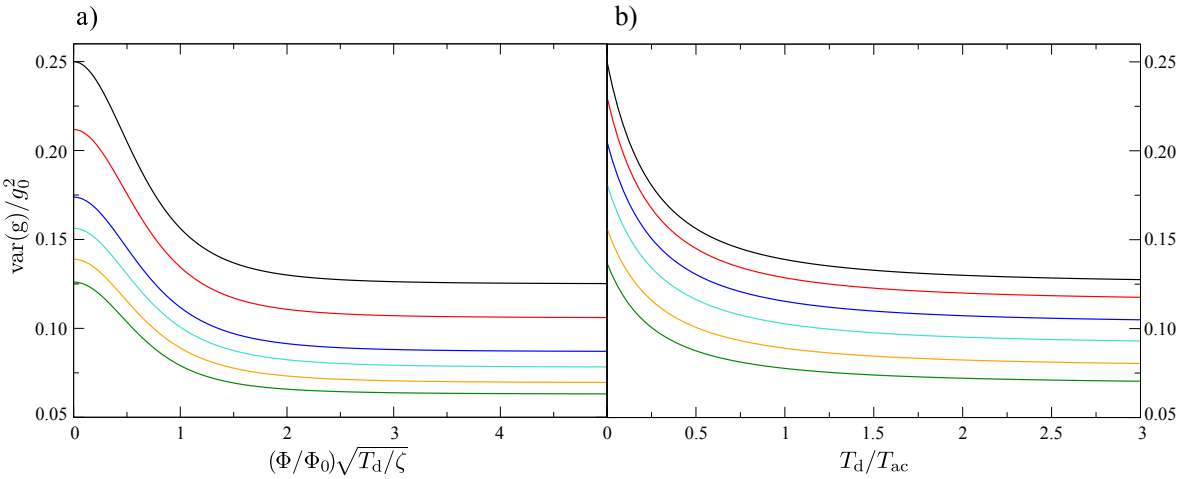

Figure 5.6: a) Variance of the conductance as a function of the magnetic flux Φ through the system obtained from our semiclassical theory, Eq. (5.79), for identical leads. The curves correspond to different values of the relative armchair scattering strength $T_\mathrm{d}/T_\mathrm{ac}$ (from top to bottom): 0 (black), 0.1 (red), 0.3 (blue), 0.5 (turquoise), 1 (orange) and 5 (green). b) The crossover as a function of $T_\mathrm{d}/T_\mathrm{ac}$ for different values of the magnetic flux $\Phi/\Phi_0\sqrt{T_\mathrm{d}/\zeta}$ (from top to bottom): 0 (black), 0.3 (red), 0.5 (blue), 0.7 (turquoise), 1 (orange) and 1.5 (green).

which is the main result of this section. Although the underlying physical mechanisms that give rise to the terms with T_B and T_ac are rather different, namely Aharonov-Bohm like dephasing and intervalley scattering, respectively, the two time scales occur in a very symmetric way in the final result (5.79), hence both have the same effect on the conductance variance. Note that the opposite is true for the weak localization, see Eq. (5.49), where an increasing magnetic dephasing rate $1/T_\mathrm{B}$ suppresses the WL effect, while an increasing ac scattering rate $1/T_\mathrm{ac}$ increases the absolute value of $\langle g_L \rangle$. For identical leads and $T_\mathrm{ac} \to \infty$, Eq. (5.79) describes a crossover from 1/4 to 1/8 with increasing flux Φ, i. e. from two degenerate unitary subsystems (4×CUE) to two independent unitary subsystems (2×CUE). On the other hand for $T_\mathrm{ac} \to 0$ we get a crossover from 1/8 to 1/16, i. e. a transition from an orthogonal (COE) to a unitary (CUE) system. This is in agreement with our findings for the average conductance and the spectral form factor. In Fig. 5.6 we show our semiclassical result (5.79) graphically. The magnetodependence of the conductance variance for different values of the ac scattering time T_ac is depicted in panel a). Panel b) shows the dependence of var(g) on the ratio $T_\mathrm{d}/T_\mathrm{ac}$ for different values of the magnetic flux.

In Fig. 5.7 we compare the semiclassical results (solid lines) for the conductance variance with tight-binding calculations (error bars). The system used for the numerical simulations is the same as we used for the average conductance. We find that Eq. (5.79) provides a good approximation to the numerical data.

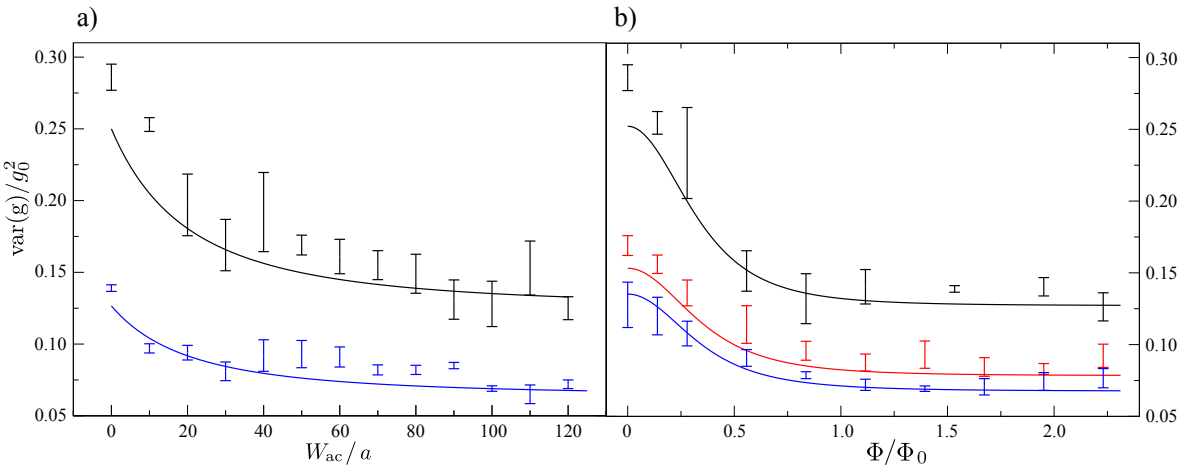

Figure 5.7: Comparison of our semiclassical theory, Eq. (5.79), with numerical tight-binding simulations. For the numerics we used the same system as for the average conductance. a) The crossover as a function of W_{ac} obtained from the semiclassical theory Eq. (5.79) (solid lines) and from the numerical data (error bars) at zero magnetic flux $\Phi = 0$ (upper black curve) and at finite flux $\Phi = 1.4\,\Phi_0$ (lower blue curve). b) Dependence of the numerical data on the magnetic flux (error bars) for systems with (from top to bottom) $W_{\mathrm{ac}} = 0$ (black), $50\,a$ (red) and $110\,a$ (blue). We find that $\zeta \approx 0.25\,T_{\mathrm{d}}$ fits the data well. The solid lines show the semiclassical result of Eq. (5.79).

5.3 Shot noise

As a last important transport property, we discuss briefly the shot noise of a ballistic graphene cavity, which contains information about temporal fluctuations in the current that are not present in the stationary conductance [69]. These fluctuations arise due to the quantized nature of the electric charge. Usually the shot noise is quantified via the *Fano factor* $\mathcal{F}$, which is defined as the ratio of the *shot noise power* S of the system and the Poissonian (classical) shot noise power S_P. The latter corresponds to charge carriers being transmitted in an uncorrelated way from one lead to the other. One example for a system with Poissonian shot noise, i. e. with $\mathcal{F} = 1$, are tunnel diodes [69]. Although in general the noise power cannot be obtained from the conductance, it can still be expressed in terms of the transmission amplitudes, $t = t_{ab}$, of the scattering matrix connecting the leads a and b [187]:

$$S = \frac{2e^3|V|}{\hbar\pi}\mathrm{Tr}\left(tt^\dagger - tt^\dagger tt^\dagger\right), \tag{5.80}$$

$$S_P = \frac{2e^3|V|}{\hbar\pi}\mathrm{Tr}\left(tt^\dagger\right), \tag{5.81}$$

with the applied bias voltage V. Therefore the Fano factor, which describes the quantum suppression of the shot noise with respect to the classical value, is given by

$$\mathcal{F} = \frac{S}{S_P} = \frac{\mathrm{Tr}\left(tt^\dagger - tt^\dagger tt^\dagger\right)}{\mathrm{Tr}\left(tt^\dagger\right)}. \tag{5.82}$$

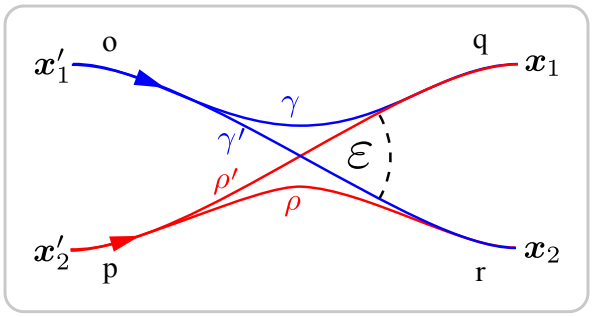

Figure 5.8: Sketch of the orbit quadruplets contributing to the shot noise in leading off-diagonal order. As opposed to the UCF, only one crossing is present. Orbits that begin at the same point, end in general at different points.

Random matrix theory for the scattering matrix predicts [149, 188]

$$\mathcal{F} = \frac{(M_a - 1 + 2/\beta)(M_b - 1 + 2/\beta)}{(M_a + M_b - 2 + 2/\beta)(M_a + M_b - 1 + 4/\beta)} = \frac{M_a M_b}{(M_a + M_b)^2} + \mathcal{O}(M_{a/b}^{-1})\,. \tag{5.83}$$

This means, to leading order the Fano factor does not depend on the symmetry class. Semiclassical calculations for shot noise in ballistic Schrödinger billiards lead to results coinciding with the RMT prediction [186, 189, 190, 191, 192]. In App. A.5.2 we show that

$$\mathrm{Tr}\left(tt^\dagger\right) = -\frac{h}{e^2}\int\limits_{C_a} dy \int\limits_{C_b} dy'\ \sigma_{ab}(\boldsymbol{x}, \boldsymbol{x'})\,, \tag{5.84}$$

with σ_{ab} as defined in Eq. (5.5), and further

$$\mathrm{Tr}\left(tt^\dagger tt^\dagger\right) = \int\limits_{C_a} dy_1 \int\limits_{C_a} dy_2 \int\limits_{C_b} dy'_1 \int\limits_{C_b} dy'_2\ \tilde{\sigma}_{ab}(\boldsymbol{x}_1, \boldsymbol{x}_2, \boldsymbol{x}'_1, \boldsymbol{x}'_2)\,, \tag{5.85}$$

with

$$\tilde{\sigma}_{ab}(\boldsymbol{x}_1, \boldsymbol{x}_2, \boldsymbol{x}'_1, \boldsymbol{x}'_2) = \mathrm{Tr}\left[\sigma_{\boldsymbol{a}} G(\boldsymbol{x}_1, \boldsymbol{x}'_1)\sigma_{\boldsymbol{b}} G^\dagger(\boldsymbol{x}_2, \boldsymbol{x}'_1)\sigma_{\boldsymbol{a}} G(\boldsymbol{x}_2, \boldsymbol{x}'_2)\sigma_{\boldsymbol{b}} G^\dagger(\boldsymbol{x}_1, \boldsymbol{x}'_2)\right]\,. \tag{5.86}$$

Inserting the semiclassical Green function (3.83) into Eq. (5.86), we obtain the fourfold sum

$$\tilde{\sigma}_{ab}(\boldsymbol{x}_1, \boldsymbol{x}_2, \boldsymbol{x}'_1, \boldsymbol{x}'_2) = \left(\frac{v_F^2}{8\pi\hbar}\right)^2 \sum_{\gamma\gamma'}\sum_{\rho\rho'} W_{\gamma,\gamma',\rho,\rho'} D_\gamma D_{\gamma'} D_\rho D_{\rho'} \exp\left[\mathrm{i}k_E \delta L_{\gamma,\gamma'} + \mathrm{i}k_E \delta L_{\rho,\rho'}\right]\,, \tag{5.87}$$

similar as for the UCF, but with

$$W_{\gamma,\gamma',\rho,\rho'} = \mathrm{Tr}\left(\sigma_{\boldsymbol{a}} K_\gamma \sigma_{\boldsymbol{b}} K_{\gamma'}^\dagger \sigma_{\boldsymbol{a}} K_\rho \sigma_{\boldsymbol{b}} K_{\rho'}^\dagger\right)\,. \tag{5.88}$$

We note that with respect to the pseudospin dependence, the difference between UCF, Eq. (5.59), and shot noise, Eq. (5.88), is very similar to the difference between spectral form

factor, Eq. (4.83), and conductance, Eq. (5.7). For the UCF the contributing classical orbits came in pairs with the same starting *and* end points. Here, the orbits with the same starting point have in general different end points and vice versa. The orbit γ starts at a point $\boldsymbol{x}_1'$ in lead b and ends at a point $\boldsymbol{x}_1$ in lead a, while γ' starts also at $\boldsymbol{x}_1'$ but ends at a point $\boldsymbol{x}_2$ in lead a. The orbits ρ and ρ' both begin at a point $\boldsymbol{x}_2'$ in lead b and ρ ends at $\boldsymbol{x}_2$ while ρ' ends at $\boldsymbol{x}_1$. The diagonal contribution corresponds to quadruplets where either $\gamma = \gamma'$ and $\rho = \rho'$, or $\gamma = \rho'$ and $\rho = \gamma'$. However, this is only possible if either the end points are equal $\boldsymbol{x}_1 = \boldsymbol{x}_2$ or the starting points $\boldsymbol{x}_1' = \boldsymbol{x}_2'$. One can show that in this case $\mathrm{Tr}\left(tt^\dagger tt^\dagger\right) = \mathrm{Tr}\left(tt^\dagger\right)$ [189, 190], and thus the Fano factor $\mathcal{F}$ is zero in diagonal approximation. This corresponds to the classical limit, where no quantum shot noise exists. The leading order contribution to $\mathcal{F}$ is known to originate from diagrams as sketched in Fig. 5.8 [189, 190]. For these quadruplets the valley part of the pseudospin trace does not depend on the edge type at all, similar as for the diagonal contribution to the average conductance, namely

$$\mathrm{Tr}\left(K_\gamma^\tau K_{\gamma'}^{\tau\dagger} K_\rho^\tau K_{\rho'}^{\tau\dagger}\right) = \mathrm{Tr}\left(K_q^\tau K_o^\tau K_o^{\tau\dagger} K_r^{\tau\dagger} K_r^\tau K_p^\tau K_p^{\tau\dagger} K_q^{\tau\dagger}\right) = 2\,,$$

due to the unitarity of the individual propagators. Also for the sublattice part, we do not find such an edge dependence. A calculation very similar to the one for the average conductance and the UCF results in

$$\mathrm{Tr}\left(\sigma_{\boldsymbol{a}} K_\gamma^\sigma \sigma_{\boldsymbol{b}} K_{\gamma'}^{\sigma\dagger} \sigma_{\boldsymbol{a}} K_\rho^\sigma \sigma_{\boldsymbol{b}} K_{\rho'}^{\sigma\dagger}\right) = 32\cos(\theta_1)\cos(\theta_1')\cos(\theta_2)\cos(\theta_2')\,. \tag{5.89}$$

Hence, to leading order in the inverse channel number, the Fano factor is edge independent. The orbit sums can be performed exactly as in the case of the Schrödinger equation [189, 192], so that we get

$$\mathrm{Tr}\left(tt^\dagger - tt^\dagger tt^\dagger\right) \approx \frac{M_a^2 M_b^2}{(M_a + M_b)^3} \tag{5.90}$$

which, together with Eq. (5.23), yields the leading order term of Eq. (5.83). For identical leads we get $\mathcal{F} = 1/4$. To leading order, the Fano factor of chaotic ballistic graphene cavities does not depend on the edge structure.

5.4 Summary

The focus of this chapter has been the electronic transport properties of ballistic chaotic graphene cavities. Starting from the linear response Kubo formula for the effective Dirac Hamiltonian and the semiclassical Green function that we derived in App. A.5.1 and Chap.3, respectively, we obtained an expression for the conductance of a graphene cavity with two leads in terms of a double sum over classical orbits, which includes the graphene specific pseudospin interference terms.

Based on this formula, we have derived analytical expressions for the most important transport properties of open ballistic graphene cavities in the semiclassical limit. First we have calculated the leading and next-to-leading order contributions to the average conductance, namely the classical conductance and the WL correction. While the former does not

depend on the edge structure, the latter does so, highlighting the prominent role of intervalley scattering ac edges. Similar as for the spectral correlations in the previous chapter, the relative size of the ac scattering time T_{ac} with respect to the two other timescales of the transport problem, namely the dwell time T_{d} and the magnetic time T_{B}, controls the crossover between effectively broken TRS in the case of decoupled valleys, and restored TRS in the fully coupled case. Our main result for the average conductance is Eq. (5.49). It gives rather generally the magnetoconductance of a graphene cavity in terms of its microscopic edge properties and provides a theoretical footing for experimental and numerical studies of graphene structures in the ballistic regime. In contrast to the corresponding expression for disordered bulk graphene [63], there is no weak antilocalization in the ballistic systems. We could confirm our semiclassical theory by means of numerical tight-binding simulations, see Fig. 5.4.

The second main result of this chapter is given by Eq. (5.79), characterizing the size of the UCF of a ballistic graphene cavity. Analogous to the average conductance, the ratios $T_{\mathrm{d}}/T_{\mathrm{ac}}$ and $T_{\mathrm{B}}/T_{\mathrm{ac}}$ determine the size of the conductance variance. In contrast to the WL, T_{ac} and T_{B} have a very similar effect on the UCF: A increase of either one leads to an increasing conductance variance. Also here we support our analytic predictions by numerical simulations, see Fig. 5.7.

Finally we have briefly studied the shot noise of a chaotic cavity in terms of the Fano factor. We find that to leading order, the Fano factor does not exhibit any imprints of the graphene edges.

Our main results, Eqs.(5.49) and (5.79), explain parts of our earlier numerical findings [43]. With this work we provide a comprehensive extension of the semiclassical theory for chaotic conductors to the case of graphene for the first time. The results of this chapter have been published in Ref. [136].

CHAPTER 6

Edge magnetism in graphene quantum dots

In the previous chapters, we have seen that the graphene zigzag edge has rather peculiar properties, owing to its low energy edge state. This became particularly clear in Sec. 4.1, where we showed that in graphene billiards, the surface term in the Weyl expansion for the electronic density of states is exclusively due to zz edge states, giving rise to a characteristic feature in the DOS at low energies. However, also for the DOS oscillations, Secs. 4.2 and 4.3, and the transport properties, Chap. 5, the zz edge state played an indirect role, in that the renormalized zz boundary condition [see e. g. Eqs. (3.70) and (3.71)] influences the (averaged) pseudospin contributions to the various observables.

In this chapter we discuss particular effects of the *real spin* in graphene quantum dots. While we neglect spin-orbit coupling throughout the whole thesis, since it is believed to be rather weak, namely in the order of a few 10 μeV [193, 194], we consider effects of spin rotation caused by a different physical mechanism here. Due to the high degeneracy of the zz edge states, these states are expected to be spin polarized. To be more precise, it has been shown by Fujita and coworkers already in 1996, that even for very weak electron-electron interaction, the spins at a zz edge show local antiparallel ordering at the two sublattices, i. e. the spin points in opposite directions on A- and B-sites of the graphene lattice [25]. Since the zz edge state is exponentially localized, this leads to a ferrimagnetic spin structure and a net spin polarization at zz edges. Later, these predictions have been supported by density functional theory calculations [195, 196, 197], and recently the existence of spin polarized zz edge states has been demonstrated experimentally using scanning tunneling spectroscopy, that revealed the magnetism-induced energy splitting [48]. Experimental evidence for magnetized edges has also been found in multi-layer samples investigating the interaction with magnetic particles [198]. Moreover, several theoretical studies have investigated the zz edge magnetism in highly symmetric systems like graphene nanoribbons [199, 200, 201, 202, 203] and triangular [204, 205, 206, 207, 208, 209] as well as hexagonal [205] graphene quantum dots. It has also been shown that zz edge states [81, 87] and edge magnetism [210] are robust against edge irregularities, i. e. also present in generic quantum dots. To the best of our knowledge, the influence of the edge magnetism on the quantum conductance of graphene quantum dots has not been investigated so far.

Here we show how information about the orientation of the localized spins is directly reflected in the magnetoconductance of chaotic graphene quantum dots. We use a simple model to account for the edge magnetism, introducing an effective boundary condition that

leads to a rotation of the real (and pseudo-) spin of the quasiparticles. Then we adapt the methods that we have developed in the previous chapters of this thesis to calculate the weak localization correction to the average conductance and the size of the universal conductance fluctuations of systems with strong valley coupling. We find that for the size of the WL and the UCF, the characteristics of the polarization directions are crucial. Two different mechanisms govern these quantum interference effects: mixing of the two spin species and time reversal symmetry breaking, both mediated through spin rotation upon edge reflections.

6.1 Model

Within mean field approximation, the edge magnetism gives rise to a staggered magnetization term $\mathcal{H}_1$ in the effective Dirac Hamiltonian [25, 61]. Then, introducing the Pauli matrices $\boldsymbol{s}$ for the real spin and the corresponding unit matrix s_0, the Hamiltonian reads

$$\mathcal{H} = \mathcal{H}_0 + \mathcal{H}_1 = v_F s_0 \otimes \tau_0 \otimes \boldsymbol{\sigma} \cdot \boldsymbol{p} + M(\boldsymbol{x}) \left[\hat{\boldsymbol{\pi}}(\boldsymbol{x}) \cdot \boldsymbol{s}\right] \otimes \tau_z \otimes \sigma_z \,. \tag{6.1}$$

Here, $M(\boldsymbol{x})$ is the local strength of the magnetization and the unit vector $\hat{\boldsymbol{\pi}}(\boldsymbol{x})$ determines its local orientation. Since the detailed form of $M(\boldsymbol{x})$ is not expected to be important for the qualitative understanding of the effects implied by the edge magnetism on the physical quantities we study here [61], we assume that $M(\boldsymbol{x})$ is constant close to the zz edges of a graphene quantum dot and vanishes elsewhere. Then we can consider the bare graphene Hamiltonian $\mathcal{H}_0$ and account for the spin-dependent part $\mathcal{H}_1$ by constructing an effective boundary condition. In Ref. [87] the authors derive the boundary condition for zz edges in presence of a spin independent mass term $M(\boldsymbol{x}) s_0 \otimes \tau_z \otimes \sigma_z$, where $M(\boldsymbol{x}) = M_0$ over a certain distance close to the zz edge and $M(\boldsymbol{x}) = 0$ otherwise. The effective boundary matrix at a point $\boldsymbol{\alpha}$ at the interface where $M(\boldsymbol{x})$ changes from zero to M_0 is then

$$\mathcal{P}_{\boldsymbol{\alpha}} = \frac{1}{2}\left[1 + \tau_z \otimes (A_{\boldsymbol{\alpha}}\, \sigma_{\boldsymbol{t}_{\boldsymbol{\alpha}}} \pm B_{\boldsymbol{\alpha}}\, \sigma_z)\right] \,, \quad \text{with } A_{\boldsymbol{\alpha}}^2 = 1 - B_{\boldsymbol{\alpha}}^2 \,, \tag{6.2}$$

where we assumed a positive mass M_0, and the lower sign holds for A-terminated zz edges, while the upper holds for B-termination. The parameters $A_{\boldsymbol{\alpha}}$ and $B_{\boldsymbol{\alpha}}$ depend on the width of the region with finite mass and on M_0 [87]. For our model we assume that the boundary consists of individual pieces of ac and zz edges where $\hat{\boldsymbol{\pi}}$ is approximately constant [81, 87]. From comparison with the magnetic part of the Hamiltonian in Eq. (6.1), $\mathcal{H}_1$, we can then directly deduce the spin-dependent effective boundary matrix for a magnetic zz edge

$$\mathcal{P}_{\boldsymbol{\alpha}} = \frac{1}{2}\left(1 + A_{\boldsymbol{\alpha}}\, s_{\boldsymbol{\alpha}} \otimes \tau_z \otimes \sigma_{\boldsymbol{t}_{\boldsymbol{\alpha}}} \pm B_{\boldsymbol{\alpha}}\, s_0 \otimes \tau_z \otimes \sigma_z\right) \,, \tag{6.3}$$

with $s_{\boldsymbol{\alpha}} = \boldsymbol{s} \cdot \hat{\boldsymbol{\pi}}(\boldsymbol{\alpha})$.

The boundary condition (6.3) is a combination of boundary conditions for a spin inactive zz edge and an infinite mass edge with an additional spin rotation, see Eqs. (2.44) and (2.74). To calculate the conductance we simplify our model, focusing only on the spin-dependent

part of the effective boundary condition. This means we neglect the spin independent second term in Eq. (6.3) containing $B_{\boldsymbol{\alpha}}$, which can be much smaller than $A_{\boldsymbol{\alpha}}$ [87], depending on the details of $M(\boldsymbol{x})$. Then we get the approximate boundary condition

$$\mathcal{P}_{\boldsymbol{\alpha}} \approx \frac{1}{2}\left(1 + s_{\boldsymbol{\alpha}} \otimes \tau_z \otimes \sigma_{\boldsymbol{t}_{\boldsymbol{\alpha}}}\right) , \tag{6.4}$$

which is in valley and sublattice pseudospin space identical to the infinite mass boundary matrix (2.74). Additionally, the real spin is projected into the direction of $\hat{\boldsymbol{\pi}}(\boldsymbol{\alpha})$ upon a reflection at an edge described by (6.4). Due to this simplification we loose in principle the information about the strength of the magnetization. However, we can nevertheless model varying strength of the edge magnetization by introducing the concept of a *spin active boundary* (sa) length W_{sa}, which is smaller than the real zz boundary length $|\partial\mathcal{V}_{\mathrm{zz}}|$. Further we focus on the limit of strong intervalley coupling. This means, in our model the boundary consists of two types of edges: One part of the boundary is made of intervalley scattering ac edges and the rest is spin active with boundary matrix (6.4). In view of this model, the form of the semiclassical Green function, Eq. (3.83), is not changed, however K_γ is now an 8×8 matrix that contains not only the propagation of the pseudospins, but also the edge-dependent rotations of the real spin. Nevertheless, we still denote K_γ as pseudospin propagator in the following. For a classical orbit γ with $N = N_\gamma$ reflections, K_γ is in our simple model given by

$$K_\gamma \;=\; \prod_{i=N}^{1} \check{K}_i \left(1 + \sigma_{\boldsymbol{\alpha}_1,\boldsymbol{x}'}\right) , \tag{6.5}$$

with [cf. Eq. (3.94)]

$$\check{K}_i = \mathrm{i}\, \mathrm{e}^{\mathrm{i}\theta_i \sigma_z} \sigma_z \otimes \begin{cases} s_0 \otimes \tau_y \, \mathrm{e}^{\mathrm{i}2Kx_i\tau_z} & \text{for ac reflections}\,, \\ s_i \otimes \tau_z & \text{for sa reflections}\,. \end{cases} \tag{6.6}$$

Here we introduced the abbreviation $s_i = s_{\boldsymbol{\alpha}_i}$.

6.2 Weak localization

The diagonal contribution to the average conductance does not depend on the edge structure, and also edges with an effective boundary matrix (6.4) do not alter the result (5.23), except that we get an additional factor of two due to the two spin species. Therefore, we first focus on the weak localization correction to the average conductance, as studied in Subsec. 5.1.2. For orbits that hit im and ac type edges, we have already found [see e. g. Eq. (5.34)] that the average pseudospin trace is $-4\cos(\theta_a)\cos(\theta_b)$, with the angles of the incoming (θ_b) and outgoing (θ_a) trajectory segments relative to the lead orientation [cf. Fig. 5.2 a) and Eqs. (5.13), (5.14)]. Including the spin dependence, we get

$$\langle Y_{\gamma,\gamma_\times} \rangle = -4\cos(\theta_a)\cos(\theta_b)\langle Y^s_{\gamma,\gamma_\times} \rangle\,, \tag{6.7}$$

with

$$Y^s_{\gamma,\gamma_\times} = \mathrm{Tr}(K^s_\gamma K^{s\dagger}_{\gamma_\times}) = \mathrm{Tr}[(K^s_L)^2]\,. \tag{6.8}$$

Here K^s_γ the spin-dependent part of the pseudospin propagator $K_\gamma = K^s_\gamma \otimes K^\tau_\gamma \otimes K^\sigma_\gamma$. As previously, the subscript L denotes the loop part of the orbit γ, see Fig. 5.2 b). The spin-dependent average in Eq. (6.7) depends on the orientation of the local magnetic moments, as we discuss in the following. We distinguish three cases, that lead to different effective symmetry classes.

Uniaxial edge magnetic moments

First we assume that all magnetic moments at the zz edges are oriented along the same direction, without loss of generality the z-direction. This means that $s_i = \pm s_z$ for all reflections i at spin active edges. Then it follows immediately that $(K^s_L)^2 = s_0$, and thus the average pseudospin trace differs from the one in the spinless case, Eq. (5.34), only by a factor of two, namely

$$\langle Y_{\gamma,\gamma_\times}\rangle = -4\cos(\theta_a)\cos(\theta_b)\,\mathrm{Tr}(s_0) = -8\cos(\theta_a)\cos(\theta_b)\,. \tag{6.9}$$

With this the WL correction is calculated exactly as in Subsec. 5.1.2 and we find

$$\langle g_L\rangle/g_0 = \approx -2\frac{M_a M_b}{(M_a+M_b)^2}\frac{1}{1+T_\mathrm{d}/T_\mathrm{B}}\,, \tag{6.10}$$

where $M_{a/b} = 4k_E W_{a/b}/\pi$ here, accounting for the two spin species. The dwell time T_d and the magnetic time T_B are defined in Eqs. (5.20) and (4.158), respectively. The result (6.10) means that the WL correction is twice as large as in the spinless case. Since all local magnetic moments are aligned along the same direction, there is no coupling between the two spin species due to reflections from the corresponding edges. The full TRS is now $s_0\mathcal{T}_y$, and it is preserved by the boundary condition (6.4) in the considered case that $s_i = \pm s_z$. The TRS operator $s_0\mathcal{T}_y$ does not couple the two spin blocks, so that the system consists of two independent orthogonal subsystems, each of them giving rise to WL. Note that we obtain the same result if we replace all spin Pauli matrices by s_0, i. e. considering spin inactive edges. Later we will see that the corresponding results for the UCF do in fact not coincide.

In-plane edge magnetic moments

In a real graphene flake it is likely that the local magnetic moments at the zz edges are spatially fluctuating and thus their polarization direction is not restricted to a single direction. One possible configuration is that the polarizations of the edge moments all lie within a preferred plane. Anisotropic spin-spin coupling could lead to such a situation for low temperatures $T \lesssim 10\,\mathrm{K}$ [211]. For convenience and without loss of generality, we assume that the edge moments lie in the x-y-plane, i. e. the spin Pauli matrices in Eq. (6.4) point on the equator of the Bloch sphere. Then we can write

$$s_i = s_x \mathrm{e}^{\mathrm{i}\varsigma_i s_z}\,, \tag{6.11}$$

where ς_i is the polar angle of the magnetic edge moment at the corresponding reflection point $\boldsymbol{\alpha}_i$. In this case, we get for the spin part of the pseudospin trace

$$Y^s_{\gamma,\gamma_\times} = 2\begin{cases}1 & \text{for odd } N_{\mathrm{sa},L}\,,\\ \cos(2\Sigma_L) & \text{for even } N_{\mathrm{sa},L}\,.\end{cases} \tag{6.12}$$

Here we have defined similar as in Eq. (4.87)

$$\Sigma_L = \sum_{i=1}^{N_{\mathrm{sa,L}}/2} (\varsigma_{2i} - \varsigma_{2i-1})\,, \tag{6.13}$$

where the sum runs only over the $N_{\mathrm{sa,L}}$ reflections at sa edges along the loop part of the orbits. To calculate the average of $Y^s_{\gamma,\gamma_\times}$, we assume that the ς_i are distributed symmetrically around zero, with a probability distribution $p(\varsigma) = p(-\varsigma)$. Note that the center of the distribution is irrelevant, since Σ_L contains only *differences* of angles. Assuming that in a chaotic billiard all ς_i can be considered independent, the average of $Y^s_{\gamma,\gamma_\times}$ is then for even $N_{\mathrm{sa},L}$, according to Eq. (6.12), given by

$$\langle Y^s_{\gamma,\gamma_\times}\rangle(N_{\mathrm{sa},L}) = 2\left(\int_{-\pi}^{\pi} d\varsigma\, p(\varsigma)\mathrm{e}^{2\mathrm{i}\varsigma}\right)^{N_{\mathrm{sa},L}} = 2\langle \mathrm{e}^{2\mathrm{i}\varsigma}\rangle^{N_{\mathrm{sa},L}}\,. \tag{6.14}$$

For odd $N_{\mathrm{sa},L}$, we have $\langle Y^s_{\gamma,\gamma_\times}\rangle = 2$. As in Subsec. 5.1.2 we get for the loop contribution to the non-local conductivity [see e. g. Eq. (5.42)]

$$\langle \sigma_L(\boldsymbol{x},\boldsymbol{x}')\rangle = -\frac{g_0}{W_a+W_b}\frac{2k_E}{\pi T_\mathrm{d}}\mathfrak{Re}\int_0^{\pi} d\varepsilon \int_{2T_{\min}(\varepsilon)}^{\infty} dT\, \mathrm{e}^{-[T-T_{\min}(\varepsilon)]/T_\mathrm{d}}\tilde{P}_{\mathrm{ip}}(\varepsilon,T)\mathrm{e}^{\mathrm{i}k_E\delta L_{\gamma,\gamma_\times}}\,, \tag{6.15}$$

where $\tilde{P}_{\mathrm{ip}}$ is the appropriately modified loop density. Due to the explicit $N_{\mathrm{sa},L}$-dependence of the spin contribution (6.14), the modification is slightly more complicated as in the spinless case. In fact we have to combine the average spin contribution with the approximate probability for an orbit to hit zz edges a certain number of times, p_n. For the latter we use the binomial distribution (4.120), where the ac boundary length W_{ac} is replaced accordingly by W_{sa}, the effective length of the spin active boundary. The modified loop density is then

$$\tilde{P}_{\mathrm{ip}}(\varepsilon,T) \approx \frac{v_F^2\varepsilon}{\pi|\mathcal{V}|}\int_{T_{\min}(\varepsilon)}^{T-T_{\min}(\varepsilon)} dT_L[T-T_L-T_{\min}(\varepsilon)]\,\langle Y^s_{\gamma,\gamma_\times}\rangle[T_L-T_{\min}(\varepsilon)]\,, \tag{6.16}$$

with

$$\begin{aligned}\langle Y^s_{\gamma,\gamma_\times}\rangle(T) &= \sum_{n=0}^{\infty}\langle Y^s_{\gamma,\gamma_\times}\rangle(n)\,p_n(N) = 2\sum_{\substack{n=0\\ \text{even}}}\langle \mathrm{e}^{2\mathrm{i}\varsigma}\rangle^n p_n(N) + 2\sum_{\substack{n=1\\ \text{odd}}} p_n(N) \\ &\approx 1-\exp(-2T/T_{\mathrm{sa}}) + \exp\left[-(1-\langle \mathrm{e}^{2\mathrm{i}\varsigma}\rangle)T/T_{\mathrm{sa}}\right] + \exp\left[-(1+\langle \mathrm{e}^{2\mathrm{i}\varsigma}\rangle)T/T_{\mathrm{sa}}\right]\,.\end{aligned} \tag{6.17}$$

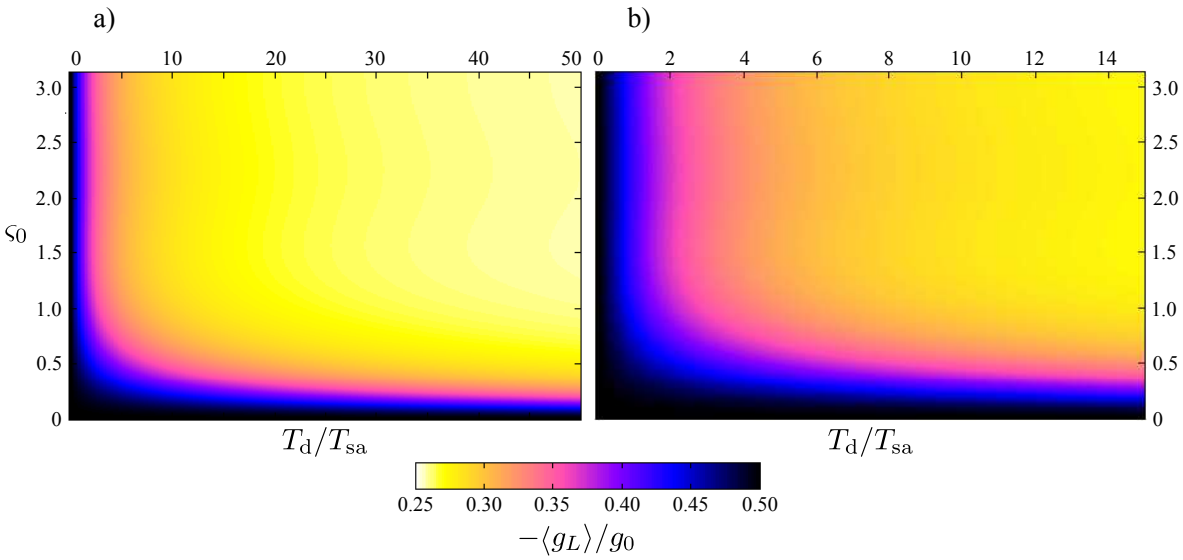

Figure 6.1: Semiclassical result (6.19) for the absolute value of the WL correction, $-\langle g_L\rangle$, for in-plane edge moments as a function of the effective spin scattering strength $T_\mathrm{d}/T_\mathrm{sa}$ and the width ς_0 of the edge moment distribution (6.20). We show the regimes $0 \leq T_\mathrm{d}/T_\mathrm{sa} \leq 50$ and $0 \leq T_\mathrm{d}/T_\mathrm{sa} \leq 15$ for identical leads in panels a) and b), respectively. In Fig. 6.2 we show the crossovers for discrete values of $T_\mathrm{d}/T_\mathrm{sa}$ and ς_0.

Here we have introduced, in analogy to T_ac in Eq. (4.125), the characteristic time scale associated to W_sa

$$T_\mathrm{sa}^{-1} = \frac{v_F W_\mathrm{sa}}{\pi|\mathcal{V}|}\,. \tag{6.18}$$

To obtain Eq. (6.17) we have assumed that W_sa is small compared to $|\partial\mathcal{V}|$. This does not change the result qualitatively, but greatly simplifies the further discussion. In App. A.7 we present the main results of this section without the assumption of small W_sa. The magnetic field dependence is included exactly as for the spinless case [cf. Eq. (5.47)], so that with Eq. (5.44) we finally get for the WL correction to the average conductance

$$\begin{aligned}\langle g_L\rangle/g_0 \;\approx\; & -\frac{M_a M_b}{(M_a+M_b)^2}\left(\frac{1}{1+T_\mathrm{d}/T_\mathrm{B}} - \frac{1}{1+2T_\mathrm{d}/T_\mathrm{sa}+T_\mathrm{d}/T_\mathrm{B}}\right. \\ & \left. +\; \frac{1}{1+T_\mathrm{d}/T_\mathrm{sa}(1+\langle \mathrm{e}^{2\mathrm{i}\varsigma}\rangle)+T_\mathrm{d}/T_\mathrm{B}} + \frac{1}{1+T_\mathrm{d}/T_\mathrm{sa}(1-\langle \mathrm{e}^{2\mathrm{i}\varsigma}\rangle)+T_\mathrm{d}/T_\mathrm{B}}\right)\,.\end{aligned} \tag{6.19}$$

The details of the distribution $p(\varsigma)$ do not qualitatively alter the result (6.19). Considering for example uniformly distributed edge moments, i. e.

$$p(\varsigma) = \frac{1-\Theta(|\varsigma|-\varsigma_0)}{2\varsigma_0} \tag{6.20}$$

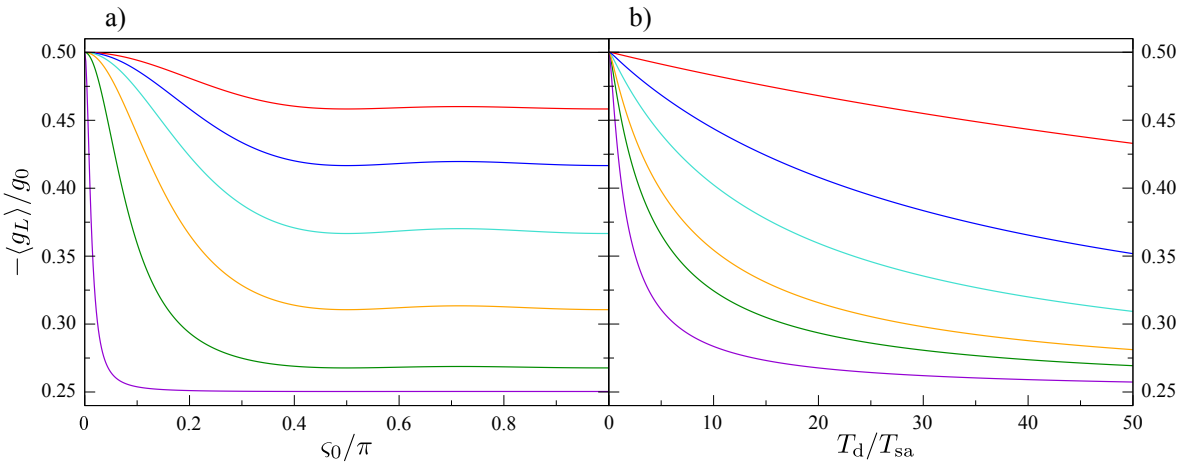

Figure 6.2: a) Absolute value of the WL correction, $-\langle g_L\rangle$, for in-plane edge moments as a function of the width ς_0 of the distribution (6.20), obtained from the semiclassical result (6.19) for identical leads. We show the crossover for different values of $T_\mathrm{d}/T_\mathrm{sa}$ (from top to bottom): 0 (black), 0.5 (red), 1 (blue), 2 (turquoise), 5 (orange), 20 (green) and 1000 (violet). b) The crossover (6.19) as a function of the effective spin scattering strength $T_\mathrm{d}/T_\mathrm{sa}$ for different widths ς_0 (from top to bottom): 0 (black), $\pi/30 \approx 0.10$ (red), $2\pi/30 \approx 0.21$ (blue), $\pi/10 \approx 0.31$ (turquoise), $3\pi/20 \approx 0.47$ (orange), $2\pi/10 \approx 0.63$ (green) and π (violet).

with $0 \leq \varsigma_0 \leq \pi$, we obtain

$$\langle \mathrm{e}^{2\mathrm{i}\varsigma}\rangle = \frac{\sin(2\varsigma_0)}{2\varsigma_0}\,, \tag{6.21}$$

which is equal to unity at $\varsigma_0 = 0$ and decays towards $\varsigma_0 = \pi$.

In Figs. 6.1 and 6.2 we show the absolute value of the WL correction at zero magnetic field obtained from Eq. (6.19) as a function of the spin scattering time T_sa and the width ς_0 of the spin distribution for the uniform case (6.20). For very weak spin scattering, $T_\mathrm{d}/T_\mathrm{sa} \ll 1$, or a very narrow distribution corresponding to the previously discussed case of uniaxial edge moments, $\varsigma_0 \ll \pi$, the absolute value of the WL is maximum, i. e. for identical leads $\langle g_L\rangle \approx -g_0/2$. On the other hand for strong spin scattering, $T_\mathrm{d}/T_\mathrm{sa} \gg 1$, and edge spins that are distributed over the whole equator of the Bloch sphere, $\varsigma_0 \to \pi$, the size of the WL correction is half as large, $\langle g_L\rangle \approx -g_0/4$. This result is quite interesting, since it means that the TRS is not broken by the in-plane edge magnetic moments, even when they are randomly distributed over the whole plane. The reason for the decrease of the WL correction is rather the mixing of the spin species, so that no substructure remains and we have only one orthogonal system, instead of two decoupled orthogonal subsystems. To see that the TRS $s_0\mathcal{T}_y = s_0 \otimes \tau_y \otimes \sigma_y \mathcal{C}$ is still intact, even though it does not commute with s_y, we consider the unitary transformation

$$\mathcal{R}^s_{zy} = \exp\left(\mathrm{i}\frac{\pi}{4}s_x\right). \tag{6.22}$$

This transformation has no effect on $s_0\mathcal{T}_y$, but rotates the s_i from the x-y-plane into the

x-z-plane, namely

$$\mathcal{R}^{s\dagger}_{zy}\, s_i\, \mathcal{R}^{s}_{zy} = s_x \mathrm{e}^{-\mathrm{i}\varsigma_i s_y}\,, \tag{6.23}$$

which in fact commutes with $s_0\mathcal{T}_y$. This means that indeed edge magnetic moments that lie all within one plane do not break the TRS, hence WL occurs.

Unpolarized edge magnetic moments

At temperatures $T \gtrsim 10\,\mathrm{K}$, mean field calculations predict isotropic correlation lengths of the edge moments below 50 nm [211]. This means that at the boundary of a mesoscopic quantum dot, spin polarizations in all three spatial directions are present. Thus we consider now our model in the case that the spin matrices in Eq. (6.6) are uniformly distributed on the Bloch sphere, i. e.

$$s_i = s_x \mathrm{e}^{\mathrm{i}\varsigma_i s_z} \sin(\chi_i) + s_z \cos(\chi_i)\,, \tag{6.24}$$

with randomly distributed $\varsigma_i \in [0, 2\pi[$ and $\chi_i \in [0, \pi]$. In this general case, $Y^s_{\gamma,\gamma_\times}$ is rather complicated and performing the matrix multiplications explicitly does not lead to a simple formula like Eq. (6.12). Therefore we perform the average over the ς_i and χ_i for a given number of sa loop reflections, $N_{\mathrm{sa,\,L}}$, *before* we do the multiplication and the tracing. As we demonstrate below, this leads to

$$\langle Y^s_{\gamma,\gamma_\times}\rangle = \langle Y^s\rangle(N_{\mathrm{sa},L}) = (-1)^{N_{\mathrm{sa},L}+1} + \frac{3}{3^{N_{\mathrm{sa},L}}}\,, \quad \text{for } N_{\mathrm{sa},L} \geq 0\,. \tag{6.25}$$

To derive this relation, we assume that the spin orientations are uniformly distributed on the Bloch sphere and calculate the average $\langle s_i \Omega\, s_i\rangle$ for an arbitrary 2×2 matrix Ω. With Eq. (6.24) we find

$$\langle s_i\, \Omega\, s_i\rangle = \frac{1}{4\pi}\int_0^\pi \sin(\chi_i)\, d\chi_i \int_0^{2\pi} d\varsigma_i\, s_i\, \Omega\, s_i = \frac{1}{3}\sum_{k\in\{x,y,z\}} s_k\, \Omega\, s_k\,. \tag{6.26}$$

Successively using (6.26) on the spin trace (6.8) yields

$$\langle Y^s\rangle(N_{\mathrm{sa},L}) = \frac{1}{3^{N_{\mathrm{sa},L}}} \sum_{k_1}\sum_{k_2}\cdots\sum_{k_{N_{\mathrm{sa},L}}} \mathrm{Tr}\left[\left(s_{k_1} s_{k_2}\ldots s_{k_{N_{\mathrm{sa},L}}}\right)^2\right]\,, \tag{6.27}$$

where each sum runs over the indices x, y and z. Now we use for products of two matrices in the multiple sum (6.27) the identity

$$s_j s_k = \delta_{jk} + \mathrm{i}\sum_l \varepsilon_{jkl}\, s_l\,, \tag{6.28}$$

with the Kronecker and Levi-Civita symbols δ_{jk} and ε_{jkl}, respectively. With this we obtain the recursion relation

$$\langle Y^s\rangle(n) = -\frac{2}{3}\langle Y^s\rangle(n-1) + \frac{1}{3}\langle Y^s\rangle(n-2)\,, \quad \text{for } n \geq 2\,. \tag{6.29}$$

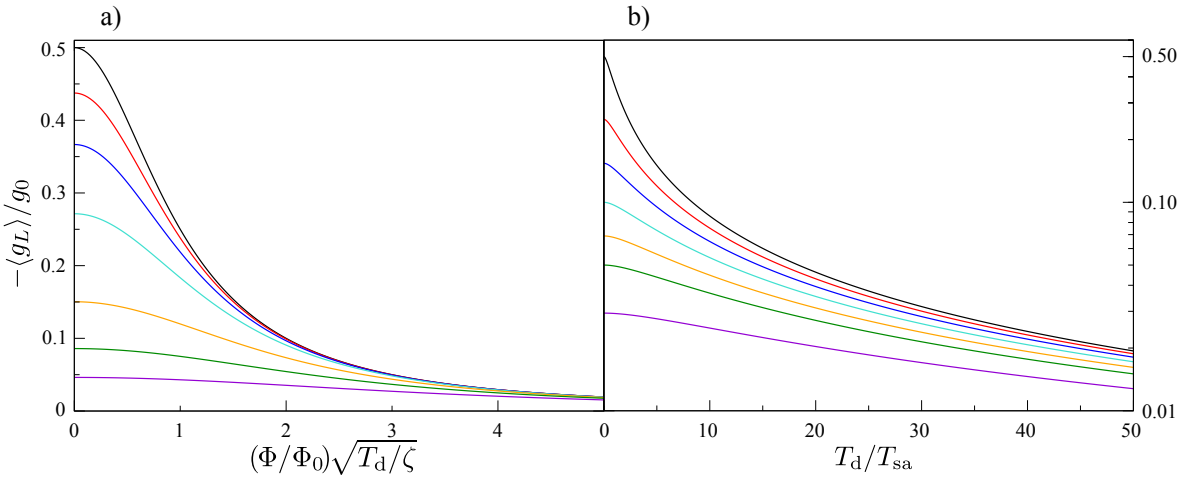

Figure 6.3: a) Absolute value of the WL correction, $-\langle g_L\rangle$, for unpolarized edge moments as a function of the magnetic flux Φ through the cavity, obtained from the semiclassical result (6.34) for identical leads. We show the crossover for different values of $T_\mathrm{d}/T_\mathrm{sa}$ (from top to bottom): 0 (black), 0.5 (red), 1 (blue), 2 (turquoise), 5 (orange), 10 (green) and 20 (violet). ζ is a system specific parameter, cf. Eq. (4.158). b) Logarithmic representation of the crossover (6.34) as a function of the effective spin scattering strength $T_\mathrm{d}/T_\mathrm{sa}$ for different values of the magnetic flux Φ (from top to bottom): 0 (black), 1.0 (red), 1.5 (blue), 2.0 (turquoise), 2.5 (orange), 3.0 (green) and 4.0 (violet).

This relation in turn is solved by $\langle Y^s\rangle(0) = \langle Y^s\rangle(1) = 2$ and

$$\langle Y^s\rangle(n) = (-1)^{n+1} + \frac{3}{3^n}\,, \quad \text{if } n \geq 2\,, \tag{6.30}$$

as one proofs by complete induction, leading to (6.25).

Analog to the in-plane case we have

$$\langle \sigma_L(\boldsymbol{x},\boldsymbol{x}')\rangle = -\frac{g_0}{W_a+W_b}\frac{2k_E}{\pi T_\mathrm{d}}\mathfrak{Re}\int_0^\pi d\varepsilon \int_{2T_\mathrm{min}(\varepsilon)}^\infty dT\, \mathrm{e}^{-[T-T_\mathrm{min}(\varepsilon)]/T_\mathrm{d}}\tilde{P}_\mathrm{up}(\varepsilon,T)\mathrm{e}^{\mathrm{i}k_E\delta L_{\gamma,\gamma_\times}}\,, \tag{6.31}$$

with

$$\tilde{P}_\mathrm{up}(\varepsilon,T) \approx \frac{v_F^2\varepsilon}{\pi|\mathcal{V}|}\int_{T_\mathrm{min}(\varepsilon)}^{T-T_\mathrm{min}(\varepsilon)} dT_L[T-T_L-T_\mathrm{min}(\varepsilon)]\,\langle Y^s_{\gamma,\gamma_\times}\rangle[T_L-T_\mathrm{min}(\varepsilon)] \tag{6.32}$$

and

$$\langle Y^s_{\gamma,\gamma_\times}\rangle(T) = \sum_{n=0}^\infty \langle Y^s_{\gamma,\gamma_\times}\rangle(n)\,p_n(N) = 3\exp[-2T/(3T_\mathrm{sa})] - \exp(-2T/T_\mathrm{sa})\,. \tag{6.33}$$

Therefore we get for the WL correction to the average conductance in the unpolarized case

$$\langle g_L\rangle/g_0 \approx -\frac{M_aM_b}{(M_a+M_b)^2}\left(\frac{3}{1+2T_\mathrm{d}/(3T_\mathrm{sa})+T_\mathrm{d}/T_\mathrm{B}} - \frac{1}{1+2T_\mathrm{d}/T_\mathrm{sa}+T_\mathrm{d}/T_\mathrm{B}}\right)\,. \tag{6.34}$$

Also here we have assumed that the ratio $W_{\mathrm{sa}}/|\partial\mathcal{V}|$ is small and refer the reader to App. A.7 for a generalization of the result. For vanishing spin scattering, $T_{\mathrm{sa}} \gg T_{\mathrm{d}}$, we recover our previous result (6.10). On the other hand for strong spin scattering, $T_{\mathrm{sa}} \ll T_{\mathrm{d}}$, the WL correction vanishes. The reason is that the unpolarized edge magnetic moments indeed break the TRS $s_0\mathcal{T}_y$. Unlike for in-plane moments, there is no unitary transformation that rotates the spin space in a way that all boundary conditions commute with the antiunitary TRS operator. In other words, we cannot get rid of the imaginary s_y in the boundary conditions, so that the TRS is broken in the case of unpolarized edge moments, while it is conserved for the in-plane case.

Our semiclassical result (6.34) is depicted in Fig. 6.3. We show the WL correction to the magnetoconductance for different values of the effective spin scattering strength $T_{\mathrm{d}}/T_{\mathrm{sa}}$ in panel a), and the crossover as a function of $T_{\mathrm{d}}/T_{\mathrm{sa}}$ for various magnetic fields in panel b). In contrast to the *symmetry restoring* due to intervalley coupling ac edges that we have studied in Subsec. 5.1.2, we have a *symmetry breaking* here.

Numerical tight-binding simulations and experimental relevance

The present results of this section suggest that the effects of the edge magnetic moments such as spin mixing and TRS breaking can be measured in magnetotransport experiments, i. e. measuring the WL correction. In Ref. [211], the edge spin correlation length has been estimated by mean field calculations to be of the order $10^1 - 10^2$ nm for temperatures below ~ 10 K and of the order $10^0 - 10^1$ nm for temperatures between ~ 10 and ~ 100 K. Therefore our theoretical results Eq. (6.19) and Eq. (6.34) predict a suppressed WL signal in a magnetotransport measurement of a chaotic graphene quantum dot. On the other hand, if the magnetic edge moments are (partially) aligned, e. g. by an applied external magnetic field that lies in the plane of the graphene sample, Eq. (6.10) predicts that the size of the WL correction is increased to at most $g_0/2$, for the ideal case that all spins are aligned along the direction of the magnetic field and for identical leads. The polarizing magnetic field has to lie in-plane, such that it does not cause a magnetic flux through the sample, in order to avoid TRS breaking.

In Figs. 6.4 and 6.5 we present the results of numerical tight-binding simulations. With the program code that we have used already for the simulations in Chap. 5, see Ref. [56], we have calculated the magnetoconductance of a chaotic graphene cavity with a staggered edge magnetization with different polarizations. The geometry of the system is the same as in Chap. 5, see Fig. 5.1 b). In view of Eq. (6.1), we chose a magnetization profile that is equal to the mass profile (5.54), i. e. $M(\boldsymbol{x})$ is zero within the system and increases quadratically towards the edges within a distance of several lattice constants.

First we focus on Fig. 6.4. The black curves correspond to uniaxial polarization of the edge magnetization, i. e. $\hat{\boldsymbol{\pi}}(\boldsymbol{x}) = \hat{\boldsymbol{z}}$, and are identical in all four panels. As expected, we find a large WL signal in this case, since the spin species are uncoupled. For the red curves we have

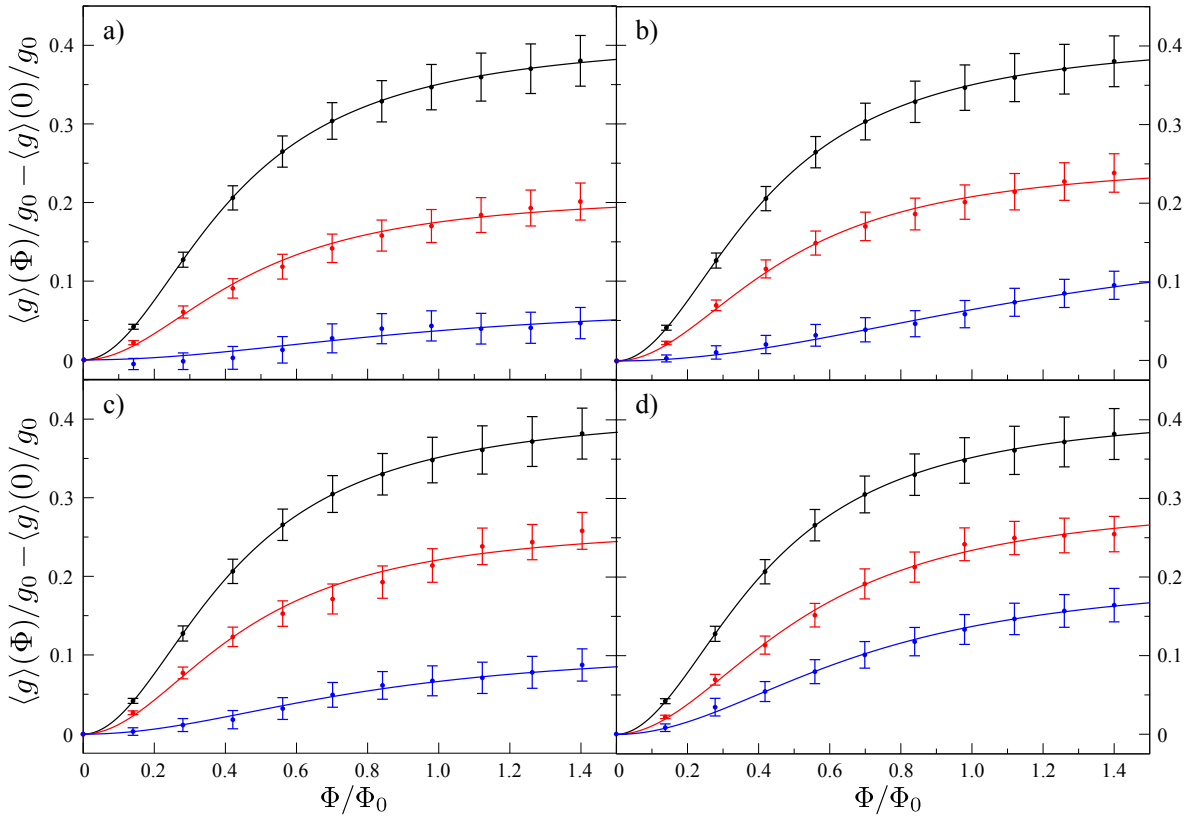

Figure 6.4: Numerically calculated magnetoconductance for a graphene cavity with edge magnetization. The geometry of the system is sketched in Fig. 5.1 b). Within a region of width $W_M = 20\,a$ close to the edges we included a staggered magnetization that increases quadratically [cf. Eq. (5.54)] towards the edges to a maximum value of $M = 0.5\,t$, cf. Eq. (6.1). The system shows strong intervalley scattering, since some pieces of ac edges are not dressed by the magnetization term. The polarization of the magnetization is in z-direction for the black curves. For the red and blue curves, the polarization is according to Eqs. (6.35) and (6.36), respectively. For the four panels we used different values for rotation period of the polarization vector: a) $\Delta_s = L_y/8$, b) $\Delta_s = L_y/4$, c) $\Delta_s = L_y$ and d) $\Delta_s = 3L_y$.

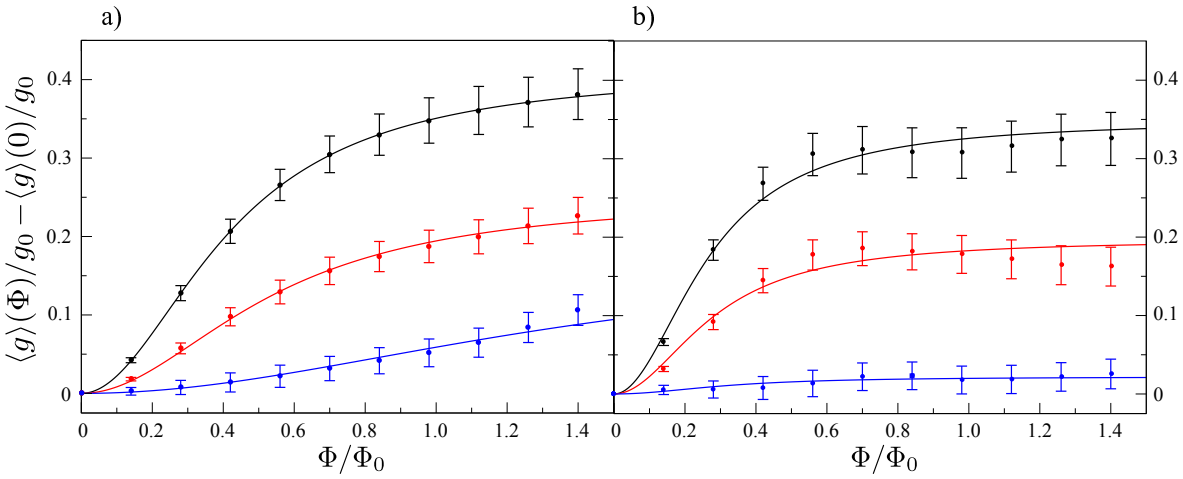

Figure 6.5: Numerically calculated magnetoconductance simulations for the piecewise constant polarizations given by Eq. (6.37) for the red and by Eq. (6.38) for the blue curves. For the black curves the polarization in constant over the whole system and points in z-direction. We used the same system as for Fig. 6.4. For the curves in panel b) we included weak Gaussian bulk disorder. To this end we included Gaussian on-site potentials that are centered at 4% of the lattice sites, which were randomly chosen. The width of the Gaussians is $2\,a$ and their height was chosen randomly from the interval $[-0.06\,t, 0.06\,t]$. For details of the disorder model see Chap. 7.

used the in-plane polarization

$$\hat{\boldsymbol{\pi}}(\boldsymbol{x}) = \begin{bmatrix} \cos(\omega\, y) \\ \sin(\omega\, y) \\ 0\,, \end{bmatrix}, \tag{6.35}$$

where y is the coordinate in transport direction, cf. Fig. 5.1 b). Finally, for the blue curves $\hat{\boldsymbol{\pi}}(\boldsymbol{x})$ has also a finite z-component

$$\hat{\boldsymbol{\pi}}(\boldsymbol{x}) = \begin{bmatrix} \sin(\omega\, y)\cos(\omega\, y) \\ \sin(\omega\, y)\sin(\omega\, y) \\ \cos(\omega\, y) \end{bmatrix}. \tag{6.36}$$

The four panels correspond to different values of the rotation frequency ω. While for panel a) several periods $\Delta_s = 2\pi/\omega$ fit inside the system, the rotation becomes slower for panels b), c) and d). The numerical results shown in Fig. 6.4 confirm our predictions concerning the suppression of the WL. For in-plane magnetization, the size of the WL signal in panel a) is about half the size of the uniaxial case, due to the mixing of the spin species. For the unpolarized case the WL is suppressed, since the TRS is partially broken in this case. In mesoscopic experimental samples, the magnetization fluctuates most probably on a scale that is only a fraction of the system size [211]. In this case the suppression of the WL signal is most prominent, as can be seen by comparison of the different panels in Fig. 6.4 [cf. also Eq. (6.19) and Figs. 6.1 and 6.2 a)]. However, also in the case of periods Δ_s that are several times

larger than the system size, a clear difference in the magnetoconductance for the different polarizations is visible, cf. Fig. 6.4 d).

To demonstrate that the qualitative results do not depend on the specific choice of $\hat{\boldsymbol{\pi}}(\boldsymbol{x})$, we show simulations for a rather simple model in Fig. 6.5. Here we have used a piecewise constant polarization, namely for the case of in-plane polarization

$$\hat{\boldsymbol{\pi}}(\boldsymbol{x}) = \begin{cases} \hat{\boldsymbol{x}} & \text{for } 0 \leq y < L_y/2\,, \\ \hat{\boldsymbol{y}} & \text{for } L_y/2 \leq y < L_y\,, \end{cases} \tag{6.37}$$

and for the unpolarized case

$$\hat{\boldsymbol{\pi}}(\boldsymbol{x}) = \begin{cases} \hat{\boldsymbol{x}} & \text{for } 0 \leq y < L_y/3\,, \\ \hat{\boldsymbol{y}} & \text{for } L_y/3 \leq y < 2L_y/3\,, \\ \hat{\boldsymbol{z}} & \text{for } 2L_y/3 \leq y < L_y\,, \end{cases} \tag{6.38}$$

where L_y is the length of the system in y-direction [cf. Fig. 5.1 b)]. The result for the WL correction remains qualitatively unchanged in Fig. 6.5 a), where apart from the form of $\hat{\boldsymbol{\pi}}(\boldsymbol{x})$, we use the very same system as for Fig. 6.4. For Fig. 6.5 b) we have additionally included weak bulk disorder. The effect of the latter is a reduction of the WL signal for all polarizations.

Our numerical findings suggest that the proposed experiments could actually provide a good method to measure the existence, the effectivity, and also polarization properties of edge magnetic moments in graphene quantum dots using only transport measurements. In particular, we have shown that the qualitative results of our semiclassical theory do not depend on the specific model for the polarization of the edge magnetic moments. However, so far we have neglected the influence of the magnetic field that is used to probe the WL on the edge moments themselves. Considering a graphene cavity where the edge magnetic moments are unpolarized, our theory and the numerical simulations predict a suppressed WL due to TRS breaking. If the magnetic field used for magnetotransport measurements, as e. g. in Figs. 6.4 and 6.5, is very strong, we expect that the magnetic moments become aligned and thus do not break the TRS anymore. This would lead to a negative magnetoconductance. On the other hand the magnetic flux breaks TRS itself, leading to the usual positive magnetoconductance. To find out whether the alignment of the moments is important or not, we first estimate the critical field for the alignment, B_1. As a function of temperature T, the spin correlation length is approximately of the order $\xi_s = 10^2\,\mathrm{nm}/(T/\mathrm{K})$ [211]. Since the net magnetic moment per zigzag edge atom is approximately $0.3\,\mu_\mathrm{B}$ [25, 197, 211], with the Bohr magneton μ_B, the relevant total magnetic moment is then $m \approx 0.3\,\mu_\mathrm{B}\,\xi_s/a$. We estimate B_1 as the field corresponding to an energy gain mB_1 due to the polarization of the moments, that is equal to the thermal energy

$$mB_1 = k_\mathrm{B}T\,, \tag{6.39}$$

where k_B is the Boltzmann constant.

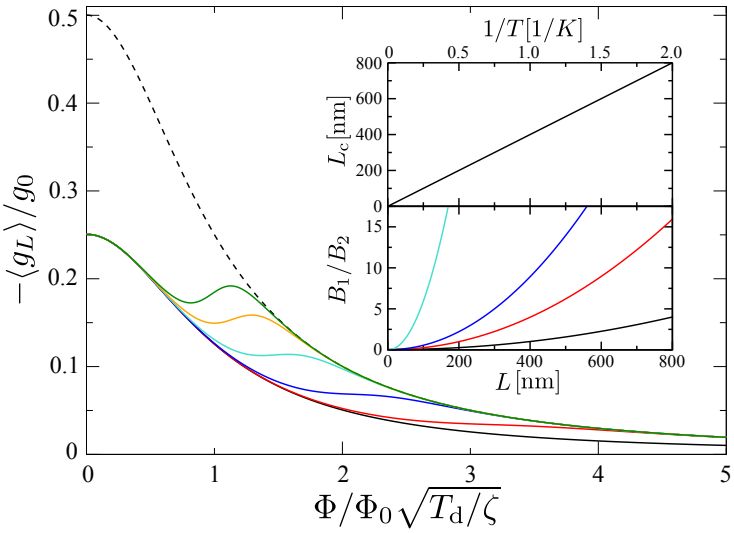

Figure 6.6: Absolute value of the WL correction, $-\langle g_L\rangle$, as a function of $T_\mathrm{d}/T_\mathrm{B}$ for the case of in-plane polarized edge moments, Eq. (6.19), in the limit of strong spin scattering $T_\mathrm{d}/T_\mathrm{sa} = 10^3$. We use the uniform angle distribution of Eqs. (6.20) and (6.21). To simulate the magnetic field dependence of the edge moment polarization, we assume the simple B-dependence (6.42) of the width ς_0. The different curves correspond to different ratios of the critical fields: (from bottom to top) $B_1/B_2 = 10$ (black), 1 (red), 0.6 (blue), 0.4 (turquoise), 0.3 (orange) and 0.25 (green). The dashed line corresponds to the case of totally polararized edge moments, i. e. $\varsigma_0 = 0$. Upper inset: Critical length, L_c, as a function of inverse temperature. Lower inset: Ratio of critical fields, B_1/B_2, as a function of the typical system size L for different temperatures: T =1 K (black), 2 K (red), 3 K (blue), and 10 K (turquoise).

On the other hand, we consider the TRS broken by the magnetic flux through the cavity, when the WL correction is about half the value at $B = 0$. Typically this corresponds to a flux in the order of Φ_0, since the corresponding crossover parameter is $T_\mathrm{d}/T_\mathrm{B} \sim \Phi^2/\Phi_0^2$. We estimate the critical flux from Fig. 6.4 to be approximately $\Phi_2 \approx \Phi_0/2$. Thus we define

$$L^2 B_2 = \Phi_0/2\,, \tag{6.40}$$

with the typical system size L. For the ratio of critical fields we obtain then

$$\frac{B_1}{B_2} = \left(\frac{L}{L_\mathrm{c}}\right)^2, \quad \text{with } L_\mathrm{c} \approx \frac{4\cdot 10^2\,\mathrm{nm}}{T/\mathrm{K}}\,. \tag{6.41}$$

The insets of Fig. 6.6 show the critical length L_c as a function of the inverse temperature, and the ratio B_1/B_2 as a function of the typical system size for different temperatures. If the system size L is larger than L_c, then the TRS is broken at smaller fields than needed for the polarization of the edge moments. This corresponds to the regime we have been discussing so far, where we neglected the polarization due to the probing magnetic field. However, also for $L \lesssim L_\mathrm{c}$ the qualitative result is not changed much. This is demonstrated in the main panel

of Fig. 6.6, where we plot the WL for the case of in-plane polarized edge moments, Eq. (6.19), for a magnetic field-dependent width ς_0 of the distribution (6.20). For our demonstration we assume the simple exponential magnetic field dependence

$$\varsigma_0(B) = \pi \exp\left(-\sqrt{\frac{T_\mathrm{d}}{T_\mathrm{B}}} \Big/ \frac{B_1}{B_2}\right) . \tag{6.42}$$

For $B_1/B_2 = 10$ (black solid line) the curve cannot be distinguished from the case where $\varsigma_0 = \pi$ for all values of $T_\mathrm{d}/T_\mathrm{B}$. The dashed line corresponds to the case of totally polararized edge moments, i. e. $\varsigma_0 = 0$ for all values of $T_\mathrm{d}/T_\mathrm{B}$, see Eq. (6.10). One can see that also for $B_1/B_2 = 1$ (red) only very small deviations occur when TRS is essentially already broken by the field. Even for $B_1/B_2 = 0.25$ (green) the qualitative behavior is changed only little. This discussion suggests that the semiclassical and numerical predictions that we have made in this section for the WL could be measured experimentally for a wide range of system sizes and temperatures.

6.3 Universal conductance fluctuations

We complete our study of the effects of edge magnetization on the transport properties of graphene quantum dots with a brief discussion of the UCF size, i. e. the conductance variance. As the WL correction, it is affected by TRS breaking and mixing of the spin species, but also the (Kramers) degeneracy of possible subsystems is important for the UCF, as we have seen already in Sec. 5.2. We consider the following form of the spin part of the boundary matrices (6.6)

$$s_i = s_x \mathrm{e}^{\mathrm{i}\varsigma_i s_z} \quad \text{or} \quad s_i = \pm s_z \, . \tag{6.43}$$

This is not exactly the same model as we had for the WL in the case of unpolarized edge moments, i. e. Eq. (6.24). However, in the limit of very large $N_{\mathrm{sa},L}$, that we focus on in this section, it leads to the same result, i. e. TRS is broken. The model (6.43) has the advantage that it allows to treat all three cases at once, i. e. uniaxial and in-plane polarization as well as unpolarized moments, as we show below. Furthermore, we can follow the lines of calculation in Sec. 5.2 to find for completely mixed valleys for the corresponding pseudospin traces, cf. Eq. (5.69),

$$\langle X_{\gamma,\gamma',\rho,\rho'} \rangle = 16 \cos(\theta_a) \cos(\theta'_a) \cos(\theta_b) \cos(\theta'_b) \langle X^s_{\gamma,\gamma',\rho,\rho'} \rangle \, . \tag{6.44}$$

The spin-dependent part is here given by [cf. Eqs. (5.67) and (5.68)]

$$X^s_{\gamma,\gamma',\rho,\rho'} = 4 \cos^2\left(\Sigma_L + N_{\mathrm{sa},L}\, \pi/2\right) \begin{cases} 1 & \text{for parallel loop propagation} \, , \\ (-1)^{N_{\mathrm{sa},L}} & \text{for antiparallel loop propagation} \, , \end{cases} \tag{6.45}$$

if the total number of reflections (along the loop part) from sa edges with in-plane polarized moments is even, and otherwise $X^s_{\gamma,\gamma',\rho,\rho'} = 0$. We consider the limit of very large effective spin scattering strength, i. e. we assume that even and odd $N_{\mathrm{sa},L}$ are equally probable, as well

as even and odd numbers of reflections from edges with in-plane polarized moments. Then we can deduce the averaged spin contribution for the three limiting cases discussed above from the general expression (6.45).

For uniaxial edge spin polarization, i. e. $s_i = \pm s_z$ for all reflections i, we set $\Sigma_L = 0$ and thus get $\langle X^s_{\gamma,\gamma',\rho,\rho'} \rangle = 2$.[1] Following the analog calculational steps as in Sec. 5.2, this results in $\mathrm{var}(g) = g_0^2/4$ (for identical leads), the leading order RMT result (5.57) for two independent, nondegenerate orthogonal systems. The reason is that the term $s_z \otimes \tau_z \otimes \sigma_z$ in the boundary condition (6.4) breaks the antiunitary symmetry $s_y \mathcal{T}_y$, which ensures Kramers' degeneracy of the spin species in the absence of spin-active edges. Indeed, if we consider $s_i = s_0$ instead of $s_i = s_z$ for all reflections, this does not change the WL results (6.9) and (6.10), but for the UCF we get $X^s_{\gamma,\gamma',\rho,\rho'} = 4$ for every orbit quadruplet, and thus the leading order RMT result for two degenerate orthogonal systems, $\mathrm{var}(g) = g_0^2/2$ for identical leads. Further, for the case of in-plane polarized edge moments, we get $\langle X^s_{\gamma,\gamma',\rho,\rho'} \rangle = 1$, leading to $\mathrm{var}(g) = g_0^2/8$ for identical leads, in agreement with RMT for a single orthogonal system. As discussed above, TRS is not broken in this case, but the spin blocks are mixed, which explains this result. Only in the general case of unpolarized edge moments, TRS is broken. For the UCF we find in this case $\langle X^s_{\gamma,\gamma',\rho,\rho'} \rangle = 1/2$, and thus for identical leads $\mathrm{var}(g) = g_0^2/16$, the RMT prediction for one unitary ensemble.

To summarize, we obtain different sizes of the UCF, depending on the polarization of the edge magnetic moments, namely

$$\frac{\mathrm{var}(g_{ab})}{g_0^2} \approx \frac{M_a^2 M_b^2}{(M_a + M_b)^4} \begin{cases} 8 & \text{for spin-inactive edges}\,, \\ 4 & \text{for uniaxial polarization}\,, \\ 2 & \text{for in-plane polarization}\,, \\ 1 & \text{for unpolarized edge moments}\,. \end{cases} \tag{6.46}$$

6.4 Summary

In this chapter we have studied the effects of edge magnetization on the electronic transport through ballistic chaotic graphene quantum dots in the limit of strong valley coupling. To this end we used an effective boundary condition that accounts for the existance of a staggered magnetization close to graphene zz edges. Using this boundary condition we have developed a semiclassical theory to calculate the WL correction to the average conductance and the UCF of a mesoscopic graphene quantum dot, taking into account the effect of spin rotation due to edge magnetization in a simplified model. We have shown that uniaxially polarized edge magnetic moments do not alter the WL correction, while the UCF are in fact smaller by a factor of two compared to the case of spin-inactive edges. This is because the TRS $s_0 \mathcal{T}_y$ remains unaffected, but the spin degeneracy $s_y \mathcal{T}_y$ is broken in this case. In terms of universality classes, this case corresponds to two non-degenerate subsystems with orthogonal symmetry.

[1] Note that the total number of reflections along the loop part from edges with in-plane polarized moments is always zero in this case, and thus even.

For edge moments with polarizations that are restricted to a plane, we found that both the WL and the size of the UCF are suppressed by a factor of two compared to the uniaxial case, if the polarizations are distributed over the whole plane ($\varsigma_0 \in [0, \pi[$) and the dwell time is large compared to the typical spin scattering time ($T_\mathrm{d}/T_\mathrm{sa} \gg 1$). In this case the TRS $s_0\mathcal{T}_y$ is still intact, however the spin species are mixed, leading to the orthogonal symmetry class. Equation (6.19) describes the crossover for the WL as a function of the related parameters also for intermediate cases. Finally, if the edge moments are unpolarized, the WL is suppressed even stronger and vanishes in the limiting case of $T_\mathrm{d}/T_\mathrm{sa} \gg 1$. The reason is that the TRS $s_0\mathcal{T}_y$ is indeed broken in this case, i. e. the symmetry class is unitary, which is also reflected in the size of the UCF. The dependence of the WL on $T_\mathrm{d}/T_\mathrm{sa}$ for unpolarized edge moments is described by Eq. (6.34). In addition to the analytical calculations we have also performed numerical simulations, that are in qualitative good agreement with our theoretical predictions. We have demonstrated that the qualitative results do not depend on the exact model for the position-dependent polarization of the edge moments. Our results suggest that in a magnetotransport experiment the effects of edge magnetization can be measured via the conductance of a graphene quantum dot [212].

CHAPTER 7

Transport simulations for disordered graphene nanoribbons

In this chapter we study numerically the conductance of graphene strips with (approximately) constant width, commonly denoted as *graphene nanoribbons* (GNR), paying particular attention to the influence of the edges. Graphene nanoribbons have been studied theoretically long before they were available experimentally. First, GNR with zz and ac boundaries have been studied in a lattice model [24, 25, 79], where the particular edge dependences of the ribbon band structure and the eigenstates of such systems have already been pointed out. Later the electronic states of GNR with zz, ac [80], and also im type edges [168] have been studied using the effective Dirac theory. In the first experiments the ribbons were produced lithographically [27, 28], and the edges were not under control on an atomic level. Meanwhile, however, different methods have been used to produce GNR with atomically well defined edges. They include 'tailoring' the edges using a scanning tunneling microscope [213], chemical derivation from the solution phase [214], 'unzipping' of carbon nanotubes [215, 216, 217], anisotropic etching using nickel clusters [218], sonochemical cutting [219], and even self-assembly within carbon nanotubes [220].

As opposed to the previous chapters, we follow here an alternative approach to calculate the Green function and in turn the conductance, namely we perform numerical simulations within a tight-binding model. In the literature this is a well established method to study GNR [85, 199, 221, 222, 223, 224, 225, 226, 227, 228, 229]. The numerical treatment allows e. g. to consider regimes of disorder that are beyond the scope of the analytical formalism we have used so far. As already in the previous chapters, we use for the numerical calculations the program code of Michael Wimmer that has been introduced in Refs. [56, 61]. The corresponding nearest-neighbor tight-binding Hamiltonian of the scattering system reads

$$H_{\mathrm{tb}} = -\sum_{\langle i,j\rangle} t_{ij} c_i^\dagger c_j + \sum_i V_i\, c_i^\dagger c_i\,, \qquad \text{with} \quad t_{ij} = t \exp\left(\mathrm{i}\frac{2\pi}{\Phi_0}\,.\int_{\boldsymbol{x}_i}^{\boldsymbol{x}_j} \boldsymbol{A}(\boldsymbol{x})\cdot d\boldsymbol{x}\right)\,. \tag{7.1}$$

Here t_{ij} is the nearest-neighbor hopping constant, t, multiplied with an exponential containing the Peierls phase [230, 231] to include a vector potential $\boldsymbol{A}(\boldsymbol{x})$. Further, the $\langle i,j\rangle$ are pairs of nearest-neighbor sites of the considered hexagonal lattice. The shape of the system is defined by 'cutting' the bonds (i. e. setting $t_{ij} = 0$) between nearest-neighbor pairs where one of the sites shall not be part of the system anymore (see grey crosses in Fig. 7.1). Moreover we use

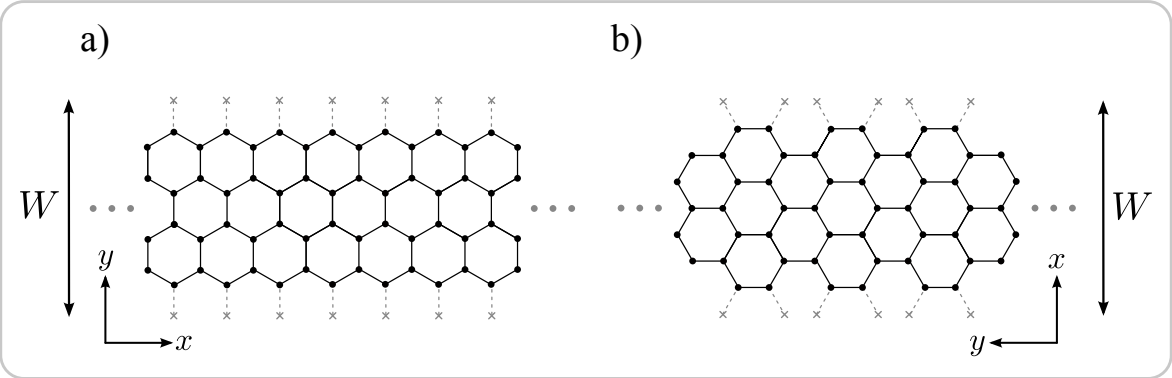

Figure 7.1: a) Zigzag graphene nanoribbon with $W = 7/\sqrt{3}\,a \approx 4\,a$. b) Armchair graphene nanoribbon with $W = 4\,a$. Note that the widths are measured between the first rows of missing lattice sites, where the boundary conditions are imposed in the effective Dirac theory (cf. Subsec. 2.2.2). In the program code, the dashed grey lines correspond to 'cut' hopping connections with $t_{ij} = 0$.

a Gaussian disorder model, where

$$V_i = \sum_{j=1}^{N_\mathrm{i}} \delta_j \exp\left(-\frac{(\boldsymbol{x}_i - \boldsymbol{X}_j)^2}{2\xi_j^2}\right) . \tag{7.2}$$

Here $\boldsymbol{x}_i$ and $\boldsymbol{X}_j$ are the position vectors of the i-th lattice site and the j-th scattering center, respectively. The GNR are attached to two leads with the same widths as the ribbon, which are free of disorder and infinitely extended. For a given energy, the retarded Green function of the scattering region is obtained by the matrix inversion

$$G_\mathrm{tb} = (E - H_\mathrm{tb} - \Sigma_\mathrm{tb})^{-1} , \tag{7.3}$$

where Σ_tb denotes the self energy of the leads, which is also calculated numerically. The conductance of the system is then obtained using a discrete version of the Fisher-Lee relations [175] (cf. App. A.5.2). For details of the numerical calculation we refer to Refs. [56, 61].

In the first section of this chapter we investigate the influence of the edge types on the total quantum conductance and the weak localization in moderately disordered GNR. In zz nanoribbons, states from the two valleys K and K′ are well separated in momentum space, as can be seen in Fig. 7.2 d). Therefore, the two valleys are usually considered independent of each other, if no short range scattering potentials are present [72]. In each individual valley, the numbers of leftmovers and rightmovers, i. e. the numbers of bands with negative and positive slope, respectively, differ by one at a given energy. This leads, in the absence of intervalley scattering, to the suppression of Anderson localization [223]: The conductance is always greater than g_0. For this, Wakabayashi and coworkers have coined the term 'perfectly conducting channel' (pcc) [223]. Later it was shown that a similar phenomenon is present in metallic ac GNR , namely it has been demonstrated in Ref. [229] by a transfer matrix analysis within the effective Dirac theory, that the lowest band in such a ribbon, cf. Fig. 7.2 b), is barely

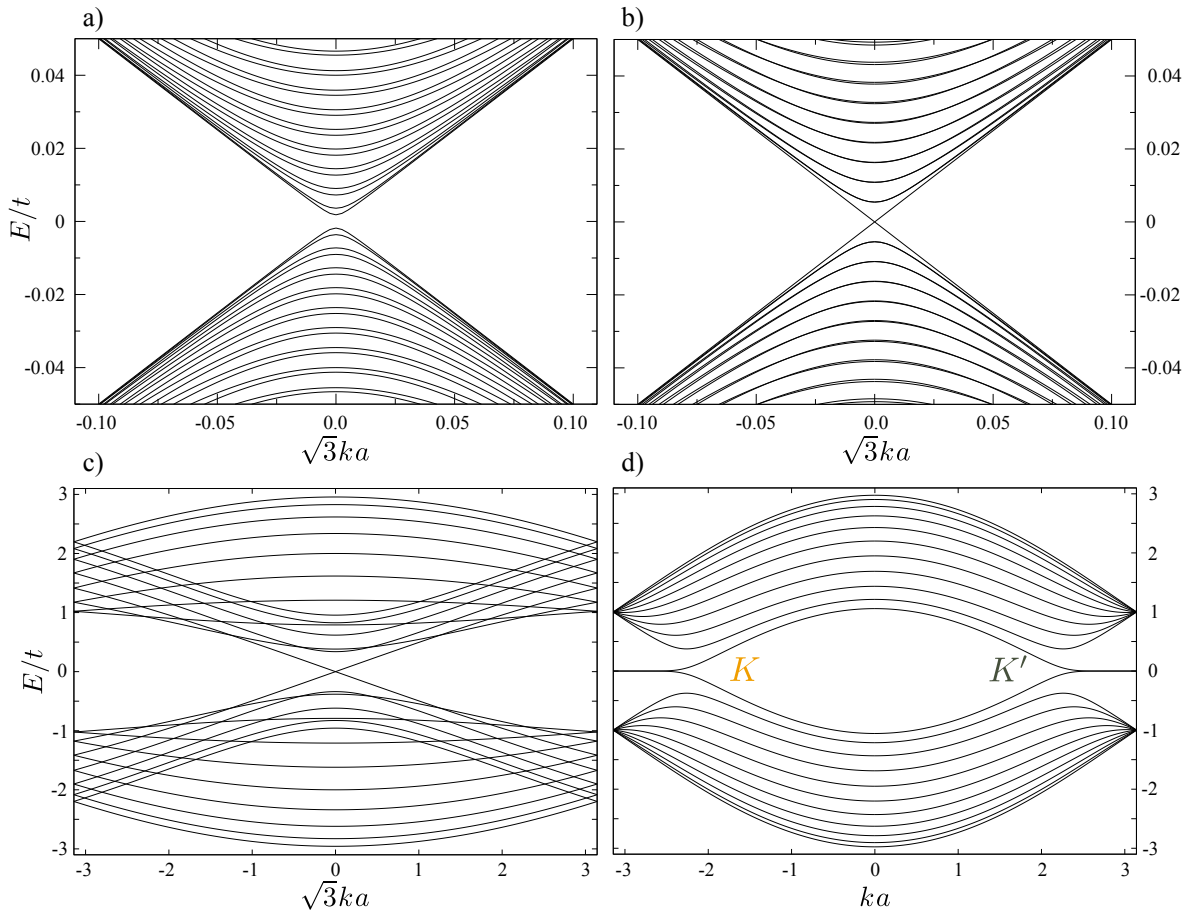

Figure 7.2: a), b) Tight-binding band structures of wide ac GNR close to the Dirac point. a) Semiconducting ac GNR with $W = 502\,a$. b) Metallic ac GNR with $W = 501\,a$. The non-linear bands are approximately degenerate for low energies. c), d) Full tight-binding band structures of narrow GNR. c) Metallic ac GNR with $W = 7.5\,a$. Clearly the band degeneracy is lifted. d) Zigzag GNR with $W = 19/\sqrt{3}\,a$. Note that the positions of the Dirac points are shifted with respect to bulk graphene [see Fig 2.1 b)] due to the zone folding that leads from the bulk bandstructure to the one of a ribbon [25]. The edge states connect the two K-points, since the regions of k-space with $\pi < ka < 2\pi$ and $-\pi < ka < 0$ are equivalent.

backscattered in the absence of short range potentials. However, the authors of Ref. [229] state that this is a particular property of the lowest band in the metallic GNR, and that the effect is only visible in single-channel transport. Here we show that this is in fact not the case. Rather the special, block-diagonal pseudovalley structure that we have discussed already in Subsec. 2.2.2 is the origin of the pcc in metallic ac GNR, leading to the analog situation as in zz GNR. We show that the pcc in the metallic ac case is also observable in the multichannel regime as a consequence of the pseudovalley substructure. Moreover we demonstrate that the pcc in zz GNR is completely destroyed also in the absence of short range potentials if the disorder is of the same order as the Fermi energy. The reason for this is an effective intervalley coupling due to backscattering via the zz edge states close to zero energy. Furthermore we correct the widespread believe that *all* ac GNR belong to the orthogonal symmetry class. As already mentioned in Subsec. 2.2.2, if the pseudovalleys in metallic ac GNR are not coupled, the system belongs to the *unitary* symmetry class, even though the real valleys are completely mixed due to the ac edges. We show by magnetotransport simulations that the WL is indeed strongly suppressed in metallic ac ribbons.

The focus of the second section is the simulation of an experiment that has been carried out by Silvia Schmidmeier and coworkers from the University of Regensburg at the Dresden High Magnetic Field Laboratory. They have measured the magnetoresistance of GNR in pulsed, perpendicular magnetic fields up to $B \approx 60\,\mathrm{T}$. For relatively high carrier densities n_c, Shubnikov-de-Haas (SdH) oscillations are observed, reflecting the shift of the Landau levels with increasing magnetic field. On the other hand for lower carrier densities, the experiment shows an increase of the conductance for fields below $10 - 40\,\mathrm{T}$, and a conductance decrease for higher fields. Our numerical simulations reproduce the experimental data for large n_c and in the low magnetic field regime also for low n_c semi-quantitatively. It is therefore possible to estimate the importance of different sources of disorder in the GNR. We show that a combination of both, edge disorder and potential disorder with a correlation length in the order of few a, is a likely disorder scenario for the experimental samples.

7.1 Perfectly conducting channels and symmetry breaking

Throughout this section we use for the potential (7.2) $N_\mathrm{i} = p\,N_\mathrm{a}$ randomly distributed Gaussian scatterers at positions $\boldsymbol{X}_j$. Here, N_a is the total number of lattice sites in the disordered scattering region, and $0 \leq p \leq 1$ is a constant that determines the relative amount of scatterers. Further, we choose the δ_j randomly from the interval $[-\delta, \delta]$ and $\xi_j = \xi$ is constant for all j.

In Fig. 7.3 a) we show the results of tight-binding simulations of the disorder averaged conductance, $\langle g \rangle$, of ac GNR as a function of their lengths L. For the size of the ribbons we used realistic values, namely $W \approx 62\,\mathrm{nm}$ and $62\,\mathrm{nm} \lesssim L \lesssim 1.2\,\mu\mathrm{m}$. The only difference between the systems corresponding to the two curves are their exact widths. While the black curve corresponds to a semiconducting GNR ($W = 251\,a$), the blue curve is the conductance of a metallic GNR [$W = 252\,a$, cf. Eq. (2.63)]. The total number of propagating lead channels is

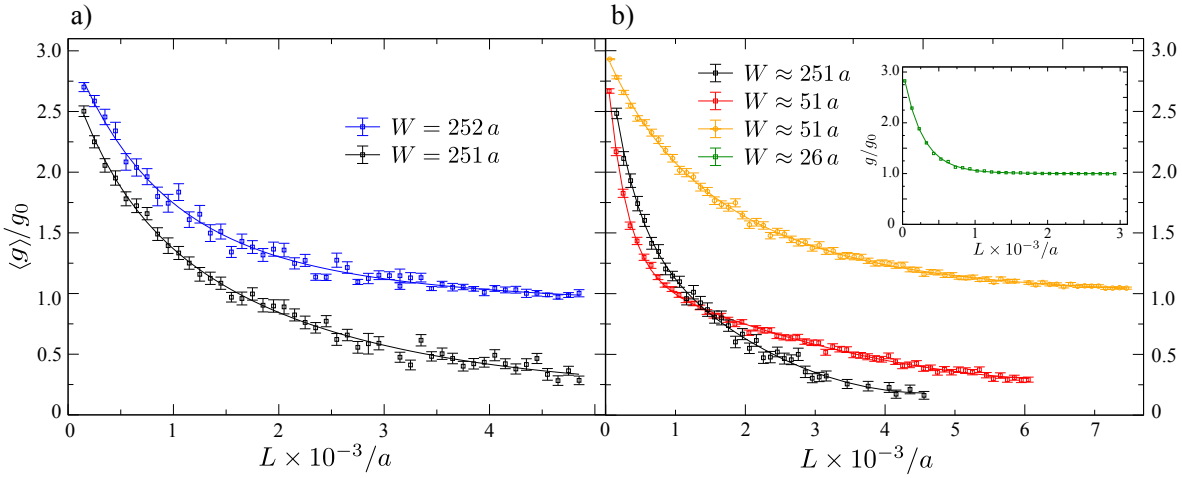

Figure 7.3: Average conductance of GNR as a function of the ribbon length. In all systems the Fermi energy corresponds to three propagating lead channels. a) Semiconducting ac ribbons with $W = 251\,a$ (black) and metallic ac ribbon with $W = 252\,a$ (blue). The Fermi energy is $E = 0.017\,t$. For the disorder parameters (cf. main text) we used $p = 0.05$, $\xi = 2.0\,a$ and $\delta = 0.08\,t$. For each data point we have averaged over 50 impurity configurations. b) Zigzag GNR with different widths and disorder parameters. For all systems we have used $p = 0.05$ and $\xi = 2.0\,a$. Black: $W = 434.5/\sqrt{3}\,a \approx 251\,a$, $E = 0.022\,t$, $\delta = 0.08\,t$, 50 impurity configurations. Red: $W = 88/\sqrt{3}\,a \approx 51\,a$, $E = 0.11\,t$, $\delta = 0.08\,t$, 200 impurity configurations. Orange: $W = 88/\sqrt{3}\,a \approx 51\,a$, $E = 0.11\,t$, $\delta = 0.04\,t$, 200 impurity configurations. Green (inset): $W = 44.5/\sqrt{3}\,a \approx 26\,a$, $E = 0.22\,t$, $\delta = 0.08\,t$, 200 impurity configurations.

three in both cases. The average conductance of the semiconducting ribbons decays approximately exponentially and tends towards zero for very long systems, i.e. Anderson localization [232] starts to set in. The conductance curve for the metallic systems is distinctly different. Also here $\langle g \rangle$ decays approximately exponentially on a similar length scale. However, instead of approaching zero conductance, the curve saturates at one conductance quantum. The origin of this particular behavior is the pseudovalley structure of metallic GNR that we have introduced in Chap. 2. The pseudovalley states are linear superpositions of states from the real valleys K and K′. In fact, while states in the real valleys K and K′ are eigenstates of τ_z, states in the pseudovalleys are eigenstates of τ_y. This means that the two corresponding pseudospin spaces are related to each other by a rotation of $\pi/2$ around the valley x-axes, $\mathcal{R}_{zy}$. We denote the pseudovalleys by $\mathrm{K}_\mathcal{R}$ and $\mathrm{K}'_\mathcal{R}$ and refer to Subsec. 2.2.2 for details. For a metallic GNR the width is such that the boundary matrices for both edges are diagonal in the pseudovalleys, as noted in Fig. 7.4 [see also Eq. (2.68)]. The rotated version of the intravalley TRS operator, $\mathcal{T}_0^{zy} = \mathcal{R}_{zy}^\dagger \mathcal{T}_0 \mathcal{R}_{zy}$, connects the two pseudovalleys, which ensures their (Kramers) degeneracy. The mechanism that leads to the absence of localization in the metallic GNR can be understood as follows. In the effective Dirac theory, the energy band

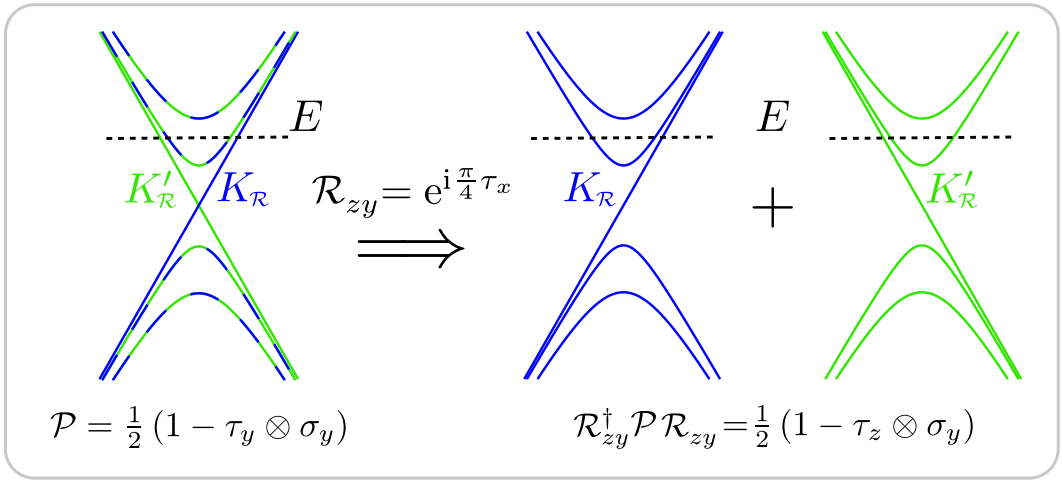

Figure 7.4: Pseudovalley structure in metallic ac GNR. After a rotation of the valley space of $\pi/2$ around the valley x-direction, the metallic ac boundary condition is diagonal in the new valley space.

structure of a metallic ac GNR with width W is given by [80]

$$k_E(k) = \frac{E(k)}{\hbar v_F} = \pm\sqrt{k^2 + \frac{n^2\pi^2}{W^2}}\,, \qquad n \in \mathbb{Z}\,, \tag{7.4}$$

with the longitudinal momentum k and the integer band index n. Here it is important to note that n and $-n$ are both allowed and lead to different eigenstates [80, 85]. In fact for $n \neq 0$, these two states are Kramers partners. On the other hand, $n = 0$ corresponds to the linear bands, see Figs. 7.2 b) and 7.4. For a given energy, the two states in the linear bands with momenta k and $-k$ are also Kramers partners. The situation is sketched in Fig. 7.4: For a given Fermi energy E, there is always an odd number of forward movers ($k > 0$) and the same number of backward movers ($k < 0$) in total. However, in each individual pseudovalley the numbers of forward and backward movers differ always by one, which leads to the absence of localization. In the pseudovalley with less forward movers ($\mathrm{K}'_{\mathcal{R}}$ in Fig. 7.4) there is no constraint on the backscattering. Thus, for long enough ribbons, the contribution to the conductance from this pseudovalley is zero. In the pseudovalley with less backward movers ($\mathrm{K}_{\mathcal{R}}$ in Fig. 7.4) the conductance cannot drop below g_0, since not enough states for backscattering are available. We stress however that it is *not* necessarily the state from the lowest band that is transmitted. In fact, in the numerical conductance, mode mixing occurs also in the regime where $\langle g \rangle \approx g_0$. As long as the symmetry $\mathcal{T}_0$ is preserved, i. e. in the absence of short range potentials, there can be no backscattering from one pseudovalley to the other, because the corresponding states are Kramers partners and thus orthogonal. To see this, we consider a forward moving state $|+\rangle$, a backward moving state $|-\rangle = \mathcal{T}_0|+\rangle$, and a potential $V(\boldsymbol{x})$ with $[V(\boldsymbol{x}), \mathcal{T}_0] = 0$. Then we have for the matrix element

$$\langle -|V(\boldsymbol{x})|+\rangle = -\langle +|\mathcal{T}_0^{\dagger}V(\boldsymbol{x})\mathcal{T}_0^2|+\rangle = -\langle +|\mathcal{T}_0^{\dagger}\mathcal{T}_0 V(\boldsymbol{x})|-\rangle = -\langle -|V(\boldsymbol{x})|+\rangle = 0\,. \tag{7.5}$$

This argumentation is valid irrespective of the number of open lead channels. Mathematically, the reason for $g \geq g_0$ is the special structure of the scattering matrix in the absence of pseudovalley mixing. In this case we have e. g. for reflection from one of the leads

$$\begin{pmatrix} out \\ out' \end{pmatrix} = \begin{pmatrix} r & 0 \\ 0 & r' \end{pmatrix} \begin{pmatrix} in \\ in' \end{pmatrix}, \tag{7.6}$$

where in and in' stand for the incoming amplitudes from pseudovalley $\mathrm{K}_{\mathcal{R}}$ and $\mathrm{K}'_{\mathcal{R}}$, respectively, and out and out' stand for the corresponding outgoing amplitudes. Note that the corresponding reflection matrices r and r' are not square matrices. Since the total number of propagating channels M is always odd, we can write $M = 2m+1$ with integer m. Considering reflection at the left side, r is then an $m \times (m+1)$ matrix and r' an $(m+1) \times m$ matrix. Therefore r and r' can be written as the singular value decompositions [233]

$$r = \mathcal{U} \begin{pmatrix} d_1 & 0 & 0 & \cdots & 0 \\ 0 & d_2 & 0 & & 0 \\ \vdots & & \ddots & & \vdots \\ 0 & \cdots & 0 & d_m & 0 \end{pmatrix} \tilde{\mathcal{U}} = \mathcal{U} d \tilde{\mathcal{U}}\,, \quad r' = \mathcal{U}' \begin{pmatrix} d'_1 & 0 & \cdots & 0 \\ 0 & d'_2 & 0 & \vdots \\ \vdots & & \ddots & 0 \\ & & & d'_m \\ 0 & 0 & \cdots & 0 \end{pmatrix} \tilde{\mathcal{U}}' = \mathcal{U}' d' \tilde{\mathcal{U}}'\,, \tag{7.7}$$

with unitary square matrices $\mathcal{U}, \tilde{\mathcal{U}}, \mathcal{U}'$, and $\tilde{\mathcal{U}}'$, and $|d_i|, |d'_i| \leq 1$. Due to current conservation and the block diagonal structure of the full reflection matrix in Eq. (7.6), the conductance from the left to the right lead is given by [234]

$$g/g_0 = 2m + 1 - \mathrm{Tr}(r^\dagger r) - \mathrm{Tr}(r'^\dagger r') = 2m + 1 - \mathrm{Tr}(d^\dagger d) - \mathrm{Tr}(d'^\dagger d')\,. \tag{7.8}$$

However, from Eq. (7.7) it follows that

$$d^\dagger d = \mathrm{diag}(|d_1|^2, \ldots, |d_m|^2, 0)\,, \qquad d'^\dagger d' = \mathrm{diag}(|d'_1|^2, \ldots, |d'_m|^2)\,, \tag{7.9}$$

and therefore

$$g/g_0 = 2m + 1 - \sum_{i=1}^{m} (|d_i|^2 + |d'_i|^2) \geq 1\,. \tag{7.10}$$

Our discussion rises the question why the pcc in the multichannel regime has not been observed by Yamamoto and coworkers [229]. The reason for this is that the ribbons that have been used for the simulations in the earlier work of Ref. [229] have been extremely narrow ($W = 7.5\,a \approx 1.8\,\mathrm{nm}$). The problem is that for such narrow ribbons the Dirac equation is not an adequate description at energies where more than one lead channel is propagating. In Fig. 7.2 c) we show the tight-binding band structure of an ac GNR with $W = 7.5\,a$. One can see that the threshold energy for the second channel is already above $0.3\,t$, and that none of the bands are degenerate, as opposed to the prediction of the Dirac equation. This is due to the fact that $\mathcal{T}_0$ is broken at such high energies because quadratic terms in the Hamiltonian

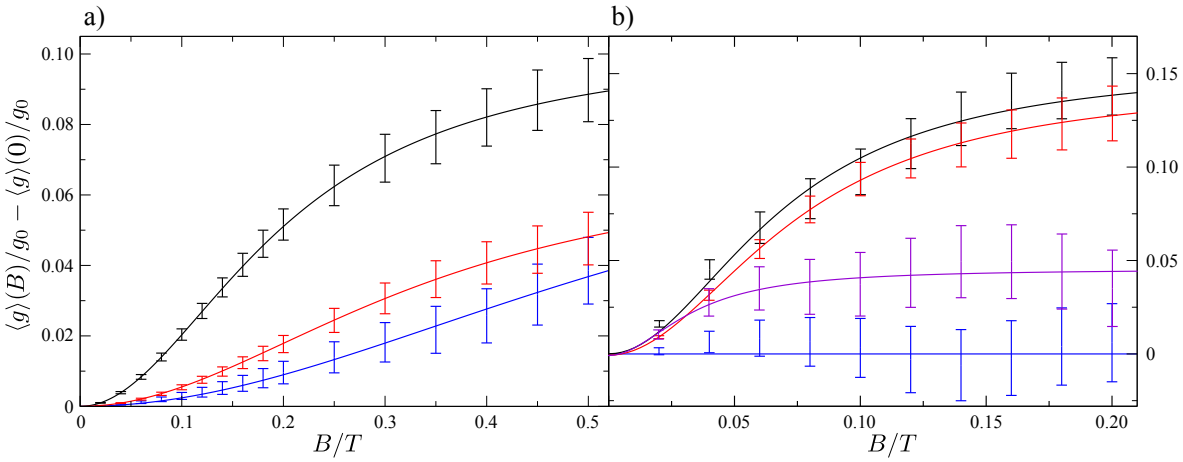

Figure 7.5: Weak localization in disordered GNR. The used disorder parameters are $p = 0.05$, $\xi = 2.0\,a$, and $\delta = 0.08\,t$, as for Fig. 7.3 a). For each point we have averaged over 600 impurity configurations. a) Black: semiconducting ac ribbon with $W = 251\,a$, $L \approx 1250\,a$, and $E = 0.017\,t$ (3 open channels). Blue: metallic ac ribbon with $W = 252\,a$, $L \approx 1250\,a$, and $E = 0.017\,t$ (3 open channels). Red: zz ribbon with $W = 434.5/\sqrt{3}\,a \approx 251\,a$ and $E = 0.022\,t$ (3 open channels). b) Black: semiconducting ac ribbon with $W = 502\,a$, $L \approx 2500\,a$, and $E = 0.017\,t$ (6 open channels). Blue: metallic ac ribbon with $W = 501\,a$, $L \approx 2500\,a$, and $E = 0.017\,t$ (7 open channels). Red: zz ribbon with $W = 865.5/\sqrt{3}\,a \approx 500\,a$ and $E = 0.017\,t$ (5 open channels). Violet: zz ribbon with $W = 865.5/\sqrt{3}\,a \approx 500\,a$ and $E = 0.1\,t$ (35 open channels).

become non-negligible [63]. One can see from Fig. 7.2 b) that for wider ribbons the bands are degenerate also in the multichannel regime.

Now we turn to the case of zz GNR. As can be seen from Fig. 7.2 d), the situation is here rather similar to the metallic ac GNR, but now the real valleys are preserved instead of the pseudovalleys. Again we have an imbalanced number of forward and backward movers in each individual valley. Here $\mathcal{T}_x$ is the symplectic symmetry operation that connects the two valleys and ensures their Kramers degeneracy, and thus the orthogonality of the partner states. The argumentation is identical to the metallic ac case: As long as the valleys are uncoupled, the valley with one additional forward mover (valley K in our case) contributes always at least one conductance quantum to g. In fact in Ref. [235] the authors explain the pcc in the zz case in terms of the reflection matrices basically in the same way as we did above for the metallic ac ribbons. In Fig. 7.3 b) we present the tight-binding simulations for GNR with zz edges. The black curve corresponds to a zz GNR with $W = 434.5/\sqrt{3}\,a \approx 251\,a$ with three propagating lead channels as in the case of the ac ribbons above. Surprisingly, we find no pcc at all in this case, although the disorder used is the very same as in the ac case, and is thus expected to cause only very little intervalley scattering. The origin of this unexpected behavior are the zz edge states. For the disorder parameter corresponding to the height of the Gaussian potential in Eq. (7.2) we have used $\delta = 0.08\,t$, while the Fermi energy was only $E = 0.022\,t$. This means that the potential is large enough to shift the Fermi energy in the scattering region locally

into the hole regime. However, the edge states with energies close to zero connect the two valleys to each other, as can be seen from Fig. 7.2 d). When the Fermi energy is shifted below $E = 0$, backscattering from one valley to the other is possible via the edge states, destroying the pcc even for long range potential disorder. A more detailed and quantitative study of this effective valley coupling will be presented elsewhere [236]. The red curve in Fig. 7.3 b) shows the conductance for ribbons with $W = 88/\sqrt{3}\,a \approx 51\,a$ with the same disorder as before and $E = 0.11\,t$ (three open channels). Even though the Fermi energy is now slightly greater than δ, there is no pcc visible in this case, since the potentials of different scatterers can overlap and thus locally lead to total potential values larger than δ. Only if in addition we reduce the potential strength to $\delta = 0.04\,t$ (blue curve), the conductance curve saturates at about g_0, but one has to consider very long ribbons to observe this. The effective intervalley coupling mediated through edge states has not been observed in the extremely narrow ribbons that have been considered earlier ($W \approx 5\,a \approx 1.2\,\mathrm{nm}$ in Ref. [223]). The inset shows a simulation for rather narrow ribbons ($W = 44.5/\sqrt{3}\,a \approx 26\,a$), where the saturation of the conductance occurs already for shorter ribbon lengths.

Figure 7.5 shows the results of magnetotransport simulations for various wide GNR. The disorder parameters are identical for all curves, namely the same as used for the ac ribbons in Fig. 7.3 a). For Fig. 7.5 a) we used $W \approx 250\,a$ and $L \approx 1250\,a$, while for panel b) the systems are twice larger, namely $W \approx 500\,a$ and $L \approx 2500\,a$. First we note that we find (suppressed) weak *localization* for all systems, *no antilocalization*. In panel a), the size of the WL correction is significantly suppressed for the ribbon with zz edges (red) and the metallic ac GNR (blue), with respect to the semiconducting ac GNR (black). The reason for the suppression of the WL is the valley and pseudovalley substructure of the systems, respectively. As discussed in Subsec. 2.2.2, cf. Eq. (2.45), zz edges break the intravalley TRS $\mathcal{T}_0$, so that each valley represents a unitary subsystem [223]. In the simulations in Fig. 7.5 a), the valleys are not completely decoupled in the zz case, since the edge state mediated intervalley coupling is also present here. As a consequence, the WL is not completely suppressed. For the metallic ac GNR the situation is similar. In fact in the rotated valley space, the symplectic symmetry $\mathcal{T}_x^{zy}$ could serve as intra-pseudovalley TRS, however it is broken by ac edges, cf. Eqs. (2.61), (2.66), and (2.68). This means that also the pseudovalley subsystems belong indeed to the unitary symmetry class, as mentioned already in Subsec. 2.2.2. Also for the metallic ac ribbon in panel a), the WL is not fully suppressed due to the weak pseudovalley coupling associated with the partial lifting of the Kramers degeneracy. For the wider ribbons in panel b), the suppression in the metallic ac case is striking, since the degeneracy of the pseudovalleys is intact here, which is reflected also in the absence of the band splitting at low energies in Fig. 7.2 b). On the other hand, for the zz ribbon with 5 propagating channels (red), the WL is nearly as large as for the semiconducting ac case, indicating strong edge state mediated valley coupling. At higher energies, namely for 35 open channels (violet), the coupling is less effective, and thus the WL is clearly suppressed also here.

Our discussion and numerical results show clearly that the correct symmetry class for ac GNR is the orthogonal class for the semiconducting and the unitary class for the metallic

case, if short range potentials are absent. We stress that, to our knowledge, this has not been noticed so far. Rather ac GNR have been classified into the orthogonal symmetry class, irrespective of whether they are semiconducting or metallic [229, 235]. The numerical results presented here indicate that the effects of the edge type on the effective universality classes are directly observable in magnetoconductance measurements.

7.2 Magnetoconductance in high magnetic fields

In this section we focus on numerical simulations of a magnetotransport experiment in disordered GNR [237]. At the Dresden High Magnetic Field Laboratory Silvia Schmidmeier and coworkers from the University of Regensburg have measured the magnetoresistance of ribbons for field strengths up to $B \approx 60\,\mathrm{T}$. With the help of our simulations it is possible to gain insight into the nature of the disorder in the ribbons.

The GNR have been produced at the University of Regensburg by electron beam lithography and subsequent oxygen plasma etching of mechanically exfoliated graphene flakes on silicon dioxide. Afterwards palladium contacts were attached by thermal evaporation. Width and length of the ribbons are $W \approx 70\,\mathrm{nm}$ and $L \approx 1\,\mu\mathrm{m}$, respectively [see the electron micrograph of a sample in Fig. 7.6 a)]. Using the substrate as a back-gate, the charge carrier density and thus the Fermi energy could be tuned by changing the applied voltage. Figure 7.6 a) shows the resistance of the GNR that has been used for the magnetotransport measurements as a function of the gate voltage, V_g, at zero magnetic field. One can see the characteristic peak indicating the Dirac point at $V_\mathrm{g} \approx V_\mathrm{D} \approx -4.4\,\mathrm{V}$.

In Fig. 7.6 b) and c) we show the experimental results for the magnetoresistance for different values of V_g. Clearly different results are obtained depending on whether the measurement is carried out close ($-9.2\,\mathrm{V} \lesssim V_\mathrm{g} \lesssim -4.8\,\mathrm{V}$) or further away ($-19\,\mathrm{V} \lesssim V_\mathrm{g} \lesssim -12\,\mathrm{V}$) from the Dirac point. Using finite element simulations to determine the capacitive gate coupling, one finds for the Fermi energy $E \approx 69\sqrt{|V_\mathrm{g} - V_\mathrm{D}|}\,\mathrm{meV}/\sqrt{\mathrm{V}}$ [237]. In the following we denote the two regimes as low energy and high energy regime, respectively. For low energies, the resistance decreases starting from $B = 0$ to $B \approx 15 - 35\,\mathrm{T}$ by nearly one order of magnitude. For higher magnetic fields, the resistance increases strongly as shown in Fig. 7.6 b). On the other hand, for higher energies one can see from Fig. 7.6 c) that the resistance does not decrease significantly at low fields, and clear *Shubnikov-de-Haas* oscillations [238] are observed for higher values of B.

In order to gain more insight into the types of disorder that can cause such behavior, we have performed tight-binding simulations of (semiconducting ac) GNR with comparable size ($W \approx 100\,a \approx 25\,\mathrm{nm}$, $L = 1300\,a \approx 320\,\mathrm{nm}$). To appropriately describe the experimental findings, we have considered different types of disorder. Apart from Gaussian scatterers as in the previous section, see Eq. (7.2), we also take into account edge disorder, that originates from the fabrication process. To this end we cut segments of circles with typical sizes of about $15\,a \approx 4\,\mathrm{nm}$ out of the graphene lattice at random positions on the edge. This simulates the large scale edge roughness that occurs due to electron beam resist roughness and

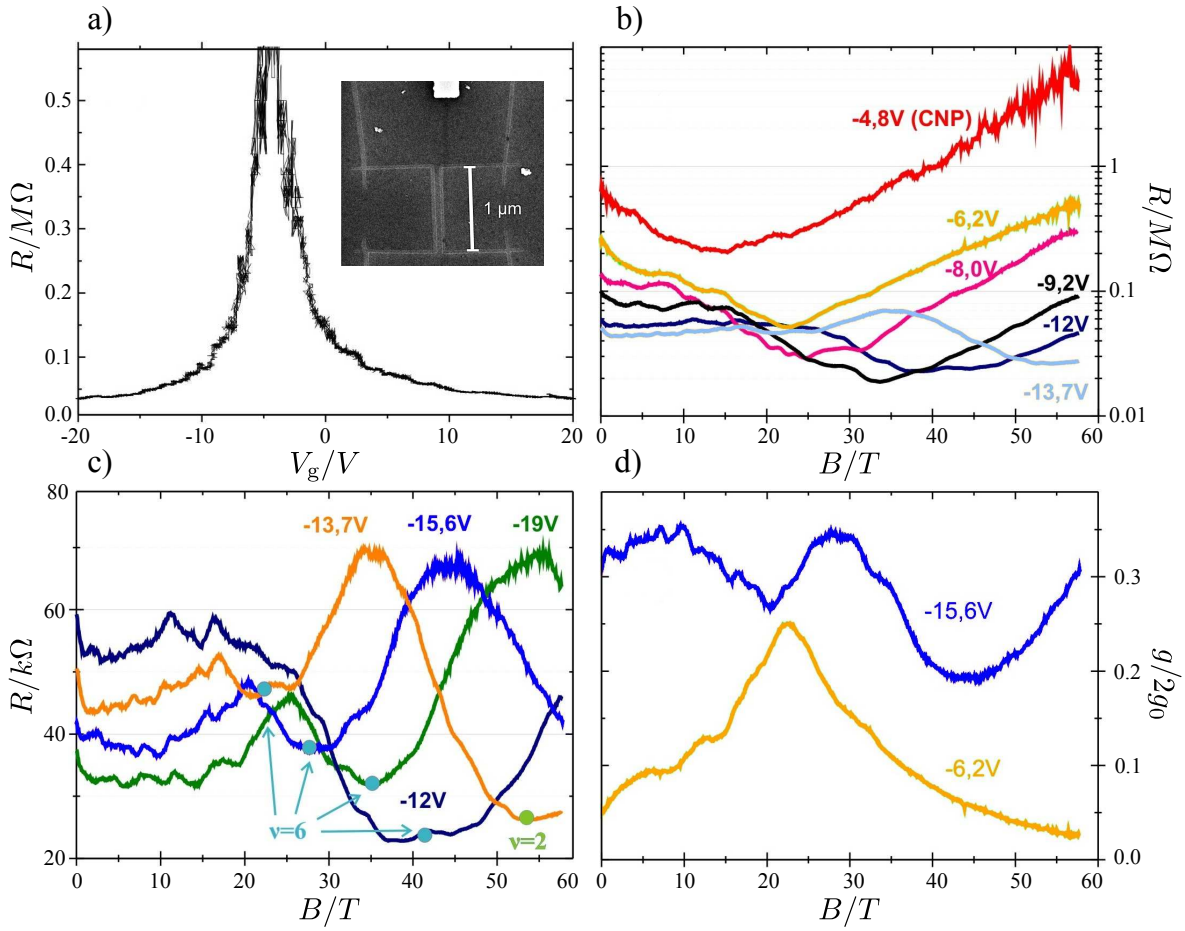

Figure 7.6: Experimental results for the resistance and conductance of GNR with width $W \approx 70\,\mathrm{nm}$ and length $L \approx 1\,\mu\mathrm{m}$ [237] (Courtesy of Silvia Schmidmeier). a) Two-terminal resistance R as a function of the gate voltage V_g at temperature $T = 25\,\mathrm{K}$ and zero magnetic field. The Dirac point is approximately at $V_\mathrm{g} = -4.4\,\mathrm{V}$. Inset: Scanning electron microscope image of a typical experimental sample. b) Magnetoresistance for different gate voltages close to the Dirac point and c) further away from the Dirac point at $T = 25\,\mathrm{K}$. d) Conductance g as a function of the magnetic field for $V_\mathrm{g} = -15.6\,\mathrm{V}$ and $V_\mathrm{g} = -6.2\,\mathrm{V}$ at $T = 25\,\mathrm{K}$.

random nature of the oxygen plasma etching. Additionally we account for edge roughness on a smaller scale of few lattice constants using a model introduced in Ref. [227]: About 10 percent of the edge atoms are randomly removed and subsequently dangling bonds are removed also. This procedure is repeated 5 times. The inset in Fig. 7.7 a) shows a section of the resulting edge. In addition to the edge disorder, we study two types of bulk potential disorder. On the one hand, we model so-called electron-hole puddles, i. e. long range potential fluctuations due to charged impurities trapped beneath the graphene ribbon in the silicon oxide substrate, (see e. g. Refs. [12, 58]). We use the disorder potential (7.2) with $N_\mathrm{i} = 10^{-4} \times N_\mathrm{a} \approx 30$ randomly distributed Gaussian scatterers with $\xi_j = 35\,a \approx 8.6\,\mathrm{nm}$ and randomly chosen $\delta_j/t \in [-0.03, 0.03]$. These values lead to a potential comparable to experimentally determined profiles [239]. Second, we also consider shorter-ranged impurity potentials, that can arise due to adsorbates, defects or charged impurities. In this case we use $\xi_j = 1.8\,a \approx 4.4\,\mathrm{nm}$, $N_\mathrm{i} = pN_\mathrm{a}$ and $\delta_j/t \in [-\delta, \delta]$.

In Fig. 7.7 we present our numerical results for magnetotransport through disordered nanoribbons at relatively high ($E \approx 0.084\,t \approx 226\,\mathrm{meV}$, blue curves) and lower ($E \approx 0.034\,t \approx 92\,\mathrm{meV}$, orange curves) energies, that correspond approximately to the gate voltages in Fig. 7.6 d), assuming the commonly used value $t \approx 2.7\,\mathrm{eV}$ for the hopping constant [58]. For each curve in Fig. 7.7 we have averaged the conductance for 10 different values of the Fermi energy, chosen from a window of $4 \times 10^{-3}\,t \approx 11\,\mathrm{meV}$ around the above mentioned values [see inset in Fig. 7.7 b)]. This accounts for the the finite bias voltage of 10 mV used in the experiment. Additionally we have performed a running average over the magnetic field with a window of $\sim 1-3\,\mathrm{T}$, accounting for the built-in (time) average in the real measurement due to the pulsed field [237]. First we consider ribbons with only edge disorder [Fig. 7.7 a)]. While the conductance at zero magnetic field is comparable to the experimental value for low energies, this is not the case for the high energy regime. With increasing magnetic field, the wavefunctions become more localized close to the edges (cf. particle densities in Fig. 7.8). Without bulk disorder, backscattering is strongly suppressed, so that we observe nearly perfect quantum hall plateaus for both energy regimes already at moderate fields, which is in contrast to the experimental findings. This means that edge disorder alone cannot explain the experiment.

Considering only long range Gaussian disorder [panel b)], we find that this has a strong effect on the conductance at low energies, while at high energies $\langle g \rangle$ is affected only little. This is plausible, since in the former case the energies are of the same size than the potential fluctuations, so that the charge carriers see relatively strong disorder. On the other hand, for energies several times higher than the potential fluctuations, the charge carriers see a smoothly modulated background potential that does not cause strong backscattering. Simulations where only the short range impurities are taken into account [panel c)], show that for strong enough scattering potentials ($p = 0.15$ and $\delta = 0.1\,t$), the zero field conductance can be very close to the experimental data for both energy regimes. However, such strong bulk disorder leads to backscattering even for very high magnetic fields, so that at high energies no SdH oscillations are observed. This means that indeed a combination of bulk and edge disorder

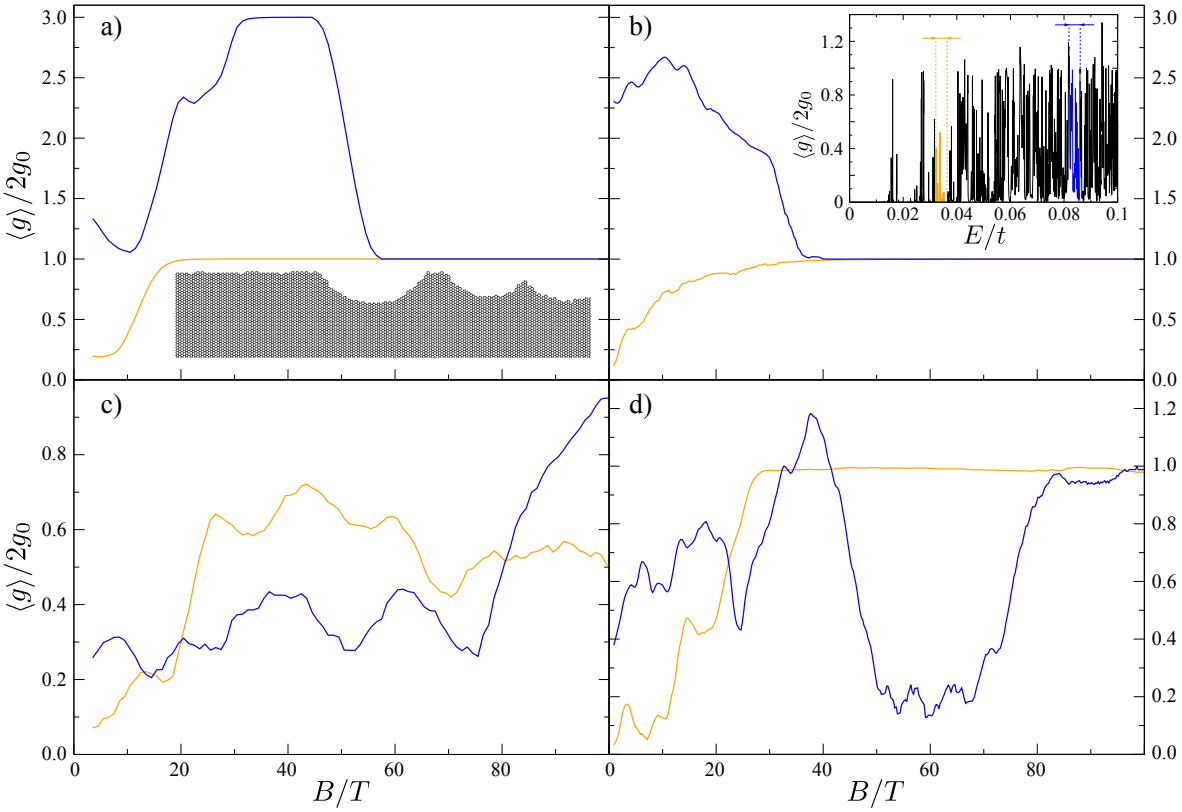

Figure 7.7: Magnetoconductance of ac GNR ($W \approx 100\,a$, $L \approx 1300\,a$) calculated numerically for different disorder models and different Fermi energies: $E \approx 0.084\,t \approx 226\,\text{meV}$ (blue) and $E \approx 0.034\,t \approx 92\,\text{meV}$ (orange). Each curve results from an average over 10 energies within a window of $4 \times 10^{-3}\,t$ around these values and a running average over the magnetic field with a window of 3 T [panels a) and c)] and 1 T [panels b) and d)], respectively. a) Edge disorder (see inset and main text). b) Long range Gaussian disorder. We use Eq. (7.2) with $N_\text{i} = 10^{-4} \times N_\text{a}$, $\xi_j = 35\,a$, and $\delta_j/t \in [-0.03, 0.03]$. c) Very strong short-range Gaussian disorder (7.2) with $N_\text{i} = 0.15\,N_\text{a}$, $\xi_j = 1.8\,a$, and $\delta_j/t \in [-0.1, 0.1]$. d) Edge disorder (see inset in panel a) and main text) and short-range Gaussian disorder (7.2) with $N_\text{i} = 0.08\,N_\text{a}$, $\xi_j = 1.8\,a$, and $\delta_j/t \in [-0.09, 0.09]$. The inset in panel a) shows the conductance of ribbons with edge and short-range bulk disorder [as in panel d)] as a function of the Fermi energy. The energy regions that were chosen for the magnetoconductance simulations are marked in orange and blue, respectively.

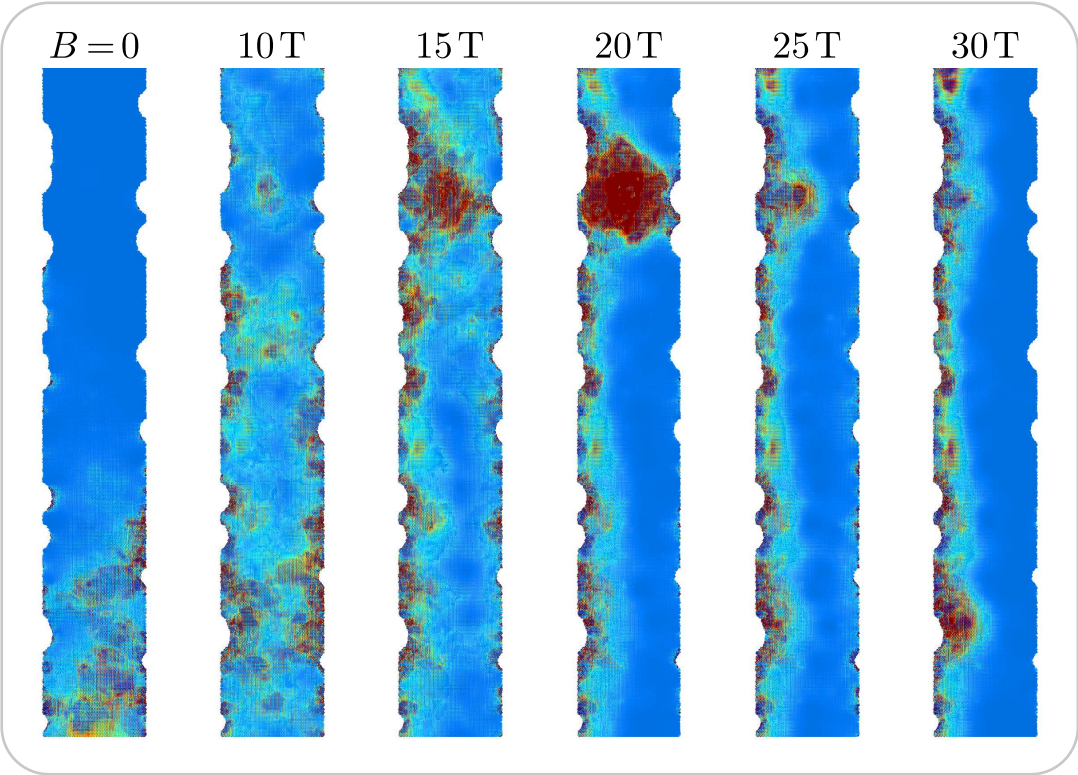

Figure 7.8: Local particle density in ac GNR with edge and bulk disorder as in Fig. 7.7 d) for $E = 0.0335\,t$ and different magnetic fields B, calculated numerically. Red corresponds to high and blue to low density. The particles enter the ribbon from the bottom, so that at high fields the quantum Hall edge channels form at the left edge.

is necessary to describe the experiments appropriately also for higher fields. In panel d) we show the results for ribbons with disordered edges and weaker short-range bulk disorder ($p = 0.08$, $\delta = 0.09\,t$). In this case, the experimental data are reproduced semi-quantitatively, except for very high magnetic fields in the low energy regime. For small and moderate fields we find in the low energy regime a strong increase of $\langle g \rangle$ due to the formation of edge channels. We plot the particle density at different magnetic fields in Fig. 7.8, confirming this picture. On the other hand, clear SdH oscillations are obtained at higher energies. Also the zero field conductance fits well with the experiment. In contrast, in simulations that additionally include the long range Gaussian potential (not shown), the difference in the zero field conductance for high and low energies is much too high, similar as in Fig. 7.7 a). Thus we conclude that it is not a dominating source of scattering in the experimental samples. From band structure calculations, we know that the SdH dip in Fig. 7.7 d) at $B \approx 60\,\mathrm{T}$ corresponds to the first Landau level above zero energy. In the experiment, the corresponding dip is observed at $B \approx 45\,\mathrm{T}$. This shift towards higher magnetic fields in the simulations is due to the fact that the GNR Landau levels develop from the ribbon energy bands that form

also at $B = 0$ due to size quantization. The corresponding distance between the bands scales inversely with the ribbon width [see e. g. Fig.7.2 b) and c)] and is therefore smaller in the experimental samples than in the simulated ribbons. At infinitely large magnetic fields, the position of the Landau levels is independent of the ribbon width, but for finite B the Landau level distance is smaller in wider ribbons. Concerning the strong decrease of the conductance at low energies, e. g. in Fig. 7.6 d) for $B \gtrsim 20\,\mathrm{T}$, our simulations do not reproduce the experimental findings. In the literature this 'transition to an insulating state' has been reported also in bulk graphene samples [240, 241, 242], and thus is probably not directly related to the confinement in GNR. While several possible mechanisms that could lead to this transition have been suggested, there is no consensus explanation so far [12]. Since the ribbons used for the experiment here are connected to rather large ($> 1\,\mu\mathrm{m}$) patches of graphene, as can be seen from the inset in Fig. 7.6 a), we suppose that the decrease of the conductance at high fields in Fig. 7.6 is a bulk effect, too.

7.3 Summary

We have carried out numerical tight-binding simulations of disordered GNR. In the first section we have studied the intimate relation of edges and the effective symmetry classes in these systems and showed that it has measurable consequences on their conductance. We have shown that for smooth potential disorder, metallic ac GNR feature a pseudovalley substructure ($\mathrm{K}_{\mathcal{R}}$ and $\mathrm{K}'_{\mathcal{R}}$), very similar to the case of zz GNR, where the real valleys (K and K′) are preserved. No such substructure is present in semiconducting ac GNR. Since the numbers of states with positive and negative velocity in each individual (pseudo)valley differ by one, the conductance of zz and metallic ac GNR is always greater than or equal to g_0 if scattering between the (pseudo)valleys is absent. While for the zz case the pcc has been recognized and associated with the preserved valley structure earlier [223], it was believed that for the metallic ac case it is a particular property of the lowest energy bands, and thus is present only in single-channel transport [229]. We have shown that this is in fact not the case and that the preserved pseudovalley structure is responsible for the pcc. Therefore the suppression of Anderson localization is also visible in the multichannel regime. Moreover, we have demonstrated that for low Fermi energies the zz edge states can lead to effective intervalley coupling even in the absence of short-range potentials, destroying the pcc. Since within each isolated (pseudo)valley there is no effective TRS, the correct universality class for metallic ac GNR is the unitary class, as for the zz case and in contrast to the case of semiconducting ac ribbons. Our numerical magnetoconductance simulations confirm this classification [236].

In the second section we have presented a numerical simulation of an experiment where the magnetoconductance of disordered GNR has been measured in pulsed magnetic fields up to $B \approx 60\,\mathrm{T}$. For low energies the experiment finds a rather strong increase of g at small fields followed by an even stronger conductance decrease at high fields. On the other hand for high energies, g is approximately constant at low fields and shows SdH oscillations for larger

values of B. Neither pure edge disorder nor pure potential disorder leads to satisfying results in view of the agreement of simulations and experiment. For a combination of realistic edge disorder and Gaussian bulk disorder with a correlation length of approximately two lattice constants, we could reproduce the experimental findings with our numerical calculations semi-quantitatively for high energies and up to moderate magnetic fields also in the low energy regime. This suggests that both mechanisms are relevant sources of disorder in the measured samples [237].

CHAPTER 8

Summary and outlook

In this thesis we have studied the electronic properties of graphene nanostructures, focusing on the spectral density of states and the quantum transport properties. In particular we have investigated the effects of edge scattering. The analytical results of this work, supported partly by numerical calculations, represent a comprehensive extension of semiclassical approaches for ballistic cavities to the case of graphene for the first time. They provide a theoretical basis for experimental and numerical studies of graphene structures in the ballistic regime. Moreover, with the numerical simulations presented in chapter 7, we have completed our work following a complementary approach. We summarize our main findings in the following.

After a short introduction into basic properties of graphene, the effective Dirac equation, and the corresponding boundary conditions in chapter 2, we turned to the calculation of the Green function for ballistic graphene nanostructures in chapter 3. Adapting the concept of Balian and Bloch's multiple reflection expansion, we have obtained an exact expression for the graphene Green function. Each term in the corresponding expansion is the collective contribution of all quantum paths with a given number of boundary reflections. While the scalar part of the Green function is closely related to the Green function of the 2D Schrödinger equation with Dirichlet boundary conditions, the graphene specific (in particular edge related) physics is contained in the boundary dependent pseudospin matrices. Since the involved multiple boundary integrations are extremely complicated for generic system shapes, we considered the contributions of leading order in $(k_E L)^{-1}$, i. e. the Green function in the semiclassical limit. Using the relation to the Schrödinger case, we have obtained the semiclassical graphene Green function as a sum over all classical trajectories, where the most important object in view of the graphene physics is the pseudospin propagator corresponding to each trajectory. It describes the edge dependent evolution of the graphene pseudospins along the classical orbits. However, we have found that zigzag edges give rise to a second leading order contribution to the Green function, which is not present at armchair or infinite mass type edges. Multiple short-range reflections at zigzag edges lead to a singular behavior of the Green function. By resumming these short-range processes, we have shown that the semiclassical graphene Green function is still given by a sum over all classical trajectories, but with renormalized zigzag reflections. The results of this chapter served as a starting point for the investigation into the spectral and transport properties of graphene cavities in the subsequent chapters.

In chapter 4 we have performed an extensive study of the spectral density of states (DOS) of graphene billiards. First we considered the smooth part of the DOS. We have calculated the leading two terms, namely the bulk and the surface term, of the corresponding Weyl series, considering boundaries that consist of zigzag, armchair, and infinite mass edges. For the bulk term we have found that it scales with the total billiard area, as expected. On the other hand, the surface term is zero for infinite mass and armchair type edges. Only zigzag edges give rise to such a contribution, due to the low energy zigzag edge states. The latter lead to a characteristic feature in the smooth DOS, and the size of this feature scales with the zigzag part of the boundary. We confirmed our analytical predictions using tight-binding simulations. Our results suggest that the structure of a graphene flake's boundary, i. e. the relative amount of zigzag type edges, can be estimated from the behavior of the smoothed density of states at low energies. Next we have studied the oscillating part of the DOS. For this purpose we have extended the Gutzwiller trace formula for chaotic billiards and the Berry-Tabor trace formulae for two specific regular billiards, the disk with infinite mass edges and the rectangle with zigzag and armchair edges, to the case of graphene. These trace formulae differ from those for the Schrödinger equation in one key aspect, namely the interference of pseudospins, which is incorporated via the trace of the pseudospin propagator along periodic classical orbits. In this way we could include the effects of the graphene edges in a particularly transparent manner. For the regular systems we have then studied in detail the edge effects on the pseudospin interference and found that they strongly affect the frequency content of the DOS. Further we computed semiclassical approximations to the energy levels, and showed that they are in very good agreement with the exact solutions of the Dirac equation. For the class of chaotic systems, the statistical properties of the DOS possess universal properties. Thus we have analytically calculated the spectral form factor, i. e. the Fourier transform of the spectral two-point correlator, to the first two orders within semiclassical approximation. To this end we have extended existing semiclassical methods to the case of graphene billiards, using our version of the Gutzwiller trace formula. We have found that the edge characteristics have a significant effect on the spectral correlations. Both leading order diagonal contributions and next-to-leading order loop contributions, are governed by the total length of intervalley scattering armchair edge segments. The ratio of the Heisenberg time and the typical armchair scattering time represents a tunable symmetry restoring parameter that drives the system from a state with effectively broken time reversal symmetry (decoupled valleys) into a time reversal symmetric state (mixed valleys). Our results suggest that the (partial) time reversal symmetry breaking should be reflected in the DOS statistics at scales of many mean level spacings, rather than in the distribution of nearest-neighbor level spacings, where the time reversal symmetry breaking is hardly observable. Since the crossover parameter can be tuned in a wide range by changing the Fermi energy, the predicted transition should be accessible in mesoscopic graphene billiards.

Experimentally, the conductance of a graphene structure is more directly accessible than the DOS. Therefore we have presented a semiclassical theory of quantum transport through ballistic chaotic graphene cavities in chapter 5. Starting from the Kubo formula for the Dirac

equation, and using similar techniques as for the spectral correlations, we have generalized the existing semiclassical approach to the case of graphene, where the inclusion of edge effects is essential. Our main results are analytical expressions for the leading order quantum corrections to the average magnetoconductance, i.e. the weak localization, and the universal conductance fluctuations. For both, the intervalley scattering mediated through armchair edges affects the results strongly. The relative size of the three relevant time scales, dwell time, armchair scattering time, and magnetic dephasing time, leads to crossovers between unitary and orthogonal symmetry class, similar to the transitions in the spectral form factor. We support our analytical findings by numerical tight-binding calculations. Moreover, we have studied the shot noise of ballistic graphene cavities. For the leading order contribution to the Fano factor, we find the same value as for systems described by an effective Schrödinger equation, irrespective of the edge characteristics. Our analytical results explain our earlier numerical transport simulations [43] semiclassically and can serve as a theoretical footing for further experimental and numerical studies.

In chapter 6 we have studied the effects of local magnetic moments at the edges of a graphene cavity on the quantum conductance. Using a simple model boundary condition, we could calculate the weak localization correction and the universal conductance fluctuations semiclassically, taking into account the spin rotation associated with reflections from magnetized edges. We have shown that two different mechanisms lead to a suppression of both the weak localization and the size of the conductance fluctuations. One is the mixing of the spin species, if the local edge moments are not uniaxially polarized. The second is time reversal symmetry breaking, which requires reflections from edges with magnetic polarizations in all three spatial directions. Performing numerical transport simulations with different models for the polarizations of the edge moments, we could confirm the qualitative predictions of our semiclassical theory.

Finally, we have performed numerical studies on the conductance of disordered graphene nanoribbons in chapter 7. We have shown that in disordered metallic armchair nanoribbons, Anderson localization is suppressed, also for more than one propagating lead channel. In terms of the effective Dirac equation we have explained this behavior by a special pseudovalley structure in these systems. The imbalance of channels with positive and negative velocity in each pseudovalley, and the orthogonality of states from different subsystems give rise to a conductance that is always greater than g_0. A very similar effect is known for zigzag nanoribbons. However, we have shown that in the latter case Anderson localization still occurs, if the valleys are effectively coupled via the zigzag edge states. By means of magnetoconductance simulations we could further show that, in the absence of short-range potentials, metallic armchair ribbons belong to the unitary universality class, as opposed to semiconducting armchair ribbons. In previous publications this distinction has not been made. In the second part we have presented a numerical simulation of a high magnetic field experiment on graphene nanoribbons. Our results show that a combination of edge disorder and bulk disorder with a range of few lattice constants can explain most of the experimental findings semi-quantitatively, namely the observation of Shubnikov-de-Haas oscillations at high Fermi

energies, and the strong resistance decrease for small and moderate magnetic fields at low energies.

Several further research directions originate from the work presented in this thesis. Some of them are related to the approximations we have made in our analytical formalism. For example, we have considered the magnetic field only as a scalar phase in the contributions of classical orbits to the Green function and the resulting quantities. On the one hand, it is interesting already at this level to investigate orbital magnetism of graphene billiards in terms of the magnetic susceptibility. However, in general, and particularly in view of the zigzag edge state contribution to the susceptibility, a more basic treatment of magnetic fields is desirable. Lisa Heße concerns herself with these topics within her Master's thesis.

Another possible extension of the present work is to include diffractive effects due to sharp corners. The multiple reflection expansion is in principle capable to treat such contributions, and they could also be taken into account within an extended semiclassical approach. The hope here would be that for the rectangle with infinite mass edges, the deviations of the semiclassical results from numerical quantum simulations could be cured, as noted in App. A.4.

Concerning bulk disorder, it would be interesting to calculate the conductance of graphene cavities in the presence of weak bulk disorder. To this end one has to go beyond the level of single impurity averaged Green functions (cf. App. A.6), and compute approximations to the impurity averaged product of Green functions.

In the present work, we have considered graphene billiards with regular and chaotic classical counterpart. One important future direction is the generalization to systems with mixed classical phase space. For example in view of the assumption of piecewise straight boundary pieces, this would be a relevant extension.

Considering the effects of edge magnetization and its polarization on weak localization and conductance fluctuations, it would be very interesting to study also disordered nanoribbons. On the one hand our discussion in Chap. 7 showed that the edge properties can influence the quantum conductance of disordered nanoribbons rather strongly. On the other hand recent experiments on graphene nanoribbons indicate that the polarization of edge magnetic moments may actually affect the conductance of these systems: At temperatures above 1 K the phase coherence length in the experiments is limited by the width of the ribbons, while for lower temperatures no such limitation is observed [243]. This could be explained by uniaxial polarization of the edge moments at very low temperatures and unpolarized edge moments at higher temperatures, leading to partial time reversal symmetry breaking or 'enhanced dephasing' in the latter case. However, further experiments and calculations are necessary to verify this explanation.

Finally, multiple reflection expansions for other related systems can serve as starting points for semiclassical studies. Graphene-based Andreev billiards, studied in terms of a Dirac-Bogoliubov-de-Gennes equation, as well as cavities in topological insulators like mercury telluride quantum wells, which are described by a massive Dirac-like Hamiltonian, are possible candidates for future investigations.

Appendix

A.1 Boundary discontinuity of the Green function

We derive Eq. (3.9), which shows that the full Green function has a discontinuity at the boundary, with a size of half of the Dirac charge layer μ at the corresponding boundary point. We follow the procedure, that has been discussed in Refs. [91, 94].

Using the short-distance asymptotic form of the Hankel function

$$H_0^+(\xi) \overset{\xi \ll 1}{\longrightarrow} \frac{2\mathrm{i}}{\pi} \ln(\xi/2)\,, \tag{A.1}$$

we obtain the short-range singularity of the free Green function from Eq. (3.8)

$$G_0(\boldsymbol{x}, \boldsymbol{x}') \overset{\boldsymbol{x} \to \boldsymbol{x}'}{\longrightarrow} -\frac{\mathrm{i}}{2\pi} \frac{\boldsymbol{\sigma} \cdot (\boldsymbol{x} - \boldsymbol{x}')}{|\boldsymbol{x} - \boldsymbol{x}'|^2}\,. \tag{A.2}$$

This means that G_0 has a pole of first order at $\boldsymbol{x} = \boldsymbol{x}'$. If $\boldsymbol{x}'$ lies in the interior of $\mathcal{V}$ and $\boldsymbol{\alpha}$ is a point on the boundary ∂V,

$$\lim_{\boldsymbol{x} \to \boldsymbol{\alpha}} G_0(\boldsymbol{x}, \boldsymbol{x}') = G_0(\boldsymbol{\alpha}, \boldsymbol{x}') \tag{A.3}$$

is well defined and the first term in Eq. (3.9) is trivially obtained from the first term in Eq. (3.4). However, if $\boldsymbol{x}'$ is on the boundary, the singular behavior of the free Green function becomes relevant. To see this, we perform the boundary integral in two parts, dividing ∂V into a small region $D_\delta(\boldsymbol{\alpha}) = C_\delta(\boldsymbol{\alpha}) \bigcap \partial V$, where $C_\delta(\boldsymbol{\alpha})$ is a disk with radius δ around $\boldsymbol{\alpha}$, and the remaining boundary $\bar{D}_\delta(\boldsymbol{\alpha}) = \partial V \setminus D_\delta(\boldsymbol{\alpha})$. At the end of the calculation, we will take the limit $\delta \to 0$.

We begin with the integration within $D_\delta(\boldsymbol{\alpha})$. We insert the asymptotic expression for G_0,

Eq. (A.2), into the second term in Eq. (3.4) to get

$$\begin{aligned} I_{D_\delta(\boldsymbol{\alpha})} &= \lim_{\delta\to 0}\lim_{\boldsymbol{x}\to\boldsymbol{\alpha}} \int\limits_{D_\delta(\boldsymbol{\alpha})} d\sigma_{\boldsymbol{\beta}} G_0(\boldsymbol{x},\boldsymbol{\beta}) \mathrm{i}\sigma_{\boldsymbol{n}_{\boldsymbol{\beta}}} \mu(\boldsymbol{\beta},\boldsymbol{x}') \\ &= \frac{\sigma_{\boldsymbol{n}_{\boldsymbol{\beta}}}}{2\pi}\mu(\boldsymbol{\alpha},\boldsymbol{x}')\boldsymbol{\sigma}\cdot\lim_{\delta\to 0}\lim_{\boldsymbol{x}\to\boldsymbol{\alpha}} \int\limits_{D_\delta(\boldsymbol{\alpha})} d\sigma_{\boldsymbol{\beta}} \frac{(\boldsymbol{x}-\boldsymbol{\beta})}{|\boldsymbol{x}-\boldsymbol{\beta}|^2}\,, \end{aligned} \tag{A.4}$$

where we took μ out of the integral and evaluated it at $\boldsymbol{\beta}=\boldsymbol{\alpha}$. Without loss of generality, we choose $\boldsymbol{\alpha}=\mathbf{0}$, $\boldsymbol{x}=|\boldsymbol{x}|\hat{\boldsymbol{y}}$, and approximate $D_\delta(\boldsymbol{\alpha})$ by a straight line along the x-axis, i. e. $D_\delta(\boldsymbol{\alpha}) = \{\, \xi\hat{\boldsymbol{x}} \mid \xi\in[-\delta,\delta] \,\}$. Then we get

$$\begin{aligned} I_{D_\delta(\boldsymbol{\alpha})} &= \frac{\sigma_{\boldsymbol{n}_{\boldsymbol{\beta}}}}{2\pi}\mu(\boldsymbol{\alpha},\boldsymbol{x}')\boldsymbol{\sigma}\cdot\lim_{\delta\to 0}\lim_{|\boldsymbol{x}|\to 0}\int\limits_{-\delta}^{\delta} d\xi \frac{|\boldsymbol{x}|\hat{\boldsymbol{y}}-\xi\hat{\boldsymbol{x}}}{|\boldsymbol{x}|^2+\xi^2} = \frac{\mu(\boldsymbol{\alpha},\boldsymbol{x}')}{\pi}\lim_{\delta\to 0}\lim_{|\boldsymbol{x}|\to 0}\arctan(\delta/|\boldsymbol{x}|) \\ &= \frac{1}{2}\mu(\boldsymbol{\alpha},\boldsymbol{x}')\,. \end{aligned} \tag{A.5}$$

Since the kernel of the integral on $\bar{D}_\delta(\boldsymbol{\alpha})$ has no singularity, it follows

$$\lim_{\delta\to 0}\lim_{\boldsymbol{x}\to\boldsymbol{\alpha}} \int\limits_{\bar{D}_\delta(\boldsymbol{\alpha})} d\sigma_{\boldsymbol{\beta}} G_0(\boldsymbol{x},\boldsymbol{\beta}) \mathrm{i}\sigma_{\boldsymbol{n}_{\boldsymbol{\beta}}} \mu(\boldsymbol{\beta},\boldsymbol{x}') = \int\limits_{\partial V} d\sigma_{\boldsymbol{\beta}} G_0(\boldsymbol{\alpha},\boldsymbol{\beta}) \mathrm{i}\sigma_{\boldsymbol{n}_{\boldsymbol{\beta}}} \mu(\boldsymbol{\beta},\boldsymbol{x}')\,. \tag{A.6}$$

It is known from potential theory that the integral on the right-hand side exists [91, 94], and thus Eq. (3.9) follows.

A.2 Zigzag edges in the presence of edge potentials

In Subsec. 2.2.2 we have derived an effective boundary condition for a zigzag graphene edge in presence of an edge potential of the form

$$\mathcal{H}_{\mathrm{nnn}} = -t' \frac{\hbar v_F}{2} \delta(y - y_1)(1 - \tau_z \otimes \sigma_z)\,. \tag{A.7}$$

Although our motivation was the approximate inclusion of nnn hopping for the zigzag edge state, the origin of a potential that is located at the edges of a graphene nanostructure can also be of different origin, e. g. impurities or dangling bonds at the edges due to the fabrication process [81].
After we derive the wavefunction of a semi-infinite piece of graphene with a zigzag edge and edge potential Eq. (A.7), we perform the resummation of short-range processes as in Subsec. 3.2.1 for the case of finite t'.

A.2.1 Solution of the Dirac equation for a single edge

We consider a zigzag edge with B-termination, so that we have to solve the Dirac equation together with the effective boundary condition (2.54)

$$\psi_{A\tau}(x, 0) = t' \psi_{B\tau}(x, 0)\,. \tag{A.8}$$

Due to the Bloch theorem we can write

$$\psi_{A\tau}(x, y) = \mathrm{e}^{\mathrm{i}kx} \phi_{A\tau}(y) = \mathrm{e}^{\mathrm{i}kx}(a\,\mathrm{e}^{\mathrm{i}qy} + b\,\mathrm{e}^{-\mathrm{i}qy})\,, \quad \text{with } k_E^2 = k^2 + q^2\,, \tag{A.9}$$

and the Dirac equation gives

$$k_E \phi_{B\tau}(y) = (\tau k + \partial_y)\phi_{A\tau}(y)\,. \tag{A.10}$$

Then Eq. (A.8) leads to the condition

$$a(k_E - t'\tau k - \mathrm{i}t'q) = -b(k_E - t'\tau k + \mathrm{i}t'q)\,. \tag{A.11}$$

For $(k_E - t'\tau k - \mathrm{i}t'q) \neq 0$ and $(k_E - t'\tau k + \mathrm{i}t'q) \neq 0$, this determines the spinors of the usual 'bulk' states. In fact in this case, Eqs. (A.10) and (A.11) lead to

$$\phi_{A\tau}(y) = \alpha(k_E - \tau t' k)\sin(qy) + \alpha\, t' q \cos(qy)\,, \tag{A.12}$$

$$\phi_{B\tau}(y) = \alpha(\tau k - t' k_E)\sin(qy) + \alpha\, q \cos(qy)\,, \tag{A.13}$$

with a normalization constant α. Since the wavefunctions $\psi_{A/B}$ have to be normalizable, both momenta q and k have to be real numbers here.

There is, however, another normalizable state that corresponds to $k_E - t'\tau k + \mathrm{i}t'q = 0$.[1] In this case a has to be zero according to Eq. (A.11) and we find a normalizable edge state for

[1] $k_E - t'\tau k - \mathrm{i}t'q = 0$ together with $b = 0$ leads to the same result.

negative τk and $q = -\sqrt{k_E^2 - k^2}$. For the energy of the edge state we get in this case

$$k_E^{\text{edge}} - t'\tau k + \mathrm{i}t'q = 0 \tag{A.14}$$

$$\Rightarrow \quad k_E^{\text{edge}} = \frac{2t'\tau k}{1+t'^2} = 2t'\tau k + \mathcal{O}(t'^2) < 0\,. \tag{A.15}$$

The transverse momentum is given by

$$q = \mathrm{i}\frac{1-t'^2}{1+t'^2}\tau k = \mathrm{i}\tau k + \mathcal{O}(t'^2)\,. \tag{A.16}$$

With a normalization constant β, the corresponding spinor entries become then

$$\psi_{A\tau}(x,y) \approx \beta\, t' \mathrm{e}^{\mathrm{i}kx} e^{\tau k y}\,, \tag{A.17}$$

$$\psi_{B\tau}(x,y) \approx \beta\, \tau \mathrm{e}^{\mathrm{i}kx} e^{\tau k y}\,. \tag{A.18}$$

This means we have obtained an edge state for negative momenta in the valley $\tau = +1$ and for positive momenta in the valley $\tau = -1$. Additionally, Eq. (A.15) shows that the edge state energy is alway negative. Note that all result we have obtained here turn into the well-known corresponding expressions without edge potential for $t' = 0$ [61, 80, 85], in particular the energy of the edge state becomes constantly zero in this case.

In Fig. A.1 we plot the spinor entries $\phi_{A/B}$ and their product for a bulk state and an edge state, with finite and zero t' respectively. The product $\phi_A \cdot \phi_B$ is directly proportional to the current density in x-direction, since the current density operator for the Dirac Hamiltonian is $\boldsymbol{j}(\boldsymbol{x}) = ev_F\boldsymbol{\sigma}\delta(\hat{\boldsymbol{x}} - \boldsymbol{x})$. For the bulk state both wavefunctions and current profile are only slightly changed for finite t'. The effect of finite t' on the edge state is more significant. Since for $t' = 0$, the A-part of the edge state spinor vanishes identically, the resulting current density is zero. A finite value of t' leads to a finite A-part and thus to a current density located at the edge. This qualitative difference has been pointed out in Ref. [61].

A.2.2 Resummation of short-range processes

We now derive the renormalization matrix (4.22), which arises due to short-range singularities at zigzag edges with an edge potential, i. e. the generalization of Eq. (3.59) to the case of finite t'. We start from the boundary matrix that we have obtained in Subsec. 2.2.2, namely Eq. (2.55)

$$\mathcal{P}_{\boldsymbol{\alpha}} = \frac{1}{2}\left(1 \pm \tau_z \otimes \sigma_z - \mathrm{i}t'\sigma_y \mp t'\tau_z \otimes \sigma_x\right)\,, \tag{A.19}$$

and insert it into Eq. (3.41) to get

$$\Gamma_\tau^{-1}(k) = 1 + \frac{\pm\tau k - t'k_E}{2a(k)} - \frac{1}{2a(k)}[(\pm\tau k_E - t'k)\sigma_x + \mathrm{i}(k_E \mp \tau t'k)\sigma_y + (\pm\tau t'k_E - k)\sigma_z]\,. \tag{A.20}$$

Then we use the formula Eq. (3.54) to perform the inversion, yielding

$$\Gamma_\tau(k) = a(k)\frac{a(k) - t'k_E \mp \tau_z k}{[a(k) - t'k_E]^2 - k^2}\left[1 - \frac{1}{a(k)}(k\sigma_z - \mathrm{i}k_E\sigma_y)(1 - \mathcal{P}_{\boldsymbol{\alpha}})\right]\,. \tag{A.21}$$

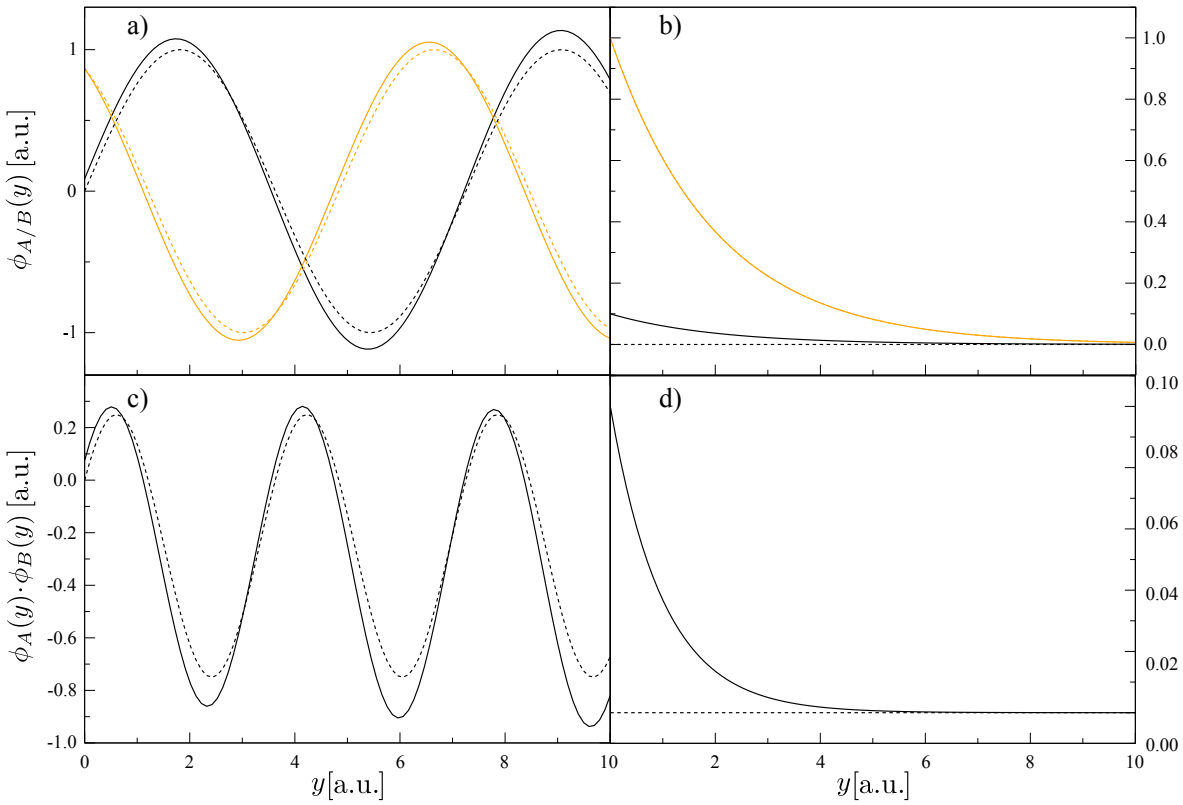

Figure A.1: Spinor entries $\phi_{A/B}$, panels a) and b), and their product $\phi_A \cdot \phi_B$, panels c) and d), for a bulk state with $k/k_E = -1/2$ and $q/k_E = -\sqrt{3}/2$ [panels a) and c), cf. Eqs. (A.12) and (A.13)] and for an edge state with $k/k_E = -1/2$ [panels b) and d), cf. Eqs. (A.17) and (A.18)]. In panels a) and b), orange lines correspond to ϕ_B and black lines to ϕ_A. Dashed lines stand for vanishing edge potential, $t' = 0$, solid lines for a finite value, namely $t' = 0.1$. Further we consider the valley $\tau = +1$ for this figure.

With that we get

$$\mathcal{Z}_{\boldsymbol{\alpha}}(k, -y') = 2\Gamma(k)\mathcal{P}_{\boldsymbol{\alpha}} G_0(k, -y') = 2\mathcal{R}(k)\mathcal{P}_{\boldsymbol{\alpha}} G_0(k, -y')\,, \tag{A.22}$$

where we have defined the momentum-dependent renormalization matrix

$$\mathcal{R}(k) = a(k)\frac{a(k) - t'k_E \mp \tau_z k}{[a(k) - t'k_E]^2 - k^2}\,. \tag{A.23}$$

First we note that in the limit of $t' = 0$, the expression for bare zigzag edges, Eq. (3.59), is recovered. Furthermore we can read off from Eq. (A.23) the dispersion of the zigzag edge state in presence of an edge potential. For this purpose we consider the values of k_E for which $\mathcal{R}^{-1}$ vanishes. We find that

$$\lim_{k_E \to k_0} \mathcal{R}_\tau^{-1} \sim \frac{\text{`} \quad 0 \quad \text{'}}{\pm\text{sign}(\tau k) - 1} \quad \text{with} \quad k_0 = -\frac{2|k|t'}{1 + t'^2}\,. \tag{A.24}$$

This means for $\pm\tau k < 0$, the inverse renormalization matrix vanishes and thus $\mathcal{R}_\tau$ diverges, indicating an edge state in this case, in agreement with our results for the edge state in the previous section, see Eq. (A.15). On the other hand, using L'Hospital's rule we get

$$\lim_{k_E \to k_0} \mathcal{R}_\tau^{-1} \neq 0 \quad \text{for} \quad \pm\tau k > 0\,, \tag{A.25}$$

so that there is no divergence, as expected, since no edge states exist in this case.

A.3 Quantization of rectangular graphene billiards

Here we present an implicit expression for the energy eigenvalues of a graphene rectangle with zigzag edges at $y = 0$ and $y = L_{\mathrm{ac}}$ and armchair edges at $x = 0$ and $x = L_{\mathrm{zz}}$, respectively. We start from a linear superposition of a forward and a backward propagating eigenmode of an armchair nanoribbon with edges at $x = 0$ and $x = L_{\mathrm{zz}}$ [80, 85]

$$\Psi(x,y) = \alpha \begin{pmatrix} (q_m - \mathrm{i}k)\mathrm{e}^{\mathrm{i}q_m x} \\ k_E \mathrm{e}^{\mathrm{i}q_m x} \\ k_E \mathrm{e}^{-\mathrm{i}q_m x} \\ (-q_m + \mathrm{i}k)\mathrm{e}^{-\mathrm{i}q_m x} \end{pmatrix} \mathrm{e}^{\mathrm{i}ky} + \beta \begin{pmatrix} (q_m + \mathrm{i}k)\mathrm{e}^{\mathrm{i}q_m x} \\ k_E \mathrm{e}^{\mathrm{i}q_m x} \\ k_E \mathrm{e}^{-\mathrm{i}q_m x} \\ (-q_m - \mathrm{i}k)\mathrm{e}^{-\mathrm{i}q_m x} \end{pmatrix} \mathrm{e}^{-\mathrm{i}ky}\,, \tag{A.26}$$

where the q_m are quantized according to

$$q_m = \frac{m\pi}{L_{\mathrm{zz}}} - K, \quad m \in \mathbb{Z}\,. \tag{A.27}$$

The spinors in Eq. (A.26) are solutions of the Dirac equation if

$$k^2 + q_m^2 = k_E^2\,. \tag{A.28}$$

Now we impose the zigzag boundary conditions $\psi_{A\tau}(x,0) = \psi_{B\tau}(x, L_{\mathrm{zz}}) = 0$, which give the two independent equations

$$(q_m - \mathrm{i}k)\alpha + (q_m + \mathrm{i}k)\beta = 0\,, \tag{A.29}$$

$$\mathrm{e}^{\mathrm{i}kL_{\mathrm{zz}}}\alpha + \mathrm{e}^{-\mathrm{i}kL_{\mathrm{zz}}}\beta = 0\,. \tag{A.30}$$

These are solved for quantized k_{nm} that fulfill the transcendental equation

$$k_{nm} = -q_m \tan(k_{nm} L_{\mathrm{zz}})\,, \tag{A.31}$$

or with n occurring explicitly

$$k_{nm} = \frac{1}{L_{\mathrm{zz}}} \arctan(q_m/k_{nm}) - \frac{\pi}{L_y}\left(n + \frac{1}{2}\right)\,. \tag{A.32}$$

With that we have formally solved the problem, and the eigenenergies can be found e. g. by solving Eq. (A.32) numerically.

A.4 Trace formula for the rectangular infinite mass billiard

In Subsec. 4.2.2 we have derived the trace formulae for the graphene disk billiard with infinite mass type edges and the rectangular graphene billiard with armchair and zigzag edges. Here we study in a sense the combination of both, namely the rectangular graphene billiard with infinite mass type edges. For the two former cases, we have found excellent agreement of the semiclassical DOS oscillations with the quantum results for both the shell effects due to the shortest orbit contributions and the actual energy levels, see Figs. 4.4, 4.8 and Table 4.1. For the infinite mass rectangle, no analytical solution of the Dirac equation with the corresponding boundary condition exists, to the best of our knowledge. When the infinite mass boundary condition was derived by Berry and Mondragon, they already noted that, while the one-dimensional infinite mass box is easily solved by a superposition of two plane waves, "It is a curious fact, that the rectangular neutrino billiard cannot be quantized in this way" [90]. In principle, our semiclassical theory can be used the obtain the DOS of this system. However, as we illustrate below, the semiclassical DOS shows substantial deviations from the results of numerical quantum simulations, when a large number of classical orbits contribute. For the short orbit contributions we still find reasonable agreement.

As for the rectangle with ac and zz edges, we identify each classical periodic orbit with N and M, the numbers of reflections from the bottom and the left edge of the billiard, respectively. For the semiclassical trace formula we need then the trace of the pseudospin propagator for an orbit (N, M) and the corresponding trace formula for rectangular Schrödinger billiard, Eq. (4.77). From Eq. (3.94) we know that we get for each reflection effectively a factor $\mathrm{i}\exp(\mathrm{i}\theta_i\sigma_z)$. Since the total number of reflections is always even for the classical periodic orbits in the rectangle (cf. Fig. 4.6), no additional σ_z or τ_z occur. Therefore we get for the trace [cf. also Eq. (4.99)]

$$\mathrm{Tr}K_{NM} = 4(-1)^{N+M}\cos(\theta_{NM})\,. \tag{A.33}$$

Defining the repetition number $r \in \mathbb{N}$, where $r = 1$ for primitive orbits and $r \geq 2$ for repeated primitive orbits, we have

$$(N, M) = (n\,r, m\,r)\,, \tag{A.34}$$

with coprime integers n and m. The classical periodic orbits of the rectangular billiard can be divided into two classes (cf. Fig. 4.6), namely such that enclose a finite directed area, e. g. the orbits (r, r) or $(3\,r, r)$, and such that do not enclose a directed area, e. g. the orbits $(2\,r, r)$ or $(3\,r, 2\,r)$. One can show in general that if and only if n and m are both odd, the corresponding orbit encloses a non-zero directed area [123]. Except for the bouncing ball orbits, each classical periodic orbit can be divided into quadrilaterals with total interior angles of 2π each. Thus we get $\theta_{NM} = r\pi$ if n and m are both odd, while $\theta_{NM} = 0$ otherwise. Therefore it follows that

$$\mathrm{Tr}K_{NM} = 4(-1)^r\,, \tag{A.35}$$

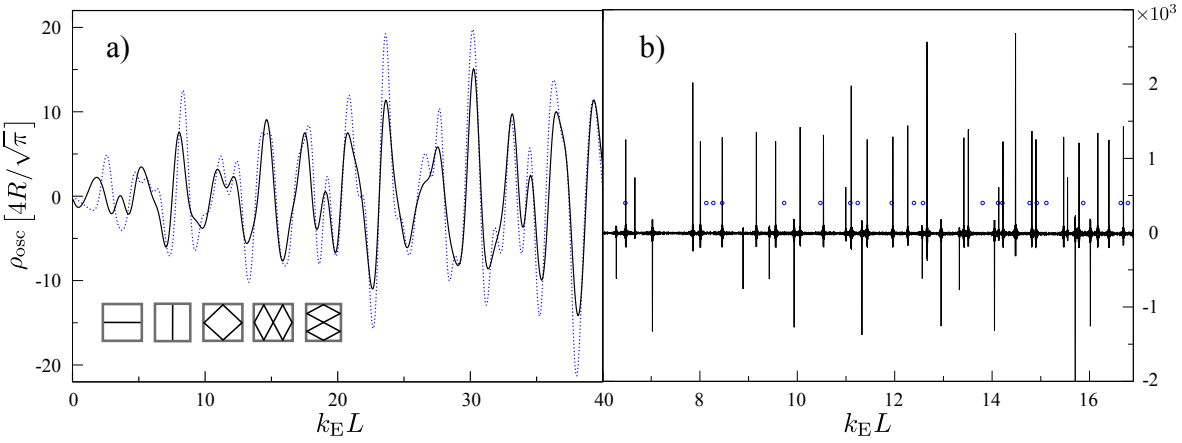

Figure A.2: Oscillating part of the density of states of a square graphene billiard with infinite mass edges ($L_x = L_y = L$). a) Gaussian convoluted $\rho_{\rm osc}(k_{\scriptscriptstyle E})$ for $\xi = 0.62/L$ (black solid line). The blue dotted curves represent the result from the numerical solution of the Dirac equation by Viktor Krückl, broadened correspondingly. b) $\rho_{\rm osc}(k_{\scriptscriptstyle E})$ without broadening ($\xi = 0$). We take all orbit families with $M, N \leq 400$ in the sum (A.36). Blue circles mark the positions of the numerically obtained quantum energy levels.

and for the semiclassical trace formula we get

$$\rho_{\rm osc}(k_{\scriptscriptstyle E}) = L_{\rm zz}L_{\rm ac}\sqrt{\frac{8k_{\scriptscriptstyle E}}{\pi^3}}\sum_{N=1}^{\infty}\sum_{M=1}^{\infty}\frac{(-1)^r f_{NM}}{\sqrt{L_{NM}}}\cos\left(k_{\scriptscriptstyle E}L_{NM} - \frac{\pi}{4}\right)\mathrm{e}^{-(\xi L_{NM}/2)^2}\,, \qquad \text{(A.36)}$$

with f_{NM} as defined below Eq. (4.76) and

$$L_{NM} = 2\sqrt{N^2L_x^2 + M^2L_y^2}\,. \qquad \text{(A.37)}$$

In Fig. A.2 we compare the oscillating part of the DOS obtained from the trace formula (A.36) with quantum mechanical calculations. Since it exists no analytical solution for the energy levels of the rectangle with infinite mass type edges, we compare our semiclassical result with numerically obtained energy levels. The numerical calculations for Fig. (A.2) have been performed by Viktor Krückl, using a wave packet propagation method [244] to compute the bound state eigenenergies of the Dirac equation with a two-dimensional step mass-potential. In panel a) we show the short orbit contributions to $\rho_{\rm osc}$ of a square $L = L_x = L_y$ with im edges, calculated with a damping of $\xi = 0.62/L$. In this case the semiclassical result (solid black line) agrees reasonably with the numerical calculation (dotted blue curve). The deviations are stronger than for the rectangle with ac and zz edges, see e. g. Fig. 4.8, which can be partially explained by the fact that the system used for the numerical simulations is not exactly identical to the rectangle with infinite mass edges. This is because the used step potential is not infinitely high and also not infinitely steep, due to the discretization of the two-dimensional space. In panel b) we show the results without level broadening, $\xi = 0$,

summing over several thousands of classical orbits. Here the numerics (blue circles) does not agree with the semiclassical result. In fact the semiclassical trace formula (solid line) produces even peaks with negative sign, which is clearly an unphysical result.

Presently we are not aware of the reason why the semiclassical trace formula (A.36) fails to approximate the quantum energy levels, while it describes the gross shell structure approximately. We believe that diffractive orbits that are not part of the standard semiclassical description [51] might be important in the im rectangle. One hint in this direction is that at the corners, which usually give rise to diffractive contributions, the boundary condition is not well defined: The im boundary condition corresponds to the sublattice pseudospin pointing in tangential direction at each boundary point, cf. Eq. (2.74), which is not defined at the corners. Clearly more research is necessary to understand the seemingly simple problem of the rectangular graphene billiard with im type boundaries.

A.5 Kubo conductivity for graphene

A.5.1 Derivation of the Kubo conductivity

Here we derive the expression (5.5) for the non-local conductivity of a graphene flake. Several calculational steps are adapted from similar calculations in Ref. [245]. We start from the effective Hamiltonian

$$\mathcal{H} + \mathcal{H}_{\boldsymbol{A}} = v_{\scriptscriptstyle F} \boldsymbol{\sigma} \cdot \boldsymbol{p} - e v_{\scriptscriptstyle F} \, \boldsymbol{\sigma} \cdot \boldsymbol{A}(\hat{\boldsymbol{x}}, t) \tag{A.38}$$

in presence of a time-dependent vector potential

$$\boldsymbol{A}(\boldsymbol{x}, t) = \boldsymbol{A}(\boldsymbol{x}, t) \, \Theta(t - t_0) \, . \tag{A.39}$$

In order to avoid confusion, we denote the position operator by $\hat{\boldsymbol{x}}$. The operator of the current density at $\boldsymbol{x}$ is for the Dirac Hamiltonian formally given by

$$\boldsymbol{j}(\boldsymbol{x}) = e v_{\scriptscriptstyle F} \boldsymbol{\sigma} \, \delta(\hat{\boldsymbol{x}} - \boldsymbol{x}) \, , \tag{A.40}$$

such that its expectation value for a state $|\Psi\rangle$ is

$$\langle \Psi | \boldsymbol{j}(\boldsymbol{x}) | \Psi \rangle = e v_{\scriptscriptstyle F} \, \Psi^\dagger(\boldsymbol{x}) \, \boldsymbol{\sigma} \, \Psi(\boldsymbol{x}) \, . \tag{A.41}$$

In terms of $\boldsymbol{j}$, the potential term in the Hamiltonian (A.38) reads

$$\mathcal{H}_{\boldsymbol{A}} = -e v_{\scriptscriptstyle F} \, \boldsymbol{\sigma} \cdot \boldsymbol{A}(\hat{\boldsymbol{x}}, t) = - \int d\boldsymbol{x} \, \boldsymbol{j}(\boldsymbol{x}) \cdot \boldsymbol{A}(\boldsymbol{x}, t) \, . \tag{A.42}$$

Within linear response theory, the a-component of the local current response to the vector potential is given by

$$\delta \langle j_a(\boldsymbol{x}, t) \rangle = - \frac{1}{\hbar} \sum_b \int d^2 \boldsymbol{x}' \int_{\infty}^{\infty} dt' \, P^R_{ab}(\boldsymbol{x}, \boldsymbol{x}', t - t') A_b(\boldsymbol{x}', t') \, , \tag{A.43}$$

with the retarded current-current correlation function

$$P^R_{ab}(\boldsymbol{x}, \boldsymbol{x}', t - t') = -\mathrm{i} \langle [j^I_a(\boldsymbol{x}, t), j^I_b(\boldsymbol{x}', t')] \rangle_0 \, \Theta(t - t') \, . \tag{A.44}$$

Here

$$\boldsymbol{j}^I(\boldsymbol{x}, t) = \mathrm{e}^{\mathrm{i}\mathcal{H}t/\hbar} \boldsymbol{j}(\boldsymbol{x}) \, \mathrm{e}^{-\mathrm{i}\mathcal{H}t/\hbar} \tag{A.45}$$

is the current operator in the interaction picture. The brackets $\langle \ldots \rangle_0$ denote averaging with respect to the thermodynamic ground state.

We now take the Fourier transform

$$P^R_{ab}(\boldsymbol{x}, \boldsymbol{x}', \omega) = \int d\tau \mathrm{e}^{\mathrm{i}\omega\tau} P^R_{ab}(\boldsymbol{x}, \boldsymbol{x}', \tau) \, , \tag{A.46}$$

so that Eq. (A.43) reads

$$\delta\langle j_a(\boldsymbol{x},t)\rangle = \int \frac{d\omega}{2\pi}\,\mathrm{e}^{-\mathrm{i}\omega t}\delta\langle \boldsymbol{j}_a(\boldsymbol{x},\omega)\rangle\,, \tag{A.47}$$

where

$$\delta\langle j_a(\boldsymbol{x},\omega)\rangle = -\frac{1}{\hbar}\sum_b \int d^2\boldsymbol{x}'\, P^R_{ab}(\boldsymbol{x},\boldsymbol{x}',\omega)A_b(\boldsymbol{x}',\omega) \tag{A.48}$$

is the current response in the frequency domain. For the Fourier transform of the electric field

$$\boldsymbol{E}(\boldsymbol{x},t) = -\frac{\partial \boldsymbol{A}(\boldsymbol{x},t)}{\partial t} \tag{A.49}$$

we have $\boldsymbol{E}(\boldsymbol{x},\omega) = \mathrm{i}\omega\boldsymbol{A}(\boldsymbol{x},\omega)$ and thus

$$\delta\langle j_a(\boldsymbol{x},\omega)\rangle = \sum_b \int d^2\boldsymbol{x}'\,\tilde{\sigma}_{ab}(\boldsymbol{x},\boldsymbol{x}',\omega)E_b(\boldsymbol{x}',\omega)\,, \tag{A.50}$$

where we have defined the generalized conductivity

$$\tilde{\sigma}_{ab}(\boldsymbol{x},\boldsymbol{x}',\omega) = \frac{\mathrm{i}}{\hbar\omega}P^R_{ab}(\boldsymbol{x},\boldsymbol{x}',\omega). \tag{A.51}$$

For a dc measurement we need its real part for vanishing frequencies, i. e. the conductivity is defined as

$$\sigma_{ab}(\boldsymbol{x},\boldsymbol{x}') = \lim_{\omega\to 0}\mathfrak{Re}\,\tilde{\sigma}_{ab}(\boldsymbol{x},\boldsymbol{x}',\omega)\,. \tag{A.52}$$

In order to obtain the conductivity, we have to calculate the retarded current-current correlation function. We start in the time domain, where with Eq. (A.45) we get

$$P^R_{ab}(\boldsymbol{x},\boldsymbol{x}',t-t') = -\mathrm{i}\,\Theta(t-t')\sum_{\lambda\lambda'}(\rho_\lambda-\rho_{\lambda'})\langle\lambda|j_a(\boldsymbol{x})|\lambda'\rangle\langle\lambda'|j_b(\boldsymbol{x}')|\lambda\rangle\,\mathrm{e}^{\mathrm{i}(E_\lambda-E_{\lambda'})(t-t')/\hbar}\,. \tag{A.53}$$

Here, $|\lambda\rangle$ are the eigenstates of $\mathcal{H}$ with eigenenergies E_λ and thermal occupation probability ρ_λ. We transform P^R_{ab} to the frequency domain

$$\begin{aligned}
P^R_{ab}(\boldsymbol{x},\boldsymbol{x}',\omega) &= -\mathrm{i}\int_0^\infty dt\,\sum_{\lambda\lambda'}(\rho_\lambda-\rho_{\lambda'})\langle\lambda|j_a(\boldsymbol{x})|\lambda'\rangle\langle\lambda'|j_b(\boldsymbol{x}')|\lambda\rangle\,\mathrm{e}^{\mathrm{i}(E_\lambda-E_{\lambda'}+\hbar\omega+\mathrm{i}\eta)t/\hbar}\\
&= \hbar\,\mathrm{e}^2v_F^2\sum_{\lambda\lambda'}\frac{\rho_\lambda-\rho_{\lambda'}}{E_\lambda-E_{\lambda'}+\hbar\omega+\mathrm{i}\eta}\,\Psi^\dagger_\lambda(\boldsymbol{x})\sigma_a\Psi_{\lambda'}(\boldsymbol{x})\,\Psi^\dagger_{\lambda'}(\boldsymbol{x}')\sigma_b\Psi_\lambda(\boldsymbol{x}')\\
&= \frac{e^2}{\hbar}\int\frac{dE'}{2\pi}\int\frac{dE}{2\pi}\frac{\rho(E)-\rho(E')}{E-E'+\hbar\omega+\mathrm{i}\eta}\mathrm{Tr}\left[\sigma_a\mathcal{A}(\boldsymbol{x},\boldsymbol{x}';E')\sigma_b\mathcal{A}(\boldsymbol{x}',\boldsymbol{x};E)\right].
\end{aligned} \tag{A.54}$$

Here we have identified $\rho(E) = \rho(E_\lambda) = \rho_\lambda$. Further we denote by η the positive imaginary part of the frequency variable. Finally, we introduced the spectral function

$$\mathcal{A}(\boldsymbol{x},\boldsymbol{x}';E) = 2\pi\hbar v_F\sum_\lambda \Psi_\lambda(\boldsymbol{x})\Psi^\dagger_\lambda(\boldsymbol{x}')\,\delta(E-E_\lambda) = G(\boldsymbol{x},\boldsymbol{x}') - G^\dagger(\boldsymbol{x},\boldsymbol{x}')\,, \tag{A.55}$$

with the retarded Green function G, as defined in Eq. (3.1). Next we use the relation

$$\lim_{\eta\to 0}\int_{-\infty}^{\infty} d\xi\,\frac{f(\xi)}{\xi-\xi_0+\mathrm{i}\eta} = \mathcal{P}\int_{-\infty}^{\infty} d\xi\,\frac{f(\xi)}{\xi-\xi_0} - \mathrm{i}\pi\, f(\xi_0)\,, \tag{A.56}$$

with the Cauchy principal value $\mathcal{P}$, to obtain

$$\begin{aligned} P^R_{ab}(\boldsymbol{x},\boldsymbol{x}',\omega) &= \frac{e^2}{\hbar}\int\frac{dE'}{2\pi}\mathcal{P}\int\frac{dE}{2\pi}\frac{\rho(E)-\rho(E')}{E-E'+\hbar\omega}\,\mathrm{Tr}\left[\sigma_a\mathcal{A}(\boldsymbol{x},\boldsymbol{x}',E')\sigma_b\mathcal{A}(\boldsymbol{x}',\boldsymbol{x},E)\right] \\ &\quad -\frac{\mathrm{i}\,e^2}{2\hbar}\int\frac{dE'}{2\pi}\left[\rho(E'-\hbar\omega)-\rho(E')\right]\,\mathrm{Tr}\left[\sigma_a\mathcal{A}(\boldsymbol{x},\boldsymbol{x}',E')\sigma_b\mathcal{A}(\boldsymbol{x}',\boldsymbol{x},E'-\hbar\omega)\right]\,. \end{aligned} \tag{A.57}$$

From Eqs. (A.51) and (A.52) we see that only the imaginary part of P^R_{ab} is of interest for us. Furthermore, we consider the dc limit $\omega\to 0$ from know on. One can show that in this limit the term containing the principal value is real and therefore does not contribute to the dc conductivity [245]. In thermodynamic equilibrium, the occupation probabilities are given by the Fermi-Dirac distribution, and for low frequencies ω and temperatures T we have

$$\rho(E'-\hbar\omega)-\rho(E') \overset{\omega\to 0}{\approx} -\hbar\omega\frac{\partial\rho(E')}{\partial E'} \overset{T\to 0}{\approx} \hbar\omega\,\delta(E'-E_F)\,, \tag{A.58}$$

and therefore

$$\mathfrak{Im}\,P^R_{ab}(\boldsymbol{x},\boldsymbol{x}',\omega) \approx -\frac{\omega\,e^2}{4\pi}\mathrm{Tr}\left[\sigma_a\mathcal{A}(\boldsymbol{x},\boldsymbol{x}',E_F)\sigma_b\mathcal{A}(\boldsymbol{x}',\boldsymbol{x},E_F)\right]\,. \tag{A.59}$$

Finally we get

$$\sigma_{ab} = \frac{1}{\hbar\omega}\mathfrak{Im}P^R_{ab}(\boldsymbol{x},\boldsymbol{x}',\omega\to 0) = -\frac{e^2}{4\pi\hbar}\mathrm{Tr}\left[\sigma_a\mathcal{A}(\boldsymbol{x},\boldsymbol{x}',E_F)\sigma_b\mathcal{A}(\boldsymbol{x}',\boldsymbol{x},E_F)\right]\,. \tag{A.60}$$

Since we want to use σ_{ab} to calculate the conductance of graphene cavities, Eq. (5.4), we are interested in the case of $\boldsymbol{x}$ and $\boldsymbol{x}'$ lying in the leads. The product of spectral functions in Eq. (A.60) leads to four terms of the form GG, $G^\dagger G^\dagger$, $G^\dagger G$ and $GG^\dagger$. While the two latter terms lead to the same result for the conductivity, in Ref. [134] the authors show that the two former terms indeed vanish, if $\boldsymbol{x}$ and $\boldsymbol{x}'$ lie in the leads.[2] For the non-local conductivity in Eq. (5.4), we thus have

$$\sigma_{ab} = \frac{e^2}{2\pi\hbar}\mathrm{Tr}\left[\sigma_a G(\boldsymbol{x},\boldsymbol{x}')\sigma_b G^\dagger(\boldsymbol{x},\boldsymbol{x}')\right]\,, \tag{A.61}$$

where the Green functions have to be evaluated at the Fermi energy. A similar formula has been presented in Ref. [246].

[2] Note that such terms would anyway not contribute to averaged quantities in the semiclassical limit we are working in throughout Chaps. 5 and 6. This is because instead of length differences as in Eq. (5.6), terms that origin from GG or $G^\dagger G^\dagger$ lead to the sum of lengths, and thus always to rapidly oscillating exponentials that vanish on average.

A.5.2 Fisher-Lee relation and Landauer formula

First we derive an equation that connects the Green function of a scattering system to the elements of its scattering matrix via projection on the lead channels, i. e. a graphene version of the Fisher-Lee relations [175]. To this end we define the wavefunction of a graphene lead in channel m as

$$\Psi_m^{\pm}(\boldsymbol{x}) = \mathrm{e}^{\pm \mathrm{i}|k_m|x}\, \psi_m^{\pm}(y)\,, \tag{A.62}$$

where x and y are the *local* coordinates of the lead, such that the positive x-axis points away from the scattering system. The signs $\pm$ denote propagation in positive (i. e. outgoing modes) and negative (i. e. incoming modes) x-direction. While the transverse wavefunctions $\psi(y)$ of states with different m are orthogonal in the case of the Schrödinger equation without magnetic field, this is in general *not the case* for graphene. However, the current operator is still diagonal in this subspace (as for the Schrödinger equation with a magnetic field [176]), namely for wavefunctions normalized to unit flux we have

$$\int_C dy\, \psi_{m'}^{\pm\dagger}(y)\, \sigma_x\, \psi_m^{\pm}(y) \;=\; \pm\frac{\delta_{mn}}{v_F}\,, \tag{A.63}$$

$$\int_C dy\, \psi_{m'}^{\mp\dagger}(y)\, \sigma_x\, \psi_m^{\pm}(y) \;=\; 0\,, \tag{A.64}$$

where C is the corresponding lead cross-section. To see this we consider two eigenmodes m and m' that fulfill the Dirac equation

$$(\sigma_x\, k_m + \sigma_y\, p_y/\hbar)|\psi_m\rangle \;=\; k_E|\psi_m\rangle\,, \tag{A.65}$$

$$\langle\psi_{m'}|(\sigma_x\, k_{m'} + \sigma_y\, p_y/\hbar) \;=\; k_E\langle\psi_{m'}|\,. \tag{A.66}$$

We multiply the first equation with $\langle\psi'_m|$ from the left and the second with $|\psi_m\rangle$ from the right and subtract the resulting equations to get

$$(k_{m'} - k_m)\langle\psi_{m'}|\sigma_x|\psi_m\rangle = 0\,. \tag{A.67}$$

Then Eqs. (A.63) and (A.64) follow directly: If $k_{m'} - k_m \neq 0$, the matrix element has to vanish. Note that $m \neq m'$ does not necessarily imply $k_{m'} - k_m \neq 0$, e. g. for metallic armchair leads or if one considers spin degenerate modes. However, in this case one can construct an orthogonal basis in the degenerate subspace so that the above still holds.

Now we consider a scattering system that is connected to an arbitrary number of leads. If an electron enters from lead b in the mode m', the wavefunction in the *asymptotic region*, i. e. far away from the scatterer, reads

$$\Phi(\boldsymbol{x}) = \begin{cases} \Psi_{m'}^{-}(\boldsymbol{x}_b) + \sum\limits_m r_{mm'}^{(b)}\, \Psi_m^{+}(\boldsymbol{x}_b) & \boldsymbol{x} \in \text{lead } b \\ \sum\limits_m t_{mm'}^{(ab)}\, \Psi_m^{+}(\boldsymbol{x}_a) & \boldsymbol{x} \in \text{lead } a \neq b\,, \end{cases} \tag{A.68}$$

where the sums run over all propagating modes m in the corresponding lead. On the other hand the equation of motion for the retarded Green function, Eq. (3.1), gives

$$\Phi(\boldsymbol{x}) = \int\limits_{\tilde{\mathcal{V}}} d^2x' \underbrace{G(\boldsymbol{x},\boldsymbol{x}')(k_E - \mathrm{i}\boldsymbol{\sigma}\cdot\overleftarrow{\boldsymbol{\nabla}}_{\boldsymbol{x}'} + \mathrm{i}\eta)}_{=\delta(\boldsymbol{x}-\boldsymbol{x}')}\Phi(\boldsymbol{x}')\,, \tag{A.69}$$

with $\overleftarrow{\boldsymbol{\nabla}}_{\boldsymbol{x}'}$ acting to the left on the second argument of G. Here $\tilde{\mathcal{V}}$ is a region in space that includes the scatterer completely, and its boundary $\partial\tilde{\mathcal{V}}$ intersects the leads perpendicularly in the asymptotic region. Integration by parts then leads to

$$\Phi(\boldsymbol{x}) = \mathrm{i}\int\limits_{C_a} dy'_a\, G(\boldsymbol{x},\boldsymbol{x}'_a)\,\sigma_{\boldsymbol{x}_a}\,\Psi^-_{m'}(\boldsymbol{x}'_a)\,, \tag{A.70}$$

where $\hat{\boldsymbol{x}}_a$ is the unit vector normal to the boundary $\partial\tilde{\mathcal{V}}$ at the point $\boldsymbol{x}'$. To obtain Eq. (A.70) we have used that in the asymptotic region the retarded Green function contains only outgoing waves and can be expanded as [176]

$$G(\boldsymbol{x}_a,\boldsymbol{x}'_b) \overset{\boldsymbol{x}'_b\to\infty}{\longrightarrow} \sum_m b_m(\boldsymbol{x}_a)\psi^{-\dagger}_m(\boldsymbol{x}'_b)\,. \tag{A.71}$$

Further we employed the current orthogonality relations (A.63) and (A.64). Now we multiply Eqs. (A.68) and (A.70) with the appropriate outgoing wavefunction in lead a and use again Eq. (A.63) to project out the transmission amplitude, yielding the graphene version of the Fisher-Lee relations (see also Ref. [247])

$$t^{(ab)}_{mm'} = \mathrm{i}v_F\int\limits_{C_a} dy_a \int\limits_{C_b} dy'_b\,\Psi^{+\dagger}_m(\boldsymbol{x}_a)\,\sigma_{\boldsymbol{x}_a}\,G(\boldsymbol{x}_b,\boldsymbol{x}'_a)\,\sigma_{\boldsymbol{x}_b}\,\Psi^-_n(\boldsymbol{x}'_b)\,. \tag{A.72}$$

Following Ref. [176], we can now derive the Landauer formula for graphene, that expresses the conductance as a sum over transmission probabilities of the individual propagating modes in the leads. First we note that, in analogy to Eq. (A.71), the advanced Green function in the asymptotic region can be constructed solely out of incoming modes [176]. Thus for the retarded Green function it follows

$$G^\dagger(\boldsymbol{x}'_b,\boldsymbol{x}_a) \overset{\boldsymbol{x}_b\to\infty}{\longrightarrow} \sum_{m'} d_{m'}(\boldsymbol{x}_a)\psi^{+\dagger}_{m'}(\boldsymbol{x}'_b) \Rightarrow G(\boldsymbol{x}_a,\boldsymbol{x}'_b) \overset{\boldsymbol{x}_a\to\infty}{\longrightarrow} \sum_{m'}\psi^+_{m'}(\boldsymbol{x}_a)\,d^\dagger_{m'}(\boldsymbol{x}'_b)\,, \tag{A.73}$$

and in combination with Eq. (A.71) we have

$$G(\boldsymbol{x}_a,\boldsymbol{x}'_b) \overset{\boldsymbol{x}_a,\boldsymbol{x}'_b\to\infty}{\longrightarrow} \sum_{mm'} f_{mm'}\psi^+_{m'}(\boldsymbol{x}_a)\psi^{-\dagger}_m(\boldsymbol{x}'_b)\,. \tag{A.74}$$

Inserting this into Eq. (A.72) and applying Eq. (A.63) twice, gives for the coefficients $f_{mm'} = \mathrm{i}v_F\,t^{(ab)}_{mm'}$. We insert the resulting expansion into the linear response expression for the non-local conductivity, Eq. (5.5), and finally use Eq. (A.63) again twice to obtain in combination

with Eq. (5.4) the Landauer formula

$$g_{ab} = \frac{e^2}{h} \sum_{mm'} |t^{ab}_{mm'}|^2 \,. \tag{A.75}$$

In a similar way, one can start from the Landauer formula and derive Eq. (5.4) using the Fisher-Lee relation. We demonstrate the idea on another example, namely we derive Eqs. (5.85) and (5.86). To this end we use the relation

$$\sum_{m'} \int\limits_C d\tilde{y}\, \psi^{\pm}_{m'}(y) \psi^{\pm\dagger}_{m'}(\tilde{y})\, \sigma_x\, \psi^{\pm}_{m}(\tilde{y}) = \pm \frac{\psi^{\pm}_m(y)}{v_{_F}} \,, \tag{A.76}$$

which follows directly from Eq. (A.63). Starting from Eq. (A.72) we define $t_{mm'} = t^{(ab)}_{mm'}$ and get

$$\begin{aligned} \mathrm{Tr}(tt^\dagger tt^\dagger) \;&=\; \sum_{\substack{m,n\in a \\ o,p\in b}} t_{mo}\, t^*_{no}\, t_{np}\, t^*_{mp} = v_{_F}^4 \int\limits_{C_a} dy_1 \ldots dy_4 \int\limits_{C_b} dy_5 \ldots dy_8 \\ &\times\; \psi^{+\dagger}_m(y_1)\, \sigma_{\boldsymbol{x}_a}\, G(\boldsymbol{x_1}, \boldsymbol{x_5})\, \sigma_{\boldsymbol{x}_b}\, \psi^-_o(y_5)\; \psi^{-\dagger}_o(y_6)\, \sigma_{\boldsymbol{x}_b}\, G^\dagger(\boldsymbol{x_2}, \boldsymbol{x_6})\, \sigma_{\boldsymbol{x}_a}\, \psi^+_n(y_2) \\ &\times\; \psi^{+\dagger}_n(y_3)\, \sigma_{\boldsymbol{x}_a}\, G(\boldsymbol{x_3}, \boldsymbol{x_7})\, \sigma_{\boldsymbol{x}_b}\, \psi^-_p(y_7)\; \psi^{-\dagger}_p(y_8)\, \sigma_{\boldsymbol{x}_b}\, G^\dagger(\boldsymbol{x_4}, \boldsymbol{x_8})\, \sigma_{\boldsymbol{x}_a}\, \psi^+_m(y_4) \,. \end{aligned} \tag{A.77}$$

With the structure of the Green function (A.74), we can use Eq. (A.76) four times and obtain Eqs. (5.85) and (5.86) after renaming the integration variables

$$\mathrm{Tr}(tt^\dagger tt^\dagger) = \int\limits_{C_a} dy_1 dy_2 \int\limits_{C_b} dy_1' dy_2'\, \mathrm{Tr}\left[\sigma_{\boldsymbol{x}_a} G(\boldsymbol{x}_1, \boldsymbol{x}_1') \sigma_{\boldsymbol{x}_b} G^\dagger(\boldsymbol{x}_2, \boldsymbol{x}_1') \sigma_{\boldsymbol{x}_a} G(\boldsymbol{x}_2, \boldsymbol{x}_2') \sigma_{\boldsymbol{x}_b} G^\dagger(\boldsymbol{x}_1, \boldsymbol{x}_2')\right] . \tag{A.78}$$

A.6 Effects of smooth bulk disorder on the Green function

We discuss the effects of weak bulk potential disorder that is smooth on the lattice scale on the semiclassical graphene Green function. Such long range potentials do not lead to intervalley scattering, so that in the effective Dirac theory we can account for them by an additional diagonal term $\mathcal{H}_V$ in the Hamiltonian [72]. The full Hamiltonian is then given by

$$\mathcal{H}_d = \mathcal{H} + \mathcal{H}_V = v_{_F}\tau_0 \otimes \boldsymbol{\sigma}\cdot\boldsymbol{p} + \hbar v_{_F}\tau_0 \otimes \sigma_0\, V(\boldsymbol{x})\,, \tag{A.79}$$

where $V(\boldsymbol{x})$ varies slowly on the scale of the lattice constant a.

First we derive the disorder averaged semiclassical Green function of a chaotic graphene flake. To this end we make the very same ansatz as for the clean case [see Eq. (3.4)]

$$\langle G_d\rangle(\boldsymbol{x},\boldsymbol{x}') = \langle G_{0,d}\rangle(\boldsymbol{x},\boldsymbol{x}') - \int\limits_{\partial\mathcal{V}} d\sigma_{\boldsymbol{\beta}}\, \langle G_{0,d}\rangle(\boldsymbol{x},\boldsymbol{\beta})\, \mathrm{i}\sigma_{\boldsymbol{n}_{\boldsymbol{\beta}}}\, \mu(\boldsymbol{\beta},\boldsymbol{x}')\,, \tag{A.80}$$

where $G_{0,d}$ denotes the Green function of infinitely extended graphene with a given disorder configuration d, and the brackets $\langle\,\rangle$ represent the impurity averaging.[3] For smooth potentials, the discontinuity of the Green function in Eq. (3.9), and consequently also the MRE, given by Eqs. (3.13) and (3.14), remain unchanged, except that the free Green function has to be replaced by its impurity averaged version. This leads to

$$\langle G_d\rangle(\boldsymbol{x},\boldsymbol{x}') = \langle G_{0,d}\rangle(\boldsymbol{x},\boldsymbol{x}') + \sum_{N=1}^{\infty}\langle G_{N,d}\rangle(\boldsymbol{x},\boldsymbol{x}')\,, \tag{A.81}$$

with

$$\begin{aligned}\langle G_{N,d}\rangle(\boldsymbol{x},\boldsymbol{x}') = (-2)^N \int\limits_{\partial\mathcal{V}} d\sigma_{\boldsymbol{\alpha}_N}\ldots d\sigma_{\boldsymbol{\alpha}_2} d\sigma_{\boldsymbol{\alpha}_1}\langle G_{0,d}\rangle(\boldsymbol{x},\boldsymbol{\alpha}_N)\mathrm{i}\sigma_{\boldsymbol{n}_{\boldsymbol{\alpha}_N}}\mathcal{P}_{\boldsymbol{\alpha}_N} \\ \ldots\,\mathrm{i}\sigma_{\boldsymbol{n}_{\boldsymbol{\alpha}_2}} P_{\boldsymbol{\alpha}_2}\langle G_{0,d}\rangle(\boldsymbol{\alpha}_2,\boldsymbol{\alpha}_1)\mathrm{i}\sigma_{\boldsymbol{n}_{\boldsymbol{\alpha}_1}}\mathcal{P}_{\boldsymbol{\alpha}_1}\langle G_{0,d}\rangle(\boldsymbol{\alpha}_1,\boldsymbol{x}')\,.\end{aligned} \tag{A.82}$$

For the impurity potential V, we assume a sum of N_{i} Gaussians that are centered at random positions $\boldsymbol{X}_j$. The width of the individual Gaussians is δ and their heights u_j are uniformingly distributed in the interval $[-u,u]$, leading to

$$V(\boldsymbol{x}) = \sum_{j=1}^{N_{\mathrm{i}}}\frac{u_j}{2\pi\delta^2}\exp\left[-\frac{(\boldsymbol{x}-\boldsymbol{X}_j)^2}{2\,\delta^2}\right]. \tag{A.83}$$

The semiclassical free Green function for the Hamiltonian $\mathcal{H}_d$ has been derived in Ref. [107]. Under the assumption that the potential is very weak, so that the classical orbits remain essentially unaffected, it is given by

$$G^{\mathrm{sc}}_{0,d}(\boldsymbol{x},\boldsymbol{x}') = G^{\mathrm{sc}}_{0}(\boldsymbol{x},\boldsymbol{x}')\exp\left[\mathrm{i}\frac{\delta S(\boldsymbol{x},\boldsymbol{x}')}{\hbar}\right], \tag{A.84}$$

[3] We denote $G_{0,d}$ still as 'free Green function' since the system boundary is not included.

with

$$\delta S(\boldsymbol{x},\boldsymbol{x}') = \frac{\hbar}{2}\int\limits_{\gamma} d\sigma_{\boldsymbol{q}} \frac{1}{k_E - V(\boldsymbol{q})}\left[\frac{\boldsymbol{x}-\boldsymbol{x}'}{|\boldsymbol{x}-\boldsymbol{x}'|}\times\boldsymbol{\nabla}V(\boldsymbol{q})\right]_z , \tag{A.85}$$

and G_0 is the free Green function in the clean case, i. e. without disorder, as given in Eq. (3.72). If the distance between $\boldsymbol{x}$ and $\boldsymbol{x}'$ is much larger than δ, the action difference δS follows a random walk and the phase is accumulated in a Gaussian way, so that [248]

$$\langle G_{0,d}\rangle(\boldsymbol{x},\boldsymbol{x}') = G_0(\boldsymbol{x},\boldsymbol{x}')\left\langle \exp\left[\mathrm{i}\frac{\delta S(\boldsymbol{x},\boldsymbol{x}')}{\hbar}\right]\right\rangle = G_0(\boldsymbol{x},\boldsymbol{x}')\exp\left[\mathrm{i}\frac{\langle\delta S^2\rangle(\boldsymbol{x},\boldsymbol{x}')}{2\hbar^2}\right] , \tag{A.86}$$

with

$$\langle\delta S^2\rangle(\boldsymbol{x},\boldsymbol{x}') = \frac{\hbar^2}{4}\int\limits_{\gamma} d\sigma_{\boldsymbol{q}}\int\limits_{\gamma} d\sigma_{\boldsymbol{q}'}\, C(\boldsymbol{q},\boldsymbol{q}') \tag{A.87}$$

and

$$C(\boldsymbol{q},\boldsymbol{q}') = \left\langle \frac{\left[\cos\varphi_{\boldsymbol{x},\boldsymbol{x}'}V_y(\boldsymbol{q}) - \sin\varphi_{\boldsymbol{x},\boldsymbol{x}'}V_x(\boldsymbol{q})\right]\left[\cos\varphi_{\boldsymbol{x},\boldsymbol{x}'}V_y(\boldsymbol{q}') - \sin\varphi_{\boldsymbol{x},\boldsymbol{x}'}V_x(\boldsymbol{q}')\right]}{\left[k_E - V(\boldsymbol{q})\right]\left[k_E - V(\boldsymbol{q}')\right]}\right\rangle . \tag{A.88}$$

Since the disorder is weak, we assume $u \ll k_E$, and thus expand the denominator in $C(\boldsymbol{q},\boldsymbol{q}')$ in powers of u/k_E. Taking only the leading order term, we get

$$\begin{aligned} C(\boldsymbol{q},\boldsymbol{q}') \;&\approx\; \frac{1}{4k_E^2}\left(\cos\varphi^2_{\boldsymbol{x},\boldsymbol{x}'}\left\langle V_y(\boldsymbol{q})V_y(\boldsymbol{q}')\right\rangle + \sin\varphi^2_{\boldsymbol{x},\boldsymbol{x}'}\left\langle V_y(\boldsymbol{q})V_y(\boldsymbol{q}')\right\rangle\right. \\ &-\; \left.\sin\varphi_{\boldsymbol{x},\boldsymbol{x}'}\cos\varphi_{\boldsymbol{x},\boldsymbol{x}'}\left\langle V_x(\boldsymbol{q})V_y(\boldsymbol{q}')\right\rangle - \sin\varphi_{\boldsymbol{x},\boldsymbol{x}'}\cos\varphi_{\boldsymbol{x},\boldsymbol{x}'}\left\langle V_y(\boldsymbol{q})V_x(\boldsymbol{q}')\right\rangle\right) . \end{aligned} \tag{A.89}$$

Assuming that the potential heights are uncorrelated, $\langle u_i u_j\rangle = u^2\delta_{ij}$, we obtain for example for the last term

$$\begin{aligned} \left\langle V_y(\boldsymbol{q})V_x(\boldsymbol{q}')\right\rangle \;&=\; \frac{u^2}{4\pi^2\delta^8|\mathcal{V}|}\sum_{j=1}^{N_\mathrm{i}}\int\limits_{-\infty}^{\infty} dX_j\int\limits_{-\infty}^{\infty} dY_j\,(q_y - Y_j)(q'_x - X_j) \\ &\quad\times\exp\left\{-\frac{1}{2\delta^2}\left[(\boldsymbol{q}-\boldsymbol{X}_j)^2 + (\boldsymbol{q}'-\boldsymbol{X}_j)^2\right]\right\} . \end{aligned} \tag{A.90}$$

All the occurring integrals are of Gaussian type and can be performed analytically, so that we end up with

$$\left\langle V_x(\boldsymbol{q})V_x(\boldsymbol{q}')\right\rangle \;=\; \frac{n_\mathrm{i}u^2\left[2\delta^2 - (q_x - q'_x)^2\right]}{16\pi\delta^6}\exp\left[-\frac{(\boldsymbol{q}-\boldsymbol{q}')^2}{2\delta^2}\right] , \tag{A.91}$$

$$\left\langle V_y(\boldsymbol{q})V_y(\boldsymbol{q}')\right\rangle \;=\; \frac{n_\mathrm{i}u^2\left[2\delta^2 - (q_y - q'_y)^2\right]}{16\pi\delta^6}\exp\left[-\frac{(\boldsymbol{q}-\boldsymbol{q}')^2}{2\delta^2}\right] , \tag{A.92}$$

$$\left\langle V_x(\boldsymbol{q})V_y(\boldsymbol{q}')\right\rangle = \left\langle V_y(\boldsymbol{q})V_x(\boldsymbol{q}')\right\rangle \;=\; -\frac{n_\mathrm{i}u^2(q_x - q'_x)(q_y - q'_y)}{16\pi\delta^6}\exp\left[-\frac{(\boldsymbol{q}-\boldsymbol{q}')^2}{2\delta^2}\right] , \tag{A.93}$$

with the density of impurities $n_\mathrm{i} = N_\mathrm{i}/|\mathcal{V}|$. Since we have assumed that the classical orbits γ remain unchanged by the potential, they are still straight lines between initial and final point, and we have

$$\cos\varphi_{\boldsymbol{x},\boldsymbol{x}'} = -\frac{q_x - q'_x}{|\boldsymbol{q}-\boldsymbol{q}'|}\,, \quad \sin\varphi_{\boldsymbol{x},\boldsymbol{x}'} = -\frac{q_y - q'_y}{|\boldsymbol{q}-\boldsymbol{q}'|}\,. \tag{A.94}$$

Hence, all direction-dependent terms in Eq. (A.89) cancel and we get

$$\left\langle \delta S^2 \right\rangle (\boldsymbol{x},\boldsymbol{x}') \approx \frac{\hbar^2 n_\mathrm{i} u^2}{32\delta^4 \pi k_E^2} \int\limits_\gamma d\sigma_{\boldsymbol{q}} \int\limits_\gamma d\sigma_{\boldsymbol{q}'} \, \exp\left[-\frac{(\boldsymbol{q}-\boldsymbol{q}')^2}{2\delta^2}\right]\,. \tag{A.95}$$

For one of the integrals, we can push the integration limits to infinity, because $|\boldsymbol{x}-\boldsymbol{x}'| \gg \delta$. Then the remaining integral gives the distance $|\boldsymbol{x}-\boldsymbol{x}'|$, and

$$\left\langle \delta S^2 \right\rangle (\boldsymbol{x},\boldsymbol{x}') \approx \frac{\hbar^2 n_\mathrm{i} u^2 |\boldsymbol{x}-\boldsymbol{x}'|}{16\,\delta^3 \sqrt{\pi} k_E^2}\,. \tag{A.96}$$

With this we get for the disorder averaged free Green function in the semiclassical limit

$$\left\langle G^\mathrm{sc}_{0,d} \right\rangle (\boldsymbol{x},\boldsymbol{x}') = G^\mathrm{sc}_0(\boldsymbol{x},\boldsymbol{x}') \mathrm{e}^{-|\boldsymbol{x}-\boldsymbol{x}'|/2l_\mathrm{sc}}\,, \tag{A.97}$$

and the mean free path

$$l_\mathrm{sc} = \frac{4\delta k_E^2}{\sqrt{\pi} C_0}\,, \quad C_0 = \frac{u^2 n_\mathrm{i}}{4\pi\delta^2}\,. \tag{A.98}$$

Interestingly, l_sc is equal to the *transport* mean free path not the *elastic* mean free path obtained from quantum calculations in the Boltzmann limit for a weak potential with Gaussian correlation [249, 250]. This is surprising, since for obtaining the transport mean free path, usually disorder averaged products of two Green functions are required. The semiclassical analysis for the Schrödinger case analog to our discussion above, gives the elastic mean free path [248].

For smooth potentials, the evaluation of Eq. (A.82) in the semiclassical limit is performed as for the clean case, except that G_0 has to be replaced by its impurity averaged version (A.97). Thus each summand in the semiclassical Green function (3.83) for a graphene cavity acquires a damping factor $\exp(-L_\gamma/2l_\mathrm{sc})$, leading to

$$\left\langle G^\mathrm{sc}_d \right\rangle (\boldsymbol{x},\boldsymbol{x}') = \frac{\hbar v_F}{2} \sum_{\gamma(\boldsymbol{x},\boldsymbol{x}')} \frac{|D_\gamma|}{\sqrt{2\pi\hbar^3}} \mathrm{e}^{\mathrm{i}k_E L_\gamma + \mathrm{i}\mu_\gamma \pi/2} \mathrm{e}^{-L_\gamma/2l_\mathrm{sc}}\, K_\gamma\,. \tag{A.99}$$

In the trace integral (4.35), the damping factors do not alter the stationary phase points, so that also in the trace formula (4.42) every periodic orbit contribution is weighted with a factor $\exp(-L_\gamma/2l_\mathrm{sc})$, which improves convergence of the semiclassical trace formula. With that we get also the effect of the weak disorder on the spectral form factor of chaotic graphene

billiards. In the semiclassical expression for $F(t)$, Eq. (4.82), it leads to a t-dependent damping of each orbit pair contribution, namely

$$\langle F_d \rangle (t) \approx \frac{\mathrm{e}^{-tT_\mathrm{H}/T_\mathrm{sc}}}{4T_\mathrm{H}} \left\langle \sum_{\gamma,\gamma'} A_\gamma A^*_{\gamma'} Z_{\gamma,\gamma'} \, \mathrm{e}^{\mathrm{i}k_E \delta L_{\gamma,\gamma'}} \, \delta\left(T - \frac{T_\gamma + T_{\gamma'}}{2}\right) \right\rangle_{k_E} , \tag{A.100}$$

where we used that only pairs with $(T_\gamma + T_{\gamma'})/2 = T$ contribute due to the delta function, and we defined $T_\mathrm{sc} = L_\mathrm{sc}/v_F$. Therefore all results for $F_D(t)$ and $F_L(t)$ throughout Sec. 4.3 obtain a factor $\exp(-tT_\mathrm{H}/T_\mathrm{sc})$ due to the weak bulk disorder. For the effects of bulk disorder on the conductance, the impurity averaged single particle Green function is not sufficient, but rather one has to consider impurity averaged *products* of Green function, which is beyond the scope of this work.

A.7 Edge magnetism - generalized results for weak localization

We generalize the two main results of Sec. 6.2, namely Eqs. (6.19) and (6.34), dropping the assumption of small $W_{\rm sa}/|\partial\mathcal{V}|$.

In-plane edge magnetic moments

We start from the averaging of the spin contribution to the pseudospin trace Eq. (6.17).

$$\langle Y^s_{\gamma,\gamma_\times}\rangle(T) = \sum_{n=0}^{\infty}\langle Y^s_{\gamma,\gamma_\times}\rangle(n)\, p_n(N)\,. \tag{A.101}$$

Inserting $\langle Y^s_{\gamma,\gamma_\times}\rangle$ from Eq. (6.14) and p_n from Eq. (4.120) with $W_{\rm ac}$ replaced $W_{\rm sa}$, we get

$$\langle Y^s_{\gamma,\gamma_\times}\rangle(T) = 1 - \exp(-2T/T_{\rm sa}) + \exp(-T/T^+_{\rm sa}) + \exp(-T/T^-_{\rm sa})\,, \tag{A.102}$$

with [cf. Eq. (4.124)]

$$T^{-1}_{\rm sa} = -\frac{v_F|\partial\mathcal{V}|}{2\pi|\mathcal{V}|}\ln\left(1-\frac{2W_{\rm sa}}{|\partial\mathcal{V}|}\right) \tag{A.103}$$

and

$$T^{\pm-1}_{\rm sa} = -\frac{v_F|\partial\mathcal{V}|}{2\pi|\mathcal{V}|}\ln\left(1-\left(1\pm\langle e^{2i\varsigma}\rangle\right)\frac{W_{\rm sa}}{|\partial\mathcal{V}|}\right)\,. \tag{A.104}$$

With Eq. (A.102) inserted into Eq. (6.16), we obtain for the WL correction

$$\begin{aligned}\langle g_L\rangle/g_0 \;\approx\; & -\frac{M_aM_b}{(M_a+M_b)^2}\left(\frac{1}{1+T_{\rm d}/T_{\rm B}} - \frac{1}{1+2T_{\rm d}/T_{\rm sa}+T_{\rm d}/T_{\rm B}}\right.\\ & \left. +\;\frac{1}{1+T_{\rm d}/T^+_{\rm sa}+T_{\rm d}/T_{\rm B}} + \frac{1}{1+T_{\rm d}/T^-_{\rm sa}+T_{\rm d}/T_{\rm B}}\right)\,.\end{aligned} \tag{A.105}$$

Note that for small $W_{\rm sa}/|\partial\mathcal{V}|$ the spin scattering rates above become

$$T^{-1}_{\rm sa} \approx \frac{v_F W_{\rm sa}}{\pi|\mathcal{V}|} \quad\text{and}\quad T^{\pm-1}_{\rm sa} \approx \left(1\pm\langle e^{2i\varsigma}\rangle\right)\frac{v_F W_{\rm sa}}{\pi|\mathcal{V}|}\,, \tag{A.106}$$

and we recover Eqs. (6.17), (6.18), and (6.19).

Unpolarized edge magnetic moments

In the same way as for the in-plane case, we insert Eq. (6.25) into Eq. (A.101) to get

$$\langle Y^s_{\gamma,\gamma_\times}\rangle(T) = 3\exp(-2T/T^*_{\rm sa}) - \exp(-2T/T_{\rm sa})\,, \tag{A.107}$$

with $T_{\rm sa}$ as defined in Eq. (A.103) and

$$T^{*-1}_{\rm sa} = -\frac{v_F|\partial\mathcal{V}|}{2\pi|\mathcal{V}|}\ln\left(1-\frac{2W_{\rm sa}}{3|\partial\mathcal{V}|}\right)\,. \tag{A.108}$$

For the WL this leads to

$$\langle g_L \rangle / g_0 \approx -\frac{M_a M_b}{(M_a + M_b)^2} \left(\frac{3}{1 + 2T_\mathrm{d}/T^*_\mathrm{sa} + T_\mathrm{d}/T_\mathrm{B}} - \frac{1}{1 + 2T_\mathrm{d}/T_\mathrm{sa} + T_\mathrm{d}/T_\mathrm{B}} \right) . \tag{A.109}$$

Also here we recover Eqs. (6.33) and (6.34) if we neglect terms of quadratic and higher order in $W_\mathrm{sa}/|\partial\mathcal{V}|$.

Thus, apart from the definition of the spin scattering time scales, the results of Eqs. (A.105) and (A.109) are identical to the approximate results of Sec. 6.2, Eqs. (6.19) and (6.34).

Bibliography

[1] P. R. Wallace. *The band theory of graphite.* Phys. Rev. **71**, 622 (1947).

[2] J. W. McClure. *Band structure of graphite and de Haas-van Alphen effect.* Phys. Rev. **108**, 612 (1957).

[3] J. C. Slonczewski and P. R. Weiss. *Band structure of graphite.* Phys. Rev. **109**, 272 (1958).

[4] D. P. DiVincenzo and E. J. Mele. *Self-consistent effective-mass theory for intralayer screening in graphite intercalation compounds.* Phys. Rev. B **29**, 1685 (1984).

[5] G. W. Semenoff. *Condensed-matter simulation of a three-dimensional anomaly.* Phys. Rev. Lett. **53**, 2449 (1984).

[6] H.-P. Boehm, A. Clauss, G. O. Fischer, and U. Hofmann. *Dünnste Kohlenstoff-Folien.* Z. Naturforsch. B **17**, 150 (1962).

[7] H.-P. Boehm. *Graphen - wie eine Laborkuriosität plötzlich äußerst interessant wurde.* Angew. Chemie **122**, 9520 (2010).

[8] K. S. Novoselov, A. K. Geim, S. V. Morozov, D. Jiang, Y. Zhang, S. Dubonos, I. Grigorieva, and A. Firsov. *Electric field effect in atomically thin carbon films.* Science **306**, 666 (2004).

[9] K. S. Novoselov, D. Jiang, F. Schedin, T. J. Booth, V. V. Khotkevich, S. V. Morozov, and A. K. Geim. *Two-dimensional atomic crystals.* Proc. Natl. Acad. Sci. U.S.A. **102**, 10451 (2005).

[10] K. S. Novoselov, A. K. Geim, S. V. Morozov, D. Jiang, M. I. Katsnelson, I. V. Grigorieva, S. V. Dubonos, and A. A. Firsov. *Two-dimensional gas of massless Dirac fermions in graphene.* Nature **438**, 197 (2005).

[11] Y. Zhang, Y.-W. Tan, H. L. Stormer, and P. Kim. *Experimental observation of the quantum Hall effect and Berry's phase in graphene.* Nature **438**, 201 (2005).

[12] S. Das Sarma, S. Adam, E. H. Hwang, and E. Rossi. *Electronic transport in two-dimensional graphene.* Rev. Mod. Phys. **83**, 407 (2011).

[13] A. Geim and A. McDonald. *Graphene: Exploring carbon flatland.* Phys. Today **60**, 35 (2007).

[14] Official Web Site of the Nobel Prize.
http://nobelprize.org/nobel_prizes/physics/laureates/2010/index.html .

[15] K. S. Novoselov, Z. Jiang, Y. Zhang, S. V. Morozov, H. L. Stormer, U. Zeitler, J. C. Maan, G. S. Boebinger, P. Kim, and A. K. Geim. *Room-temperature quantum Hall effect in graphene.* Science **315**, 1379 (2007).

[16] K. Bolotin, K. Sikes, Z. Jiang, M. Klima, G. Fudenberg, J. Hone, P. Kim, and H. Stormer. *Ultrahigh electron mobility in suspended graphene.* Solid State Commun. **146**, 351 (2008).

[17] X. Du, I. Skachko, A. Barker, and E. Y. Andrei. *Approaching ballistic transport in suspended graphene.* Nature Nanotech. **3**, 491 (2008).

[18] A. S. Mayorov, R. V. Gorbachev, S. V. Morozov, L. Britnell, R. Jalil, L. A. Ponomarenko, P. Blake, K. S. Novoselov, K. Watanabe, T. Taniguchi, and A. K. Geim. *Micrometer-scale ballistic transport in encapsulated graphene at room temperature.* Nano Lett. **11**, 2396 (2011).

[19] K. I. Bolotin, K. J. Sikes, J. Hone, H. L. Stormer, and P. Kim. *Temperature-dependent transport in suspended graphene.* Phys. Rev. Lett. **101**, 096802 (2008).

[20] T. Ando, T. Nakanishi, and R. Saito. *Berry's phase and absence of back scattering in carbon nanotubes.* J. Phys. Soc. Jpn. **67**, 2857 (1998).

[21] Y.-M. Lin, C. Dimitrakopoulos, K. A. Jenkins, D. B. Farmer, H.-Y. Chiu, A. Grill, and P. Avouris. *100-GHz transistors from wafer-scale epitaxial graphene.* Science **327**, 662 (2010).

[22] Y. Wu, Y. Ming Lin, A. A. Bol, K. A. Jenkins, F. Xia, D. B. Farmer, Y. Zhu, and P. Avouris. *High-frequency, scaled graphene transistors on diamond-like carbon.* Nature **472**, 74 (2011).

[23] Y.-M. Lin, A. Valdes-Garcia, S.-J. Han, D. B. Farmer, I. Meric, Y. Sun, Y. Wu, C. Dimitrakopoulos, A. Grill, P. Avouris, and K. A. Jenkins. *Wafer-scale graphene integrated circuit.* Science **332**, 1294 (2011).

[24] K. Tanaka, S. Yamashita, H. Yamabe, and T. Yamabe. *Electronic properties of one-dimensional graphite family.* Synth. Met. **17**, 143 (1987).

[25] M. Fujita, K. Wakabayashi, K. Nakada, and K. Kusakabe. *Peculiar localized edge state at zigzag graphite edge.* J. Phys. Soc. Jpn. **65**, 1920 (1996).

[26] C. Berger, Z. Song, X. Li, X. Wu, N. Brown, C. Naud, D. Mayou, T. Li, J. Hass, A. N. Marchenkov, E. H. Conrad, P. N. First, and W. A. de Heer. *Electronic confinement and coherence in patterned epitaxial graphene.* Science **312**, 1191 (2006).

[27] M. Y. Han, B. Özyilmaz, Y. Zhang, and P. Kim. *Energy band-gap engineering of graphene nanoribbons.* Phys. Rev. Lett. **98**, 206805 (2007).

[28] Z. Chen, Y.-M. Lin, M. J. Rooks, and P. Avouris. *Graphene nano-ribbon electronics.* Physica E **40**, 228 (2007).

[29] F. Molitor, A. Jacobsen, C. Stampfer, J. Güttinger, T. Ihn, and K. Ensslin. *Transport gap in side-gated graphene constrictions.* Phys. Rev. B **79**, 075426 (2009).

[30] P. Gallagher, K. Todd, and D. Goldhaber-Gordon. *Disorder-induced gap behavior in graphene nanoribbons.* Phys. Rev. B **81**, 115409 (2010).

[31] C. Stampfer, J. Güttinger, F. Molitor, D. Graf, T. Ihn, and K. Ensslin. *Tunable coulomb blockade in nanostructured graphene.* Appl. Phys. Lett. **92**, 012102 (2008).

[32] C. Stampfer, E. Schurtenberger, F. Molitor, J. Güttinger, T. Ihn, and K. Ensslin. *Tunable graphene single electron transistor.* Nano Lett. **8**, 2378 (2008).

[33] L. A. Ponomarenko, F. Schedin, M. I. Katsnelson, R. Yang, E. W. Hill, K. S. Novoselov, and A. K. Geim. *Chaotic Dirac billiard in graphene quantum dots.* Science **320**, 356 (2008).

[34] S. Schnez, F. Molitor, C. Stampfer, J. Güttinger, I. Shorubalko, T. Ihn, and K. Ensslin. *Observation of excited states in a graphene quantum dot.* Appl. Phys. Lett. **94**, 012107 (2009).

[35] J. Güttinger, C. Stampfer, S. Hellmüller, F. Molitor, T. Ihn, and K. Ensslin. *Charge detection in graphene quantum dots.* Appl. Phys. Lett. **93**, 212102 (2008).

[36] J. Güttinger, C. Stampfer, F. Libisch, T. Frey, J. Burgdörfer, T. Ihn, and K. Ensslin. *Electron-hole crossover in graphene quantum dots.* Phys. Rev. Lett. **103**, 046810 (2009).

[37] J. Güttinger, T. Frey, C. Stampfer, T. Ihn, and K. Ensslin. *Spin states in graphene quantum dots.* Phys. Rev. Lett. **105**, 116801 (2010).

[38] P. G. Silvestrov and K. B. Efetov. *Quantum dots in graphene.* Phys. Rev. Lett. **98**, 016802 (2007).

[39] B. Trauzettel, D. V. Bulaev, D. Loss, and G. Burkard. *Spin qubits in graphene quantum dots.* Nature Phys. **3**, 192 (2007).

[40] P. Recher, B. Trauzettel, A. Rycerz, Y. M. Blanter, C. W. J. Beenakker, and A. F. Morpurgo. *Aharonov-Bohm effect and broken valley degeneracy in graphene rings.* Phys. Rev. B **76**, 235404 (2007).

[41] F. Libisch, S. Rotter, J. Güttinger, C. Stampfer, and J. Burgdörfer. *Transition to landau levels in graphene quantum dots.* Phys. Rev. B **81**, 245411 (2010).

[42] J. H. Bardarson, M. Titov, and P. W. Brouwer. *Electrostatic confinement of electrons in an integrable graphene quantum dot.* Phys. Rev. Lett. **102**, 226803 (2009).

[43] J. Wurm, A. Rycerz, I. Adagideli, M. Wimmer, K. Richter, and H. U. Baranger. *Symmetry classes in graphene quantum dots: Universal spectral statistics, weak localization, and conductance fluctuations.* Phys. Rev. Lett. **102**, 056806 (2009).

[44] F. Libisch, C. Stampfer, and J. Burgdörfer. *Graphene quantum dots: Beyond a Dirac billiard.* Phys. Rev. B **79**, 115423 (2009).

[45] R. Yang, L. Huang, Y.-C. Lai, and C. Grebogi. *Quantum chaotic scattering in graphene systems.* Eur. Phys. Lett. **94**, 40004 (2011).

[46] C. W. J. Beenakker. *Colloquium: Andreev reflection and Klein tunneling in graphene.* Rev. Mod. Phys. **80**, 1337 (2008).

[47] O. Klein. *Die Reflexion von Elektronen an einem Potentialsprung nach der relativistischen Dynamik von Dirac.* Z. Phys. A **53**, 157 (1929).

[48] C. Tao, L. Jiao, O. V. Yazyev, Y.-C. Chen, J. Feng, X. Zhang, R. B. Capaz, J. M. Tour, A. Zettl, S. G. Louie, H. Dai, and M. F. Crommie. *Spatially resolving spin-split edge states of chiral graphene nanoribbons.* Nature Phys. **7**, 616 (2011).

[49] M. Gutzwiller. *Chaos in Classical and Quantum Mechanics.* (Springer, New York, 1990).

[50] K. Richter. *Semiclassical Theory of Mesoscopic Quantum Systems.* (Springer, Berlin, 2000).

[51] M. Brack and R. Bhaduri. *Semiclassical Physics.* (Westview Press, Boulder, 2003).

[52] D. Waltner and K. Richter. *Classical Correlations and Quantum Interference in Ballistic Conductors* in: *Nonlinear Dynamics in Nanosystems*, edited by G. Radons, B. Rumpf, and H. G. Schuster. (Wiley-VCH, New York, 2010).

[53] A. Kormányos, P. Rakyta, L. Oroszlány, and J. Cserti. *Bound states in inhomogeneous magnetic field in graphene: Semiclassical approach.* Phys. Rev. B **78**, 045430 (2008).

[54] P. Rakyta, A. Kormányos, J. Cserti, and P. Koskinen. *Exploring the graphene edges with coherent electron focusing.* Phys. Rev. B **81**, 115411 (2010).

[55] P. Carmier, C. Lewenkopf, and D. Ullmo. *Graphene $n-p$ junction in a strong magnetic field: A semiclassical study.* Phys. Rev. B **81**, 241406 (2010).

[56] M. Wimmer and K. Richter. *Optimal block-tridiagonalization of matrices for coherent charge transport.* J. Comp. Phys. **228**, 8548 (2009).

[57] A. H. Castro Neto, F. Guinea, N. M. R. Peres, K. S. Novoselov, and A. K. Geim. *The electronic properties of graphene.* Rev. Mod. Phys. **81**, 109 (2009).

[58] N. M. R. Peres. *Colloquium: The transport properties of graphene: An introduction.* Rev. Mod. Phys. **82**, 2673 (2010).

[59] R. Saito, G. Dresselhaus, and M. S. Dresselhaus. *Physical Properties of Carbon Nanotubes.* (Imperial College Press, London, 1998).

[60] J. Wurm. *Quantum transport in graphene-based nanosystems.* Diploma thesis, Universität Regensburg (2008).

[61] M. Wimmer. *Quantum transport in nanostructures: From computational concepts to spintronics in graphene and magnetic tunnel junctions.* Ph.D. thesis, Universität Regensburg (2008).

[62] A. R. Akhmerov and C. W. J. Beenakker. *Detection of valley polarization in graphene by a superconducting contact.* Phys. Rev. Lett. **98**, 157003 (2007).

[63] E. McCann, K. Kechedzhi, V. I. Fal'ko, H. Suzuura, T. Ando, and B. L. Altshuler. *Weak-localization magnetoresistance and valley symmetry in graphene.* Phys. Rev. Lett. **97**, 146805 (2006).

[64] X. Wu, X. Li, Z. Song, C. Berger, and W. A. de Heer. *Weak antilocalization in epitaxial graphene: Evidence for chiral electrons.* Phys. Rev. Lett. **98**, 136801 (2007).

[65] F. Haake. *Quantum Signatures of Chaos.* (Springer, Berlin, 2004).

[66] S. Gnutzmann and B. Seif. *Universal spectral statistics in Wigner-Dyson, chiral, and Andreev star graphs. I. Construction and numerical results.* Phys. Rev. E **69**, 056219 (2004).

[67] F. Evers and A. D. Mirlin. *Anderson transitions.* Rev. Mod. Phys. **80**, 1355 (2008).

[68] M. L. Mehta. *Random Matrices.* (Elsevier Inc., San Diego, 2004).

[69] C. W. J. Beenakker. *Random-matrix theory of quantum transport.* Rev. Mod. Phys. **69**, 731 (1997).

[70] O. Bohigas, M. J. Giannoni, and C. Schmit. *Characterization of chaotic quantum spectra and universality of level fluctuation laws.* Phys. Rev. Lett. **52**, 1 (1984).

[71] J. Wurm, M. Wimmer, H. U. Baranger, and K. Richter. *Graphene rings in magnetic fields: Aharonov-Bohm effect and valley splitting.* Semicond. Sci. and Technol. **25**, 034003 (2010).

[72] H. Suzuura and T. Ando. *Crossover from symplectic to orthogonal class in a two-dimensional honeycomb lattice.* Phys. Rev. Lett. **89**, 266603 (2002).

[73] M. I. Katsnelson, K. S. Novoselov, and A. K. Geim. *Chiral tunnelling and the Klein paradox in graphene.* Nature Phys. **2**, 620 (2006).

[74] E. Rossi, J. H. Bardarson, P. W. Brouwer, and S. Das Sarma. *Signatures of Klein tunneling in disordered graphene $p-n-p$ junctions.* Phys. Rev. B **81**, 121408 (2010).

[75] J. Schelter, D. Bohr, and B. Trauzettel. *Interplay of the Aharonov-Bohm effect and Klein tunneling in graphene.* Phys. Rev. B **81**, 195441 (2010).

[76] A. F. Young and P. Kim. *Quantum interference and Klein tunnelling in graphene heterojunctions.* Nature Phys. **5**, 222 (2009).

[77] N. Stander, B. Huard, and D. Goldhaber-Gordon. *Evidence for Klein tunneling in graphene $p-n$ junctions.* Phys. Rev. Lett. **102**, 026807 (2009).

[78] E. McCann and V. I. Fal'ko. *Symmetry of boundary conditions of the Dirac equation for electrons in carbon nanotubes.* J. Phys.: Condens. Mat. **16**, 2371 (2004).

[79] K. Nakada, M. Fujita, G. Dresselhaus, and M. S. Dresselhaus. *Edge state in graphene ribbons: Nanometer size effect and edge shape dependence.* Phys. Rev. B **54**, 17954 (1996).

[80] L. Brey and H. A. Fertig. *Electronic states of graphene nanoribbons studied with the Dirac equation.* Phys. Rev. B **73**, 235411 (2006).

[81] M. Wimmer, A. R. Akhmerov, and F. Guinea. *Robustness of edge states in graphene quantum dots.* Phys. Rev. B **82**, 045409 (2010).

[82] Y. Kobayashi, K.-I. Fukui, T. Enoki, K. Kusakabe, and Y. Kaburagi. *Observation of zigzag and armchair edges of graphite using scanning tunneling microscopy and spectroscopy.* Phys. Rev. B **71**, 193406 (2005).

[83] Y. Niimi, T. Matsui, H. Kambara, K. Tagami, M. Tsukada, and H. Fukuyama. *Scanning tunneling microscopy and spectroscopy of the electronic local density of states of graphite surfaces near monoatomic step edges.* Phys. Rev. B **73**, 085421 (2006).

[84] K. Sasaki, Y. Shimomura, Y. Takane, and K. Wakabayashi. *Hamiltonian decomposition for bulk and surface states.* Phys. Rev. Lett. **102**, 146806 (2009).

[85] J. Wurm, M. Wimmer, I. Adagideli, K. Richter, and H. U. Baranger. *Interfaces within graphene nanoribbons.* New J. Phys. **11**, 095022 (2009).

[86] S. Bhowmick and V. B. Shenoy. *Weber-Fechner type nonlinear behavior in zigzag edge graphene nanoribbons.* Phys. Rev. B **82**, 155448 (2010).

[87] A. R. Akhmerov and C. W. J. Beenakker. *Boundary conditions for Dirac fermions on a terminated honeycomb lattice.* Phys. Rev. B **77**, 085423 (2008).

[88] G. Giovannetti, P. A. Khomyakov, G. Brocks, P. J. Kelly, and J. van den Brink. *Substrate-induced band gap in graphene on hexagonal boron nitride: Ab initio density functional calculations.* Phys. Rev. B **76**, 073103 (2007).

[89] S. Y. Zhou, G.-H. Gweon, A. V. Fedorov, P. N. First, W. A. de Heer, D.-H. Lee, F. Guinea, A. H. C. Neto, and A. Lanzara. *Substrate-induced bandgap opening in epitaxial graphene.* Nature Mat. **6**, 770 (2007).

[90] M. Berry and R. Mondragon. *Neutrino billiards: time-reversal symmetry-breaking without magnetic fields.* Proc. R. Soc. Lond. A **412**, 53 (1987).

[91] R. Balian and C. Bloch. *Distribution of eigenfrequencies for the wave equation in a finite domain I. Three-dimensional problem with smooth boundary surface.* Ann. Phys. **60**, 401 (1970).

[92] E. Bogomolny and E. Hugues. *Semiclassical theory of flexural vibrations of plates.* Phys. Rev. E **57**, 5404 (1998).

[93] G. Tanner and N. Søndergaard. *Short wavelength approximation of a boundary integral operator for homogeneous and isotropic elastic bodies.* Phys. Rev. E **75**, 036607 (2007).

[94] I. Adagideli and P. M. Goldbart. *Quantum andreev billiards: Semiclassical approach to mesoscale oscillations in the density of states.* Int. J. Mod. Phys. B **16**, 1381 (2002).

[95] I. Adagideli, P. Jacquod, M. Scheid, M. Duckheim, D. Loss, and K. Richter. *Geometric correlations and breakdown of mesoscopic universality in spin transport.* Phys. Rev. Lett. **105**, 246807 (2010).

[96] J.-D. Urbina, M. Wimmer, D. Bauernfeind, D. Espitia, I. Adagideli, and K. Richter. *Universal spatial correlations in random spinor fields.* Preprint, arXiv:1108.2652 (2011).

[97] T. H. Hansson and R. L. Jaffe. *The multiple reflection expansion for confined scalar, Dirac, and gauge fields.* Ann. Phys. **151**, 204 (1983).

[98] H. Mathur and A. D. Stone. *Quantum transport and the electronic Aharonov-Casher effect.* Phys. Rev. Lett. **68**, 2964 (1992).

[99] J. Bolte and S. Keppeler. *A semiclassical approach to the Dirac equation.* Ann. Phys. **274**, 125 (1999).

[100] M. Pletyukhov, C. Amann, M. Mehta, and M. Brack. *Semiclassical theory of spin-orbit interactions using spin coherent states.* Phys. Rev. Lett. **89**, 116601 (2002).

[101] O. Zaitsev, D. Frustaglia, and K. Richter. *Role of orbital dynamics in spin relaxation and weak antilocalization in quantum dots.* Phys. Rev. Lett. **94**, 026809 (2005).

[102] I. Adagideli. Personal communications.

[103] R. Balian and C. Bloch. *Distribution of eigenfrequencies for the wave equation in a finite domain: III. Eigenfrequency density oscillations.* Ann. Phys. **69**, 76 (1972).

[104] H. Goldstein. *Classical Mechanics.* (Addison-Wesley, Reading, 1980).

[105] M. Gutzwiller. *Phaseintegral approximation in momentum space and the bound states of an atom. II.* J. Math. Phys. **10**, 1004 (1969).

[106] M. Gutzwiller. *Periodic orbits and classical quantization conditions.* J. Math. Phys. **12**, 343 (1971).

[107] P. Carmier and D. Ullmo. *Berry phase in graphene: Semiclassical perspective.* Phys. Rev. B **77**, 245413 (2008).

[108] J. Wurm, K. Richter, and I. Adagideli. *Edge effects in graphene nanostructures: From multiple reflection expansion to density of states.* Phys. Rev. B **84**, 075468 (2011).

[109] H. Weyl. *Über die asymptotische Verteilung der Eigenwerte.* Kgl. Ges. d. Wiss. Nachrichten. Math. Phys. Klasse **2**, 110 (1911).

[110] M. Berry and M. Tabor. *Closed orbits and the regular bound spectrum.* Proc. R. Soc. Lond. A **349**, 101 (1976).

[111] J. Cserti, A. Csordás, and U. Zülicke. *Electronic and spin properties of Rashba billiards.* Phys. Rev. B **70**, 233307 (2004).

[112] H.-J. Stöckmann. *Quantum Chaos.* (Cambridge Univ. Press, Cambridge, 1999).

[113] M. Tabor. *Chaos and Integrability in Nonlinear Dynamics: An Introduction.* (Wiley, New York, 1989).

[114] A. Einstein. Verh. Dtsch. Phys. Ges. **19**, 82 (1917).

[115] L. Brillouin. *Remarques sur la mécanique ondulatoire.* J. Phys. Radium **7**, 353 (1926).

[116] J. Keller. *Corrected Bohr-Sommerfeld quantum conditions for nonseparable systems.* Ann. Phys. **4**, 180 (1958).

[117] M. Berry and M. Tabor. *Level clustering in the regular spectrum.* Proc. R. Soc. Lond. **356**, 375 (1977).

[118] F. Haake and K. Richter. *Pfade, Phasen, Fluktuationen.* Physik Journal **10** , No. 4, 35 (2011).

[119] S. C. Creagh, J. M. Robbins, and R. G. Littlejohn. *Geometrical properties of Maslov indices in the semiclassical trace formula for the density of states.* Phys. Rev. A **42**, 1907 (1990).

[120] S. M. Reimann, M. Brack, A. G. Magner, J. Blaschke, and M. V. N. Murthy. *Circular quantum billiard with a singular magnetic flux line.* Phys. Rev. A **53**, 39 (1996).

[121] E. Bogachek and G. Gogadze. *Oscillation effects of the "flux quantization" type in normal metals.* J. Exp. Theor. Phys. **36**, 973 (1973).

[122] B. Tatievski, P. Stampfli, and K. Bennemann. *Electronic shell structure of cluster quantum mechanical effects in the semiclassical approximation.* Comp. Mat. Sci. **2**, 459 (1994).

[123] K. Richter, D. Ullmo, and R. Jalabert. *Orbital magnetism in the ballistic regime: Geometrical effects.* Phys. Rep. **276**, 1 (1996).

[124] R. U. Haq, A. Pandey, and O. Bohigas. *Fluctuation properties of nuclear energy levels: Do theory and experiment agree?* Phys. Rev. Lett. **48**, 1086 (1982).

[125] H. S. Camarda and P. D. Georgopulos. *Statistical behavior of atomic energy levels: Agreement with random-matrix theory.* Phys. Rev. Lett. **50**, 492 (1983).

[126] M. Berry. *Semiclassical theory of spectral rigidity.* Proc. R. Soc. Lond. A **400**, 229 (1985).

[127] M. Sieber and K. Richter. *Correlations between periodic orbits and their role in spectral statistics.* Phys. Scr. **128**, 128 (2001).

[128] S. Heusler, S. Müller, A. Altland, P. Braun, and F. Haake. *Periodic-orbit theory of level correlations.* Phys. Rev. Lett. **98**, 044103 (2007).

[129] J. H. Hannay and A. M. Ozorio de Almeida. *Periodic orbits and a correlation function for the semiclassical density of states.* J. Phys. A **17**, 3429 (1984).

[130] G. Benettin and J. M. Strelcyn. *Numerical experiments on the free motion of a point mass moving in a plane convex region: Stochastic transition and entropy.* Phys. Rev. A **17**, 773 (1978).

[131] O. Legrand and D. Sornette. *First return, transient chaos, and decay in chaotic systems.* Phys. Rev. Lett. **66**, 2172 (1991).

[132] S. Heusler, S. Müller, P. Braun, and F. Haake. *Universal spectral form factor for chaotic dynamics.* J. Phys. A: Math. Gen. **37**, L31 (2004).

[133] S. Müller, S. Heusler, P. Braun, F. Haake, and A. Altland. *Periodic-orbit theory of universality in quantum chaos.* Phys. Rev. E **72**, 046207 (2005).

[134] H. U. Baranger, R. A. Jalabert, and A. D. Stone. *Quantum-chaotic scatterings effects in semiconductor microstructures.* Chaos **3**, 665 (1993).

[135] M. Turek and K. Richter. *Leading off-diagonal contribution to the spectral form factor of chaotic quantum systems.* J. Phy. A **36**, L455 (2003).

[136] J. Wurm, K. Richter, and I. Adagideli. *Edge effects in graphene nanostructures: Semiclassical theory of spectral fluctuations and quantum transport.* Phys. Rev. B **84**, 205421 (2011).

[137] L. A. Bunimovich. *On the ergodic properties of nowhere dispersing billiards.* Commun. Math. Phys. **65**, 295 (1979).

[138] L. A. Bunimovich. *Conditions of stochasticity of two-dimensional billiards.* Chaos **1**, 187 (1991).

[139] H. van Houten, J. van Wees, M. G. J. Heijman, and J. P. André. *Submicron conducting channels defined by shallow mesa etch in GaAs-AlGaAs heterojunctions.* Appl. Phys. Lett. **49**, 1781 (1986).

[140] L. Gor'kov, A. Larkin, and D. Khmel'nitskii. *Particle conductivity in a two-dimensional random potential.* J. Exp. Theor. Phys. **30**, 228 (1979).

[141] P. W. Anderson, E. Abrahams, and T. V. Ramakrishnan. *Possible explanation of nonlinear conductivity in thin-film metal wires.* Phys. Rev. Lett. **43**, 718 (1979).

[142] G. Bergmann. *Weak localization in thin films: a time-of-flight experiment with conduction electrons.* Phys. Rep. **107**, 1 (1984).

[143] P. A. Lee and T. V. Ramakrishnan. *Disordered electronic systems.* Rev. Mod. Phys. **57**, 287 (1985).

[144] S. Chakravarty and A. Schmid. *Weak localization: The quasiclassical theory of electrons in a random potential.* Phys. Rep. **140**, 193 (1986).

[145] C. W. J. Beenakker and H. van Houten. *Quantum transport in semiconductor nanostructures.* Solid State Phys. **44**, 1 (1991).

[146] H. U. Baranger, R. A. Jalabert, and A. D. Stone. *Weak localization and integrability in ballistic cavities.* Phys. Rev. Lett. **70**, 3876 (1993).

[147] A. M. Chang, H. U. Baranger, L. N. Pfeiffer, and K. W. West. *Weak localization in chaotic versus nonchaotic cavities: A striking difference in the line shape.* Phys. Rev. Lett. **73**, 2111 (1994).

[148] H. U. Baranger and P. A. Mello. *Mesoscopic transport through chaotic cavities: A random S-matrix theory approach.* Phys. Rev. Lett. **73**, 142 (1994).

[149] R. A. Jalabert, J.-L. Pichard, and C. W. J. Beenakker. *Universal quantum signatures of chaos in ballistic transport.* Europhys. Lett. **27**, 255 (1994).

[150] K. Richter and M. Sieber. *Semiclassical theory of chaotic quantum transport.* Phys. Rev. Lett. **89**, 206801 (2002).

[151] D. V. Khveshchenko. *Electron localization properties in graphene.* Phys. Rev. Lett. **97**, 036802 (2006).

[152] A. F. Morpurgo and F. Guinea. *Intervalley scattering, long-range disorder, and effective time-reversal symmetry breaking in graphene.* Phys. Rev. Lett. **97**, 196804 (2006).

[153] I. L. Aleiner and K. B. Efetov. *Effect of disorder on transport in graphene.* Phys. Rev. Lett. **97**, 236801 (2006).

[154] S. V. Morozov, K. S. Novoselov, M. I. Katsnelson, F. Schedin, L. A. Ponomarenko, D. Jiang, and A. K. Geim. *Strong suppression of weak localization in graphene.* Phys. Rev. Lett. **97**, 016801 (2006).

[155] F. V. Tikhonenko, D. W. Horsell, R. V. Gorbachev, and A. K. Savchenko. *Weak localization in graphene flakes.* Phys. Rev. Lett. **100**, 056802 (2008).

[156] J. Eroms and D. Weiss. *Weak localization and transport gap in graphene antidot lattices.* New J. Phys. **11**, 095021 (2009).

[157] J. Berezovsky and R. M. Westervelt. *Imaging coherent transport in graphene (part II): probing weak localization.* Nanotech. **21**, 274014 (2010).

[158] E. Mucciolo and C. Lewenkopf. *Disorder and electronic transport in graphene.* J. Phys.: Condens. Matter **22**, 273201 (2010).

[159] F. Ortmann, A. Cresti, G. Montambaux, and S. Roche. *Magnetoresistance in disordered graphene: The role of pseudospin and dimensionality effects unraveled.* Europhys. Lett. **94**, 47006 (2011).

[160] P. A. Lee and A. D. Stone. *Universal conductance fluctuations in metals.* Phys. Rev. Lett. **55**, 1622 (1985).

[161] B. Al'tshuler. *Fluctuations in the extrinsic conductivity of disordered conductors.* J. Exp. Theor. Phys. **41**, 648 (1985).

[162] D. Horsell, A. Savchenko, F. Tikhonenko, K. Kechedzhi, I. Lerner, and V. Fal'ko. *Mesoscopic conductance fluctuations in graphene.* Solid State Comm. **149**, 1041 (2009).

[163] M. B. Lundeberg and J. A. Folk. *Spin-resolved quantum interference in graphene.* Nature Phys. **5**, 894 (2009).

[164] J. Berezovsky, M. F. Borunda, E. J. Heller, and R. M. Westervelt. *Imaging coherent transport in graphene (part I): mapping universal conductance fluctuations.* Nanotechnology **21**, 274013 (2010).

[165] A. Rycerz, J. Tworzydło, and C. W. J. Beenakker. *Anomalously large conductance fluctuations in weakly disordered graphene.* Europhys. Lett. **79**, 57003 (2007).

[166] K. Kechedzhi, O. Kashuba, and V. I. Fal'ko. *Quantum kinetic equation and universal conductance fluctuations in graphene.* Phys. Rev. B **77**, 193403 (2008).

[167] M. Y. Kharitonov and K. B. Efetov. *Universal conductance fluctuations in graphene.* Phys. Rev. B **78**, 033404 (2008).

[168] J. Tworzydło, B. Trauzettel, M. Titov, A. Rycerz, and C. W. J. Beenakker. *Sub-poissonian shot noise in graphene.* Phys. Rev. Lett. **96**, 246802 (2006).

[169] V. V. Cheianov and V. I. Fal'ko. *Selective transmission of Dirac electrons and ballistic magnetoresistance of $n-p$ junctions in graphene.* Phys. Rev. B **74**, 041403 (2006).

[170] A. Wiener and M. Kindermann. *Signatures of evanescent mode transport in graphene.* Preprint, arXiv:1108.4442 (2011).

[171] R. Danneau, F. Wu, M. F. Craciun, S. Russo, M. Y. Tomi, J. Salmilehto, A. F. Morpurgo, and P. J. Hakonen. *Shot noise in ballistic graphene.* Phys. Rev. Lett. **100**, 196802 (2008).

[172] L. DiCarlo, J. R. Williams, Y. Zhang, D. T. McClure, and C. M. Marcus. *Shot noise in graphene.* Phys. Rev. Lett. **100**, 156801 (2008).

[173] R. Landauer. *Spatial variation of currents and fields due to localized scatterers in metallic conduction.* IBM J. Res. Dev. **1**, 223 (1957).

[174] M. Büttiker, Y. Imry, R. Landauer, and S. Pinhas. *Generalized manychannel conductance formula with application to small rings.* Phys. Rev. B **31**, 6207 (1985).

[175] D. S. Fisher and P. A. Lee. *Relation between conductivity and transmission matrix.* Phys. Rev. B **23**, 6851 (1981).

[176] H. U. Baranger and A. D. Stone. *Electrical linear-response theory in an arbitrary magnetic field: A new fermi-surface formation.* Phys. Rev. B **40**, 8169 (1989).

[177] S. Heusler, S. Müller, P. Braun, and F. Haake. *Semiclassical theory of chaotic conductors.* Phys. Rev. Lett. **96**, 066804 (2006).

[178] J. Bolte and D. Waltner. *Semiclassical theory of ballistic transport through chaotic cavities with spin-orbit interaction.* Phys. Rev. B **76**, 075330 (2007).

[179] M. Sieber. *Geometrical theory of diffraction and spectral statistics.* J. Phys. A: Math. Gen. **32**, 7679 (1999).

[180] G. M. Zaslavsky. *Stochasticity in quantum systems.* Phys. Rep. **80**, 157 (1981).

[181] I. L. Aleiner and A. I. Larkin. *Divergence of classical trajectories and weak localization.* Phys. Rev. B **54**, 14423 (1996).

[182] I. Adagideli. *Ehrenfest-time-dependent suppression of weak localization.* Phys. Rev. B **68**, 233308 (2003).

[183] P. Jacquod and R. S. Whitney. *Semiclassical theory of quantum chaotic transport: Phase-space splitting, coherent backscattering, and weak localization.* Phys. Rev. B **73**, 195115 (2006).

[184] S. Rahav and P. W. Brouwer. *Ehrenfest time and the coherent backscattering off ballistic cavities.* Phys. Rev. Lett. **96**, 196804 (2006).

[185] P. W. Brouwer and S. Rahav. *Semiclassical theory of the Ehrenfest time dependence of quantum transport in ballistic quantum dots.* Phys. Rev. B **74**, 075322 (2006).

[186] S. Müller, S. Heusler, P. Braun, and F. Haake. *Semiclassical approach to chaotic quantum transport.* New J. Phys. **9**, 12 (2007).

[187] M. Büttiker. *Scattering theory of thermal and excess noise in open conductors.* Phys. Rev. Lett. **65**, 2901 (1990).

[188] D. V. Savin and H.-J. Sommers. *Shot noise in chaotic cavities with an arbitrary number of open channels.* Phys. Rev. B **73**, 081307 (2006).

[189] A. Lassl. *Semiklassik jenseits der Diagonalnäherung: Anwendung auf ballistische mesoskopische Systeme.* Diploma thesis, Universität Regensburg (2003).

[190] H. Schanz, M. Puhlmann, and T. Geisel. *Shot noise in chaotic cavities from action correlations.* Phys. Rev. Lett. **91**, 134101 (2003).

[191] P. Braun, S. Heusler, S. Müller, and F. Haake. *Semiclassical prediction for shot noise in chaotic cavities.* J. Phys. A: Math. Gen. **39**, L159 (2006).

[192] R. S. Whitney and P. Jacquod. *Shot noise in semiclassical chaotic cavities.* Phys. Rev. Lett. **96**, 206804 (2006).

[193] J. C. Boettger and S. B. Trickey. *First-principles calculation of the spin-orbit splitting in graphene.* Phys. Rev. B **75**, 121402 (2007).

[194] M. Gmitra, S. Konschuh, C. Ertler, C. Ambrosch-Draxl, and J. Fabian. *Band-structure topologies of graphene: Spin-orbit coupling effects from first principles.* Phys. Rev. B **80**, 235431 (2009).

[195] S. Okada and A. Oshiyama. *Magnetic ordering in hexagonally bonded sheets with first-row elements.* Phys. Rev. Lett. **87**, 146803 (2001).

[196] Y.-W. Son, M. Cohen, and S. Louie. *Energy gaps in graphene nanoribbons.* Phys. Rev. Lett. **97**, 216803 (2006).

[197] Y.-W. Son, M. Cohen, and S. Louie. *Half-metallic graphene nanoribbons.* Nature **444**, 347 (2006).

[198] H. Zhou, H. Yang, C. Qiu, Z. Liu, F. Yu, M. Chen, L. Hu, X. Xia, H. Yang, C. Gu, and L. Sun. *Experimental evidence of local magnetic moments at edges of n-layer graphenes and graphite.* J. Phys. Chem. C **115**, 15785 (2011).

[199] M. Wimmer, I. Adagideli, S. Berber, D. Tománek, and K. Richter. *Spin currents in rough graphene nanoribbons: Universal fluctuations and spin injection.* Phys. Rev. Lett. **100**, 177207 (2008).

[200] D. A. Areshkin and B. K. Nikolić. *$I-V$ curve signatures of nonequilibrium-driven band gap collapse in magnetically ordered zigzag graphene nanoribbon two-terminal devices.* Phys. Rev. B **79**, 205430 (2009).

[201] J. Jung, T. Pereg-Barnea, and A. H. MacDonald. *Theory of interedge superexchange in zigzag edge magnetism.* Phys. Rev. Lett. **102**, 227205 (2009).

[202] J. Jung. *Nonlocal exchange effects in zigzag-edge magnetism of neutral graphene nanoribbons.* Phys. Rev. B **83**, 165415 (2011).

[203] O. V. Yazyev, R. B. Capaz, and S. G. Louie. *Theory of magnetic edge states in chiral graphene nanoribbons.* Phys. Rev. B **84**, 115406 (2011).

[204] M. Ezawa. *Metallic graphene nanodisks: Electronic and magnetic properties.* Phys. Rev. B **76**, 245415 (2007).

[205] J. Fernández-Rossier and J. J. Palacios. *Magnetism in graphene nanoislands.* Phys. Rev. Lett. **99**, 177204 (2007).

[206] M. Ezawa. *Quasi-ferromagnet spintronics in the graphene nanodisc-lead system.* New J. Phys. **11**, 095005 (2009).

[207] A. D. Güçlü, P. Potasz, O. Voznyy, M. Korkusinski, and P. Hawrylak. *Magnetism and correlations in fractionally filled degenerate shells of graphene quantum dots.* Phys. Rev. Lett. **103**, 246805 (2009).

[208] M. Ezawa. *Complex structure of triangular graphene: Electronic, magnetic and electromechanical properties.* Preprint, arXiv:1101.3612 (2011).

[209] O. Voznyy, A. D. Güçlü, P. Potasz, and P. Hawrylak. *Effect of edge reconstruction and passivation on zero-energy states and magnetism in triangular graphene quantum dots with zigzag edges.* Phys. Rev. B **83**, 165417 (2011).

[210] S. Bhowmick and V. B. Shenoy. *Edge state magnetism of single layer graphene nanostructures.* J. Chem. Phys. **128**, 244717 (2008).

[211] O. V. Yazyev and M. I. Katsnelson. *Magnetic correlations at graphene edges: Basis for novel spintronics devices.* Phys. Rev. Lett. **100**, 047209 (2008).

[212] J. Wurm, I. Adagideli, and K. Richter. *Quantum transport in graphene quantum dots with magnetic edges.* Manuscript in preparation.

[213] L. Tapaszto, G. Dobrik, P. Lambin, and L. Biro. *Tailoring the atomic structure of graphene nanoribbons by scanning tunnelling microscope lithography.* Nature Nanotech. **3**, 397 (2008).

[214] X. Li, X. Wang, L. Zhang, S. Lee, and H. Dai. *Chemically derived, ultrasmooth graphene nanoribbon semiconductors.* Science **319**, 1229 (2008).

[215] D. V. Kosynkin, A. L. Higginbotham, A. Sinitskii, J. R. Lomeda, A. Dimiev, B. K. Price, and J. M. Tour. *Longitudinal unzipping of carbon nanotubes to form graphene nanoribbons.* Nature **458**, 872 (2009).

[216] L. Jiao, X. Wang, G. Diankov, H. Wang, and H. Dai. *Facile synthesis of high-quality graphene nanoribbons.* Nature Nanotech. **5**, 321 (2010).

[217] X. Wang, Y. Ouyang, L. Jiao, H. Wang, L. Xie, J. Wu, J. Guo, and H. Dai. *Graphene nanoribbons with smooth edges behave as quantum wires.* Nature Nanotech. **6**, 563 (2011).

[218] L. C. Campos, V. R. Manfrinato, J. D. Sanchez-Yamagishi, J. Kong, and P. Jarillo-Herrero. *Anisotropic etching and nanoribbon formation in single-layer graphene.* Nano Lett. **9**, 2600 (2009).

[219] Z.-S. Wu, W. Ren, L. Gao, B. Liu, J. Zhao, and H.-M. Cheng. *Efficient synthesis of graphene nanoribbons sonochemically cut from graphene sheets.* Nano Res. **3**, 16 (2010).

[220] A. Chuvilin, E. Bichoutskaia, M. C. Gimenez-Lopez, T. Chamberlain, G. A. Rance, N. Kuganathan, J. Biskupek, U. Kaiser, and A. N. Khlobystov. *Self-assembly of a sulphur-terminated graphene nanoribbon within a single-walled carbon nanotube.* Nature Mat. **10**, 687 (2011).

[221] F. Muñoz Rojas, D. Jacob, J. Fernández-Rossier, and J. J. Palacios. *Coherent transport in graphene nanoconstrictions.* Phys. Rev. B **74**, 195417 (2006).

[222] D. A. Areshkin, D. Gunlycke, and C. T. White. *Ballistic transport in graphene nanostrips in the presence of disorder: Importance of edge effects.* Nano Lett. **7**, 204 (2007).

[223] K. Wakabayashi, Y. Takane, and M. Sigrist. *Perfectly conducting channel and universality crossover in disordered graphene nanoribbons.* Phys. Rev. Lett. **99**, 036601 (2007).

[224] M. Evaldsson, I. V. Zozoulenko, H. Xu, and T. Heinzel. *Edge-disorder-induced Anderson localization and conduction gap in graphene nanoribbons.* Phys. Rev. B **78**, 161407 (2008).

[225] T. C. Li and S.-P. Lu. *Quantum conductance of graphene nanoribbons with edge defects.* Phys. Rev. B **77**, 085408 (2008).

[226] A. Iyengar, T. Luo, H. A. Fertig, and L. Brey. *Conductance through graphene bends and polygons.* Phys. Rev. B **78**, 235411 (2008).

[227] E. R. Mucciolo, A. H. Castro Neto, and C. H. Lewenkopf. *Conductance quantization and transport gaps in disordered graphene nanoribbons.* Phys. Rev. B **79**, 075407 (2009).

[228] I. Martin and Y. M. Blanter. *Transport in disordered graphene nanoribbons.* Phys. Rev. B **79**, 235132 (2009).

[229] M. Yamamoto, Y. Takane, and K. Wakabayashi. *Nearly perfect single-channel conduction in disordered armchair nanoribbons.* Phys. Rev. B **79**, 125421 (2009).

[230] R. Peierls. *Zur Theorie des Diamagnetismus von Leitungselektronen.* Z. Phys. **80**, 763 (1933).

[231] J. M. Luttinger. *The effect of a magnetic field on electrons in a periodic potential.* Phys. Rev. **84**, 814 (1951).

[232] P. W. Anderson. *Absence of diffusion in certain random lattices.* Phys. Rev. **109**, 1492 (1958).

[233] K. Hirose, T. Ohtsuki, and K. Slevin. *Quantum transport in novel Chalker-Coddington model.* Physica E **40**, 1677 (2008).

[234] S. Datta. *Electronic Transport in Mesoscopic Systems.* (Cambridge Univ. Press, Cambridge, 2005).

[235] K. Wakabayashi, Y. Takane, M. Yamamoto, and M. Sigrist. *Electronic transport properties of graphene nanoribbons.* New J. Phys. **11**, 095016 (2009).

[236] J. Wurm, M. Wimmer, and K. Richter. *Symmetries and the conductance of graphene nanoribbons with long-range disorder.* Manuscript in preparation.

[237] S. Schmidmeier, S. H. Jhang, J. Wurm, Y. Skourski, J. Wosnitza, C. Strunk, D. Weiss, K. Richter, and J. Eroms. *Magnetotransport through graphene nanoribbons in high magnetic fields.* Preprint, arXiv:1111.4330 (2011).

[238] N. Ashcroft and N. Mermin. *Solid State Physics.* (Saunders, New York, 1976).

[239] J. Martin, N. Akerman, G. Ulbricht, T. Lohmann, J. H. Smet, K. von Klitzing, and A. Yacobi. *Observation of electron-hole puddles in graphene using a scanning single electron transistor.* Nature Phys. **4**, 144 (2008).

[240] J. G. Checkelsky, L. Li, and N. P. Ong. *Divergent resistance at the Dirac point in graphene: Evidence for a transition in a high magnetic field.* Phys. Rev. B **79**, 115434 (2009).

[241] A. J. M. Giesbers, L. A. Ponomarenko, K. S. Novoselov, A. K. Geim, M. I. Katsnelson, J. C. Maan, and U. Zeitler. *Gap opening in the zeroth landau level of graphene.* Phys. Rev. B **80**, 201403 (2009).

[242] L. Zhang, J. Camacho, H. Cao, Y. P. Chen, M. Khodas, D. E. Kharzeev, A. M. Tsvelik, T. Valla, and I. A. Zaliznyak. *Breakdown of the $n = 0$ quantum hall state in graphene: Two insulating regimes.* Phys. Rev. B **80**, 241412 (2009).

[243] S. Schmidmeier, J. Eroms, D. Weiss, and C. Strunk. unpublished.

[244] V. Krueckl and T. Kramer. *Revivals of quantum wave packets in graphene.* New J. Phys. **11**, 093010 (2009).

[245] J. Rammer. *Quantum Transport Theory* (Westview Press, Reading, 2004).

[246] A. Crépieux and P. Bruno. *Theory of the anomalous Hall effect from the Kubo formula and the Dirac equation.* Phys. Rev. B **64**, 014416 (2001).

[247] P. Carmier, C. Lewenkopf, and D. Ullmo. *Semiclassical magnetotransport in graphene n-p junctions.* Phys. Rev. B **84**, 195428 (2011).

[248] K. Richter, D. Ullmo, and R. A. Jalabert. *Smooth-disorder effects in ballistic microstructures.* Phys. Rev. B **54**, R5219 (1996).

[249] S. Adam, P. W. Brouwer, and S. Das Sarma. *Crossover from quantum to Boltzmann transport in graphene.* Phys. Rev. B **79**, 201404 (2009).

[250] F. T. Vasko and I. V. Zozoulenko. *Conductivity of a graphene strip: Width and gate-voltage dependencies.* Appl. Phys. Lett. **97**, 092115 (2010).

List of publications

- S. Schmidmeier, S. H. Jhang, J. Wurm, Y. Skourski, J. Wosnitza, C. Strunk, D. Weiss, K. Richter, and J. Eroms. *Magnetotransport through graphene nanoribbons in high magnetic fields.* preprint, arXiv:1111.4330 (2011).
- J. Wurm, K. Richter, and I. Adagideli. *Edge effects in graphene nanostructures: Semiclassical theory of spectral fluctuations and quantum transport.* Phys. Rev. B **84**, 205421 (2011).
- J. Wurm, K. Richter, and I. Adagideli. *Edge effects in graphene nanostructures: From multiple reflection expansion to density of states.* Phys. Rev. B **84**, 075468 (2011).
- J. Wurm, M. Wimmer, H.U. Baranger, and K. Richter. *Graphene rings in magnetic fields: Aharonov-Bohm effect and valley splitting.* Semicond. Sci. Technol. **25**, 034003 (2010).
- J. Wurm, M. Wimmer, I. Adagideli, K. Richter, and H.U. Baranger. *Interfaces within graphene nanoribbons.* New J. Phys. **11**, 095022 (2009).
- J. Wurm, A. Rycerz, I. Adagideli, M. Wimmer, K. Richter, and H.U. Baranger. *Symmetry classes in graphene quantum dots: Universal spectral statistics, weak localization, and conductance fluctuations.* Phys. Rev. Lett. **102**, 056806 (2009).

Danksagung

An dieser Stelle möchte ich mich bei allen bedanken, die zum Gelingen dieser Dissertation beigetragen haben.
Zunächst gilt mein Dank Prof. Dr. Klaus Richter, der sich zur Betreuung dieser Arbeit bereit erklärt hat. Er hat sich stets die nötige Zeit genommen, mir bei Problemen weitergeholfen und mich in jeder Hinsicht unterstützt und motiviert. Außerdem möchte ich ihm für die problemlose Ermöglichung zahlreicher Reisen zu Tagungen und nach Istanbul danken.
Ich danke Prof. Dr. İnanç Adagideli für seine Einführung in die Methode der *Multiple Reflection Expansion* und seine Hilfestellung bei vielen Fragen zu unterschiedlichsten Themen. Außerdem danke ich ihm und seiner Familie für die Gastfreundschaft während meiner Aufenthalte in Istanbul.
Besonderer Dank gebührt Dr. Michael Wimmer, der mir seinen Programmcode für meine numerischen Rechnungen zur Verfügung gestellt hat und mir immer mit Rat und Tat zur Seite stand.
Des Weiteren möchte ich Viktor Krückl für seine Hilfe bei vielen unterschiedlichen Problemen danken. Außerdem danke ich ihm für die Bereitstellung seiner Simulationsergebnisse und natürlich für die Bereicherung meines Alltags an der Uni.
Ich danke Dr. Juan-Diego Urbina für zahlreiche Diskussionen fachlicher und sonstiger Natur. Er war für mich stets eine Quelle der Motivation.
Bei Dr. Jack Kuipers und Dr. Daniel Waltner möchte ich mich ebenfalls für viele fachliche Diskussionen und wichtige Ratschläge und Hinweise bedanken.
Für das Korrekturlesen von Teilen dieser Arbeit danke ich herzlich Jan Bundesmann, Dr. Jan Fischer, Dr. Jack Kuipers und Dr. Juan-Diego Urbina.
Ein spezieller Dank geht an Angela Reißer und Ulla Turba, die mir das Leben an der Universität immens erleichtert haben.
Danke auch an alle weiteren (ehemaligen) Kollegen, die zur angenehmen Atmosphäre am Lehrstuhl beigetragen haben.
Für die Finanzierung meiner Arbeit im Rahmen der Graduiertenkollegs 638 und 1570 und des Sonderforschungsbereichs 689 danke ich der DFG.
Zum Schluss bedanke ich mich ganz besonders bei meinen Eltern und vor allem bei Teresa. Danke für Eure ständige Unterstützung während der letzten Jahre und meiner gesamten Studienzeit!

Regensburg, Oktober 2011